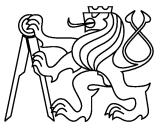

ČESKÉ VYSOKÉ UČENÍ TECHNICKÉ V PRAZE
Fakulta jaderná a fyzikálně inženýrská
Katedra fyzikální elektroniky

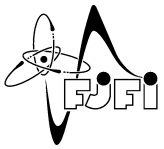

Studium interakce laserového záření s pevnými terči v kontextu urychlování iontů a zapálení jaderné fúze rázovou vlnou

Ing. Ondřej Klimo, Ph.D.

HABILITAČNÍ PRÁCE

Září 2014

Abstrakt

Při interakci vysoce intenzivního laserového impulsu s hmotou vzniká horké plazma. Tento fakt je znám již od poloviny 70. let 20. století a ze stejné doby pochází i myšlenka o využití intenzivního laserového záření k zapálení termojaderné fúze. Tato myšlenka byla do značné míry hnacím motorem vědeckého a technologického vývoje v oblasti pulzních laserových systémů s vysokou energií. Ačkoliv se tehdy zdálo, že k průlomové události demonstrující možnost výroby energie za pomocí laserem zapálené termojaderné fúze dojde již v blízké budoucnosti, na takovou událost stále čekáme i dnes. Překážku na cestě k dosažení inerciální fúzi tvoří dva hlavní faktory. Jsou to hydrodynamické nestability a nestability laserového plazmatu.

Nestability laserového plazmatu vznikají v dlouhé koroně před povrchem terče a vedou převážně k rozptylu laserového záření a urychlování elektronů. Rychlost jejich růstu se zvyšuje s intenzitou a vlnovou délkou laserového záření. Proto mohou představovat problém zejména v nově představeném způsobu zapálení inerciální fúze tzv. "Shock ignition", kdy má být k zapálení reakce v již stlačeném palivu použita dodatečná silná rázová vlna, vyvolaná absorpcí laserového záření o zvýšené intenzitě. I když tento přístup k zapálení fúze sebou přináší některé výhody, jako například lepší hydrodynamickou stabilitu a vyšší energetický zisk, není jasné, zda jeho úspěšné použití neznemožní právě nestability interakce laserového záření s plazmatem. Studiu těchto nestabilit v podmínkách relevantních pro zapálení inerciální fúze dodatečnou silnou rázovou vlnou se věnuje první část této habilitační práce, která prezentuje souhrn publikací autora na toto téma.

Kromě aplikací v termojaderné fúzi se s rozvojem technologie generování a zesilování krátkých laserových impulsů objevila i perspektivní možnost použití laserové interakce jako mikroskopického krátko-pulzního zdroje energetických částic, zejména elektronů, iontů a fotonů (ale sekundárně například i neutronů a pozitronů). Elektrony v terči jsou urychlovány rovněž samotným elektrickým a magnetickým polem laserové vlny, ale k urychlování nabitých částic na velmi vysoké energie se obecně používají pole indukovaná v průběhu laserové interakce s plazmatem. K urychlování iontů tak dochází především na povrchu pevných terčů v důsledku porušení kvazineutrality plazmatu, které je způsobené pohybem urychlených elektronů. Druhá část této habilitační práce prezentuje souhrn publikací autora, zabývajících se novými možnostmi v urychlování iontů, s důrazem na efektivitu tohoto procesu a na možnosti generace iontových svazků s úzkým energetickým spektrem.

Poděkování

V první řadě bych rád poděkoval všem kolegům z Katedry fyzikální elektroniky Fakulty jaderné a fyzikálně inženýrské ČVUT v Praze, kteří se podíleli na výsledcích obsažených v této habilitační práci. Jsou to jmenovitě prof. Ing. Jiří Limpouch, CSc., Ing. Jan Pšikal, Ph.D., RNDr. Jan Proška, Ing. Filip Novotný, Ing. Lucie Štolcová, Ing. Milan Květoň a Ing. Martin Possolt. Všem jim vřele děkuji za skvělou spolupráci na výzkumu týkajícím se urychlování iontů s použitím intenzivních laserových impulsů. Rád bych také poděkoval doc. Ing. Danielu Klírovi, Ph.D. z Fakulty elektrotechnické za rady ohledně formální stránky této práce a dalších podkladů pro habilitační řízení. Velmi děkuji rovněž Ing. Petru Hříbkovi, CSc. a RNDr. Jiřímu Skálovi za informace ohledně historie výzkumu laserových systémů s vysokou energií v tehdejším Československu.

Velmi děkuji také všem zahraničním spolupracovníkům, se kterými jsem měl možnost spolupracovat. Především musím poděkovat profesoru V. Tikhonchukovi, jehož široký přehled, vědecké nadšení i cit pro důležitá témata mi byly velkou inspirací. V neposlední řadě bych rád zmínil skvělou spolupráci s doktorem S. Weberem, doktorem T. Ceccottim a profesorem A. Macchim.

Za podporu výzkumu spojeného s touto habilitační prací děkuji také následujícím projektům:

- Projektu MŠMT č. LC528
- Projektu MŠMT LD - COST CZ č. LD14089
- Postdoktorskému projekt GA ČR č. P205/11/P660
- Standardnímu projekt GA ČR č. GAP205/11/1165
- Projektu MŠMT Kontakt - Barrande č. MEB021029

Výpočetní prostředky byly poskytnuty v rámci projektů:

- Server JADE CINES projekt GENCI 2013-056129
- Prostředky MetaCentra program LM2010005
- Prostředky CERIT-SC program Centre CERIT Scientific Cloud, který je částí OPVVI č. CZ.1.05/3.2.00/08.0144.

Obsah

Úvod

V LETOŠNÍM roce je tomu právě 50 let od konstrukce prvního laserového systému na Katedře fyzikální elektroniky (KFE) na Fakultě jaderné a fyzikálně inženýrské (FJFI), tehdejší Fakultě technické a jaderné fyziky (FTJF) [1]. Jednalo se o jeden z prvních laserových systémů v Československu [2]. Katedru fyzikální elektroniky tehdy vedl prof. Ing. B. Kvasil, DrSc. (později akademik), který zformuloval státní výzkumný úkol "Interakce koherentního záření s hmotou". Na jeho základě byl zkonstruován skupinou vedenou prof. Ing. K. Hamalem, DrSc. a doc. Ing. V. Sochorem, DrSc., ve které působili i (tehdejší studenti) Ing. T. Daříček, CSc. a doc. Ing. A. Novotný, CSc., rubínový laser. Některé součásti laseru byly dodány československými podniky Spolkem pro chemickou a hutní výrobu v Ústí nad Labem a Meoptou v Přerově, další byly pořízeny od zahraniční firmy Preisler, nebo vyrobeny přímo na KFE. S konstrukcí laseru pomáhali také pracovníci Ústavu radiotechniky a elektroniky ČSAV a Fyzikálního ústavu ČSAV [2]. Rubínový laser na KFE byl záhy uzpůsoben pomocí metody Q-spínání ke generaci gigantických impulsů [3, 4] o délce 60 ns a energii 0.2 J a následně bylo dosaženo s použitím pasivního saturovatelného absorbéru dalšího zkrácení generovaného impulsu až na 15 ns [5]. Výkon tohoto systému byl řádově 10 MW a to bylo dostatečné k ionizaci vzduchu a vytvoření plazmatu [6].

Skutečný výzkum laserového plazmatu v Československu začíná na přelomu 70. a 80. let minulého století. V té době (1972-1976) byl na KFE zkonstruován laserový systém založený na neodymem dopovaném skle. Na konstrukci systému, který byl umístěn v objektu fakulty v Břehové ulici, se podíleli zejména Ing. T. Daříček, CSc., prof. Ing. K. Hamal, DrSc., doc. Ing. A. Novotný, CSc., Ing. P. Schmitberger, CSc. a Ing. P. Hříbek, CSc. Špičkový výkon tohoto laseru dosahoval 1 GW a laser byl využíván ke studiu dynamiky vyzařování v mikrovlnné oblasti spektra z laserového plazmatu generovaného ve vzduchu [7].

V letech 1981 - 1984 byl obdobný avšak několikrát výkonnější laserový systém vybudován opět na KFE, tentokrát ale pod vedením prof. Ing. G. Lončara, CSc. a v budově těžkých laboratoří v objektu FJFI v Troji. Tento laserový systém byl pojmenován GOLEM a je spojován se jmény Ing. P. Hříbek, CSc., Ing. P. Schmitberger, CSc. a Ing. I. Čáp. Později v něm byl za účasti Ing. V. Kmetíka, CSc. instalován nový budící oscilátor založený na Nd:YAG. Laser GOLEM sloužil ke studiu interakce laserového záření s pevnolátkovými terči, kterou se zabývali zejména doc. Ing. L. Pína, CSc., prof. Ing. M. Vrbová, CSc. a doc. Ing. M. Kálal, CSc.

V roce 1981 na KFE vznikl rovněž laserový systém na bázi plazmového zrcadla a Nd:sklo zesilovačů bez budícího laserového oscilátoru. Tento systém byl schopen generovat sled pikosekun-

dových impulsů [8, 9] a protože fokusovaný paprsek dosahoval intenzity přibližně 10^{14} W/cm^2, stalo se plazmové zrcadlo zajímavým zdrojem rentgenového záření [10]. Podotkněme, že již tehdy bylo fungování plazmového zrcadla, které umožnilo získávání relativně krátkých laserových impulsů s vysokým výkonem, považováno za projev parametrické nestability (konkrétně stimulovaného Brillouinova rozptylu) a že v dnešní době se rovněž uvažuje o použití této nestability pro zesilování laserových impulsů [11].

V první polovině 80. let minulého století byl na Fyzikálním ústav (FZÚ) ČSAV z iniciativy tehdejšího ředitele akademika B. Kvasila instalován výkonný fotodisociační jodový laserový systém (o výkonu až 0.1 TW), který byl darován z Lebeděvova ústavu v Moskvě. Z původního laserového systému s koncovými stupni buzenými explodujícím drátem byla však využita na FZÚ jenom část, konkrétně oscilátor a dva zesilovače. Další dva výkonové zesilovače byly vyvinuty až v Praze [12]. Tento systém byl zprovozněn v roce 1985 a pojmenován PERUN [13]. Laser PERUN slavil úspěchy zejména při výzkumu laserových zdrojů mnohonásobně nabitých iontů [14]. Později (po roce 2002) byl laser PERUN přebudován na hybridní fotodisociační jodový systém s pevnolátkovým oscilátorem, který byl pojmenován SOFIA [15].

V roce 1998 pak byla ve spolupráci Fyzikálního ústavu AV ČR a Ústavu fyziky plazmatu AV ČR založena nová laserová laboratoř - badatelské centrum PALS, kam byl přemístěn kilojoulový jodový laser ASTERIX IV z Ústavu fyziky plazmatu Maxe Plancka v Garchingu u Mnichova (o výkonu až několik TW). Laser ASTERIX je stále v provozu a badatelské centrum PALS se věnuje zejména výzkumu spojenému s inerciální termojadernou fúzí [16–18], rentgenovými lasery [19, 20], urychlováním iontů [21, 22] a vznikem a interakcí plazmových výtrysků (jetů) [23]. Po vzoru laseru SOFIA se uvažovalo rovněž o přebudování laseru PALS na hybridní systém s pevnolátkovým oscilátorem. Od tohoto projektu však bylo z nedostatku finančních prostředků upuštěno.

V roce 2008 byl na KFE pořízen a instalován desetimilijoulový titan-safírový laser (o výkonu 0.1 TW). Tento laser je využíván k pokusům, které se týkají modifikace materiálů a povrchů [24, 25], nebo vyzařování záření v ultrafialové resp. rentgenové oblasti spektra. V roce 2011 byl podobný, ale mnohem výkonnější laser s energií 0.9 J (o výkonu 25 TW) instalován rovněž v prostorách badatelského centra PALS [26]. Tento laser je používán k urychlování částic [27] a generaci rentgenového záření včetně rentgenového laseru. V současné době je dokonce možné použít v rámci jednoho experimentu oba lasery badatelského centra PALS současně, a to poměrně dobře synchronizované [28].

V roce 2009 byl spuštěn přípravný projekt pro stavbu nového laserového výzkumného centra ELI Beamlines v Dolních Břežanech, které by mělo být plně dokončeno v horizontu několika let (pravděpodobně v roce 2017). V rámci tohoto centra bude provozováno několik různých laserových systémů, většinou s velmi vysokým výkonem v řádu PW a relativně vysokou opakovací frekvencí výstřelů. Toto výzkumné centrum by v době svého spuštění mělo poskytnout

jedinečné nástroje pro výzkum a využití laserového plazmatu, které budou na nejvyšší světové úrovni.

Z předchozího je zřejmé, že experimentální výzkum laserového plazmatu má v ČR i na KFE poměrně dlouhou tradici. Ruku v ruce s experimenty jde i výzkum v oblasti teoretické, jehož nedílnou součástí jsou i počítačové simulace. Na KFE existuje tedy i teoretická skupina zabývající se fyzikou laserového plazmatu a autor této práce je jejím členem od roku 2001. V rámci této skupiny se postupně věnoval studiu rentgenového vyzařování (K-α) z pevných terčů ozařovaných krátkými intenzivními laserovými impulsy [29, 30], vzniku a transportu rychlých elektronů v pevných terčích [31], průběhu ionizace plazmatu silným polem a vlivu ionizace na probíhající procesy [32], vlastnímu vyzařování nabitých částic při pohybu ve velmi silném laserovém poli [33], urychlování iontů [34–40] a parametrickým nestabilitám a absorpci delších laserových impulsů v souvislosti s inerciální fúzí [41–46]. Nejdůležitější práce vzniklé v poslední době v rámci dvou posledně zmíněných témat jsou i obsahem této habilitační práce.

Tato práce je členěna do šesti částí. V první části je stručně shrnut vývoj výzkumu v oblasti inerciální fúze a rozebrán princip zapálení inerciální termojaderné fúze silnou rázovou vlnou včetně role parametrických nestabilit v tomto procesu. Jsou zde diskutovány zejména tři nejdůležitější parametrické procesy relevantní v inerciální fúzi, stimulovaný Ramanův a Brillouinův rozptyl a dvouplazmonový rozpad. Ve druhé části jsou prezentovány nejdůležitější autorovy příspěvky publikované na toto téma, je uveden jejich vědecký přínos a výsledky jsou zasazeny do kontextu současného výzkumu inerciální fúze zapálené silnou rázovou vlnou. Ve třetí části je stručný úvod do problematiky urychlování iontů, které probíhá při interakci krátkých intenzivních laserových impulsů s pevnými terči. Výsledky publikované na toto téma jsou uvedeny, okomentovány a shrnuty v kapitole čtvrté. Pátá kapitola obsahuje závěrečné shrnutí, výhled do budoucna a je zde také zmíněn podíl studentů na tomto výzkumu. Na konci práce jsou pak vloženy diskutované publikace.

Výsledky popsané v této habilitační práci byly většinou získány ve spolupráci s kolegy z KFE resp. s kolegy z jiných, ať již českých nebo především zahraničních institucí. Nicméně, na všech výsledcích uvedených v této práci se autor podílel velmi významnou měrou, což dokládá fakt, že je ve většině případů prvním a korespondenčním autorem diskutované publikace. Výjimku tvoří pouze jedna teoretická publikace týkající se parametrických nestabilit při interakci laserového záření s terči [43] a tři experimentální publikace [38–40], kde je první autorem většinou vedoucí experimentálního týmu. Nicméně i v těchto případech je podíl teoretického studia a přípravy experimentů, na nichž se autor podílel, velmi významný.

1 Interakce laserového záření s plazmatem v kontextu inerciální fúze a jejího zapálení silnou rázovou vlnou

Ke slučování jader dochází v důsledku silných přitažlivých jaderných sil, které působí efektivně pouze na velmi krátké vzdálenosti. Aby se k sobě dvě jádra dostatečně přiblížila, je třeba překonat značný Coulombův potenciál, a proto musí mít interagující jádra vysokou kinetickou energii. Urychlování jednotlivých jader a následné srážky s materiálem o nižší teplotě však nevedou k celkovému zisku energie. Získávat energii je možné pouze z termojaderné fúze probíhající v přibližné lokální tepelné rovnováze, při které Coulombovské srážky nevedou k disipaci energie jader schopných uskutečnění fúzní reakce. K výrobě energie pomocí inerciální termojaderné fúze tedy musíme nejdříve mnoho energie dodat a palivo zahřát na velmi vysokou tzv. zápalnou teplotu, která závisí především na hustotě a konfiguraci paliva. Zahřátí paliva na tuto vysokou teplotu a jeho následné udržení je velmi komplikované a nelze ho v našich podmínkách realizovat jednoduchými postupy.

1.1 Počátky a vývoj výzkumu inerciální termojaderné fúze

Výzkum inerciální termojaderné fúze je od samého počátku spojen s válečným úsilím. Až později se začalo seriózně uvažovat i o mírovém využití jaderné fúze. Toho by si měl být každý zodpovědný vědec, působící v této oblasti, vědom. Proto je zde na úvod stručně shrnuta i historie vojenského výzkumu, ze kterého dnes vychází i velká část výzkumu civilního.

První úvahy o realizaci inerciální termojaderné fúze se objevily v období druhé světové války v rámci projektu Manhattan. Uvádí se, že myšlenku zapálení termojaderné fúze pomocí energie uvolněné při jaderném výbuchu navrhl E. Fermi při rozhovoru s E. Tellerem již v září 1941 [47]. Tehdy byl tímto návrhem sledován cíl umocnění výbuchu primární štěpné nálože jaderné bomby. E. Teller a další později tento koncept dále rozpracovávali a v roce 1951 byla demonstrována iniciace fúzních reakcí jadernou explozí v rámci operace Greenhouse pod kódovým označením George [47]. Vzápětí pak byla E. Tellerem a S. Ulamem navržena možnost umístění fúzního paliva odděleně od jaderné nálože, avšak ve stejném obalu, a bylo předpokládáno použití měkkého rentgenového záření, které se vytvoří v obalu bomby díky absorpci energie uvolněné jaderným výbuchem, ke stlačení a ohřátí fúzního paliva na požadovanou teplotu. Tento koncept se ukázal jako velmi úspěšný a byl otestován v roce 1952 pod kódovým označením Ivy Mike [48].

V roce 1957 se na schůzce svolané E. Tellerem začalo seriózně uvažovat o mírovém využití

energie uvolněné při inerciální termojaderné fúzi. Jedním z výsledků byla operace Plowshare ("radlice"), která jednak usilovala o využití menších výbuchů uzavřených v podzemních prostorách k získávání energie a dále usměrnění velkých termojaderných explozí například k hloubení tunelů, frakování při těžbě plynu apod. Tato operace však byla po několika letech zastavena z důvodu rozsáhlého znečištění životního prostředí nebo produktů těžby radiací [49].

Jiným výsledkem schůzky byla snaha o minimalizaci fúzní exploze tak, aby ji bylo možné kontrolovat a provádět v laboratořích. Tomuto problému se začal věnovat J. Nuckolls. Jeho první koncept počítal s podobnou konfigurací, jaká byla použita u vodíkové bomby a jaké dnes říkáme nepřímé zapálení fúze (v anglické terminologii "indirect drive"). Malé množství paliva je umístěno v kovovém pouzdře (tzv. "hohlraumu"), jehož povrch je zahřátý na velmi vysokou teplotu a produkuje rentgenové záření, které stlačuje a ohřívá palivo uvnitř [50]. Komprese terče je v tomto případě velmi důležitá, neboť pokud dojde k zapálení inerciální fúze, závisí množství spáleného paliva v podstatě přímo úměrně na jeho hustotě. Záhy bylo J. Nuckollsem upraveno uspořádání hmoty terče a časového průběhu impulsu dodávané energie tak, že došlo ke značnému zvýšení energetického zisku daného procesu. V tomto uspořádání byla většina paliva koncentrována v povrchové slupce kulatého terče a vnitřek terče byl téměř prázdný. Pro impuls dodávané energie byl navrhován takový časový průběh, že intenzita energie na terči s časem rychle narůstala, čímž byla významně zvýšena účinnost adiabatické komprese pomocí série slabých rázových vln [51]. Navržený terč je schematicky znázorněn na Obr. 1.1.

Trajektorie slabých rázových vln, které terč stlačují, se přitom protnou až uvnitř terče, kde je relativně řídké palivo. Tím dojde k zahřátí tohoto malého množství paliva na vysokou teplotu a později k zapálení fúze. Horké palivo uvnitř terče, kde dochází k zapálení fúze, se pak nazývá horká tečka (v anglické terminologii "hot spot"). Většina paliva v tomto případě shoří až v důsledku vlny hoření, která se šíří ze středu terče ven. Počítačovými simulacemi bylo předpovězeno, že tímto postupem bude možné zapálit 1 mg fúzního paliva dodáním 1 MJ energie a získaná energie bude zhruba 50 MJ [50]. Později bylo dokonce předpovězeno dosažení tzv. marginálního zapálení (hraniční situace, kdy k zapálení fúze ještě dojde, ale v důsledku nedostatečného prohoření paliva nedochází ke znatelnému zisku energie) s dodanou energií pouze několika desítek kJ [51]. S postupem času se však ukázalo, že marginální energie je mnohem vyšší. Dnes se předpokládá, že zhruba o tři řády [52]. To je způsobeno velmi silnou závislostí energie potřebné pro marginální zapálení na rychlosti imploze, jež je naopak omezená rozvojem nestabilit.

První práce týkající se zapálení kontrolované termojaderné inerciální fúze předpokládaly tehdy neznámý zdroj energie, založený např. na pulzních výkonových zařízeních jako pinčích, urychlovačích nabitých částic, případně urychlení nějakých makroskopických projektilů apod. Po prvním úspěšném zkonstruování a demonstraci laseru T. Mainmanem [53] byla záhy navržena možnost použití laserového záření k nepřímému zapálení inerciální fúze. Laserové záření se zdálo velmi vhodné z hlediska soustředění velkého množství energie a zároveň možnosti tvarování

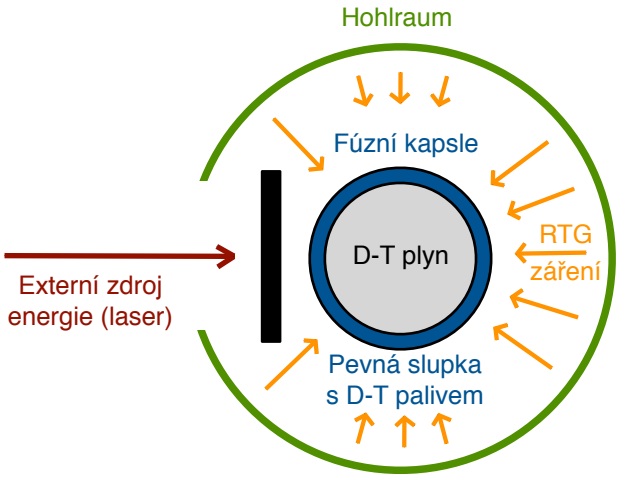

Obrázek 1.1: Schématické znázornění počátečních návrhů zapálení kontrolované termojaderné fúze podle návrhů J. Nuckollse. Slupkový terč je umístěn v tzv. hohlraumu, tedy obálce, která je ohřáta externím (tzv. primárním) zdrojem na vysokou teplotu řádu stovek eV a následně vyzařuje intenzivně v měkké rentgenové oblasti. Na konci komprese terče dojde v D-T plynu uprostřed k silnému ohřevu a zapálení fúze.

časového profilu impulsu této energie. Záhy bylo také navrženo zapálení inerciální fúze přímým ozařováním terče pomocí laserových svazků a to R. Kidderem [50] v USA a N. G. Basovem a O. N. Krokhinem [54] v tehdejší SSSR. Dnes je tento koncept nazýván přímým zapálením fúze (v anglické terminologii "direct drive").

Po zkušenostech z projektu Manhattan bylo od samého počátku výzkumu inerciální fúze jasné, že limitujícím faktorem stlačení paliva je udržení velmi dobré symetrie komprese. V opačném případě dochází k rychlému rozvoji hydrodynamických nestabilit, které vedou ke zvyšování nesymetrie, oslabování tloušťky slupky a míchání horkého a studeného paliva [55]. Omezení rozvoje hydrodynamických nestabilit klade velké nároky zejména na symetrii ozařování terče, symetrii terče samého a nerovnosti na povrchu terče (vnitřním i vnějším). Hydrodynamické nestability limitují použití větších terčů s tenčí povrchovou slupkou, které je možné lépe urychlit na vysokou implozní rychlost.

Druhým limitujícím faktorem, který se v počátcích výzkumu laserového plazmatu objevil, byla laserová absorpce a nestability v laserovém plazmatu, především tzv. parametrické nestability [56, 57]. Absorpce inverzním brzdným zářením (neboli Coulombovskými srážkami elektronů s ionty), která je v inerciální fúzi žádoucí, závisí na teplotě elektronů a pro vysoké teploty se může stát neefektivní. Zároveň s klesající efektivitou Coulombovských srážek přestávají být disipovány plazmové vlny a vznikají tak vhodné podmínky pro jejich šíření a růst. Za významný problém byl považován zejména negativní dopad plazmových vln na možnou kompresi terče v důsledku předehřátí elektrony zachycenými a urychlenými v těchto vlnách. Začíná se tedy uvažovat o použití krátkých vlnových délek, které tento problém mohou potlačit [51].

1.2 Neizobarická konfigurace a její rychlé zapálení

Uspořádání terče a jeho ozařování navržené J. Nuckollsem vytváří v době zapálení přibližně izobarickou konfiguraci paliva. Uprostřed terče vzniká velmi horká a méně hustá část, která je obklopena studenější hustou částí. Jako hlavní problém této konfigurace se v současných experimentech v Lawrence Livermore National Laboratory (LLNL) na laseru National Ignition Facility -NIF (jediném již funkčním laserovém systému, jehož parametry jsou teoreticky dostačující k zapálení inerciální fúze), jeví obtížnost dosažení dostatečné teploty resp. tlaku v horkém palivu uvnitř terče. Důvodem jsou pravděpodobně hydrodynamické nestability, které způsobují promíchávání studeného a horkého paliva [58].

Samotná komprese paliva se nezdá natolik obtížná a potřebná plošná hustota terče, která je v případě isobarické konfigurace přibližně 0.3 g/cm^3 [55], byla již několikanásobně překonána [59]. Objevila se tedy i myšlenka oddělení fáze komprese a následného rychlého ohřevu již stlačeného paliva. Zde se v okamžiku zapálení nejedná o izobarickou konfiguraci, ale v některých případech spíše o izochorickou. Myšlenka oddělení komprese a zapálení byla zmiňována již v 60. letech minulého století [60], avšak v té době nebylo známo, jak lze dostatečně rychlého ohřevu dosáhnout. Atraktivita neizobarické konfigurace paliva je zřejmá, když se na kinetický tlak díváme jako na hustotu kinetické energie. Vysoká hustota kinetické energie je nutná v místě, ve kterém má dojít k zapálení fúze, ne však v okolním palivu. Z toho vyplývá, že neizobarická konfigurace může být energeticky výhodnější a může poskytnout větší zisk energie, resp. možnost zapálení fúze pomocí laserů s nižší energií, pokud však samotné ohřátí paliva nebude energeticky příliš náročné. Další nesporná výhoda neizobarické konfigurace, která vyplývá z nižší požadované implozní rychlosti, je možnost použití silnější slupky terče, a tedy omezení vlivu hydrodynamických nestabilit [55].

Krátce po objevení zesilování krátkých laserových impulsů technikou Chirped Pulse Amplification [61] bylo navrženo rychlé zapálení neizobarické konfigurace (v anglické terminologii "fast ignition") pomocí svazků elektronů [62] a později i svazků iontů [63] urychlených petawatovými lasery. Tato myšlenka je v současné době intenzivně zkoumána, ale zdá se, že naráží také na těžko překonatelné problémy [64]. Například u elektronů je značným problémem široké úhlové rozdělení svazku, které způsobuje, že se ohřívá mnohem větší oblast, než je třeba. Jiná možnost zapálení fúze v již stlačeném palivu je dodání energie prostřednictvím velmi silné rázové vlny (v anglické terminologii "shock ignition"). S tímto návrhem přišel již v roce 1983 V. A. Scherbakov [65], avšak v jeho návrhu je energie, kterou je potřeba dodat silnou rázovou vlnou, příliš velká (neboť teplota terče je před průchodem této rázové vlny pouze 1 keV) a z hlediska možností současných laserů nereálná. Realističtější návrh R. Bettiho [66] počítá v podstatě s do jisté míry kompromisním řešením, kdy je palivo uprostřed terče ohřáto již během komprese na relativně vysokou teplotu 2-3 keV a silná rázová vlna nemusí palivu dodat tak velké množství energie. Tato silná rázová vlna je navíc zesílena nejdříve svou konvergencí

a dále srážkou v hustém materiálu stlačené slupky s divergujícími rázovými vlnami odraženými od středu terče [67].

Ať již mluvíme o zapálení fúze pomocí svazků energetických částic nebo o zapálení silnou rázovou vlnou, můžeme se na danou situaci dívat i tak, že na konci interakce dojde k výraznému zvýšení intenzity laserového záření. Jedná se tedy svým způsobem jen o jiné tvarování časového profilu impulsu dodávané energie, než jaké navrhl J. Nuckolls. Procesy, které vedou k zapálení paliva, jsou však v těchto případech odlišné. Jiné tvarování časového profilu laserového impulsu je relevantní zejména v případě "shock ignition", kdy je intenzita laserového záření zvýšena pouze zhruba o jeden řád po dobu několika stovek pikosekund a je nutný i určitý stupeň symetrie ozařování. Takové konfigurace lze totiž dosáhnout i se stávajícími laserovými systémy (např. NIF, OMEGA). Zvýšená intenzita laserového záření je však tak vysoká, že při interakci laserového impulsu s plazmatem začínají hrát důležitou roli také nelineární procesy, které nejsou v této oblasti parametrů dosud dostatečně experimentálně ani teoreticky prozkoumány. Zatím se tedy pouze předpokládá, že absorpce laserového záření bude dostatečná k vytvoření potřebného tlaku v ablační oblasti a že nedojde k předehřátí terče případným vznikem horkých elektronů. Fyzikou interakce laserového záření s plazmatem v podmínkách "shock ignition" se zabýváme dále v této práci.

1.3 Interakce laserového záření s plazmatem

1.3.1 Počáteční podmínky interakce

Než začneme diskutovat interakci samotnou, stanovme si nejprve podmínky, za kterých v případě zapálení inerciální fúze rázovou vlnou probíhá. Budeme zde předpokládat pouze přímé ozařování terče laserovými impulsy. O nepřímém zapálení inerciální termojaderné fúze pomocí dodatečné silné rázové vlny se v současné době neuvažuje pravděpodobně proto, že by to vyžadovalo příliš vysokou a obtížně dosažitelnou teplotu záření v hohlraumu. Budeme rovněž uvažovat situaci, kdy je palivo uprostřed terče zahřáto částečně již před příchodem silné rázové vlny, tak jak to bylo navrženo R. Bettim v [66] a budeme se zabývat pouze interakcí intenzivního laserového impulsu, který má vytvořit silnou rázovou vlnu. Nelineární procesy při interakce laserového záření s plazmatem během komprese terče nejsou považovány za tak důležité z důvodu relativně nízké laserové intenzity (nižší než při standartní schématu zapálení).

Pro zapálení termojaderné fúze v deuterio-tritiovém terči můžeme použít kritérium v následujícím tvaru [68]

$$p_h > 520 \left(\frac{30\ \mu\text{m}}{R_h} \sqrt{\frac{6}{\rho_c/\rho_h}} \right)\ \text{Gbar}\ , \tag{1.1}$$

kde R_h je poloměr terče v μm, ρ_h a p_h jsou hustota a tlak v oblasti horkého paliva uprostřed terče a ρ_c je hustota paliva v okolní stlačené slupce. Podle současných výpočtů a návrhů terčů je hodnota $\rho_c/\rho_h \approx 10$ a $R_h \approx 50\ \mu$m [55]. Pro zapálení je tedy nutný tlak řádově několik set Gbar. K dosažení tak vysokého tlaku v oblasti zapálení je nutné, aby silná rázová vlna šířící se směrem do terče z ablační oblasti měla sama tlak zhruba o tři řády nižší. Ablační oblast se v čase vzniku silné rázové vlny nachází většinou zhruba v polovině původního poloměru terče, tedy pro většinu terčů zhruba 0.3 mm od středu [68]. Silná rázová vlna je pak zesílena nejprve sférickou konvergencí do místa vzdáleného od středu zhruba 60 μm, kde se sráží s divergujícími rázovými vlnami odraženými od středu terče. Radiální závislost tlaku konvergující rázové je v tomto případě přibližně popsána jedním z Guderleyových řešení [69], $p \propto R^{-0.9}$ a rázová vlna je tedy zesílena téměř o jeden řád [70]. K dalšímu zesílení o více než jeden řád dochází při srážce s několika divergujícími rázovými vlnami ve stlačené slupce (maximální zesílení při srážce s jednou vlnou je přitom šestinásobné) [70] a k poslednímu zesílení dochází při sférické konvergenci do středu terče v horkém palivu uvnitř slupku. Toto zesílení je opět přibližně popsáno jedním z Guderleyových řešení [71] a zesílení je opět zhruba o jeden řád [72] .

Pro zapálení inerciální termojaderné fúze tedy potřebujeme vytvořit rázovou vlnu, jejíž tlak v ablační oblasti bude přibližně 300 Mbar. Vytvoření tak silné rázové vlny dosud nebylo demonstrováno. Tlak rázové vlny v ablační oblasti se řídí přibližně vztahem [46]

$$p_a \approx 57 \left(\eta_{abs} I_L/\lambda_L\right)^{2/3}\ \text{Mbar}\ , \tag{1.2}$$

kde η_{abs} je absorpční koeficient a I_L a λ_L jsou intenzita laserového záření v PW/cm^2 a vlnová délka v μm. Pro předpokládané ultrafialové laserové záření o vlnové délce 351 nm a 60% absorpci potřebujeme tedy pro zapálení fúze rázovou vlnou laserovou intenzitu $I_L \approx 5{-}10$ PW/cm^2. Tím máme v podstatě dané základní parametry laserového záření. Podotkněme ještě, že v poslední době se uvažuje i vytvoření silné rázové vlny pomocí laserového záření delších vlnových délek, např. druhé harmonické laserové frekvence. Výhoda tohoto přístupu spočívá v tom, že není nutná další ztrátová konverze na 3. harmonickou frekvenci, která se jinak používá především.

Parametry plazmatu jsou známé z hydrodynamických simulací. Vzhledem k tomu, že časové okno pro vytvoření silné rázové vlny je dlouhé zhruba 300 ps [67] a časové měřítko, na kterém se výrazně mění parametry plazmatu, je delší, jsou parametry plazmatu dány poměrně jednoznačně. Z hydrodynamických simulací pak vyplývá, že charakteristická délka hustotního profilu

v okolí kritické hustoty (místa, kde je frekvence laserového záření rovna frekvenci plazmových vln) je zhruba 200 μm, teplota elektronů je o něco vyšší než 2 keV a je v oblasti interakce relativně homogenní a teplota iontů je zhruba 2-3 krát nižší. Slupka terče je pak většinou plastová a budeme tedy předpokládat, že je složena z uhlíku a vodíku v poměru 1:2.

1.3.2 Absorpce laserové vlny a vznik a útlum plazmových vln

Laserová vlna šířící se prostředím rozkmitává nabité částice, zejména elektrony. Pohyb elektronů je doprovázen Coulombovskými srážkami s méně pohyblivými ionty a tím dochází k absorpci energie laserového záření do tepelného pohybu elektronů. Tento proces se nazývá srážková absorpce nebo inverzní brzdné záření a jeho účinnost závisí na teplotě elektronů (T_e), hustotě iontů (n_i) a náboji iontů (Z_i) [73]

$$\nu_{ei} = \frac{4\sqrt{2\pi}\ n_i Z_i^2 e^4 \ln\Lambda}{3\left(4\pi\varepsilon_0\right)^2 \sqrt{m_e}\ T_{e,eV}^{3/2}} \quad , \tag{1.3}$$

kde m_e je hmotnost elektronů a ε_0 je permitivita vakua. Teplota elektronů $T_{e,eV}$ je v tomto případě v jednotkách eV, jak je to ve fyzice plazmatu běžné. Koeficient srážkové absorpce laserového záření v plazmatu lze pak teoreticky vyjádřit jako [73]

$$\alpha = 1 - \exp\left(-\int \frac{\nu_{ei}(n_c)}{c}\left(\frac{n_e}{n_c}\right)^2\left(1-\frac{n_e}{n_c}\right)^{-1/2} dx\right) \quad , \tag{1.4}$$

kde n_e je elektronová a n_c kritická hustota, c je rychlost světla a meze integrálu jsou souřadnice vakua před terčem a kritické hustoty v terči. Pokud tento koeficient absorpce vyčíslíme pro výše uvedené parametry plazmatu, dostáváme $\alpha \approx 1$. Z experimentů však víme, že koeficient absorpce závisí pro vysoké intenzity laserového záření i na této intenzitě a pro intenzity vyšší než 10^{15} W/cm^2 (pro vlnovou délku 351 nm) se srážková absorpce stává postupně méně efektivní [74]. Podle modelu v [55] je například koeficient srážkové absorpce pro výše zmíněné parametry a pro intenzitu laserového záření 10 PW/cm^2 pouze 0.27. V takovém případě začínají být důležité i jiné, nelineární procesy, které mohou rovněž vést k absorpci energie laserového záření.

Laserové záření interaguje s plazmatem také tím, že způsobuje vznik plazmových vln. Tyto vlny mohou být indukovány buď přímo elektrickým polem laserové vlny, nebo tzv. ponderomotorickou silou. V plazmatu s nenulovou teplotou se tyto vlny šíří a mohou zachycovat a urychlovat částice nebo i zpětně interagovat s laserovým zářením. Indukované plazmové vlny

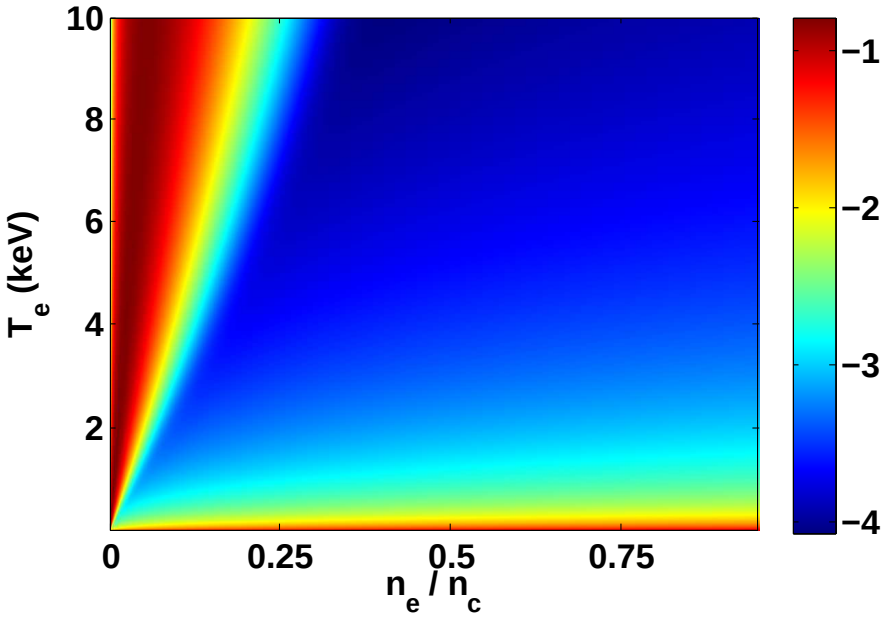

Obrázek 1.2: Tlumení elektronových plazmových vln. Na obrázku je zobrazen logaritmus srážkové frekvence pro Coulombovské srážky elektronů s ionty sečtený s frekvencí Landauova útlumu. Pro parametry plazmové vlny předpokládáme frekvenci a vlnové číslo shodné s laserovou vlnou o vlnové délce 351 nm. Výsledek je normován na lokální frekvenci elektronový plazmových oscilací a zobrazen v závislosti na elektronové teplotě a hustotě (normované na kritickou hustotu). Ve srážkové frekvenci předpokládáme průměrný náboj iontů $Z = 2.67$.

se mohou rovněž tlumit srážkovými procesy, ale existuje zde i jiný způsob jejich tlumení, Landaův útlum. Princip tohoto útlumu je poměrně jednoduchý. Plazmová vlna se šíří plazmatem s určitou fázovou rychlostí a částice, které mají rychlost menší, urychluje, zatímco částice s vyšší rychlostí jsou vlnou brzděny. Jelikož v plazmatu s Maxwellovským rychlostním rozdělením je větší počet částic s rychlostí nižší než je fázová rychlost vlny, dochází k úbytku energie plazmové vlny a jejímu postupnému útlumu. Rychlost Landauova útlumu je možné vyjádřit jako [75]

$$\gamma_L = -\left(\frac{\pi}{8}\right)^{1/2} \frac{\omega_e}{(k_e\lambda_D)^3} \exp\left[-\frac{1}{2(k_e\lambda_D)^2} - \frac{3}{2}\right] \quad , \tag{1.5}$$

kde ω_e a k_e jsou frekvence a vlnové číslo tlumené elektronové plazmové vlny a λ_D je Debyeova délka. Stejné tlumící mechanismy se vyskytují i u iontových plazmových vln, ale pro parametry plazmatu, které nás zajímají, jsou tyto procesy méně důležité.

Rychlost útlumu elektronových plazmových vln v porovnání s plazmovou frekvencí je znázorněna na Obr. 1.2 v závislosti na hustotě a elektronové teplotě plazmatu. Pro elektronové

plazmové vlny tlumené Landauovým útlumem předpokládáme frekvenci a vlnovou délku shodnou s laserovou vlnou o vlnové délce $\lambda = 351$ nm. Tento předpoklad je opodstatněný tím, že indukované elektronové plazmové vlny mají většinou tyto parametry podobné parametrům laserové vlny. Z obrázku je zřejmé, že elektronové plazmové vlny jsou velmi silně tlumeny v případě nízké teploty ($T_e \lesssim 1$keV) Coulombovskými srážkami a v případě nižší hustoty a vyšší teploty Landauovým útlumem. Oblast vyšších teplot a hustot plazmatu, kde převládá modrá barva můžeme pokládat za oblast s relativně nízkým útlumem a možným rychlých růstem plazmových vln. Důležitý je rovněž fakt, že s rostoucí teplotou plazmatu se rozšiřuje oblast silného Landauova útlumu až ke čtvrtině kritické hustoty, přičemž vysoká teplota není reálná jako počáteční podmínka, nicméně může být dosažena v průběhu interakce.

1.3.3 Parametrické nestability

V oblastech, kde nedochází k silnému útlumu plazmových vln se tyto vlny mohou šířit a jejich amplituda může postupně narůstat. K tomu dochází především vlivem parametrických nestabilit, což jsou nelineární procesy vzájemné interakce několika vln, pro něž je použitelný teoretický popis pomocí parametrického oscilátoru. Parametrickou nestabilitou můžeme obecně nazvat nelineární jev, v němž periodická změna parametrů prostředí způsobuje nárůst oscilací s jinou frekvencí. Roli nelinearity v tomto kontextu hraje především ponderomotorická síla spojená s tlakem záření elektromagnetické vlny. V laserovém plazmatu se nejčastěji vyskytují třívlnové parametrické procesy, při nichž interaguje laserová vlna s plazmovou vlnou za účasti další elektromagnetické nebo plazmové vlny. Mechanismus parametrické nestability si můžeme představit nejlépe na stimulovaném rozptylu, kdy třetí vlnou je rozptýlené laserové záření.

Dopadající laserová vlna interaguje s volnými elektrony v plazmatu a rozkmitává je. Příčné oscilace elektronů jsou spojeny s proměnným příčným proudem a tedy se vznikem rozptýleného světla. Frekvence tohoto světla může být modulována periodickou poruchou hustoty plazmatu. Tato porucha přitom nemusí být v plazmatu přítomna od začátku ve formě vlny, ale vlna může postupně narůstat z původně náhodných fluktuací prostředí. Obě elektromagnetické vlny, dopadající i rozptýlená, se spolu skládají a v místech jejich konstruktivní interference působí silnější ponderomotorická síla. Tato síla se projevuje jako změna v kinetickém tlaku a zpětně ovlivňuje poruchu hustoty plazmatu a tedy i vznik a růst plazmové vlny. Pokud jsou splněny rezonanční podmínky pro existenci všech tří vln, rozptýlená a plazmová vlna postupně narůstají a odčerpávají energii z dopadající laserové vlny.

Rezonanční podmínky jsou vyjádřeny Manley-Roweovými vztahy [76],

$$\omega_0 = \omega_1 + \omega_2 \ , \quad \overrightarrow{k_0} = \overrightarrow{k_1} + \overrightarrow{k_2} \ , \tag{1.6}$$

kde ω jsou frekvence a $\overrightarrow{k}$ vlnové vektory interagujících vln a index 0 označuje vlnu dopadající. Každá vlna přitom musí splňovat vlastní disperzní vztah příslušející danému typu vlny.

Parametrické nestability mohou narůstat buď jako absolutní nebo jako konvektivní. Absolutní nestabilita se vyznačuje tím, že její amplituda roste lokálně s časem. Tyto nestability se vyskytují především v okolí rezonančních bodů s hustotou rovnou čtvrtině kritické hustoty nebo kritické hustotě. U konvektivní nestability se maximum, které narůstá v čase, šíří také v prostoru (ne však vždy v důsledku šíření plazmové vlny). V nehomogenním plazmatu je pak šíření konvektivní nestability omezeno oblastí platnosti rezonančních podmínek podle rovnice (1.6).

Zpětnou vazbou, která umožňuje růst parametrické nestability, je ponderomotorická síla. Tato síla je přímo úměrná druhé mocnině vlnové délky laserového záření a gradientu jeho intenzity. Parametrické nestability se pak v laserovém plazmatu objevují, až když je ponderomotorická síla dostatečně silná, tedy je překonána určitá prahová hodnota laserové intenzity. Tato prahová hodnota je zjevně vyšší pro kratší vlnové délky a závisí zpravidla také na parametrech plazmatu, zejména na charakteristické délce hustotního profilu, případně na elektronové teplotě plazmatu. Důvod existence prahové hodnoty intenzity je disipace zesilovaných vln, která je pod prahovou intenzitou rychlejší než koeficient růstu dané nestability. Prahová hodnota bývá rovněž vyšší u konvektivní nestability než u absolutní, neboť šíření vln z místa rezonance lze pokládat za dodatečný mechanismus omezující růst této nestability.

Podle druhu interagujících vln rozlišujeme čtyři základní parametrické nestability. Jsou to (v závorkách jsou uvedeny další dvě vlny účastnící se daného procesu):

- Parametrický rozpad (elektronová plazmová a iontová akustická)
- Dvouplazmonový rozpad (dvě elektronové plazmové)
- Stimulovaný Ramanův rozptyl (elektronová plazmová a rozptýlená elektromagnetická)
- Stimulovaný Brillouinův rozptyl (iontová akustická a rozptýlená elektromagnetická)

Parametrický rozpad

V případě parametrického rozpadu[77] se laserová vlna rozpadá na elektronovou plazmovou vlnu šířící se zpět ven z terče a iontovou akustickou vlnu šířící se do terče. Z rovnic (1.6) a disperzních vztahů jednotlivých vln vyplývá, že k tomuto procesu musí docházet v blízkosti místa s kritickou hustotou, kde se frekvence elektronové plazmové vlny téměř rovná frekvenci vlny laserové. Frekvence iontové akustické vlny je totiž vzhledem k oběma těmto vlnám zanedbatelná. Z týchž vztahů je zřejmé, že tento proces vede k absorpci energie laserového záření do elektronové plazmové vlny a jedná se tedy o proces absorpční. Vzhledem k tomu, že k tomuto procesu

dochází pouze v okolí kritické hustoty a všechny ostatní parametrické procesy se vyskytují v plazmatu s nižší hustotou blíže k povrchu terče, je tento proces z hlediska laserové fúze méně důležitý.

Dvouplazmonový rozpad

Při dvouplazmonovém rozpadu [78] se laserová vlna absorbuje do dvou elektronových plazmových vln. Jelikož je frekvence plazmových vln dána převážně lokální hustotou plazmatu (která je pro obě vlny stejná), je zřejmé, že k tomuto procesu může docházet jenom v místě, kde je frekvence laserové vlny přibližně rovna dvojnásobku frekvence elektronové plazmové vlny. To nastává přibližně v místě s hustotou rovnou čtvrtině kritické hustoty. Z teorie růstu této nestability v závislosti na vlnovém vektoru dále vyplývá, že se elektronové plazmové vlny šíří vzhledem k dopadající laserové vlně šikmo. V případě homogenního plazmatu bez tlumení je potom optimální úhel šíření 45° [79]. Jde tedy o vícerozměrný proces, který v případě jednorozměrného popisu interakce neexistuje. I když se tato nestabilita může vyskytovat pouze v omezeném prostoru okolo čtvrtiny kritické hustoty, bývá považována za nebezpečnou z hlediska možného vzniku relativně horkých elektronů. Některé nestabilní módy totiž mají relativně dlouhou vlnovou délku plazmové vlny, což vede k urychlování zachycených částic na dosti vysoké energie. V experimentech byly naměřeny teploty přesahující 90 keV [80].

Stimulovaný Brillouinův rozptyl

Stimulovaný Brillouinův rozptyl [81] představuje v podstatě pružný rozptyl fotonů na iontové akustické vlně. Obě vlny, rozptýlená i akustická, jsou přitom buzeny ze šumové úrovně na úkor energie dopadající vlny. Energie absorbovaná iontovou vlnou, která se ve většině případů šíří dovnitř do terče, je přitom zanedbatelná. Z rezonančních podmínek a vlastností iontové vlny vyplývá, že se tento proces může vyskytovat všude v plazmatu s hustotou nižší než je kritická hustota. Jedná se tedy o proces, který je velmi významný v prostředí s dlouhou charakteristickou délkou hustotního profilu, a pokud není speciálními metodami omezen, vede v laserové fúzi k významnému zpětnému rozptylu laserového záření [82]. Tuto nestabilitu je možné studovat v jednorozměrné geometrii, jelikož má největší koeficient růstu právě pro zpětný rozptyl laserového záření [79].

Stimulovaný Ramanův rozptyl

V neposlední řadě je velmi významným parametrickým procesem také stimulovaný Ramanův rozptyl, jehož teoretický popis lze najít například v [83]. Při tomto procesu se laserová vlna rozptyluje od elektronové plazmové vlny šířící se dovnitř to terče. Podobně jako v případě

Brillouinova rozptylu má tato nestabilita maximální koeficient růstu pro zpětný rozptyl laserového záření, existuje však také rozptyl do stran a dopředný rozptyl. Ten je důležitý zejména v případě velmi horkého plazmatu, neboť jeho vlnové číslo je menší, a tento proces je tedy méně tlumen Landauovým útlumem [84]. Jak vyplývá ze vztahů (1.6) a vlastností elektronové plazmové vlny, tato nestabilita se může vyskytovat v plazmatu s hustotou menší, než je čtvrtina kritické hustoty. Frekvence elektronové plazmové vlny je tedy nejvíce rovna polovině laserové frekvence a absorpce v důsledku tohoto procesu (pokud k němu nedochází kaskádovitě) je omezena na 50%.

Z hlediska inerciální termojaderné fúze jsou parametrické nestability nepříznivé z několika důvodů. Jedním z nich je, že stimulované rozptyly přispívají ke zvýšené reflektivitě a omezují tedy absorpci laserového záření. Toto nastává zejména u stimulovaného Brillouinova rozptylu, kde je absorpce velmi nízká a tento rozptyl může efektivně působit v celé délce hustotního profilu až po kritickou hustotu. Druhým významným důvodem je častá bezesrážková disipace elektronových plazmových vln. Ta probíhá pomocí Landauova útlumu, zachycování a urychlováním částic, případně dochází k nárůstu vlny až do bodu, kdy se začínají dezintegrovat a dochází k jejich lámání [79]. Tyto procesy mohou způsobit vznik svazků nabitých elektronů s relativně vysokou energií desítek až stovek keV, které při průniku komprimovanou slupkou výrazně omezují stlačitelnost paliva [85]. V neposlední řadě dochází vlivem některých nestabilit k absorpci relativně daleko před kritickou hustotou, což snižuje efektivitu procesu zapálení a vede k nutnosti použití laserového impulsu s vyšším výkonem [86].

1.3.4 Další významné nelineární procesy

Mezi další významné nelineární procesy, které jsou u vyšších intenzit laserového záření také projevem ponderomotorické síly, patří samofokusace a následná filamentace laserového svazku. Ponderomotorická síla vytlačuje elektrony z místa s vysokou intenzitou záření uprostřed svazku. Klesá zde tedy plazmová hustota a zvyšuje se dielektrická konstanta. V důsledku této poruchy se plazma chová jako spojná čočka a laserový svazek se fokusuje. K tomuto procesu dochází všude v podkritickém plazmatu a to v případě, že je překročena hodnota tzv. kritického výkonu laserového svazku [87, 88]

$$P_c = 34\ T_{keV}(n_c/n_e)\sqrt{1 - n_e/n_c}\ \ \mathrm{MW}\ \ , \tag{1.7}$$

kde T_{keV} je elektronová teplota v keV. Samofokusace je částečně kompenzována přirozenou difrakcí laserového svazku. K samofokusaci může docházet i lokálně v jednotlivých místech laserového svazku, pokud je v každé této fokusující se části překročen prahový výkon daný rovnicí (1.7). V tomto případě dochází k rozdělení svazku na intenzivní filamenty. V každém

filamentu se dále samofokusací zvyšuje intenzita laserového záření, což následně vede k rozvoji a zrychlenému růst parametrických nestabilit. Závěrem ještě podotkněme, že tento proces je třeba studovat také ve vícerozměrné geometrii.

1.3.5 Úloha počítačových simulací

Pro studium interakce laserového záření s plazmatem v souvislosti se zapálením inerciální fúze hrají velmi důležitou roli rozsáhlé počítačové simulace. Experimenty za odpovídajících podmínek (teploty a délky hustotního profilu) jsou velmi drahé a náročné a některé jevy a jejich vzájemné souvislosti jsou obtížně diagnostikovatelné. Zároveň ale není možné v počítačových simulacích studovat jednotlivé jevy v malém měřítku a odděleně. Ukazuje se například, že procesy související se stimulovaným Ramanovým rozptylem ovlivňují stimulovaný Brillouinův rozptyl dále v terči [41] nebo dvouplazmonový rozpad poblíž čtvrtiny kritické hustoty [43]. Počítačové simulace celé interakční oblasti jsou však velmi náročné a pro některé případy je stále nutné, navzdory velké výpočetní kapacitě, uchýlit se k jednorozměrnému přiblížení interakce.

Zásadní otázky interakce laserového záření s plazmatem v souvislosti se zapálením inerciální fúze silnou rázovou vlnou jsou:

- Jaká jsou specifika interakce laserového záření s plazmatem v podmínkách zapálení inerciální fúze rázovou vlnou?
- Jaká je celková absorpce energie laserového záření a kde se odehrává?
- Jaká je role srážkových procesů a parametrických nestabilit?
- Jaké vlastnosti mají horké elektrony urychlené v laserové koroně?
- Jak tyto elektrony transportují energii dovnitř terče?
- Jakým způsobem lze režim a průběh interakce ovlivnit?

Především na tyto otázky se snažíme odpovědět v publikacích zahrnutých v následující kapitole této práce.

2 Komentáře k vybraným publikacím popisující náš výzkum laserové interakce

2.1 Článek č. 1: Particle-in-cell simulations of laser-plasma interaction for the shock ignition scenario

V tomto článku představujeme výsledky rozsáhlých jednorozměrných kinetických částicových simulací interakce laserového záření s plazmatem v podmínkách zapálení inerciální fúze silnou rázovou vlnou. Simulace jsou prováděny pro realistické parametry laserového impulsu a plazmatu (intenzity a vlnové délky laserového záření, hustoty a teploty plazmatu i hmotnosti iontů). Počáteční podmínky simulací jsou voleny na základě hydrodynamických simulací a odpovídají času, kdy na terč dopadá maximum intenzivního laserového impulsu. Počáteční charakteristická délka exponenciálního hustotního profilu je 300 μm, teplota elektronů je 5 keV a intenzita laserového impulsu o vlnové délce 351 nm je 10 PW/cm^2. Simulace jsou zároveň dostatečně dlouhé (více než 50 pikosekund), aby bylo dosaženo kvazi-stacionárního průběhu interakce. Tyto simulace jsou velmi náročné z hlediska numerické stability a bylo třeba pro ně speciálně upravit náš výpočetní kód.

Výsledky simulací demonstrují, že dlouhý hustotní profil plazmatu s vysokou teplotou dokáže efektivně absorbovat většinu laserového záření i s relativně vysokou intenzitou 10 PW/cm^2. Toto zjištění je v kontrastu s možným očekáváním nízké efektivity srážkové absorpce a vysoké reflektivity na základě silného stimulovaného Brillouinova rozptylu. Většina laserového záření není však absorbována srážkově, ale díky parametrickým nestabilitám a v hustotních kavitách. Tyto kavity se vytváří v místech výskytu absolutního stimulovaného Ramanova rozptylu, což je nejprve pouze čtvrtina kritické hustoty, ale později i jedna šestnáctina kritické hustoty.

Celý proces lze popsat následujícím způsobem. V důsledku vysoké teploty je v řídkém plazmatu silný Landaův útlum. Ten omezuje růst stimulovaného Ramanova rozptylu všude kromě místa absolutní nestability u čtvrtiny kritické hustoty. Ramanův rozptyl roste tedy pouze lokálně a postupně nabývá vysoké amplitudy. Ponderomotorická síla spojená s tímto rozptylem je tak silná, že z místa rozptylu vytlačí většinu elektronů, které postupně v důsledku Coulombovské exploze následují i ionty. Tím vzniká hustotní kavita, ve které zůstává uvězněna část energie elektromagnetického pole. Toto pole nemůže z kavity nijak uniknout a jeho energie je postupně absorbována částicemi.

Intenzita zpětně rozptýleného světla vznikajícího při stimulovaném Ramanově rozptylu rychle narůstá. Když překročí jistou prahovou hodnotu, může rozptýlené záření indukovat další

stimulovaný Ramanův rozptyl na své cestě ven z terče, tentokrát okolo 1/16 kritické hustoty. Tento sekundární rozptyl je také doprovázen vznikem kavit. Hustotní kavity přispívají k absorpci energie laserového záření a omezují růst nežádoucího stimulovaného Brillouinova rozptylu. Hrají tedy v interakci klíčovou roli.

Výsledky simulací naznačují z hlediska zapálení inerciální fúze silnou rázovou vlnou relativně příznivou situaci, neboť dochází k více než 70% absorpci laserové energie a vznikající horké elektrony mají teplotu nižší než 30 keV. Podle odhadů [89] tyto elektrony nezpůsobí předehřátí terče, neboť budou absorbovány ve stlačené slupce a naopak mohou přispět k efektivnímu vytvoření silné rázové vlny [90].

Obecně se také dá říci, že naše simulace demonstrují nový potenciál provádění rozsáhlých výpočtů pro reálné parametry interakcí. Specifický režim interakce, který byl pozorován v našich simulacích není možné simulovat v menší objemu plazmatu nebo v kratším časovém měřítku. Podle našich znalostí dosud podobné výpočty nebyly prováděny a nebyla tedy známa možná významná role hustotních kavit při interakci laserového záření s plazmatem. O významném přínosu tohoto článku svědčí i fakt, že byl zařazen do výběru 25 nejstahovanějších publikací v časopisu Plasma Physics and Controlled Fusion v roce 2010 [91].

2.2 Článek č. 2: Laser plasma interaction studies in the context of shock ignition-Transition from collisional to collisionless absorption

V předchozím článku bylo demonstrováno, že při intenzitě laserového záření 10 PW/cm^2 jsou dominantním jevem interakce s podkritickým plazmatem na povrchu terče parametrické nestability a jiné nelineární procesy. Na druhou stranu je známo, že při nižších intenzitách $\lesssim$ 1 PW/cm^2 jsou dominantní jevem Coulombovské srážky doprovázené efektivní srážkovou absorpcí. Zajímavá je tedy otázka přechodu mezi těmito dvěma režimy interakce, které se právě věnujeme v tomto článku. Interakce laserového záření s plazmatem je zde studována v závislosti na laserové intenzitě v rozmezí $1 - 8$ PW/cm^2.

V jednodimenzionálních simulacích tentokrát používáme počáteční podmínky získané z hydrodynamických simulací podle reálného experimentu na laseru OMEGA [92]. Rozdíl proti předchozím simulacím je zejména v kratší délce charakteristického hustotního profilu (přibližně 150 μm), nižší teplotě ($T_e \approx 2.5$ keV) a použití nenulové rychlosti hydrodynamické expanze, která má navíc nehomogenní profil.

V simulacích se podle očekávání ukázalo, že u nižších laserových intenzit hrají při interakci parametrické nestability jen malou roli, o čemž svědčí i relativně malá reflektivita, efektivní ohřev tepelných elektronů a malé množství horkých elektronů. Coulombovské srážky potlačují

růst stimulovaného Brillouinova rozptylu a reflektivita v důsledku tohoto procesu je nižší než 30%. V důsledku závislosti srážkové frekvence na hustotě se posunuje oblast maximálního růstu stimulovaného Brillouinova rozptylu do plazmatu s nižší hustotou. Přibližně 70% laserové energie je absorbováno díky srážkové absorpci, což je v souladu s absorpčním koeficientem daným rovnicí (1.4).

V oblasti vyšších intenzit laserového záření ($\gtrsim 2.4$ PW/cm^2) je však situace zcela jiná. Srážkové procesy nejsou efektivní a převládají procesy spojené s kolektivním chováním plazmatu. Na začátku interakce je přechodná fáze, při které je až 80% reflektivita způsobená stimulovaným Brillouinovým rozptylem. V průběhu této fáze interakce dochází postupně k nárůstu absolutního stimulovaného Ramanova rozptylu a ke vzniku hustotních kavit v místech 1/4 a 1/16 kritické hustoty. Délka přechodné fáze interakce je dána dobou vzniku kavit a v našem případě se pohybuje v desítkách pikosekund, přičemž klesá s rostoucí intenzitou laserového záření.

Po přechodné fázi následuje kvazi-stacionární stav, v němž je reflektivita menší než 35%. Absorpce probíhá především v důsledku vzniku hustotních kavit a stimulovaného Ramanova rozptylu a odehrává se v plazmatu s nízkou hustotou daleko před kritickou hustotou. Tato bezesrážková absorpce dává vzniknout populaci horkých elektronů, které mají teplotu přibližně 25 keV. Zásadní zjištění pak je, že ve studovaném rozmezí intenzit je teplota horkých elektronů v podstatě konstantní a s intenzitou roste pouze počet horkých elektronů. Důležité je rovněž potvrzení jevů pozorovaných v prvním článku pro dosti rozdílné počáteční podmínky. To dokazuje, že pozorované jevy jsou relativně robustní a vyskytují se v širší oblasti parametrů interakce laserového záření s plazmatem.

Výsledky těchto simulací byly také konfrontovány s experimentálními daty získanými na laseru OMEGA. Dobrá shoda panuje v celkové reflektivitě, i reflektivitě v důsledku stimulovaného Ramanova rozptylu. Rovněž teplota horkých elektronů je ve shodě s experimenty. Nesrovnalosti jsou však ve spektru rozptýleného záření a v počtu horkých elektronů při vyšších intenzitách. Objasnění těchto nesrovnalostí bude vyžadovat další studium.

2.3 Článek č. 3: Laser-plasma interaction studies in the context of shock ignition: the regime dominated by parametric instabilities

V posledním ze série článků vycházejících z jednorozměrných simulací se detailně věnujeme oblasti vyšších intenzit laserového záření ($2.4 - 24$ PW/cm^2), při kterých jsou důležité parametrické procesy, a zaměřujeme se na detailnější studium jednotlivých absorpčních procesů. Počáteční podmínky jsou stejné jako v případě článku diskutovaného v sekci 2.2. Interakce zde rovněž probíhá ve dvou fázích popsaných již dříve, přičemž větší pozornost je věnována fázi

kvazi-stacionární. Tato fáze je relevantnější z hlediska delších laserových impulsů používaných v experimentech.

Během kvazi-stacionární fáze interakce je v našich simulacích naměřen absorpční koeficient zhruba 70% a tato hodnota je nezávislá na laserové intenzitě. Není však zřejmé, jakou měrou k této hodnotě jednotlivé procesy přispívají a kde k této absorpci dochází. V tomto článku se nám na základě výsledků několika simulací s omezenou částí hustotního profilu podařilo oddělit od sebe a lépe pochopit a popsat jednotlivé absorpční procesy. Většina, 50%, energie laserového záření je absorbována v místě s 1/4 kritické hustoty. Zbývajících 19% je absorbováno okolo 1/16 kritické hustoty. Stimulovaný Ramanův rozptyl je zodpovědný za absorpci 52% laserové energie a horké elektrony, které v jeho důsledku vznikají, mají teplotu 30 keV. Hustotní kavity jsou zodpovědné za zbývajících 17% absorpce elektromagnetického záření a jsou zdrojem elektronů s teplotou 10 keV a téměř izotropním rozdělením. Tyto výsledky tedy nasvědčují tomu, že více energie je absorbováno v důsledku stimulovaného Ramanova rozptylu než v důsledku vzniku hustotních kavit, což nebylo z předchozích výsledků zřejmé.

V případě vyšších intenzit laserového záření začíná docházet rovněž ke konvektivnímu zesilování stimulovaného Ramanova rozptylu a to navzdory vysokému Landauovu útlumu. Tomuto jevu se říká inflační režim [93] a dochází k němu při vysokých intenzitách laserového záření, kdy je distribuční funkce částic značně odlišná od rovnovážné Maxwell-Boltzmannovy distribuce. Ke konvektivnímu zesilování stimulovaného Ramanova rozptylu dochází v našich simulacích mezi místy s 1/16 a 1/4 kritické hustoty. Tato nestabilita tedy neinteraguje s nestabilitami v rezonančních bodech s výskytem hustotních kavit.

V simulacích je rovněž pozorováno velké zesilování relativně krátkých impulsů (0.3 ps) stimulovaného Brillouinova rozptylu. Intenzita těchto impulsů je tak vysoká, že navzdory své relativně krátké délce jsou schopny vyvolat vznik dalších parametrických nestabilit. V našich simulacích je pozorován právě konvektivní stimulovaný Ramanův rozptyl způsobený těmito silnými impulsy. Důsledkem vzniku sekundárních parametrických nestabilit je také saturace maximální intenzity rozptýlených impulsů.

2.4 Článek č. 4: Fast saturation of the two-plasmon-decay instability for shock-ignition conditions

Jednodimenzionální simulace nám poskytly relativně dobrou představu o vzájemné koexistenci stimulovaného Ramanova a Brillouinova rozptylu v oblasti interakce laserového záření s plazmatem v podmínkách relevantních pro zapálení inerciální fúze rázovou vlnou. Navzdory tomu, že v inerciální fúzi jsou ohniska laserových svazků relativně velká, není jednorozměrný přístup dostačující. Důvodem jsou jednak nestability, které vyžadují vícerozměrnou geometrii (dvou-

plazmonový rozpad, samofokusace a filamentace laserového svazku), ale také to, že laserový svazek není většinou homogenní. Naopak bývá záměrně rozdělen do množství malých filamentů, jejichž statistické vlastnosti jsou dobře známy. To se provádí s použitím tzv. náhodné vlnové destičky (random phase plate), a to právě z důvodu potlačení růstu některých parametrických nestabilit. Pro ucelenější představu o průběhu interakce je tedy nutné uchýlit se k vícerozměrným simulacím. To je však často nemožné, neboť i jednorozměrné simulace vyžadují obrovské výpočetní prostředky (řádově desítky tisíc CPU hodin) a dvourozměrné simulace stejné oblasti a délky interakce jsou v ideálním případě o 3 až 4 řády časově náročnější. Ve vícerozměrných simulacích je tedy reálně možné studovat jenom omezenou část oblasti interakce a je nutné se uchýlit k některým zjednodušením. V této publikaci představujeme první dvourozměrné simulace zabývající se parametrickými nestabilitami v relevantních podmínkách ne příliš odlišných od předchozích jednorozměrných simulací.

Z jednorozměrných simulací víme, že nejdůležitější procesy se odehrávají v okolí 1/4 a 1/16 kritické hustoty a zároveň, že průběh těchto procesů není výrazně ovlivněn tím, co se děje hlouběji v terči. Proto je možné omezit studovanou oblast plazmatu maximální hustotou např. 2/5 kritické hustoty. Kvůli numerické stabilitě simulací je třeba, aby byla velikost simulačních buněk srovnatelná s Debyeovou délkou a z tohoto důvodu používáme vyšší teplotu elektronů (5 keV). Charakteristická délka hustotního profilu je zkrácena na 60 μm a intenzita laserového záření zvýšena na 50 PW/cm^2, což by mělo urychlit vývoj nestabilit. V jednorozměrných simulacích jsme přitom ověřili, že procesy v interakční oblasti zůstávají stejné jako u nižších intenzit a delších hustotních profilů. Velikost ohniska Gaussovského laserového svazku je v dvourozměrných simulacích 24 μm FWHM (plná šířka v polovině výšky).

Velmi významným výsledkem těchto dvourozměrných simulací je potvrzení vzniku hustotních kavit v oblasti 1/4 kritické hustoty. Tyto kavity vznikají tentokrát nejdříve v důsledku dvouplazmonového rozpadu. Vznik kavit vede následně k omezení růstu dvouplazmonového rozpadu a stimulovaný Ramanův rozptyl převládá. Horké elektrony vznikající v důsledku stimulovaného Ramanova rozptylu se šíří směrem do terče a mají teplotu přibližně v rozmezí 30-50 keV. Tato teplota je relativně v souladu s jednorozměrnými simulacemi. Na druhou stranu reflektivita v důsledku stimulovaného Brillouinova rozptylu je ve dvourozměrných simulacích vyšší a v časovém měřítku simulace (4.7 ps) nedochází k výraznému sekundárnímu stimulovanému Ramanovu rozptylu a vzniku kavit u místa s 1/16 kritické hustoty. Další významný rozdíl oproti jednorozměrným simulacím je, že hustotní kavity nejsou stabilní a s časem expandují a mizí, zatímco se v jejich okolí objevují nové. První dvourozměrné simulace tedy kvalitativně potvrzují závěry jednorozměrných simulací co se týká vzniku a významu hustotních kavit. Rovněž relativně dobrý souhlas v teplotě horkých elektronů je velmi významný.

2.5 Článek č. 5: Two-dimensional simulations of laser-plasma interaction and hot electron generation in the context of shock-ignition research

Dvourozměrné simulace diskutované v předchozím článku byly počítány až do času 4.7 ps. Na druhou stranu okrajové podmínky pro částice v těchto simulacích lze pro delší simulační časy považovat za problematické, neboť mnoho horkých elektronů bylo při dosažení zadní hranice odraženo zpět a v simulační oblasti tak s časem výrazně narůstala teplota a počet horkých elektronů. Z tohoto důvodu také nebylo možné přesně stanovit absorpci a teplotu horkých elektronů. K překonání těchto problémů jsme navrhli a implementovali do nově vytvořeného simulačního kódu speciální okrajovou podmínku, která horké částice termalizuje tak, že teplota zpětného proudu (od zadní hranice do simulační oblasti) je v průběhu simulace téměř konstantní.

Výsledky dosažené s novým simulačním kódem jsou v souladu s předchozími výsledky dvourozměrných simulací, ale poskytují i některé nové informace. Počáteční podmínky jsou přitom téměř shodné. Celková reflektivita je v nových simulacích rovna 36%, což je hodnota dosti podobná jednorozměrným simulacím. Na rozdíl od jednorozměrných simulací je však absorpce pouze okolo 34% a 30% energie projde simulovanou částí hustotního profilu s podkritickou hustotou na druhou stranu. Domníváme se, že většina tohoto záření by byla v případě reálné situace absorbována srážkami, neboť se dostává do oblastí vyšších hustot a nižších teplot plazmatu, a v reálné situaci by laserový impuls měl několikrát nižší intenzitu. Toto tvrzení bohužel nemůžeme v našich dvourozměrných simulacích v současné době z výpočetních důvodů ověřit.

Hustotní kavity jsou opět pozorovány u 1/4 kritické hustoty avšak stále ne u 1/16 kritické hustoty (délka simulací je tentokrát 6.5 ps). Vznikající kavity mají v inerciální fúzi význam z několika důvodů. Jednak omezují růst stimulovaného Brillouinova rozptylu a dvouplazmonového rozpadu a dále přispívají k absorpci laserového záření. V neposlední řadě způsobují také náhodný rozptyl do terče se šířícího laserového záření, čímž omezují možný růst dalších nestabilit hlouběji v terči. Horké elektrony urychlené polem v hustotních kavitách mají teplotu okolo 13 keV a přesto, že je jejich úhlové rozdělení v podstatě izotropické, transportují dále do terče největší část absorbovaného laserového záření. Horké elektrony vznikající v důsledku stimulovaného Ramanova rozptylu mají teplotu okolo 31 keV a šíří se přímo do terče s úhlovým rozptylem přibližně 70°. Relativně malé a z hlediska energetické bilance zanedbatelné množství horkých elektronů vytváří i dvouplazmonový rozpad. Tyto elektrony mají teplotu 63 keV a šíří se šikmo směrem ven z terče v souladu s koeficientem maximálního růstu této nestability. Teploty horkých elektronů jsou tedy také v souladu s našimi jednorozměrnými simulacemi.

2.6 Článek č. 6: Physics issues for shock ignition

Předchozí publikace poskytují relativně ucelený (i když zdaleka ne kompletní) pohled na roli parametrických nestabilit při interakci laserového záření s plazmatem v podmínkách inerciální fúze zapálené silnou rázovou vlnou. V této publikaci jsou pak diskutovány jak teorie tak simulace a experimenty zabývající se tímto tématem. Kromě shrnutí většiny výsledků prezentovaných v předchozích publikacích obsahuje tato publikace i širší teoretické pojednání a experimentální výsledky z mnoha kampaní na různých laserových instalacích. Výsledky většiny experimentů nejsou však s našimi simulacemi přímo porovnatelné, neboť odpovídají jiným podmínkám interakce. Především teplota plazmatu bývá v experimentech (s výjimkou laseru OMEGA nebo LIL) mnohem nižší a jak bylo patrné na Obr. 1.2, při nižších teplotách je růst plazmových vln výrazně tlumen srážkami. Nicméně v mnoha experimentech jsou reflektivity v důsledku stimulovaného Ramanova a především Brillouinova rozptylu v řádu několika desítek procent nebo i výrazně nižší, což je v souladu s teoretickými odhady a počítačovými simulacemi. Některé experimenty rovněž demonstrují vznik horkých elektronů s teplotou, která je v souladu se simulacemi. Z experimentů na laseru OMEGA je rovněž patrný menší význam dvouplazmonového rozpadu v porovnání se stimulovaným Ramanovým rozptylem.

2.7 Hlavní přínos uvedených publikací

V následujících několika bodech shrňme hlavní vědecké přínosy uvedených publikací. Jsou to:

- První detailní publikovaná práce zabývající se interakcí laserového záření s plazmatem v podmínkách relevantních pro zapálení inerciální fúze silnou rázovou vlnou.
- Popis vzniku a významné role hustotních kavit při interakci.
- Stanovení intenzity, při které začínají být důležité nelineární procesy a nestability.
- Předpovězení efektivní absorpce pro vyšší intenzity laserového záření v okolí 1/4 kritické hustoty v důsledku parametrických nestabilit a nelineárních procesů.
- Vypočtení absorpčního koeficientu a předpovězení jeho malé závislosti na intenzitě laserového záření v relevantním rozmezí hodnot.
- Stanovení teploty horkých elektronů a taktéž předpovězení její nezávislosti na laserové intenzitě.
- Předpovězení malé důležitosti dvouplazmonového rozpadu v porovnání s jinými procesy.

3 Urychlování iontů pomocí intenzivních laserových impulsů

3.1 Počátky a vývoj výzkumu urychlování iontů v laserovém plazmatu

Měření rychlostí iontů vyletujících z terče bylo prováděno již při výzkumu inerciální termojaderné fúze a používáno jako diagnostika procesů probíhajících v terči [94]. Ionty urychlené na poměrně vysoké kinetické energie přesahující MeV byly pak pozorovány již ve fúzních experimentech v 80. letech minulého století [95]. Tehdy se k těmto experimentům používaly také velké CO_2 lasery a po zaostření jejich svazku na terč bylo dosaženo relativně vysokého potenciálu elektromagnetického pole, který do značné míry určuje výslednou energii urychlených iontů [96]. Tento potenciál se často ve fyzice laserového plazmatu používá v bezrozměrné podobě

$$a_0 = \frac{eA}{m_e c^2} = \frac{eE}{m_e \omega c} = \sqrt{\frac{e^2}{2\pi^2 m_e^2 \varepsilon_0 c^5}} \sqrt{I_L \lambda_L^2} \quad . \tag{3.1}$$

Hodnota potenciálu je přímo úměrná vlnové délce a pro získání vysokých energií iontů je tedy výhodnější používat laserové záření s delší vlnovou délkou. U CO_2 laserů je tato délka zhruba 10 krát delší, než u většiny jiných dostupných laserových systémů s vysokou energií. Proto byly první vysoké energie iontů zaznamenány právě u těchto laserových systémů.

Před rokem 2000 bylo publikováno několik dalších měření energetických iontů v laserových experimentech, např. [97], ale emise urychlených iontů v těchto případech byla většinou téměř izotropní a tedy nevhodná pro další použití. Přelomové experimentální výsledky byly publikovány až v roce 2000, kdy se při použití tenkých fólií jako terčů na třech laserových systémech nezávisle ukázalo, že nejrychlejší ionty letí téměř kolmo k povrchu ze zadní strany terče v poměrně úzkém a laminárním svazku [98–100]. Rekordních vlastností iontového svazku přitom bylo dosaženo v experimentu [100] v laboratoři Lawrence Livermore National Laboratory, kdy bylo urychleno kolem 2×10^{13} energetických protonů s maximální energií až 58 MeV.

Tyto i další podobné experimenty vykazují jeden společný rys. Urychlené ionty jsou především protony a to navzdory tomu, že terč podle chemického složení protony neobsahuje (například často používaným terčem je hliníková fólie). Jak již bylo známo v 80. letech minu-

lého století, protony pochází z nečistot usazených na povrchu terče v terčové komoře (vodní pára, sloučeniny uhlíku a vodíku pocházející z vakuové pumpy a podobně) [95]. Z těchto informací je zřejmé, že k efektivnímu urychlování iontů dochází především na povrchu terče. V několika následujících letech se pak vedla debata o tom, jestli nejrychlejší urychlené ionty pochází z přední nebo ze zadní strany terče [101, 102], protože původní experimenty publikované v roce 2000 poskytovaly v tomto ohledu rozdílně interpretovatelné výsledky. K vysvětlení procesu urychlování iontů ze zadní strany terče byl publikován model tzv. "Target Normal Sheath Acceleration"(TNSA) [103], který je dnes považován za nejpravděpodobnější vysvětlení pozorovaných energetických iontů ve většině experimentů s krátkými a intenzivními laserovými impulsy.

3.2 Model TNSA

Již dříve jsme zmiňovali dva druhy procesů vedoucích k absorpci laserového záření a ohřevu elektronů. Byly to srážková absorpce, která vede k ohřevu všech elektronů při zachování Maxwell-Boltzmannovy distribuční funkce, a parametrické nestability vedoucí spíše k urychlování elektronů v plazmových vlnách. Oba tyto procesy jsou efektivní především v plazmatu s delším hustotním profilem na povrchu (srážková absorpce navíc jen při nižších intenzitách laserového záření). Při urychlování iontů z tenkých fólií je však optimální, pokud fólie může být velmi tenká [104]. Zároveň nesmí být na zadní straně terče delší hustotní profil plazmatu již před začátkem procesu TNSA, jinak je efektivita tohoto procesu výrazně snížena [105]. Proto jsou k urychlování iontů používány spíše laserové impulsy s vyšším kontrastem a hustotní profil plazmatu na povrchu terče má v době interakce krátkou charakteristickou délku.

Kromě srážkové absorpce a parametrických nestabilit existuje řada dalších procesů absorpce laserové energie, které mohou být efektivní i v plazmatu s relativně krátkým hustotním profilem. Mezi tyto procesy patří například rezonanční absorpce [106], vakuový ohřev [107], normální a anomální skinový efekt [108, 109] nebo stochastický ohřev [110]. Pro vysoké hodnoty bezrozměrného potenciálu, $a_0 \gtrsim 1$, které jsou dnes používány ve většině experimentů s urychlováním iontů, začínají elektrony oscilovat v laserové vlně s relativistickou rychlostí blízkou rychlosti světla. V takovém případě má na pohyb elektronů nezanedbatelný vliv také $\overrightarrow{v} \times \overrightarrow{B}$ složka Lorentzovy síly. Tato síla vede k urychlování elektronů směrem do terče a je v případě vysokých intenzit zodpovědná za vznik velkého množství horkých elektronů s teplotou přibližně danou vzorcem [103]

$$k_B T_h = m_e c^2 \left(\sqrt{1 + a_0^2} - 1 \right) \quad . \tag{3.2}$$

Za předpokladu vysoké laserové intenzity můžeme také předpokládat, že většina elektronů se pohybuje rychlostí blízkou rychlosti světla. Hustotu horkých elektronů urychlených v interakční oblasti pak můžeme přibližně odhadnout jako

$$n_h = \frac{\eta I_L}{c k_B T_h} \quad , \tag{3.3}$$

kde η je koeficient absorpce. Tento odhad je samozřejmě použitelný jen za předpokladu $n_h \ll n_c$, neboť do interakční oblasti musí přicházet i zpětný proud méně horkých elektronů. V případě nesplnění tohoto předpokladu je pravděpodobný nárůst teploty horkých elektronů výrazně nad hodnotu danou vztahem (3.2). Nepřipouštíme také indukovanou relativistickou transparenci, neboť pro ní není TNSA model adekvátní. Budeme dále pro jednoduchost předpokládat, že rozměr ohniska laserového svazku na terči je větší než tloušťka terče a že úhlové rozdělení horkých elektronů není příliš široké. V takovém případě můžeme předpokládat, že se hustota elektronů během šíření terčem výrazně nemění a je možné použít jednorozměrné přiblížení. Rovněž zanedbáme vliv všech nestabilit (zejména dvousvazkové a Weibelovy), polí indukovaných v terči i srážkových procesů na transport horkých elektronů. U tenkých fólií z vodivého materiálu je tento předpoklad možný. Svazek horkých elektronů má v tomto případě na zadní straně terče stejné parametry jako na straně přední.

V důsledku toho, že horké elektrony na zadní straně vyletují ven z terče, terč přestává být kvazineutrální a vzniká elektrostatické pole s amplitudou

$$E_f = \sqrt{\frac{n_h k_B T_h}{\varepsilon_0}} = \sqrt{\frac{2\eta I_L}{\varepsilon_0 c}} \quad . \tag{3.4}$$

Pokud budeme předpokládat Boltzmannovo rozdělení horkých elektronů, pak toto silné pole klesá přibližně exponenciálně se vzdáleností od povrchu terče a charakteristická délka tohoto poklesu je Debyeova délka horkých elektronů

$$\lambda_{D,hot} = \sqrt{\frac{\varepsilon_0 k_B T_h}{n_h e^2}} = \sqrt{\frac{\varepsilon_0 m_e^2 c^5 \left(\sqrt{1 + \frac{I_L \lambda_L^2 e^2}{2\pi^2 \varepsilon_0 m_e^2 c^5}} - 1 \right)^2}{\eta I_L e^2}} \quad , \tag{3.5}$$

Například pro laserový impuls s $\lambda_L = 0.8$ μm a $I_L = 10^{18}$ W/cm^2 a koeficient absorpce $\eta = 0.5$ dostáváme $E_f \approx 1.4$ TV/m a $\lambda_{D,hot} \approx 79$ nm. Indukované pole je tedy o mnoho

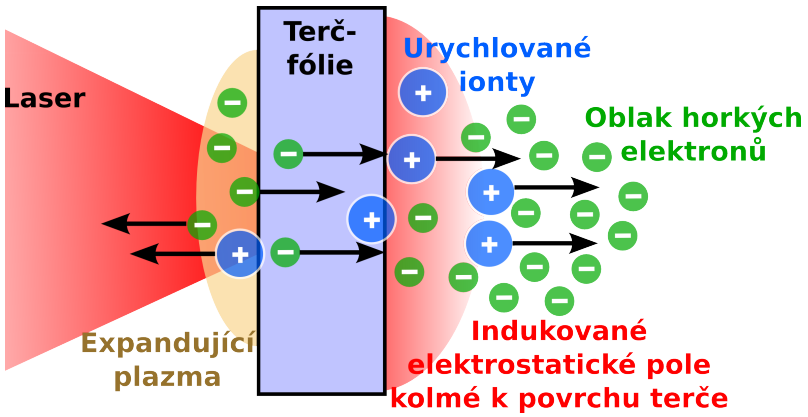

Obrázek 3.1: Schématické znázornění urychlování iontů z povrchu laserem ozařovaného terče v procesu TNSA.

řádů vyšší, než pole, které váže elektron v atomu vodíku (≈ 5 GV/m). Je tedy schopné ionizovat atomy na zadní straně terče a následně urychlovat vzniklé ionty. Iont, který proletí elektrostatickým polem na zadní straně terče je přitom urychlen řádově na energii

$$E_{ion} = eZE_f\lambda_{D,hot} = \sqrt{2}Zm_ec^2\left(\sqrt{1+\frac{I_L\lambda_L^2e^2}{2\pi^2\varepsilon_0m_e^2c^5}}-1\right) = \sqrt{2}Zk_BT_h \quad . \tag{3.6}$$

Podobný vztah pro maximální energii iontů urychlených na povrchu terče můžeme dostat i z jednorozměrného modelu izotermální expanze plazmatu do vakua [111]. Tento model však navíc obsahuje jeden volný parametr, dobu urychlování, u kterého není vždy jasné, jak volit jeho konkrétní hodnotu. Izotermální model expanze však poskytuje i další zajímavou informaci. Tou je energetická distribuční funkce urychlených iontů

$$\frac{dN}{dE}(E,t) = \frac{Zn_et}{\sqrt{2m_iE}}\exp\left[-\sqrt{\frac{2E}{Zk_BT_h}}\right] \quad , \tag{3.7}$$

kde n_e je počáteční hustota elektronů v terči před expanzí a m_i je náboj iontů. Jak je vidět, amplituda této distribuční funkce také závisí na čase t, ale tvar distribuční funkce je stále stejný. Pro vyšší energie iontů přitom převládá exponenciální člen a distribuční funkce má exponenciální závislost, která je skutečně pozorována v mnoha experimentech urychlování iontů v režimu TNSA [100, 104, 105].

Zatímco ionty jsou v indukovaném elektrostatickém poli vně terče urychlovány, horké elek-

trony jsou naopak zpomalovány a urychlovány zpět do terče. V důsledku toho, že indukované pole zároveň urychluje ionty, mění se jeho hodnota i profil s časem. Elektrony pak v tomto poli nezískají zpět všechnu svou energii, kterou poli předají, a jejich teplota se postupně snižuje. Pokud je terč dostatečně tenký a teplota horkých elektronů vysoká, jsou elektrony urychlené zpět do terče schopny proletět zpět na přední stranu. Zde mohou opět interagovat s laserovým impulsem nebo později vytvářet stejné podmínky vedoucí k urychlování iontů, jako na zadní straně terče. Tomuto procesu se říká recirkulace horkých elektronů a vede obecně k vyšší efektivitě urychlování iontů [104, 112].

Podle přibližných vzorců (3.6) a (3.7) urychlování iontů překvapivě nezávisí na koeficientu absorpce laserového záření. Problém spočívá v předpokladu izotermálnosti elektronů. Ve skutečnosti množství urychlených elektronů a následně i urychlených iontů na koeficientu absorpce závisí a zvýšení absorpce je v mnoha případech velmi žádoucí a vede k vyšší efektivitě urychlování iontů, jak bude patrné z výsledků v další části této práce [37, 38].

Pro mnoho aplikací využívajících svazky energetických iontů (radiografické zobrazování, produkce radioisotopů, isochorický ohřev, medicínské aplikace apod. [113]), je důležitý velký počet iontů s vysokou energií. Některé aplikace (například protonová terapie) pak mohou profitovat i z nerovnoměrné depozice energie iontů v materiálu s ostrým Braggovským maximem ke konci dráhy jejich letu. Jsou pro ně tedy výhodné iontové svazky s relativně úzkým energetickým spektrem. V procesu TNSA je však úbytek počtu rychlých iontů s energií téměř exponenciální, což je nevýhodné. V tomto případě je největší množství energie koncentrováno v relativně málo energetických iontech a počet iontů s vysokou energií je vůči celkové energii urychlených iontů relativně malý. Rovněž závislost maximální energie urychlených protonů na laserové intenzitě $\sim\sqrt{I_L\lambda_L^2}$, která je patrná i z rovnice (3.6) a která byla ověřena v mnoha experimentech [99, 114, 115], není z hlediska dosažení vysokých energií protonů příliš povzbudivá. Pokud vezmeme v úvahu, že se 150 TW laserem Draco bylo za optimálních podmínek dosaženo maximální energie 17 MeV [116], potom nová generace laserů s výkonem PW bude urychlovat protony v TNSA režimu přibližně na energii 45 MeV. To je například pro plánované studie aplikací v radioterapii nádorů oka nedostatečné [117]. Z tohoto důvodu se vědecká komunita soustředí především na výzkum možností, jak zvýšit maximální energii urychlených protonů a efektivitu urychlování a jak změnit energetické spektrum protonů, aby vyšších energií dosahovalo více částic (nejlépe aby bylo dosaženo kvazi-monoenergetického svazku).

3.3 Vylepšení procesu TNSA a alternativní způsoby urychlování iontů

Zvýšit efektivitu a maximální energii urychlených iontů můžeme i přímo v procesu TNSA, a to zvýšením účinnosti absorpce laserového záření a teploty horkých elektronů, nebo omezením

ztráty energie horkých elektronů uvnitř terče, nejlépe pak využitím obou možností. Omezení energetických ztrát horkých elektronů v terči vede na použití terčů s co nejmenší tloušťkou, a proto se v experimentech začaly často používat velmi tenké folie. Použití těchto folií však vyžaduje velmi vysoký kontrast [112] mezi intenzitou a energií hlavního laserového impulsu a předpulsu, který mu předchází. V opačném případě dochází k destrukci terče před hlavní částí interakce a transformace energie horkých elektronů do urychlených iontů je v předexpandovaném plazmatu omezena. Laserový kontrast tak omezuje minimální tloušťku terče a vede k tomu, že různé laserové systémy s různým kontrastem mají rozdílnou optimální tloušťku terčů pro maximální efektivitu urychlování iontů v procesu TNSA. Jelikož svazek urychlených elektronů má i nenulovou divergenci, je žádoucí omezit rovněž další rozměry terče, což vede k použití terčů s omezenou hmotou (tzv. mass limited target) [118].

Zvýšení absorpce laserové energie a teploty horkých elektronů lze dosáhnout buď optimalizací úhlu dopadu a profilu hustoty plazmatu nebo použitím speciálně navržených terčů, které absorpci zvyšují. Tento postup se v poslední době volí častěji, neboť jiné možnosti optimalizace TNSA procesu jsou na stávajících laserových zařízeních téměř vyčerpány a zároveň se s rozvojem nanotechnologií a mikroskopického "obrábění" objevují možnosti přípravy takových speciálních terčů. Tyto terče byly použity také v našich publikacích [37–40] a bude o nich dále diskutováno v následující kapitole.

Kromě procesu TNSA existují i jiné procesy, které mají z hlediska účinnosti, maximální energie iontů nebo tvaru jejich energetického spektra lepší vlastnosti. Patří sem zejména urychlování bezesrážkovou rázovou vlnou (tzv. shock acceleration) [119], urychlování v režimu relativistické transparence terče (tzv. Break-Out Afterburn - BOA) [120] a urychlování radiačním tlakem (Radiation Pressure Acceleration - RPA) [121–123]. Pro tyto procesy je charakteristické, že vyžadují velmi intenzivní laserové záření (resp. vysoký potenciál a_0) a zároveň vhodnou hustotu (případně i tloušťku) terče. Tyto procesy budou stručně popsány v dalších odstavcích této části.

Bezesrážková rázové vlny

Excitované iontové zvukové vlny v plazmatu mohou narůstat, zachycovat částice a postupně se změnit v rázové vlny. V případě plazmatu s relativně nízkou srážkovou frekvencí (resp. velkou střední volnou dráhou částic ve srovnání s šířkou čela rázové vlny) se jedná o bezesrážkové elektrostatické rázové vlny. Pokud je zároveň elektrostatický potenciál na čele rázové vlny větší, než je kinetická energie iontů před ní, tedy $Ze\Phi > m_i v_i^2/2$, ionty se od čela rázové vlny odrážejí a získávají rychlost rovnou dvojnásobku rychlosti této vlny. Bezesrážková rázová vlna s vyšším Machovým číslem ($M > 1$) tak může efektivně urychlovat ionty. Vytvoření takové rázové vlny bylo demonstrováno v počítačových simulacích interakce laserového záření s plazmatem, kde $a_0\sqrt{2} > n_e/n_c$ [119]. Rázová vlna je přitom vytvořena urychlením iontů tlakem záření laserového impulsu na rychlost v_{HB}, která bude diskutována níže. Pomocí počítačových simulací [124] bylo

také ukázáno, že při urychlování iontů pomocí bezesrážkové rázové vlny je možné dosáhnout vyšších energií iontů než u TNSA nicméně za cenu menší účinnosti. Výhodou urychlování iontů bezesrážkovou rázovou vlnou je také možnost dosažení relativně úzkého energetického spektra, jak bylo nedávno demonstrováno v experimentech s plynnými terči a CO_2 laserovým systémem Neptun [125].

Relativistická transparence terče

Pokud je terčem pro urychlování iontů velmi tenká fólie a laserový impuls je velmi intenzivní, $a_0 \gtrsim n_e/n_c$ (na rozdíl od urychlování rázovou vlnou se jedná o hustotu pevného materiálu), terč může být transparentní i když je jeho hustota klasicky nadkritická. Je to způsobeno tím, že elektronová plazmová frekvence je při relativistickém pohybu elektronů snížena γ-krát, kde γ je průměrný relativistický faktor elektronů, který je přibližně $\gamma \approx \sqrt{1 + a_0^2/2}$ (pro lineární polarizaci laserového impulsu). V režimu relativistické transparence laserové záření interaguje s mnohem vyšší hustotou elektronů a množství urychlených elektronů je tedy mnohem větší. Také dráha, na které jsou elektrony urychlovány je delší (je přibližně rovna tloušťce relativistické skinové vrstvy) a tedy jejich teplota je vyšší. Obojí pak přispívá k vyšší efektivitě urychlování a vyšší maximální energii iontů.

Nejvyšší energie urychlených protonů, a to přes 120 MeV, byly dosud zaznamenány v experimentech probíhajících v režimu BOA [126]. Experimenty byly prováděny na laseru Trident v LANL s laserovými impulsy o délce 500-700 fs a s uhlíkovými terči o tloušťce 140 nm. Maximální intenzita použitého laserového impulsu byla $a_0 \approx 27$ a terč tedy nebyl pro laserové záření transparentní hned od začátku interakce. V průběhu interakce však terč velmi rychle expandoval a stal se postupně nejdříve relativisticky a pak i klasicky transparentní. Pro efektivitu urychlování je pak rozhodující právě fáze mezi těmito dvěma režimy transparence.

Režim relativistické transparence není dosud dostupný na krátkopulzních laserových systémech (s délkou impulsu v desítkách femtosekund). Terč během interakce nestihne dostatečně expandovat a hustota zůstává vyšší než jaká odpovídá relativistické transparenci. Nabízí se však jedna zajímavá možnost jak režimu BOA dosáhnout i s těmito laserovými impulsy. Při konverzi laserového záření na vyšší harmonické se zmenšuje bezrozměrný potenciál elektromagnetického pole přímo úměrně vlnové délce impulsu, tedy $a_0 \propto \lambda_L$. Na druhou stranu kritická hustota roste s druhou mocninou vlnové délky, tedy $n_c \propto \lambda_L^2$. Konverzí na vyšší harmonické lze tedy dosáhnout relativistické transparence i s krátkopulzními laserovými systémy a běžnými, např. plastovými, pevnými terči. Tato možnost byla navržena v naší nedávné publikaci [127].

Urychlování tlakem záření

Tlak záření předpověděl již Johannes Kepler v roce 1619 [128] k vysvětlení pozorování ohonu komety, který je vždy orientován směrem od Slunce. Na rozdíl od kosmu však na Zemi tlak záření za normálních podmínek nemá reálný význam, neboť je pro většinu zdrojů malý v porovnání například s tlakem okolního prostředí. Výjimku tvoří zdroje velmi intenzivního záření a v poslední době zejména velmi intenzivní laserové impulsy, kde samotný tlak záření fokusovaného paprsku může téměř dosahovat řádu Tbar. Projev vysokého tlaku záření je podobný, jako bychom na povrch terče tlačili pomocí pístu, který působí především na elektrony. Někdy se v anglické terminologii používá termín "laser piston effect". V případě reálného laserového svazku s vysokou intenzitou způsobuje tlak záření parabolickou deformaci povrchu a umožňuje svazku proniknout hlouběji do terče. Pokud je laserový impuls dostatečně dlouhý, parabolická deformace se prohlubuje a celý jev připomíná vrtání díry. Pro tento proces se v angličtině ustálil termín "hole boring". Rychlost s jakou postupuje povrch terče dovnitř v_{HB} pak můžeme odhadnout na základě zákona zachování hybnosti a za předpokladu téměř 100% reflektivity dostáváme

$$\frac{2I_L}{c}\frac{1-v_{HB}/c}{1+v_{HB}/c} = 2n_i m_i v_{HB}^2 \gamma_{HB}^2 \quad , \tag{3.8}$$

kde γ_{HB} je γ-faktor příslušný k v_{HB} [123]. Ionty uvnitř terče jsou pak urychleny jako u bezesrážkové rázové vlny na rychlost $2v_{HB}$.

Z hlediska urychlování iontů se tento režim stává zajímavým především v případě velmi tenkých terčů, kdy je laserový impuls dost dlouhý, aby urychlil všechny ionty obsažené v ozařované části fólie, a zároveň terč zůstává netransparentní pro laserové záření. Tento režim tedy můžeme přibližně vymezit podmínkami [129]

$$\tau v_{HB} > l \quad , \quad a_0 < \pi \frac{n_e}{n_c}\frac{l}{\lambda_L} \quad , \tag{3.9}$$

kde l je tloušťka terče a τ je délka laserového impulsu. Zjednodušeně lze na situaci nahlížet tak, že laserový impuls roztlačí část terče před sebou.

Pokud by se podařilo udržet stabilitu tohoto procesu dostatečně dlouho, bylo by možné dosáhnout vysoké energie urychlených iontů, vysoké účinnosti i relativně úzkého energetického spektra a jednalo by se o ideální proces z hlediska dalších aplikací. Velmi zajímavý je rovněž fakt, že maximální energie urychlených iontů je úměrná laserové intenzitě a ne její odmocnině jak je tomu u procesu TNSA. To přináší naději na dosažení vysokých energií urychlených protonů

(> 100 MeV) již s generací PW laserů. Bohužel podobně jako u laserové fúze i zde působí Rayleigh-Taylorova nestabilita, která vede k desintegraci terče [130] a celý proces urychlování značně komplikuje. Získání kvazimonoenergetického spektra iontů pak komplikuje také radiální profil intenzity laserového záření jemuž odpovídá také profil působícího tlaku záření. Režim urychlování iontů tlakem záření bude diskutován v popisu jedné z přiložených publikací [35].

Ve velmi malých terčích jako klastrech, vodních kapičkách nebo některých velmi tenkých fóliích může dojít k tomu, že laserový impuls vytlačí všechny nebo téměř všechny elektrony ven z terče, případně elektrony urychlí tak, že Debyeova délka je větší než velikost terče. V takovém případě přestává být terč kvazineutrální a ionty se začínají odpuzovat Coulombovskou silou. Urychlování iontů pak probíhá v režimu Coulombovské exploze [131]. Coulombovská exploze je do určité míry přítomna i v jiných procesech urychlování, neboť oblast urychlování iontů není nikdy zcela kvazineutrální. S výjimkou velmi tenkých fólií a širšího ohniska laserového svazku není Coulombovská exploze vhodná k urychlování svazků částic. Coulombovská síla je radiální a urychlování je tedy přirozeně izotropní. Z tohoto důvodu se tímto procesem nezabýváme.

4 Komentáře k vybraným publikacím popisující náš výzkum urychlování iontů

Vyšší efektivity urychlování iontů v procesu TNSA lze dosáhnout zvýšením absorpce laserové energie a teploty horkých elektronů. Absorpce laserového záření však na rovném povrchu pevného terče nemusí být příliš vysoká, a to zejména pokud není optimální úhel dopadu a profil plazmatu na povrchu terče před samotnou interakcí. Již v 80. letech minulého století však bylo v experimentech dokázáno, že mikroskopické nerovnosti nebo struktury na povrchu terče zvyšují absorpci laserové energie a vyzařování rentgenového záření [132–134]. Ve spolupráci s týmem Prof. Kawaty [36] jsme přišli s návrhem použití mikroskopické struktury na povrchu terčů sloužících k urychlování iontů za účelem zvýšení efektivity TNSA. Tato myšlenka je dále rozvíjena v následujících čtyřech článcích zahrnutých v této práci. V pátém článku je pak diskutováno urychlování iontů tlakem záření kruhově polarizované laserové vlny.

4.1 Článek č. 7: Short pulse laser interaction with micro-structured targets: simulations of laser absorption and ion acceleration

Tento článek je z velké části založen na výsledcích dvourozměrných částicových simulacích. Demonstruje, že mikrostruktura na povrchu terče může výrazně zvyšovat absorpci intenzivních laserových impulsů s vysokým kontrastem. Tento efekt se projevuje zvýšením teploty a počtu horkých elektronů. U tenkých terčů je pak pozorováno efektivnější urychlování iontů a zvýšení jejich maximální energie. Použití mikrostruktury na povrchu terče rozšiřuje úhlové rozdělení horkých elektronů, avšak úhlová distribuce rychlých iontů tím ovlivněna není.

Absorpce laserového záření závisí jednak na tvaru a jednak na velikosti pravidelné mikrostruktury. Závislost na velikosti struktury se přitom jeví jako důležitější. Navrhujeme proto relativně jednoduchý terč s kuličkami na povrchu uspořádanými tak, aby vzdálenost mezi kuličkami byla co nejmenší. Pro tento terč se ukazuje, že optimální průměr kuliček je v rozmezí 0.5-1 krát vlnová délka laserového záření. Simulace dokazují, že vrstva mikrokuliček na povrchu terče nemusí být ani zcela rovnoměrná, pokud je v průměru zachována přibližně optimální velikost kuliček. To je dobrá zpráva z hlediska citlivosti procesu na kvalitu a rovnoměrnost vrstvy mikrokuliček v experimentu. Kolegové z KFE zároveň navrhli možnosti výroby tohoto terče, terč připravili a pořídili několik snímků s použitím elektronového mikroskopu a AFM (z anglického termínu Atomic Force Microscopy).

Abychom se přiblížili reálným experimentům, studovali jsme rovněž závislost výsledků na úhlu dopadu laserového záření na terč. Zjistili jsme, že na rozdíl od rovného povrchu terče při použití mikrokuliček výsledky na úhlu dopadu příliš nezávisí. Také byl studován vliv malého hustotního profilu, který může vzniknout na přední straně terče v důsledku absorpce laserového předpulsu. Bylo zjištěno, že tento profil částečně zeslabuje vliv mikrostruktury na povrchu terče. Pokud by délka hustotního profilu byla srovnatelná s velikostí mikrostruktury, její vliv na absorpci laserového záření by pravděpodobně byl zanedbatelný.

Kvůli usnadnění prvních experimentů prokazujících vliv povrchové mikrostruktury na urychlování iontů byla v článku navržena i možnost pozorování iontů urychlených z přední strany terče ve směru zpět do vakua. To by umožnilo použití tlustších terčů, což usnadňuje manipulaci a přípravu mikrostruktury. V případě tlustších terčů bez mikrostruktur je možné i vyleštění jejich povrchu. Dobrá znalost kvality povrchu terče je přitom pro experimentální porovnání klíčová.

Jeden z hlavních přínosů tohoto článku spočívá v přiblížení teorie směrem k experimentům. Je nalezena jednoduchá konfigurace mikrostruktury na povrchu terče, která může sloužit v prvních experimentech k prokázání jejího pozitivního vlivu na urychlování iontů v procesu TNSA. Zároveň je navržen konkrétní terč a jsou studovány další aspekty, které by mohly ovlivnit výsledek navrhovaného experimentu. Účelem této publikace bylo především připravit podmínky pro experimentální potvrzení našich teoretických závěrů a pro získání experimentálního času na relevantních laserových instalacích.

4.2 Článek č. 8: Laser-Driven Proton Acceleration Enhancement by Nanostructured Foils

Pro realizaci experimentu urychlování iontů z terče s mikrostrukturou na povrchu je důležitá jednak vysoká intenzita, ale také omezení expanze terče před příchodem hlavního pulsu. To bylo ukázáno již v závěru předchozí publikace. Dosažení potřebného kontrastu laserového impulsu je obtížné, a proto se za tímto účelem začala používat plazmová zrcadla. Ta odráží jen malé množství záření předtím, než na jejich povrchu vznikne plazma, a tedy je potlačena počáteční část laserového impulsu s nižší intenzitou. Při realizaci experimentu s terčem s povrchovou mikrostrukturou bylo třeba spolupracovat s pracovištěm, kde se již plazmová zrcadla používají. První úspěšné experimenty probíhaly na pracovišti APRI-GIST v Jižní Koreji a jejich výsledky jsou publikovány v tomto článku.

V experimentu byly použity jako terče 1 μm tlusté plastové fólie, na jejichž povrch byly kolegy z KFE naneseny polystyrenové mikrokuličky. Terč byl ozařován 100 TW laserovým impulsem s použitím dvojitého plazmového zrcadla pro zlepšení kontrastu. Maximální energie

urychlených protonů v případě fólií s kuličkami vzrostla o 60% oproti fólii bez kuliček a optimální velikost kuliček byla stanovena na přibližně 535 nm. Tato optimální velikost přibližně odpovídá výsledkům našich simulací. Vliv mikrostruktury se neprojevil pouze zvýšením maximální energie urychlených protonů, ale především nárůstem efektivity urychlování. Pokud vezmeme v úvahu pouze protony s kinetickou energií vyšší než 1 MeV, tak jejich počet vzrostl použitím terče s mikrokuličkami přibližně pětinásobně. Experimentům přitom předcházela příprava založená na našich simulacích. Výsledky experimentů byly s těmito výpočty v dobré shodě v maximální energii protonů a v přibližné shodě i v závislosti této energie na velikosti mikrokuliček.

Tento článek je vůbec první úspěšnou demonstrací vlivu povrchové mikrostruktury na urychlování iontů při interakci intenzivních laserových impulsů s terči. Díky tomu byl také přijat k publikaci v prestižním vědeckém časopise Physical Review Letters.

4.3 Článek č. 9: Micro-sphere layered targets efficiency in laser driven proton acceleration

Druhý úspěšný experiment demonstrující zvýšení efektivity urychlování protonů pomocí mikrokuliček na povrchu terče proběhl v laboratoři CEA Saclay ve Francii. Parametry použitého laserového systému byly podobné jako u laseru v APRI-GIST. Experiment byl proveden se třemi tloušťkami terče a pod různým úhlem dopadu laserového záření. To bylo umožněno použití speciálního detektoru rychlých iontů umístěného přímo v terčové komoře. Efekt mikrokuliček na urychlování iontů bohužel nebyl zaznamenán u terčů s nejmenší tloušťkou (0.9 μm), avšak byl jednoznačně potvrzen u tlustších terčů. U těchto terčů bylo také prokázáno, že na rozdíl od fólie s rovným povrchem, urychlování iontů z fólie s mikrokuličkami výrazně nezávisí na úhlu dopadu laserového svazku a pro velké úhly dopadu (45°) není již efekt mikrokuliček patrný. Tento efekt byl zaznamenán a předpovězen i v našich předchozích simulacích.

Článek rovněž podrobněji diskutuje absorpci a urychlování elektronů v případě použití mikrokuliček na povrchu terče. Na základě několika reprezentativních trajektorií elektronů získaných z našich simulací je ukázáno, jakým způsobem zvyšují mikrokuličky absorpci laserového záření. Velmi často dochází k situaci, kdy je elektron během poloviny periody laserové vlny urychlen ze strany jedné kuličky ven do vakua a následně vletí dovnitř do sousední kuličky, kde jeho další pohyb není ovlivňován polem laserové vlny. Elektron si tedy uchová energii získanou v elektromagnetickém poli vně terče.

4.4 Článek č. 10: Evidence of Resonant Surface-Wave Excitation in the Relativistic Regime through Measurements of Proton Acceleration from Grating Targets

V předcházejících experimentech byla ke zvýšení absorpce laserového záření použita rovnoměrná mikrostruktura z kuliček. Mikrokuličky byly zvoleny proto, že tento terč je možné relativně jednoduše realizovat na povrchu tenké fólie (bez náročného přístrojového vybavení). Z hlediska urychlování iontů však tento terč nemusí být ideální. Je známo, že velkého zvýšení absorpce lze dosáhnou excitací povrchových plazmových vln, což bylo pozorováno v experimentech s laserovým zářením o nižších intenzitách [135]. Pro excitaci povrchových plazmových vln je potřeba periodická struktura, jejíž perioda d odpovídá úhlu dopadu α laserového svazku podle vztahu $\sin\alpha + \lambda_L/d = \sqrt{(1 - n_e/n_c)/(2 - n_e/n_c)}$. Pro pevný terč ($n_e \gg n_c$) a úhel dopadu $\alpha = 30°$, vychází $d = 2\lambda_L$ a tedy optimální perioda mikrostruktury je dvojnásobek vlnové délky laserového záření. Z tohoto vztahu je také vidět, že k excitaci povrchových plazmových vln nedochází, pokud je perioda mikrostruktury menší než vlnová délka laserového záření (což je případ terčů s mikrokuličkami v předchozích experimentech, pokud uvažujeme jako periodu nejkratší vzdálenost středů kuliček od sebe).

Excitace povrchových plazmových vln byla demonstrována na základě měření reflektivity laserového záření a maximální energie protonů urychlených ze zadní strany terče v procesu TNSA v závislosti na úhlu dopadu laserového svazku. Jako terče byly použity plastové fólie, do nichž byl reliéf mřížky s požadovanou periodou vylisován z připravené matrice kolegy z KFE. Vznik povrchových plazmových vln byl pozorován i v simulacích zahrnutých v článku, avšak jejich vliv na celkovou absorpci laserového záření nebyl tak zřejmý jako v experimentu. Článek je nicméně vůbec prvním zdokumentovaným pozorováním povrchových plazmových vln při relativistických laserových intenzitách. Díky tomu byl také přijat k publikaci v prestižním vědeckém časopise Physical Review Letters.

4.5 Článek č. 11: Monoenergetic ion beams from ultrathin foils irradiated by ultrahigh-contrast circularly polarized laser pulses

Urychlování iontů pomocí tlaku záření laserového impulsu se zdá jako velmi slibná možnost pro budoucí generaci velmi výkonných laserových systémů. Toto urychlování bylo v diskutovaném článku studováno na základě částicových počítačových simulací. Rozhodujícím přínosem k danému tématu je použití kruhové polarizace laserového záření. Ve výpočtech se ukazuje, že v případě kruhové polarizace je potlačen ohřev horkých elektronů, neboť ponderomotorická

síla laserového záření nemá oscilující vysokofrekvenční složku, která je často za urychlování elektronů odpovědná. V případě kruhové polarizace tedy nejsou elektrony výrazně urychlovány směrem do terče, terč příliš neexpanduje kvůli nízké efektivitě procesu TNSA a reflektivita laserového záření je relativně vysoká. Za těchto podmínek je v jednorozměrném přiblížení dosaženo maximálního tlaku záření a zároveň relativně stabilního urychlování celého kompaktního terče, držícího dlouhou dobu pohromadě.

K urychlování iontů dochází na přední straně terče. Tlak záření vytlačí elektrony z povrchové vrstvy směrem dovnitř do terče. Tím se indukuje silné elektrostatické pole, které urychluje také ionty. Po urychlení dovnitř již nejsou ionty vystaveny dalšímu silnému poli a pohybují se pohybem rovnoměrným. Pokud urychlování pokračuje dostatečně dlouho, dojde postupně k urychlení všech iontů a ionty urychlené na začátku interakce jsou dohnány a předehnány ostatními rychlejšími ionty. V této fázi dochází vždy k urychlování nejpomalejších iontů, které se v důsledku toho, že je předstihnou rychlejší ionty, dostávají na přední stranu terče. To vede k přirozeně kvazimonoenergetickému spektru iontů a rovněž k urychlování všech druhů iontů na přibližně stejnou rychlost.

Ve vícerozměrném případě je situace komplikovanější a urychlování iontů je méně efektivní. Hlavním problémem je deformace povrchu terče v důsledku nerovnoměrné intenzity, která vede postupně ke zvýšení účinnosti urychlování elektronů a k rychlé expanzi terče. Jako řešení tohoto problému je navrženo použití supergaussovského profilu intenzity v ohnisku laserového svazku. Dalším problémem je výskyt Raileigh-Taylorovy nestability mezi fotony laserového záření a oblakem volných elektronů. I tato nestabilita postupně přispívá k desintegraci terče a omezuje efektivitu urychlování iontů.

V době svého zveřejnění byl tento článek jedním z prvních (v rozmezí několika měsíců vyšlo několik dalších článků zabývajících se stejným problémem), které představily a popsaly urychlování iontů tlakem záření relativistického laserového impulsu s použitím kruhové polarizace a velmi tenkých terčů. Tento způsob urychlování iontů je z hlediska aplikací velmi slibný, neboť potenciálně umožňuje současně dosáhnout velké efektivity, vysokých energií urychlených iontů a kvazimonoenergetického spektra. O tom svědčí i fakt, že tento článek vyvolal velký ohlas v naší vědecké komunitě a v současné době je podle vyhledávání na stránkách APS druhým nejcitovanějším článkem v historii časopisu Physical Review Special Topics - Accelerators and Beams hned po článku [136].

4.6 Hlavní přínos uvedených publikací

V následujících několika bodech shrňme hlavní vědecké přínosy uvedených publikací. Jsou to:

- Popis vlivu povrchové mikrostruktury na urychlování iontů při interakci intenzivních la-

serových impulsů s terči.

- Prostudování různých typů struktur a navržení vhodné povrchové struktury pro první demonstrační experimenty včetně jejich optimálních parametrů.
- Popis procesů přispívajících ke zvýšené absorpci laserového záření v navržených terčích.
- Návrh a úspěšná spolupráce na realizaci prvních experimentů prokazujících významný vliv povrchové mikrostruktury na urychlování iontů s několikanásobným zvýšením efektivity tohoto procesu.
- První úspěšná demonstrace excitace povrchových plazmových vln velmi intenzivním laserovým impulsem na mřížce s vhodně zvolenými parametry a vlivu této excitace na urychlování iontů.
- Předpovězení velmi zajímavého a efektivního způsobu urychlování kvazi-monoenergetického svazku iontů tlakem záření intenzivní kruhově polarizované laserové vlny při jejím dopadu na velmi tenký terč. Popis procesu urychlování iontů a závislosti výsledků na parametrech interakce.

5 Závěr

Výzkum interakce intenzivního laserového záření s terči a inerciální fúze jsou velmi aktuální a rychle se vyvíjející témata. O významu těchto témat svědčí i to, že projekt National Ignition Facility bývá zmiňován mezi současnými deseti nejambicióznějšími vědeckými projekty na světě po boku projektů jako je LHC (Large Hadron Collider) nebo ISS (International Space Station) [137, 138]. Dostat se mezi tyto projekty bylo i původním záměrem tvůrců projektu ELI a než byl projekt rozdělen na čtyři části, jeho potenciál v tomto směru byl veliký.

Kromě využití laserových systémů s vysokou energií pro výzkum inerciální fúze může další studium v oblasti interakce intenzivního laserového záření s hmotou přinést také zdroje energetických částic s jedinečnými vlastnostmi. Známy jsou v dnešní době například projekty jako Table-Top Free-Electron-Laser [139, 140]. Pracuje se také na urychlování elektronů a v této oblasti mají lasery velký potenciál nahradit v budoucnu konvenční urychlovače [141]. Záření z laserové interakce se používá i ke snímkování jevů s jedinečným časovým rozlišením a v budoucnosti snad bude možné s attosekundovými impulsy sledovat dynamiku pohybu elektronů v molekulách a pevných materiálech [142]. Další výzkum v oblasti velmi vysokých intenzit nám může přinést i mnohé informace o základní podstatě fyzikálních vlastností našeho světa. Například samotná síla "reakce záření" (v anglické terminologii "radiation reaction"), která je dosud většinou opomíjenou součástí pohybové rovnice nabitých částic (vyskytuje se v Loretnz-Abrahm-Dirakově pohybové rovnici) a pro jejíž tvar nebylo dosud nalezeno uspokojivé analytické řešení [143], by mohla být v brzké budoucnosti potvrzena a studována v experimentech. Ve vzdálenější budoucnosti pak leží otázky jako existence a možnost dosažení Schwingerova limitního pole, nelinearita vakua při velmi vysokých intenzitách a podobné. Je tedy zřejmé, že výzkum v oblasti interakce intenzivního laserového záření s plazmatem skýtá stále velké množství nedořešených otázek a velký potenciál pro další výzkum a významné vědecké objevy.

K výzkumu v oblasti interakce intenzivního laserového záření s hmotou se ve vší skromnosti a pokoře snaží určitým dílem přispět i autor této práce. V této práci jsou shrnuty hlavní výsledky tohoto výzkumu za posledních několik let. Výsledky se týkají dvou na první pohled zdánlivě nesouvisejících témat, a to "interakce laserového záření s plazmatem v podmínkách zapálení inerciální fúze silnou rázovou vlnou"a "urychlování iontů pomocí intenzivních laserových impulsů". Pojítkem těchto témat je jejich společný základ vycházející z výzkumu inerciální termojaderné fúze a dále možnost studia těchto jevů pomocí částicových počítačových simulací. Těmto simulacím (včetně rozvoje simulačních kódů) se autor práce i vědecká skupina, v níž působí, věnují již dlouhou dobu.

V oblasti výzkumu interakce laserového záření s plazmatem jsou zde uvedeny výsledky týka-

jící se především absorpce laserového záření v horké a dlouhé plazmové koroně před povrchem terče, procesů účastnících se této absorpce a jejich vzájemného ovlivňování. Tyto výsledky přinášejí nový pohled na některé parametrické nestability a jejich roli v inerciální fúzi zapálené silnou rázovou vlnou.

Z hlediska výzkumu urychlování iontů jsou prezentovány výsledky zvyšující efektivitu stávajících procesů urychlování za pomocí speciálních terčů s mikroskopickou strukturou na povrchu. Tento výzkum začínal čistě teoreticky s pomocí počítačových simulací a postupně se vyvíjel směrem k experimentům, které by tyto výsledky potvrzovaly. Pravděpodobně nejznámější práce autora se pak týká jiného pokročilého způsobu urychlování iontů s použitím velmi intenzivních laserových impulsů s kruhovou polarizací a velmi tenkých terčů. Tento způsob urychlování iontů přináší mnohá zlepšení a nové možnosti oproti těm stávajícím a s příchodem nové generace laserových systémů přináší naději na výrazné zlepšení výsledků v této oblasti.

5.1 Výhled do budoucna

V oblasti interakce intenzivního laserového záření s plazmatem je velký prostor pro další práci a studium. Ve stručnosti je zde nastíněn možný směr dalšího výzkumu v této oblasti.

Interakce laserového záření s plazmatem v souvislosti s inerciální fúzí

Výsledky týkající se interakce laserového záření s terčem v podmínkách inerciální fúze, diskutované v minulých částech této práce, pokrývají pouze velmi omezený prostor parametrů a možných procesů. Možností pro další výzkum je tedy celá řada a nastíníme zde jen několik zajímavých. Za prvé by bylo vhodné prozkoumat větší prostor parametrů, zejména délek hustotního profilu a teplot plazmatu. V tomto směru bychom se rádi posunuli zejména k parametrům většiny současných experimentů na menších laserových zařízeních jako jsou PALS nebo LULI ve Francii. Zde bývá charakteristická délka hustotního profilu menší a nižší plazmová teplota způsobuje mnohem větší četnost srážek. To vede pravděpodobně k menšímu vlivu parametrických nestabilit a k jejich rozvoji především v řidším plazmatu, kde bývají při vysokých teplotách tlumeny Landauovým útlumem.

Další zajímavou možností by bylo studium interakce ve dvourozměrné geometrii v celé oblasti zahrnující rovněž kritickou hustotu a to alespoň pro jeden nebo několik filamentů laserového záření. Tyto filamenty by simulovaly rozložení intenzity laserového svazku v experimentech při použití náhodných fázových destiček. V neposlední řadě by bylo zajímavé studovat také šikmý dopad laserového záření nebo mírně zakřivit povrch terče. To více odpovídá experimentální geometrii v inerciální fúzi a může tedy přispět k jejímu přesnějšímu popisu.

Urychlování iontů

V oblasti urychlování iontů se chceme soustředit na další možnosti spolupráce na experimentech s kolegy z APRI-GIST v Jižní Koreji a CEA Saclay ve Francii. Spolu s kolegy z naší katedry máme možnost přípravy terčů pro další pokročilé způsoby urychlování iontů. Velmi zajímavé by například bylo zkombinování malé tloušťky terče s celkově malými rozměry terče a s povrchovou mikrostrukturou pro zvýšení absorpce. V teoretické části výzkumu bychom se rádi zaměřili na proces urychlování iontů při velmi vysokých intenzitách laserového záření $> 10^{22}$ W/cm^2, neboť za takových podmínek nejsou procesy urychlování iontů ještě prozkoumány ani teoreticky.

Oblast vysokých intenzit laserového záření

V souvislosti s výstavbou laserového centra ELI Beamlines v České republice se náš výzkum začíná více koncentrovat na vysoké intenzity laserového záření. Fyzika interakce laserového záření s materiálem se zde opět kvalitativně mění, neboť se i terče z pevného materiálu mohou stávat relativisticky transparentními. Dochází zde také k velmi výraznému vyzařování pohybujícími se elektrony, mohou vznikat elektron-pozitronové páry a energetické částice mohou indukovat i některé jaderné procesy. Tato neprobádaná oblast není zatím dostupná v reálných experimentech, a o to více je zde prostor pro využití počítačových simulací a teoretického výzkumu k předpovězení nových procesů a jevů.

5.2 Spolupráce se studenty

K práci na vysoké škole patří samozřejmě i výchova studentů a spolupráce s nimi. Na experimentech, týkajících se urychlování iontů diskutovaných v publikacích v této práci se významnou měrou podílel i student doktorského studia Bc. Ing. Jan Prokůpek a některé výsledky těchto experimentů budou součástí jeho doktorské práce. Další současný student doktorského studia, Ing. Jiří Vyskočil, v rámci své diplomové práce porovnával simulace interakce laserového impulsu s mikrostrukturou na povrchu terče ve dvourozměrné a trojrozměrné geometrii. Na reálných trojrozměrných simulacích interakce laserového záření pracuje i nyní ve svém doktorském studiu. Urychlování iontů v případě velmi vysokých intenzit laserového záření bylo částečně diskutováno i v diplomové práci Ing. Martina Jirky, rovněž současného studenta doktorského studia.

Na tématu interakce laserového záření s plazmatem v podmínkách inerciální fúze zapálené silnou rázovou vlnou spolupracuje také Bc. Petr Valenta, který na toto téma v roce 2014 napsal a obhájil svou bakalářskou práci. S dalšími studenty bakalářského a doktorského studia spolupracuje nyní autor této práce na jiných oblastech výzkumu laserové interakce s plazmatem.

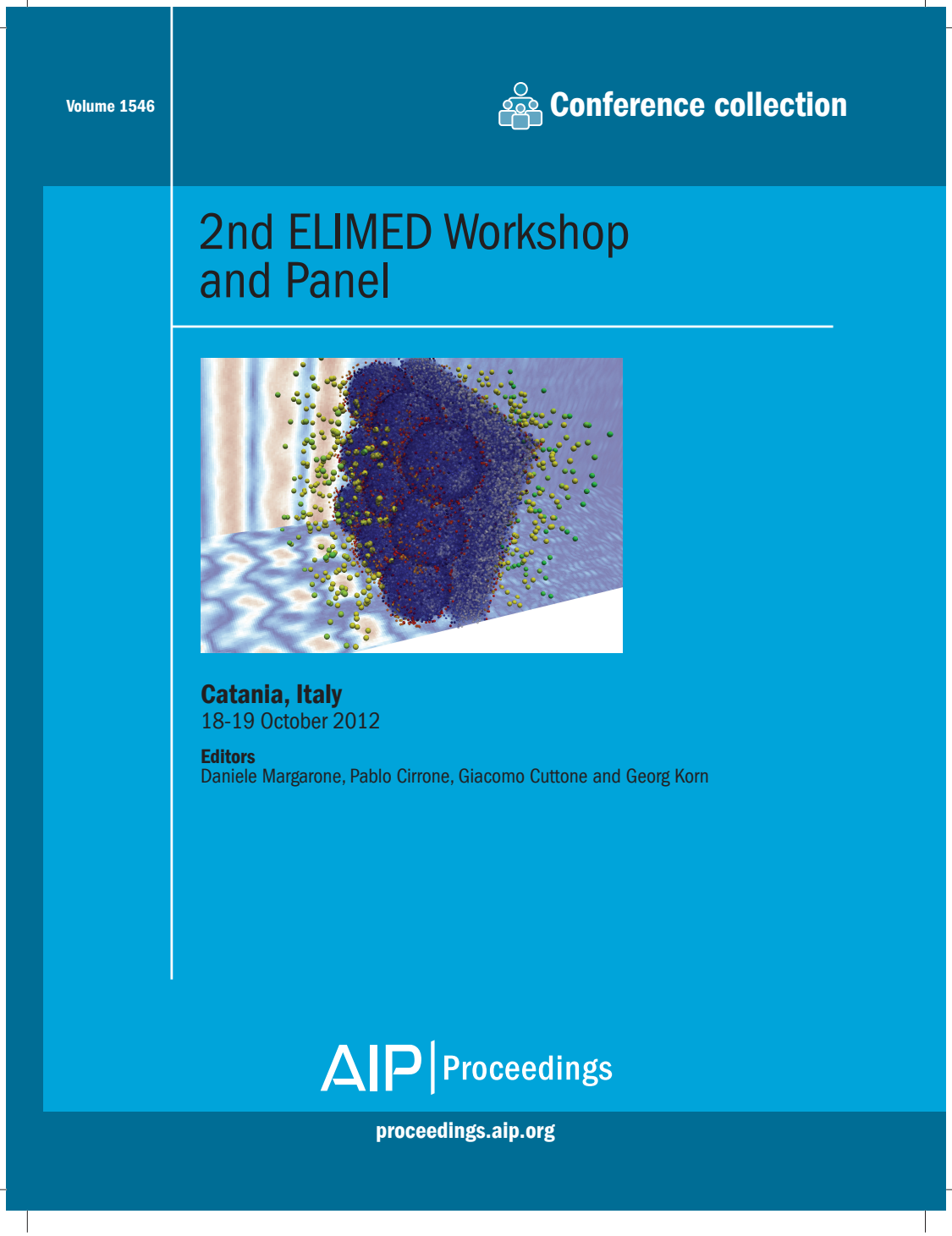

Obrázek 5.1: Obrázek z 3D simulace urychlování iontů intenzivním laserovým impulsem z terče s mikroskopickými kuličkami na povrchu na titulní stránce sborníku z konference. Simulaci provedl Ing. Jiří Vyskočil.

Literatura

[1] A. Novotny, H. Jelinkova, V. Kubecek, M. Cech, I. Prochazka *et al.*, Lasery na Fakultě jaderné a fyzikálně inženýrské ČVUT. *Československý časopis pro fyziku* **(2010)**, Vol. 60, p. 280.

[2] V. Sochor, *Lasery a koherentní svazky*, Academia, Praha **(1990)**.

[3] A. Novotny, Modulace činitele jakosti Fabry-Perrotova rezonátoru I. Diplomová práce, FTJF ČVUT Praha **(1965)**.

[4] T. Daricek, Modulace činitele jakosti Fabry-Perrotova rezonátoru II. Diplomová práce, FTJF ČVUT Praha **(1965)**.

[5] K. Hamal, V. Sochor, T. Daricek, and A. Novotny, Comparison of rotating mirror and liquid bleacher as a Q switch for a ruby laser. *Journal of Scientific Instruments* **(1967)**, Vol. 44, p. 548.

[6] V. Sochor and A. Novotny, Ionizace plynného prostředí intensivním laserovým svazkem. *Československý časopis pro fyziku* **(1968)**, Vol. 18, p. 672.

[7] P. Hribek, private communication, hribek@fzu.cz.

[8] P. Hribek, V. Kubecek, and M. Vrbova, Picosecond ND-Glass-Laser System with Plasma Mirror. *Applied Physics B-Photophysics and Laser Chemistry* **(1982)**, Vol. 29, p. 177.

[9] P. Hribek and M. Vrbova, Nd:Glass Laser with Plasma Mirror. *Czechoslovak Journal of Physics* **(1985)**, Vol. B 35, p. 1331.

[10] M. Kalal, L. Pina, and M. Vrbova, The X-Ray-Emission from an ND-Glass Laser Plasma Mirror. *Kvantovaya Elektronika* **(1984)**, Vol. 11, pp. 2361–2364.

[11] S. Weber, C. Riconda, L. Lancia, J. R. Marques, G. A. Mourou *et al.*, Amplification of Ultrashort Laser Pulses by Brillouin Backscattering in Plasmas. *Physical Review Letters* **(2013)**, Vol. 111, art. no. 055004.

[12] J. Skála, private communication, skala@pals.cas.cz.

[13] M. Chvojka, V. Hermoch, B. Kralikova, J. Krasa, L. Laska *et al.*, 100-GW Pulsed Iodine Photodissociation Laser System PERUN-I. *Czechoslovak Journal of Physics* **(1988)**, Vol. 38, p. 1337.

[14] L. Laska, J. Krasa, K. Masek, M. Pfeifer, P. Trenda *et al.*, Multiply charged ion generation from NIR and visible laser-produced plasma. *Review of Scientific Instruments* **(1996)**, Vol. 67, pp. 950–952.

[15] J. Dostal, H. Turcicova, B. Kralikova, L. Kral, and J. Huynh, Iodine photodissociation laser SOFIA with MOPO-HF as a solid-state oscillator. *Applied Physics B* **(2009)**, Vol. 97, pp. 687–694.

[16] D. Batani, H. Stabile, A. Ravasio, G. Lucchini, F. Strati *et al.*, Ablation pressure scaling at short laser wavelength. *Physical Review E* **(2003)**, Vol. 68, art. no. 067403.

[17] M. Kalal, J. Limpouch, E. Krousky, K. Masek, K. Rohlena *et al.*, Thermal smoothing by laser-produced plasma of porous matter. *Fusion Science and Technology* **(2003)**, Vol. 43, pp. 275–281.

[18] D. Batani, F. Strati, H. Stabile, M. Tomasini, G. Lucchini *et al.*, Hugoniot data for carbon at megabar pressures. *Physical Review Letters* **(2004)**, Vol. 92, art. no. 065503.

[19] B. Rus, T. Mocek, A. R. Prag, J. C. Lagron, M. Hudecek *et al.*, X-ray laser facility at the PALS centre. *Journal de Physique IV* **(2001)**, Vol. 11, pp. 589–596.

[20] B. Rus, T. Mocek, A. R. Prag, M. Kozlova, G. Jamelot *et al.*, Multimillijoule, highly coherent x-ray laser at 21 nm operating in deep saturation through double-pass amplification. *Physical Review A* **(2002)**, Vol. 66, art. no. 063806.

[21] J. Wolowski, J. Badziak, F. P. Boody, H. Hora, V. Hnatowicz *et al.*, Fast ion emission from the plasma produced by the PALS laser system. *Plasma Physics and Controlled Fusion* **(2002)**, Vol. 44, pp. 1277–1283.

[22] L. Laska, K. Jungwirth, B. Kralikova, J. Krasa, M. Pfeifer *et al.*, Generation of multiply charged ions at low and high laser-power densities. *Plasma Physics and Controlled Fusion* **(2003)**, Vol. 45, pp. 585–599.

[23] T. Pisarczyk, A. Kasperczuk, E. Krousky, K. Masek, R. Miklaszewski *et al.*, The PALS iodine laser-driven jets. *Plasma Physics and Controlled Fusion* **(2007)**, Vol. 49, pp. B611–B619.

[24] M. Momcilovic, J. Limpouch, V. Kmetik, R. Redaelli, J. Savovic *et al.*, Surface modification of copper using high intensity, 10^{15} W/cm^2, femtosecond laser in vacuum. *Applied Surface Science* **(2012)**, Vol. 258, pp. 8908–8914.

[25] M. Trtica, D. Batani, R. Redaelli, J. Limpouch, V. Kmetik *et al.*, Titanium surface modification using femtosecond laser with $10^{13} - 10^{15}$ W/cm^2 intensity in vacuum. *Laser and Particle Beams* **(2013)**, Vol. 31, pp. 29–36.

[26] J. Hrebicek, B. Rus, J. C. Lagron, J. Polan, T. Havlicek *et al.*, 25 TW Ti:sapphire laser chain at PALS. *Conference on Diode-Pumped High Energy and High Power Lasers/ELI: Ultrarelativistic Laser-Matter Interactions and Petawatt Photonics/HiPER: the European Pathway to Laser Energy*, Proceedings of SPIE Series, L. A. Gizzi, C. Edwards, J. Hein, L. O. Silva, and G. Korn, Editors **(2011)**, Vol. 8080, art. no. 80800u.

[27] J. Prokupek, D. Margarone, J. Hrebicek, M. Krus, A. Velyhan *et al.*, Pilot experiment on proton acceleration using the 25 TW femtosecond Ti:Sapphire laser system at PALS. *Nuclear Instruments & Methods in Physics Research Section A-Accelerators Spectrometers Detectors and Associated Equipment* **(2012)**, Vol. 690, pp. 48–52.

[28] J. Dostal, R. Dudzak, J. Huynh, J. Ullschmied, and T. Pisarczyk, New 3-frame Femtosecond Plasma-Probing Techniques at the PALS Research Infrastructure. *Plasma Physics and Technology* **(2014)**, to be published.

[29] J. Limpouch, V. Bina, T. Dytrych, and O. Klimo, Laser absorption, electron acceleration and K-alpha emission in short-pulse laser-target interactions. *Czechoslovak Journal of Physics* **(2002)**, Vol. 52, pp. 342–348.

[30] J. Limpouch, O. Klimo, V. Bina, and S. Kawata, Numerical studies on the ultrashort pulse K-alpha emission sources based on femtosecond laser-target interactions. *Laser and Particle Beams* **(2004)**, Vol. 22, pp. 147–156.

[31] O. Klimo, V. Tikhonchuk, and A. Debayle, High-current fast electron beam propagation in a dielectric target. *Physical Review E* **(2007)**, Vol. 75, art. no. 016403.

[32] J. Psikal, O. Klimo, and J. Limpouch, Field ionization effects on ion acceleration in laser-irradiated clusters. *Nuclear Instruments & Methods in Physics Research Section A-Accelerators Spectrometers Detectors and Associated Equipment* **(2011)**, Vol. 653, pp. 109–112.

[33] O. Klimo, M. Jirka, M. Masek, J. Limpouch, M. Bussmann *et al.*, The radiation reaction effect in ultra intense laser foil interactions. *Conference on High-Power, High-Energy, and High-Intensity Laser Technology; and Research Using Extreme Light - Entering New Frontiers with Petawatt-Class Lasers*, Proceedings of SPIE Series, J. Hein, G. Korn, and L. O. Silva, Editors **(2013)**, Vol. 8780, art. no. UNSP 87801O.

[34] A. V. Brantov, V. T. Tikhonchuk, O. Klimo, D. V. Romanov, S. Ter-Avetisyan *et al.*, Quasi-mono-energetic ion acceleration from a homogeneous composite target by an intense laser pulse. *Physics of Plasmas* **(2006)**, Vol. 13, art. no. 122705.

[35] O. Klimo, J. Psikal, J. Limpouch, and V. Tikhonchuk, Monoenergetic ion beams from ultrathin foils irradiated by ultrahigh-contrast circularly polarized laser pulses. *Physical Review Special Topics - Accelerators and Beams* **(2008)**, Vol. 11, art. no. 031301.

[36] Y. Nodera, S. Kawata, N. Onuma, J. Limpouch, O. Klimo *et al.*, Improvement of energy-conversion efficiency from laser to proton beam in a laser-foil interaction. *Physical Review E* **(2008)**, Vol. 78, art. no. 046401.

[37] O. Klimo, J. Psikal, J. Limpouch, J. Proska, F. Novotny *et al.*, Short pulse laser interaction with micro-structured targets: simulations of laser absorption and ion acceleration. *New Journal of Physics* **(2011)**, Vol. 13, art. no. 053028.

[38] D. Margarone, O. Klimo, I. J. Kim, J. Prokupek, J. Limpouch *et al.*, Laser-Driven Proton Acceleration Enhancement by Nanostructured Foils. *Physical Review Letters* **(2012)**, Vol. 109, art. no. 234801.

[39] V. Floquet, O. Klimo, J. Psikal, A. Velyhan, J. Limpouch *et al.*, Micro-sphere layered targets efficiency in laser driven proton acceleration. *Journal of Applied Physics* **(2013)**, Vol. 114, art. no. 083305.

[40] T. Ceccotti, V. Floquet, A. Sgattoni, A. Bigongiari, O. Klimo *et al.*, Evidence of Resonant Surface-Wave Excitation in the Relativistic Regime through Measurements of Proton Acceleration from Grating Targets. *Physical Review Letters* **(2013)**, Vol. 111, art. no. 185001.

[41] O. Klimo, S. Weber, V. T. Tikhonchuk, and J. Limpouch, Particle-in-cell simulations of laser-plasma interaction for the shock ignition scenario. *Plasma Physics and Controlled Fusion* **(2010)**, Vol. 52, art. no. 055013.

[42] O. Klimo, V. T. Tikhonchuk, X. Ribeyre, G. Schurtz, C. Riconda *et al.*, Laser plasma interaction studies in the context of shock ignition-Transition from collisional to collisionless absorption. *Physics of Plasmas* **(2011)**, Vol. 18, art. no. 082709.

[43] S. Weber, C. Riconda, O. Klimo, A. Heron, and V. T. Tikhonchuk, Fast saturation of the two-plasmon-decay instability for shock-ignition conditions. *Physical Review E* **(2012)**, Vol. 85, art. no. 016403.

[44] O. Klimo and V. T. Tikhonchuk, Laser-plasma interaction studies in the context of shock ignition: the regime dominated by parametric instabilities. *Plasma Physics and Controlled Fusion* **(2013)**, Vol. 55, art. no. 095002.

[45] O. Klimo, J. Psikal, V. T. Tikhonchuk, and S. Weber, Two-dimensional simulations of laser-plasma interaction and hot electron generation in the context of shock-ignition research. *Plasma Physics and Controlled Fusion* **(2014)**, Vol. 56, art. no. 055010.

[46] D. Batani, S. Baton, A. Casner, S. Depierreux, M. Hohenberger *et al.*, Physics issues for shock ignition. *Nuclear Fusion* **(2014)**, Vol. 54, art. no. 054009.

[47] R. Rhodes, *Dark Sun: The Making Of The Hydrogen Bomb*, Simon & Schuster, New York **(1995)**.

[48] E. Teller, The Work of Many People. *Science* **(1955)**, Vol. 121, pp. 267–275.

[49] B. C. Hacker, Fallout from Plowshare: Peaceful Nuclear Explosions and the Environment 1956-1973, Technical Report, Lawrence Livermore National Laboratory (LLNL), Livermore, CA **(1995)**, report no. LLNL–CONF–464374. https://e-reports-ext.llnl.gov/pdf/401977.pdf.

[50] J. H. Nuckolls, Early Steps Toward Inertial Fusion Energy (IFE) (1952 to 1962), Technical Report, Lawrence Livermore National Lab., CA (United States) **(1998)**, report no. UCRL–ID–131075. http://www.osti.gov/scitech/servlets/purl/658936.

[51] J. H. Nuckolls, L. Wood, A. Thiessen, and G. Zimmerman, Laser Compression of Matter to Super-High Densities: Thermonuclear (CTR) Applications. *Nature* **(1972)**, Vol. 239, pp. 139–142.

[52] J. Lindl, Development of the indirect-drive approach to inertial confinement fusion and the target physics basis for ignition and gain. *Physics of Plasmas* **(1995)**, Vol. 2, pp. 3933–4024.

[53] T. H. Maiman, Stimulated optical radiation in ruby. *Nature* **(1960)**, Vol. 187, pp. 493–494.

[54] N. G. Basov and O. N. Krokhin, Conditions for heating up of a plasma by the radiation from an optical generator. *Journal of Experimental and Theoretical Physics* **(1964)**, Vol. 46, pp. 171–175.

[55] S. Atzeni and J. Meyer-ter Vehn, *The Physics of Inertial Fusion: Beam Plasma Interaction, Hydrodynamics, Hot Dense Matter*, Clarendon Press, Oxford **(2004)**.

[56] D. F. DuBois and M. V. Goldman, Radiation-Induced Instability of Electron Plasma Oscillations. *Physical Review Letters* **(1965)**, Vol. 14, pp. 544–546.

[57] M. N. Rosenbluth, Parametric Instabilities in Inhomogeneous Media. *Physical Review Letters* **(1972)**, Vol. 29, pp. 565–567.

[58] T. Ma, P. K. Patel, N. Izumi, P. T. Springer, M. H. Key *et al.*, Onset of Hydrodynamic Mix in High-Velocity, Highly Compressed Inertial Confinement Fusion Implosions. *Physical Review Letters* **(2013)**, Vol. 111, art. no. 085004.

[59] V. A. Smalyuk, L. J. Atherton, L. R. Benedetti, R. Bionta, D. Bleuel *et al.*, Performance of High-Convergence, Layered DT Implosions with Extended-Duration Pulses at the National Ignition Facility. *Physical Review Letters* **(2013)**, Vol. 111, art. no. 215001.

[60] E. Harrison, Alternative Approach to the Problem of Producing Controlled Thermonuclear Power. *Physical Review Letters* **(1963)**, Vol. 11, pp. 535–537.

[61] D. Strickland and G. Mourou, Compression of amplified chirped optical pulses. *Optics Communications* **(1985)**, Vol. 55, pp. 447–449.

[62] M. Tabak, J. Hammer, M. E. Glinsky, W. L. Kruer, S. C. Wilks *et al.*, Ignition and high gain with ultrapowerful lasers. *Physics of Plasmas* **(1994)**, Vol. 1, pp. 1626–1634.

[63] M. Roth, T. Cowan, M. Key, S. Hatchett, C. Brown *et al.*, Fast Ignition by Intense Laser-Accelerated Proton Beams. *Physical Review Letters* **(2001)**, Vol. 86, pp. 436–439.

[64] S. Atzeni, Inertial Confinement Fusion with Advanced Ignition Schemes: Fast Ignition and Shock Ignition. in *Laser-Plasma Interactions and Applications*, P. McKenna, D. Neely, R. B. Dino, and A. Jaroszynski, Editors, Springer **(2013)**, Chapter 10, pp. 243–277.

[65] V. A. Shcherbakov, Calculation of thermonuclear laser target ignition by focusing shock wave. *Soviet Journal of Plasma Physics* **(1983)**, Vol. 9, p. 240.

[66] R. Betti, C. Zhou, K. Anderson, L. Perkins, W. Theobald *et al.*, Shock Ignition of Thermonuclear Fuel with High Areal Density. *Physical Review Letters* **(2007)**, Vol. 98, art. no. 155001.

[67] X. Ribeyre, G. Schurtz, M. Lafon, S. Galera, and S. Weber, Shock ignition: an alternative scheme for HiPER. *Plasma Physics and Controlled Fusion* **(2009)**, Vol. 51, art. no. 015013.

[68] S. Atzeni, X. Ribeyre, G. Schurtz, A. J. Schmitt, B. Canaud *et al.*, Shock ignition of thermonuclear fuel: principles and modelling. *Nuclear Fusion* **(2014)**, Vol. 54, art. no. 054008.

[69] X. Ribeyre, M. Lafon, G. Schurtz, M. Olazabal-Loumé, J. Breil *et al.*, Shock ignition: modelling and target design robustness. *Plasma Physics and Controlled Fusion* **(2009)**, Vol. 51, art. no. 124030.

[70] M. Lafon, X. Ribeyre, and G. Schurtz, Gain curves and hydrodynamic modeling for shock ignition. *Physics of Plasmas* **(2010)**, Vol. 17, art. no. 052704.

[71] G. Guderley, Starke kugelige und zylindrische Verdichtungsstösse in der Nähe des Kugelmittelpunktes bzw. der Zylinderachse. *Luftfahrtforschung* **(1942)**, Vol. 19, pp. 302–312.

[72] X. Ribeyre, V. T. Tikhonchuk, J. Breil, M. Lafon, and E. Le Bel, Analytic criteria for shock ignition of fusion reactions in a central hot spot. *Physics of Plasmas* **(2011)**, Vol. 18, art. no. 102702.

[73] S. Eliezer, *The Interaction of High-Power Lasers with Plasmas*, Institute of Physics Publishing, London **(2002)**.

[74] C. Garban-Labaune, E. Fabre, C. Max, R. Fabbro, F. Amiranoff *et al.*, Effect of Laser Wavelength and Pulse Duration on Laser-Light Absorption and Back Reflection. *Physical Review Letters* **(1982)**, Vol. 48, pp. 1018–1021.

[75] C. J. McKinstrie, R. E. Giacone, and E. A. Startsev, Accurate formulas for the Landau damping rates of electrostatic waves. *Physics of Plasmas* **(1999)**, Vol. 6, pp. 463–466.

[76] J. M. Manley and H. E. Rowe, Some General Properties of Nonlinear Elements-Part I. General Energy Relations. *Proceedings of the IRE* **(1956)**, Vol. 44, pp. 904–913.

[77] K. Nishikawa, Parametric Excitation of Coupled Waves. II. Parametric Plasmon-Photon Interaction. *Journal of the Physical Society of Japan* **(1968)**, Vol. 24, pp. 1152–1158.

[78] C. S. Liu and M. N. Rosenbluth, Parametric decay of electromagnetic waves into two plasmons and its consequences. *Physics of Fluids* **(1976)**, Vol. 19, p. 967.

[79] W. L. Kruer, *The Physics Of Laser Plasma Interactions*, Westview Press, Colorado **(2003)**.

[80] D. H. Froula, B. Yaakobi, S. X. Hu, P.-Y. Chang, R. S. Craxton *et al.*, Saturation of the Two-Plasmon Decay Instability in Long-Scale-Length Plasmas Relevant to Direct-Drive Inertial Confinement Fusion. *Physical Review Letters* **(2012)**, Vol. 108, art. no. 165003.

[81] Y. R. Shen and N. Bloembergen, Theory of Stimulated Brillouin and Raman Scattering. *Physical Review* **(1965)**, Vol. 137, pp. A 1787–A 1805.

[82] A. Mostovych, S. Obenschain, J. Gardner, J. Grun, K. Kearney *et al.*, Brillouin scattering measurements from plasmas irradiated with spatially and temporally incoherent laser light. *Physical Review Letters* **(1987)**, Vol. 59, pp. 1193–1196.

[83] J. F. Drake, P. K. Kaw, Y. C. Lee, G. Schmid, C. S. Liu *et al.*, Parametric instabilities of electromagnetic waves in plasmas. *Physics of Fluids* **(1974)**, Vol. 17, p. 778.

[84] K. Estabrook and W. L. Kruer, Theory and simulation of one-dimensional Raman backward and forward scattering. *Physics of Fluids* **(1983)**, Vol. 26, pp. 1892–1903.

[85] P. Nicolaï, J.-L. Feugeas, M. Touati, X. Ribeyre, S. Gus'kov *et al.*, Deleterious effects of nonthermal electrons in shock ignition concept. *Physical Review E* **(2014)**, Vol. 89, art. no. 033107.

[86] M. Temporal, B. Canaud, W. J. Garbett, R. Ramis, and S. Weber, Irradiation uniformity at the Laser MegaJoule facility in the context of the shock ignition scheme. *High Power Laser Science and Engineering* **(2014)**, Vol. 2, p. e8.

[87] R. Chiao, E. Garmire, and C. Townes, Self-Trapping of Optical Beams. *Physical Review Letters* **(1964)**, Vol. 13, pp. 479–482.

[88] D. Pesme, S. Huller, J. Myatt, C. Riconda, A. Maximov *et al.*, Laser-plasma interaction studies in the context of megajoule lasers for inertial fusion. *Plasma Physics and Controlled Fusion* **(2002)**, Vol. 44, pp. B53–B67.

[89] L. Perkins, R. Betti, K. LaFortune, and W. Williams, Shock Ignition: A New Approach to High Gain Inertial Confinement Fusion on the National Ignition Facility. *Physical Review Letters* **(2009)**, Vol. 103, art. no. 045004.

[90] S. Guskov, X. Ribeyre, M. Touati, J.-L. Feugeas, P. Nicolaï *et al.*, Ablation Pressure Driven by an Energetic Electron Beam in a Dense Plasma. *Physical Review Letters* **(2012)**, Vol. 109, art. no. 255004.

[91] Plasma physics and controlled fusion, highlights of 2010. http://iopscience.iop.org/0741-3335/page/Highlights%20of%202010, accessed: 2014-09-22.

[92] W. Theobald, K. S. Anderson, R. Betti, R. S. Craxton, J. A. Delettrez *et al.*, Advanced-ignition-concept exploration on omega. *Plasma Physics and Controlled Fusion* **(2009)**, Vol. 51, art. no. 124052.

[93] H. Vu, D. DuBois, and B. Bezzerides, Transient Enhancement and Detuning of Laser-Driven Parametric Instabilities by Particle Trapping. *Physical Review Letters* **(2001)**, Vol. 86, pp. 4306–4309.

[94] C. Yamanaka, T. Yamanaka, T. Sasaki, K. Yoshida, M. Waki *et al.*, Anomalous Heating of a Plasma by a Laser. *Physical Review A* **(1972)**, Vol. 6, pp. 2335–2342.

[95] S. J. Gitomer, R. D. Jones, F. Begay, A. W. Ehler, J. F. Kephart *et al.*, Fast ions and hot electrons in the laser-plasma interaction. *Physics of Fluids* **(1986)**, Vol. 29, p. 2679.

[96] J. Fuchs, P. Antici, E. D'Humières, E. Lefebvre, M. Borghesi *et al.*, Laser-driven proton scaling laws and new paths towards energy increase. *Nature Physics* **(2005)**, Vol. 2, pp. 48–54.

[97] F. N. Beg, A. R. Bell, A. E. Dangor, C. N. Danson, A. P. Fews *et al.*, A study of picosecond laser-solid interactions up to 10^{19} Wcm^{-2}. *Physics of Plasmas* **(1997)**, Vol. 4, p. 447.

[98] A. Maksimchuk, S. Gu, K. Flippo, and D. Umstadter, Forward Ion Acceleration in Thin Films Driven by a High-Intensity Laser. *Physical Review Letters* **(2000)**, Vol. 84, pp. 4108–4111.

[99] E. Clark, K. Krushelnick, J. Davies, M. Zepf, M. Tatarakis *et al.*, Measurements of Energetic Proton Transport through Magnetized Plasma from Intense Laser Interactions with Solids. *Physical Review Letters* **(2000)**, Vol. 84, pp. 670–673.

[100] R. Snavely, M. Key, S. Hatchett, T. Cowan, M. Roth *et al.*, Intense High-Energy Proton Beams from Petawatt-Laser Irradiation of Solids. *Physical Review Letters* **(2000)**, Vol. 85, pp. 2945–2948.

[101] K. Krushelnick, E. L. Clark, M. Zepf, J. R. Davies, F. N. Beg *et al.*, Energetic proton production from relativistic laser interaction with high density plasmas. *Physics of Plasmas* **(2000)**, Vol. 7, p. 2055.

[102] Y. Sentoku, T. E. Cowan, a. Kemp, and H. Ruhl, High energy proton acceleration in interaction of short laser pulse with dense plasma target. *Physics of Plasmas* **(2003)**, Vol. 10, p. 2009.

[103] S. C. Wilks, a. B. Langdon, T. E. Cowan, M. Roth, M. Singh *et al.*, Energetic proton generation in ultra-intense laser-solid interactions. *Physics of Plasmas* **(2001)**, Vol. 8, p. 542.

[104] A. Mackinnon, Y. Sentoku, P. Patel, D. Price, S. Hatchett *et al.*, Enhancement of Proton Acceleration by Hot-Electron Recirculation in Thin Foils Irradiated by Ultraintense Laser Pulses. *Physical Review Letters* **(2002)**, Vol. 88, art. no. 215006.

[105] M. Kaluza, J. Schreiber, M. Santala, G. Tsakiris, K. Eidmann *et al.*, Influence of the Laser Prepulse on Proton Acceleration in Thin-Foil Experiments. *Physical Review Letters* **(2004)**, Vol. 93, art. no. 045003.

[106] V. L. Ginzburg, *The Propagation of Electromagnetic Waves in Plasmas*, Pergammon Press, New York **(1964)**.

[107] F. Brunel, Not-so-resonant, resonant absorption. *Physical Review Letters* **(1987)**, Vol. 59, pp. 52–55.

[108] R. M. More, Z. Zinamon, K. H. Warren, R. Falcone, and M. Murnane, Heating of solids with ultra-short laser-pulses. *Journal de Physique* **(1988)**, Vol. 49, pp. 43–51.

[109] E. G. Gamalii and V. T. Tikhonchuk, Effect of intense ultrashort light-pulses on a substance. *JEPT Letters* **(1988)**, Vol. 48, pp. 453–455.

[110] Z.-M. Sheng, K. Mima, Y. Sentoku, M. Jovanović, T. Taguchi *et al.*, Stochastic Heating and Acceleration of Electrons in Colliding Laser Fields in Plasma. *Physical Review Letters* **(2002)**, Vol. 88, art. no. 055004.

[111] P. Mora, Thin-foil expansion into a vacuum. *Physical Review Letters* **(2003)**, Vol. 90, art. no. 185002.

[112] T. Ceccotti, a. Lévy, H. Popescu, F. Réau, P. D'Oliveira *et al.*, Proton Acceleration with High-Intensity Ultrahigh-Contrast Laser Pulses. *Physical Review Letters* **(2007)**, Vol. 99, art. no. 185002.

[113] M. Borghesi, J. Fuchs, and O. Willi, Laser-accelerated high-energy ions: state of-the-art and applications. *Journal of Physics: Conference Series* **(2007)**, Vol. 58, p. 74.

[114] M. Allen, Y. Sentoku, P. Audebert, A. Blazevic, T. Cowan *et al.*, Proton spectra from ultraintense laser-plasma interaction with thin foils: Experiments, theory, and simulation. *Physics of Plasmas* **(2003)**, Vol. 10, p. 3283.

[115] Y. Oishi, T. Nayuki, T. Fujii, Y. Takizawa, X. Wang *et al.*, Dependence on laser intensity and pulse duration in proton acceleration by irradiation of ultrashort laser pulses on a Cu foil target. *Physics of Plasmas* **(2005)**, Vol. 12, art. no. 073102.

[116] K. Zeil, S. D. Kraft, S. Bock, M. Bussmann, T. E. Cowan *et al.*, The scaling of proton energies in ultrashort pulse laser plasma acceleration. *New Journal of Physics* **(2010)**, Vol. 12, art. no. 045015.

[117] B. Damato, A. Kacperek, M. Chopra, I. R. Campbell, and R. D. Errington, Proton beam radiotherapy of choroidal melanoma: the Liverpool-Clatterbridge experience. *International journal of radiation oncology, biology, physics* **(2005)**, Vol. 62, pp. 1405–1411.

[118] S. Buffechoux, J. Psikal, M. Nakatsutsumi, L. Romagnani, A. Andreev *et al.*, Hot Electrons Transverse Refluxing in Ultraintense Laser-Solid Interactions. *Physical Review Letters* **(2010)**, Vol. 105, art. no. 015005.

[119] L. O. Silva, M. Marti, J. R. Davies, and R. A. Fonseca, Proton Shock Acceleration in Laser-Plasma Interactions. *Physical Review Letters* **(2004)**, Vol. 92, art. no. 015002.

[120] L. Yin, B. J. Albright, K. J. Bowers, D. Jung, J. C. Fernández *et al.*, Three-Dimensional Dynamics of Breakout Afterburner Ion Acceleration Using High-Contrast Short-Pulse Laser and Nanoscale Targets. *Physical Review Letters* **(2011)**, Vol. 107, art. no. 045003.

[121] J. Denavit, Absorption of high-intensity subpicosecond lasers on solid density targets. *Physical Review Letters* **(1992)**, Vol. 69, pp. 3052–3055.

[122] T. Z. Esirkepov, S. V. Bulanov, K. Nishihara, T. Tajima, F. Pegoraro *et al.*, Proposed Double-Layer Target for the Generation of High-Quality Laser-Accelerated Ion Beams. *Physical Review Letters* **(2002)**, Vol. 89, art. no. 175003.

[123] T. Schlegel, N. Naumova, V. T. Tikhonchuk, C. Labaune, I. V. Sokolov *et al.*, Relativistic laser piston model: Ponderomotive ion acceleration in dense plasmas using ultraintense laser pulses. *Physics of Plasmas* **(2009)**, Vol. 16, art. no. 083103.

[124] E. D'Humières, E. Lefebvre, L. Gremillet, and V. Malka, Proton acceleration mechanisms in high-intensity laser interaction with thin foils. *Physics of Plasmas* **(2005)**, Vol. 12, art. no. 062704.

[125] D. Haberberger, S. Tochitsky, F. Fiuza, C. Gong, R. A. Fonseca *et al.*, Collisionless shocks in laser-produced plasma generate monoenergetic high-energy proton beams. *Nature Physics* **(2011)**, Vol. 8, pp. 95–99.

[126] B. M. Hegelich, Towards Extreme Field Physics: Relativistic Optics and Particle Acceleration in the Transparent-Overdense Regime. *Bulletin of the American Physical Society* **(2011)**, Vol. 56, p. 322.

[127] J. Psikal, O. Klimo, S. Weber, and D. Margarone, Increased efficiency of ion acceleration by using femtosecond laser pulses at higher harmonic frequency. *Physics of Plasmas* **(2014)**, Vol. 21, art. no. 073108.

[128] J. Kepler, *De cometis libelli tres*, Augustae Vindelicorum [Augsburg] : typis Andrae Apergeri; sumptibus Sebastiani Mylii, Augsburg **(1619)**, http://www.e-rara.ch/zut/content/titleinfo/272385.

[129] A. Macchi, S. Veghini, and F. Pegoraro, "Light Sail" Acceleration Reexamined. *Physical Review Letters* **(2009)**, Vol. 103, art. no. 085003.

[130] F. Pegoraro and S. V. Bulanov, Photon Bubbles and Ion Acceleration in a Plasma Dominated by the Radiation Pressure of an Electromagnetic Pulse. *Physical Review Letters* **(2007)**, Vol. 99, art. no. 065002.

[131] M. Lezius, S. Dobosz, D. Normand, and M. Schmidt, Explosion Dynamics of Rare Gas Clusters in Strong Laser Fields. *Physical Review Letters* **(1998)**, Vol. 80, pp. 261–264.

[132] G. Kulcsar, D. AlMawlawi, F. Budnik, P. Herman, M. Moskovits *et al.*, Intense picosecond X-Ray pulses from laser plasmas by use of nanostructured "Velvet" targets. *Physical Review Letters* **(2000)**, Vol. 84, pp. 5149–5152.

[133] T. Nishikawa, H. Nakano, K. Oguri, N. Uesugi, K. Nishio *et al.*, Nanohole-array size dependence of soft x-ray generation enhancement from femtosecond-laser-produced plasma. *Journal of Applied Physics* **(2004)**, Vol. 96, p. 7537.

[134] H. Sumeruk, S. Kneip, D. Symes, I. Churina, A. Belolipetski *et al.*, Control of Strong-Laser-Field Coupling to Electrons in Solid Targets with Wavelength-Scale Spheres. *Physical Review Letters* **(2007)**, Vol. 98, art. no. 045001.

[135] S. Kahaly, S. Yadav, W. Wang, S. Sengupta, Z. Sheng *et al.*, Near-Complete Absorption of Intense, Ultrashort Laser Light by Sub-λ Gratings. *Physical Review Letters* **(2008)**, Vol. 101, art. no. 145001.

[136] W. Lu, M. Tzoufras, C. Joshi, F. S. Tsung, W. B. Mori *et al.*, Generating multi-gev electron bunches using single stage laser wakefield acceleration in a 3d nonlinear regime. *Physical Review Special Topics - Accelerators and Beams* **(2007)**, Vol. 10, art. no. 061301.

[137] J. Brandon, The World's 10 Most Massive Science Experiments. http://www.foxnews.com/slideshow/scitech/2010/10/13/massive-science-experiments **(2010)**, accessed: 2014-09-18.

[138] G. Mone, B. Borel, K. Bagley, and J. Abbasi, Big Science: The Universe's Ten Most Epic Projects. http://www.popsci.com/science/gallery/2011-07/big-science-universes-ten-most-epic-projects **(2011)**, accessed: 2014-09-18.

[139] F. Grüner, S. Becker, U. Schramm, T. Eichner, M. Fuchs *et al.*, Design considerations for table-top, laser-based VUV and X-ray free electron lasers. *Applied Physics B* **(2007)**, Vol. 86, pp. 431–435.

[140] K. Nakajima, Compact X-ray sources: Towards a table-top free-electron laser. *Nature Physics* **(2008)**, Vol. 4, pp. 92–93.

[141] S. M. Hooker, Developments in laser-driven plasma accelerators. *Nature Photonics* **(2013)**, Vol. 7, pp. 775–782.

[142] P. B. Corkum and F. Krausz, Attosecond science. *Nature Physics* **(2007)**, Vol. 3, pp. 381–387.

[143] R. T. Hammond, Relativistic Particle Motion and Radiation Reaction in Electrodynamics. *Electronic Journal of Theoretical Physics* **(2010)**, Vol. 7, pp. 221–258.

Vložené publikace

IOP PUBLISHING PLASMA PHYSICS AND CONTROLLED FUSION

Plasma Phys. Control. Fusion **52** (2010) 055013 (18pp) doi:10.1088/0741-3335/52/5/055013

Particle-in-cell simulations of laser–plasma interaction for the shock ignition scenario

O Klimo[1,2], S Weber[2], V T Tikhonchuk[2] and J Limpouch[1]

[1] Czech Technical University in Prague, Faculty of Nuclear Sciences and Physical Engineering, Brehova 7, 11519, Prague, Czech Republic
[2] Centre Lasers Intenses et Applications, Université Bordeaux 1-CEA-CNRS, 33405 Talence Cedex, France

E-mail: ondrej.klimo@fjfi.cvut.cz

Received 8 January 2010, in final form 22 February 2010
Published 9 April 2010
Online at stacks.iop.org/PPCF/52/055013

Abstract

Numerical simulations of the laser pulse interaction with an inhomogeneous, large size, high temperature plasma are presented. The laser pulse intensity, 10^{16} W cm^{-2}, plasma temperature, 5 keV, and the density scale length of 300 μm correspond to the conditions of the shock ignition scenario. It is demonstrated that after a short initial burst of backscattering, a significant part of the incident laser radiation is absorbed in the underdense plasma and the energy is transported to the dense plasma by electrons with energies 20–40 keV. The absorption mechanism is associated with a self-organized resonator and cavitation of large-amplitude plasma waves in the density range below the quarter critical density. The temporal and spectral properties of reflected light are discussed.

(Some figures in this article are in colour only in the electronic version)

1. Introduction

The inertial confinement thermonuclear fusion (ICF) could be a source of relatively clean and cheap energy. A fuel contained in a small target pellet is adiabatically compressed to a very high density and heated until the conditions of efficient fuel burn occur [1]. Large Nd : glass laser systems, NIF [2] and LMJ [3], are expected to demonstrate ignition of fusion reaction in the next coming years from the central hot spot.

In order to improve the robustness and efficiency of the ICF process, it has been proposed to separate the phases of the fuel assembly and ignition [4]. The fuel can thus be compressed more slowly on a low adiabat and using a driver with a lower energy. An additional energy for the hot spot ignition can be transported either with a beam of energetic particles (fast ignition) [5] or with a strong converging shock (shock ignition, SI) [6]. Both schemes require

the laser energy carried to the plasma with an intense laser pulse to be efficiently absorbed and transported to the ablation zone by energetic electrons.

In the SI scenario [7], a power of the order of 200–300 TW should be transported to the plasma at the end of the stagnation phase with a laser pulse of intensity above 10^{16} W cm^{-2}. Recent hydrodynamic simulations demonstrate that SI is a relatively robust scenario with regard to hydrodynamic instabilities and time synchronization. However, the intensity of the ignition pulse is significantly higher than the intensity of compression pulses for directly driven fusion and nonlinear phenomena in the laser–plasma interaction cannot be avoided. The most important nonlinear processes in this context are three-wave parametric instabilities: stimulated Raman (SRS) or Brillouin (SBS) scattering, two plasmon decay (TPD) and filamentation instability [8].

They can undermine the laser pulse absorption in several ways: the scattered laser light from a low density plasma due to the SBS increases the total reflectivity; the generation of plasma waves associated with the SRS may result in the transformation of a large amount of energy into electron beams with energy much higher than the thermal energy of the surrounding plasma; finally, the absorption may take place in the underdense plasma far from the critical surface, and the transport of energy to the denser plasma may be suppressed. Fortunately, the preheat of a precompressed fuel by fast electrons is a less important issue in the SI context, because the ignition pulse is applied at the end of the implosion phase and the shell areal density is sufficiently high to ensure stopping and absorption of most of the hot electrons. Nevertheless, it is important to understand the nonlinear processes involved in the interaction of the ignition laser pulse with the large scale coronal plasma and the interplay between these processes under the particular conditions of SI characterized by a large density scale length and plasma temperatures of several kiloelectronvolts.

The linear theory of parametric instabilities predicts the amplification of daughter wave in the temporal or in the spatial domain [8] depending on the resonance conditions. Each particular three-wave process was considered separately in the theory and the wave coupling depends strongly on the geometry of interaction and boundary conditions. The linear gain factor analysis provides information about the importance of each parametric process, but it is insufficient in the case of nonlinear wave coupling, strong density perturbations and nonthermal particle distributions. Numerical simulations, on the other hand, are limited by the computational performance, precision and stability of the methods employed. In many previous publications, the interaction conditions were limited to small spatial scales and low temperatures, where kinetic effects are not very important and the nonlinear saturation is related to secondary wave decays [9].

Recent studies of SRS and SBS processes in high temperature plasmas and at high laser intensities are based on the full kinetic simulations using the Vlasov or particle-in-cell (PIC) codes [10–15]. They demonstrate new strongly nonlinear regimes of interaction related to strong deformation of particle distribution function, generation of harmonics of daughter waves and formation of deep small-scale density cavities. The SBS saturation is related to the nonlinear frequency shift and harmonic generation of ion acoustic waves [16] as well as trapping of backscattered radiation in deep density cavities [12, 13]. The SRS in the domain of strong Landau damping demonstrates an explosive behavior (so-called inflation regime [10]), and the formation of long-living vortical structures in the electron phase space (so-called KEEN waves and beam-plasma modes [15, 17]). Moreover, a cascade of parametric processes in a high temperature plasma and at high laser intensities was reported in [18, 19].

The aim of this paper is to study laser–plasma interaction relevant to the SI interaction conditions that were not exploited yet in previous publications. The calculations are performed using a fully kinetic massively parallel PIC code in the one-dimensional geometry, which

enables us to simulate a millimeter scale plasma on the time scale of at least several tens of picoseconds. Numerical modeling presented here is dedicated to study the physical processes in a plasma with density less than or of the order of the critical density. We would like to characterize the laser absorption and its dependence on the main interaction parameters such as temperature, plasma density scale length and laser intensity. This will provide an input for further SI modeling.

The plasma interaction conditions are chosen to be compatible with those expected in the SI scheme on HiPER [7]. Namely, the scale length of the plasma density profile is very large ($L_n \sim 0.3$ mm), the density range is from 0.02 to 1.1 critical density, the initial temperature of the plasma is high ($T_e \sim 4$–5 keV) and the laser pulse intensity ($I_0 \sim 10^{16}$ W cm^{-2} at the wavelength $\lambda_0 = 0.35\,\mu$m) is also high in comparison with the usual direct drive conditions. Our simulations indicate that SRS plays a more important role in the SI context than SBS. The SBS instability is responsible for the large backscattered signal observed in the initial stage of the interaction, but it is soon suppressed by the growth of SRS instability, which is initially delayed due to a very strong Landau damping. The SRS develops at the quarter critical density as an absolute instability. It results in the cavitation of the plasma and the generation of scattered light at half-harmonic frequency of the incident wave.

The coupling between the SRS processes localized at different plasma densities plays an important role under the SI conditions. The Raman wave generated at the quarter critical density is scattered at its own resonance point at 1/16 of the critical density on its way out of the plasma. This second step of the Raman cascade is again accompanied by cavitation and efficient electron and ion acceleration. The development of multiple cavities in the range from 0.06 to 0.25 of the critical density provides a strong laser wave absorption and maintains the intensity of the scattered wave on a quasi-stationary level. The absorbed energy is transported into the dense plasma by hot electrons with an average energy $T_h \sim 30$ keV.

The rest of this paper provides detailed information on the laser–plasma interaction under the SI conditions. It is organized as follows. The simulation model is presented in section 2 and the parameters used in our calculations are also introduced there. The theory of parametric instabilities relevant in the context of SI is briefly described in section 3. The simulation results are presented and discussed in section 4. In section 5, we present our concluding remarks.

2. Simulation model

The development of parametric instabilities is a multi-scale process that involves plasma wave excitation, change of the electron distribution function under wave–particle interactions, excitation of the ion density perturbations under the effect of the ponderomotive force, coupling between the parametric instabilities in different spatial regions of the plasma due to propagation of daughter waves, etc. This complicated process of plasma self-organization is very difficult to foresee in reduced models, and direct simulation is a desirable option. It became available recently due to the fast development of parallel computing and software that allows precision calculations over tens of thousands of plasma periods.

Numerical simulations of the laser beam interaction with an underdense plasma were performed with a relativistic, electromagnetic PIC code that accounts for three components of particle velocities, the electric and the magnetic fields [20]. It evolved from the code LPIC [21] and was parallelized using MPI with dynamical load balancing. These features make it possible to access the very long simulation times and very large spatial scales. At the moment, we restrict ourselves to the one-dimensional geometry and consider the parametric processes related to the forward and the backward propagating waves. The inclusion of stimulated side scattering, filamentation instability and two plasmon decay requires multidimensional

treatment, which requires more computational resources and it will be addressed in the near future. The one-dimensional simulations allow us to understand the basic interplays between parametric scattering instabilities and secondary processes in large time and spatial scales. This will help us develop physical models and to reduce two-dimensional simulations to the scales that are computationally feasible and physically realistic.

The code also includes relativistic Coulomb collisions and plasma ionization processes using a Monte Carlo algorithm [22]. The latter is irrelevant in the context of this paper, but electron–electron and electron–ion collisions may play some role. Their influence was investigated in several runs, which include only the higher density part of the profile. The collisions do not affect the SRS evolution, as will be discussed in the next section.

2.1. Initial and boundary conditions

The simulations are performed with laser–plasma interaction parameters obtained in hydrodynamic simulations of a baseline HiPER target [7]. They correspond to the time when the first half of the ignition pulse has already interacted with the target [23]. At that time, the initial temperature of electrons T_e is 5 keV and the temperature of ions T_i is 1 keV. The relatively long Debye length enables us to use computational cells as large as 5 nm. The computational time step is about 0.017 fs (i.e. $\frac{1}{70}$ of the laser period). The simulation includes only one species of ions with the charge $Z = 1$ and the mass $m_i = 2.5m_p$, where m_p is the proton mass. The shape of the density profile of plasma is supposed to be exponential with a scale length of $L_n = 308\,\mu$m.

The minimum and the maximum values of density in the density profile are 2% and 110% of the critical density in the largest simulations. In the simulations devoted to SBS studies, the minimum density was chosen above the quarter critical density to suppress SRS. The maximum density is chosen to avoid any transmission of the laser pulse and to accommodate the electron energy flux. The minimum density of 2% corresponds to two particles per cell per species. The reliability of processes taking place in the low density part of the profile is restricted by the number of particles per cell. In particular, the correct description of the linear Landau damping in our PIC simulations would require a higher number of particles per cell so that the distribution function is represented with a sufficient accuracy. However, the excitation of SRS in the low density parts of the plasma takes place in a strongly nonlinear regime in the case of the parameters considered here and thus the fine resolution of the distribution function is not so important. Nevertheless, to demonstrate that the resolution that we are using routinely is sufficient we have performed an additional shorter simulation with two times higher number of particles but only with the low density part of the profile, where the most important processes take place (up to the maximum density of $0.3n_c$). The overall scenario of the interaction (initially strong SBS signal followed by the absolute SRS and cavitation) was only affected quantitatively (not more than 20%) but not qualitatively. The reflectivity was at a similar level after the initial phase of strong SBS and the absorption process took place in the same region.

The laser wavelength in the simulations is $0.35\,\mu$m, which corresponds to the third harmonic of the neodymium laser system. The laser pulse has a trapezoidal temporal profile with the 5–10 ps long rising edge followed by a plateau with the intensity of $I_0 = 10^{16}\,\mathrm{W\,cm^{-2}}$. The simulations are usually stopped after several tens of picoseconds and thus the pulse duration used here corresponds approximately to 10% of the one required to launch the ignition shock at HiPER [7]. Nevertheless, the pulse is sufficiently long so that the important effects manifest themselves and the processes can reach a quasi-steady state during the simulation. The density profile may slightly change during the long simulations presented

in this paper. However, the changes in the profile take place at the plasma edges, while the bulk of the profile remains unaltered. Thus the processes taking place deeper inside the profile are not influenced by plasma expansion. Considering the characteristic velocity of plasma expansion (the sound velocity), the front side of the density profile may expand several tens of micrometers during the simulation. This plasma expansion is not negligible in the simulations of SBS and it will be discussed below in this context. The laser pulse in the SBS simulations has a very steep rising edge with the same maximum intensity. This allows one to reduce the length of these simulations but it also accelerates the plasma expansion.

The simulation box is about 1.3 mm long and it contains 50–100 μm of empty space at the front side of the density profile to enable expansion of plasma. The boundary of the simulation box at the laser side of the profile reflects the particles, the rear boundary absorbs them and re-emits the particles with an initial energy distribution. Neither of these boundary conditions is physically correct in the strict sense, and one has to be careful that they do not influence the simulation results. The boundary condition at the laser side is less important because of the sufficiently large free space in front of the target, where most electrons are reflected by the self-induced quasi-static electric field of charge separation. The boundary condition at the rear side of the simulation box is, however, quite important as the current of 'non-thermal' electrons in the dense plasma may be relatively high due to a high laser absorption and associated kinetic effects.

Thermalization of fast electrons at this boundary may induce a relatively strong quasi-static electric field, which accelerates the electrons forming the return current. This is observed after several tens of picoseconds of the interaction. In reality, most of the fast electrons will be thermalized in Coulomb collisions in the dense shell surrounding the core of the target and will not return into the corona. To lessen the influence of the boundary condition at the rear side of the simulation box and to account for thermalization of fast electrons, we add a 40 μm density plateau to the higher density part of the exponential profile, where the electrons are thermalizing with a given probability.

This process can be simulated using the collisional algorithm with an enhanced collisional frequency calculated with the parameters corresponding to the dense plasma in the shell. This approach avoids the presence of fast electrons in the return current, but, on the other hand, the temperature of the return current electrons increases due to heating of the collisional layer at the rear boundary. In reality, the heat capacity of the dense shell is high enough so that the temperature of the plasma there does not significantly increase due to fast electron heating during several tens of picoseconds. In order to support a constant temperature in the layer near the rear boundary the following procedure has been used. Each particle in the 40 μm layer at the rear side is randomly thermalized (assigned the initial thermal velocity) with a linearly increasing collisional rate. The thermalization rate increases from 0.001 25 of the laser frequency ω_0 to the maximum value of $0.5\omega_0$ as the electron approaches the boundary. The procedure described here, in fact, spreads the absorbing boundary condition at the rear side of the simulation box over a wider region where thermalization is realized with a varying probability.

Long and large scale simulations with a very hot plasma and not so high laser intensity may suffer from the energy conservation problem. In the case of our simulations, the initial areal energy density of the plasma in the simulation box, $\int \mathrm{d}x\, n_\mathrm{e} T_\mathrm{e}$, is about 0.3 MJ cm^{-2}. The same energy is brought into the box by the laser pulse with an intensity of 10^{16} W cm^{-2} and a duration of 30 ps. Therefore, the numerical heating must be suppressed as much as possible to stay on a few percent level on the time scale such that $\omega_0 t$ is several hundred thousand. This has been achieved by using higher order shape forms for the particles [24].

3. Stimulated scattering instabilities in the context of SI

SBS and SRS arise from the decay of the incident electromagnetic wave ($\boldsymbol{k}_0$, ω_0) into a scattered electromagnetic wave ($\boldsymbol{k}_1$, ω_1) and an ion acoustic wave ($\boldsymbol{k}_\mathrm{i}$, ω_i) or an electron plasma wave ($\boldsymbol{k}_\mathrm{e}$, ω_e), respectively. The phase matching conditions for the resonance of the three waves involved are

$$\Delta\omega \equiv \omega_0 - \omega_1 = \omega_{\mathrm{i/e}}, \qquad \Delta k \equiv \boldsymbol{k}_0 - \boldsymbol{k}_1 = \boldsymbol{k}_{\mathrm{i/e}}, \tag{1}$$

where $k_{0,1}^2 c^2 = \omega_{0,1}^2 - \omega_\mathrm{pe}^2$ is the dispersion relation of the electromagnetic waves and $\omega_\mathrm{pe} = (e^2 n_\mathrm{e}/m_\mathrm{e}\epsilon_0)^{1/2}$ is the electron plasma frequency. These conditions together with the dispersion relations for the plasma, k_e, and ion acoustic, k_i, waves determine the frequencies and the wave vectors of the scattered modes in a homogeneous plasma, or the position of the resonance point in an inhomogeneous plasma. Since $\omega_\mathrm{i} \ll \omega_\mathrm{e} \approx \omega_\mathrm{pe}$, the SBS can be excited in the entire plasma with density smaller than the critical density. In contrast, the SRS is limited to the zone of plasma with density smaller than the quarter critical density, where the laser frequency is twice the local plasma frequency.

The conditions of SBS and SRS excitation depend strongly on the damping of daughter plasma waves, which are defined by the wave–particle interaction in a hot low density plasma. The parameter $k_\mathrm{e}\lambda_\mathrm{D}$ that defines the Landau damping of electron plasma wave in the SRS process ranges from 1.28 in the low density plasma ($0.02\,n_\mathrm{c}$) to 0.17 in the plasma near the quarter critical density. That means that SRS is suppressed almost everywhere with the exception of a narrow region near the quarter critical density where the Landau damping is sufficiently small. Moreover, because of a very small group velocity of the scattered wave near the zone $n_\mathrm{c}/4$, the SRS could be an absolute instability, temporally growing until the nonlinear processes intervene.

Except the special zone near quarter critical density, both SBS and SRS are the convective parametric instabilities. Their amplification near the resonance point is limited due to the wave vector mismatch. The amplification coefficients of the daughter waves depend on the characteristic scales of plasma density (SRS) and the expansion velocity and temperature (SBS) [8]. The gain factor can be presented as follows [8, 25]:

$$G = \frac{2\pi\gamma_0^2}{v_1 v_{\mathrm{e,i}} |K'|}, \tag{2}$$

where γ_0 is the growth rate of the corresponding instability in a homogeneous plasma, v_1 and $v_{\mathrm{e,i}}$ are the group velocities of the daughter waves, $K(x) = k_0 - k_1 - k_{\mathrm{e,i}}$ is the wave vector mismatch due to wave propagation out of the resonance point (defined as $K(x_\mathrm{r}) = 0$), and the prime denotes its spatial derivative along the path of the wave amplification.

For the case of SBS, the wave vector mismatch, $K = \Delta k - \Delta\omega/(c_\mathrm{s} + V_\mathrm{e})$, is determined essentially by the inhomogeneity in the expansion velocity V_e and the ion acoustic velocity that depends on the plasma temperature. However, according to the hydrodynamic simulations [23] both these parameters are nearly constant in the low density part of the plasma. Therefore, the characteristic spatial scale length of the SBS amplification is defined by the density scale length L_n. (According to [8], it dominates the velocity scale length L_v if $L_n < 0.5 L_v n_\mathrm{e}/n_\mathrm{c}$.) The SBS convective gain factor in that case does not depend on the density and thus it is constant along the density profile used in our simulation. It reaches the values about 250 under our conditions, which implies a very strong reflected signal.

The plasma density inhomogeneity is the most important factor for the wave vector mismatch in the SRS process. The convective SRS gain factor reads as [8]

$$G_\mathrm{SRS} = \pi^2 \left(\frac{v_\mathrm{osc}}{c}\right)^2 \frac{k_\mathrm{e}^2}{k_0 k_1} \frac{L_n}{\lambda_0}, \tag{3}$$

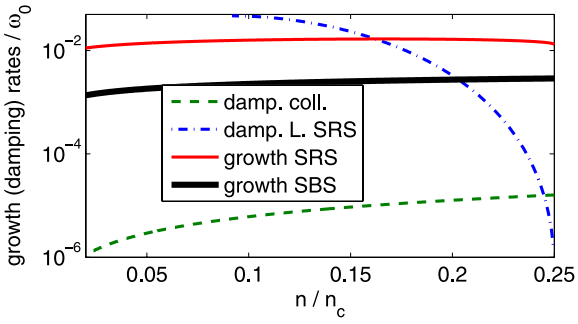

Figure 1. The growth rates for SBS and SRS instabilities normalized to the frequency of the incident laser wave (ω_0) and plotted against plasma density in the units of critical density (n_c). The collisional damping rate (damp. coll.) and Landau damping of the SRS induced wave (damp. L. SRS) are also included. The rates are calculated using formulae given in [26].

where $v_{osc} = eE_0/m_e\omega_0$ is the quiver electron velocity in the laser wave of amplitude E_0. The Raman gain factor is much lower than the Brillouin gain almost everywhere. It is almost constant and equal to 4 in the low density plasma, where $n_e/n_c \ll 0.25$. When approaching the quarter critical density, the wave number of the scattered wave tends to zero and the SRS takes a form of an absolute instability. Although the simple gain formula (3) cannot be applied there, this fact implies that Raman scattering would be particularly important in this region. As a consequence, the gain analysis for our simulation conditions indicates that the SBS should dominate the SRS everywhere with the exception of the quarter critical point, where the Raman instability is absolute.

It is important to know also the temporal growth rate of both parametric instabilities that define the plasma response at the initial stage of evolution. The Brillouin scattering instability under the conditions of interest is in the strong coupling regime where the growth rate reads as

$$\gamma_{0,\mathrm{SBS}} = \frac{\sqrt{3}}{2}\left(k_0^2 v_{osc}^2 \omega_{pi}^2/\omega_0\right)^{1/3}, \tag{4}$$

where ω_{pi} is the ion plasma frequency. This growth rate is plotted in figure 1 against the density normalized to the critical density. It is of the order of 1 ps^{-1}. The damping of ion acoustic wave in this regime is small. Collisional damping of the acoustic wave is not important due to the very high temperature. The Landau damping rate depends on the temperature ratio T_i/T_e. It is approximately constant along the density profile and it is about $4 \times 10^{-4}\omega_0$. Consequently, neglecting all the damping mechanisms, the threshold intensity for SBS instability can be estimated as $(v_{osc}/v_{te})^2 > 8/(k_0 L_n)$, where $v_{te} = \sqrt{T_e/m_e}$ is the electron thermal velocity. For our initial conditions this threshold corresponds to 2×10^{14} W cm^{-2}, two orders of magnitude lower than the actual laser intensity.

The growth rate for the Raman instability near the quarter critical density reads as

$$\gamma_{0,\mathrm{SRS}} \approx \frac{k_e v_{osc}}{2}. \tag{5}$$

The daughter electron plasma wave is damped mainly due to coupling to resonant electrons. The collisional damping is negligible. The growth and damping rates for stimulated Raman backscattering are also plotted in figure 1. Whereas the growth rate depends weakly on the density, the Landau damping is very strong and in the lower density region and for $n_e/n_c < 0.17$, it is higher than the growth rate. The high Landau damping rate comes from its strong dependence on the parameter $k_e\lambda_D$ that exceeds the value of 1 in the lower density

part of the profile. Consequently the Raman backscattering instability develops initially in the vicinity of the quarter critical point. The threshold condition for the SRS close to the quarter critical density is essentially defined by convection of the daughter waves [8],

$$\left(\frac{v_{\mathrm{osc}}}{c}\right)^2 (k_0 L_n)^{4/3} > 1. \tag{6}$$

This threshold corresponds to $10^{14}\,\mathrm{W\,cm^{-2}}$, again, two orders of magnitude lower than the actual laser intensity.

The Raman scattering in a plasma with temperatures exceeding 10 keV has recently been studied in connection with x-ray sources in [18]. In connection with laser fusion, Raman scattering at such high plasma temperatures has been studied already many years ago [27] and it has been observed that the SRS takes place in particular at $n_c/4$. It has also been found [28] that the forward Raman scattering can actually dominate the backscattering under similar conditions due to the weaker Landau damping of the electron plasma waves excited in the forward scattering instability.

The analysis of parametric instabilities in two or three spatial dimensions is difficult as the conditions are strongly nonlinear and much larger computing resources are needed. Supposing that the SRS-cavitation process evolves similar to the SBS-cavitation described in [13], one may expect that the cavities are produced also in two-dimensional geometry, but their lifetime would be much shorter than the pulse duration. The cavities evolve on the time scale of the ion plasma period and they might collapse after several picoseconds while the new ones will be created. The two-dimensional geometry gives rise to two additional parametric processes: the TPD and the filamentation instability. The growth rate of TPD is of the same order as the growth rate of absolute SRS at the quarter critical density. These two processes will compete but most likely produce different hot electron spectra and different angular openings because the corresponding daughter plasma waves propagate in different directions and have different wavelengths. The TPD produces light waves at 1/2 and 3/2 of ω_0. The wave at $1/2\omega_0$ will contribute to the cavitation process at 1/16th of n_c like the Raman scattered wave, while the second wave will leave the plasma unaffected. The filamentation instability is on the other hand a nonresonant process and thus it should grow slower than SBS and SRS. One may therefore expect that a similar scenario will take place also in two-dimensional geometry. Initially, the SBS instability will be the most important, later on the filamentation and the SRS/TPD instabilities at the quarter critical density should dominate.

4. Results of simulations

4.1. Stimulated Brillouin scattering

According to the gain analysis presented in the previous section, SBS should be the dominant process under the conditions of our simulations, while SRS can take place only in the vicinity of the quarter critical density. For this reason, we first considered a dense plasma layer with the density varying from 0.3 to 1.1 of the critical density. As the temperature is relatively high and the simulations are long, the plasma undergoes expansion and a low density tail develops in front of the initial density profile. The characteristic scale length $L_n \simeq c_s t$ is of the order of $20\,\mu$m at $t = 40$ ps. Therefore, SRS is not completely forbidden in these simulations, but it is strongly suppressed.

The power spectrum of the light reflected from the target irradiated by a 35 ps long laser pulse with a constant intensity of $10^{16}\,\mathrm{W\,cm^{-2}}$ is plotted in in figure 2(*a*) as the curve denoted SBS. In this run the plasma expansion velocity was set to zero and the electron collisions were neglected. The signal near ω_0 is slightly red shifted, and the frequency shift is approximately

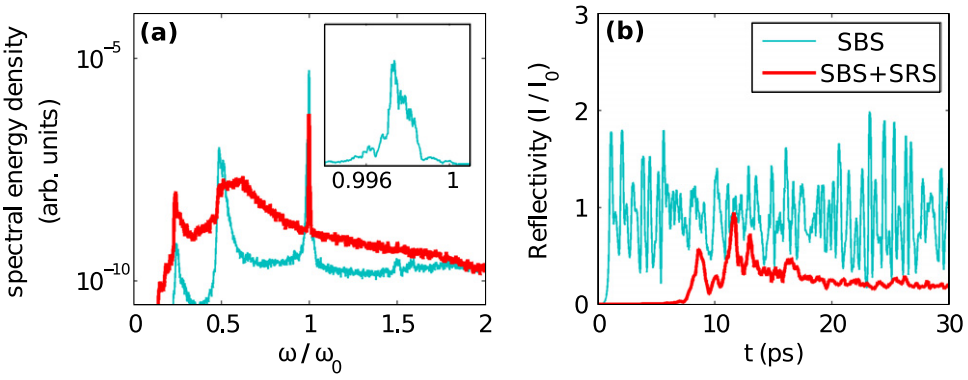

Figure 2. (*a*) Spectral energy density of the pulse reflected from the target in simulation with the minimum initial plasma density in the profile $0.3n_c$ (plotted in blue and denoted SBS) and with the minimum density $0.02n_c$ (plotted in red and denoted SBS + SRS). The region around the incident laser frequency (ω_0) is plotted in linear scale in the inset for the SBS simulation. (*b*) The reflectivity in relative units with respect to the maximum incident laser pulse intensity (I_0) resulting from the SBS and SBS+SRS simulations plotted versus time.

equal to $2k_0c_s$, which corresponds to Brillouin backscattering. This can be seen in the inset, where the domain around ω_0 is shown in a linear scale. The SBS signal dominates the frequency spectrum and it contains about 80% of the entire backscattered energy. The signal at about $0.5\omega_0$ that comes from SRS at the quarter critical density is also clearly seen. There is also a relatively weak but still well remarkable peak in the spectrum around $0.25\omega_0$. This peak is also related to SRS and it will be discussed in detail in the next section.

The temporal evolution of reflectivity resulting in our simulations is plotted in figure 2(*b*) (blue curve). The reflected signal is integrated over the whole frequency domain. It shows an irregular series of relatively short (less than a picosecond long) bunches with intensity often exceeding the laser intensity. This simulation was repeated taking into account the electron collisions and also with the plasma expansion velocity taken from hydrodynamic simulations [23] with no significant difference in the overall results. The periodicity of spikes in the temporal evolution of reflectivity changed, but the average reflectivity remained nearly on the same level. This disappointing result is, however, strongly related to our particular choice of the density profile with the low density part cut off. The simulations with the full density profile show a completely different result. It is shown by the curve denoted SBS + SRS in figure 2(*b*).

4.2. SRS and formation of density cavities

The influence of the Raman scattering has been studied using the full density profile with the minimum density of 2% of the critical density (figure 3). The ovals drawn by dashed lines and the numbers in this figure denote two regions, which will be studied in detail below. Region 1 is at the quarter critical density, which is the point where the absolute Raman instability develops. Region 2 is around 1/16th of the critical density and it will be shown later that this is the place, where most of the laser pulse energy is absorbed.

The results obtained with the full density profile are substantially different, which is clearly seen in figure 2, where they are denoted SBS + SRS. In figure 2(*a*), one can see that the spectral energy density below ω_0 is much higher and the peak due to SBS is much less pronounced. Only about 30% of the energy of the reflected light is now contained in the SBS peak, whereas

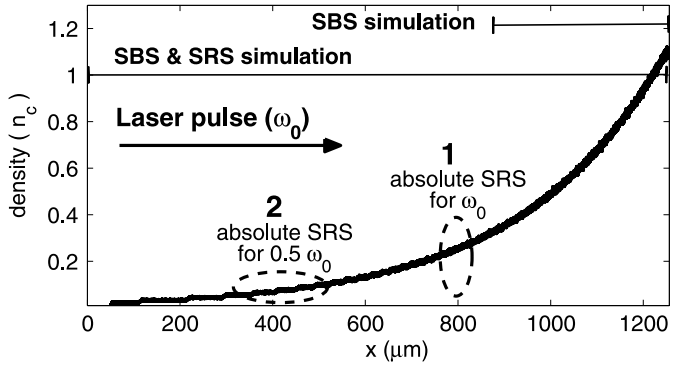

Figure 3. The density profile used in our PIC simulations. The length of the density profile used in SBS simulations is reduced to about 400 μm as depicted at the top of the figure. The full density profile is used in simulations denoted as SBS & SRS. The two important regions of absolute SRS instability for the fundamental and the half-harmonic frequency are marked up.

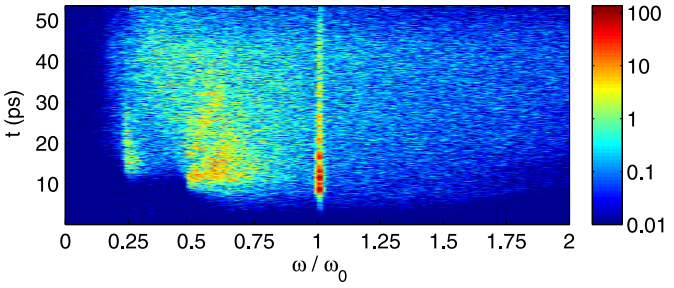

Figure 4. The temporal evolution of the spectral energy density (in arbitrary units) in the SBS & SRS simulation. It is possible to distinguish clear signals in the three distinct frequency ranges. The signal around the fundamental frequency ω_0 is due to SBS, the signal around $0.5\omega_0$ is due to primary SRS and the signal around $0.25\omega_0$ is due to secondary SRS coming from the Raman cascade.

the energy content in the spectral range of SRS (0.5–0.8) ω_0 is about 46%. The difference is even more pronounced in the temporal evolution of the reflectivity plotted in figure 2(*b*) as the curve denoted SBS. At this point, we have to recall the difference in the rise time of the laser pulse used in the SBS simulation (very short rise time) and in the simulation with the full density profile (rise time about 10 ps). In the simulation with the full density profile, there are several relatively broad and small peaks in the reflectivity at an early time (at about 8 and 12 ps), but on the longer time scale the reflectivity saturates on the level of about 20%. As will be shown below, the early peaks correspond to the Brillouin scattering, whereas the reflectivity at later times is mostly due to the Raman scattering.

The processes taking place during the laser interaction with the full plasma density profile will be discussed hereafter in their temporal order. The temporal evolution of the frequency spectrum of the reflected light (recorded in the vacuum at the left boundary of the simulation box) is plotted in figure 4. One can distinguish three different signals in this temporal evolution, which correspond to the peaks in the temporally integrated spectrum in figure 2(*a*), namely the signals at about $0.25\omega_0$, $0.5\omega_0$ and $1\omega_0$. Note that these signals appear successively, in the order from the highest (SBS) to the lowest frequency.

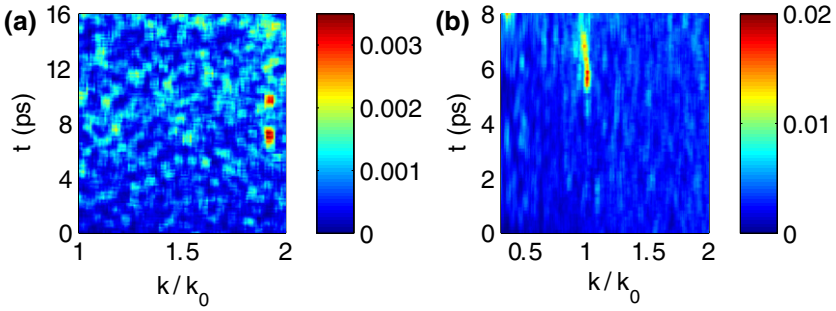

Figure 5. (*a*) The temporal evolution of the k-spectrum of the ion density fluctuations recorded in region 2 of figure 3 (around 1/16th of n_c). Several clear peaks in the otherwise noisy signal can be identified and ascribed to SBS. (*b*) The temporal evolution of the k-spectrum of electron density fluctuations in region 1 of figure 3 (around quarter of n_c). The signal can be ascribed to the electron plasma wave induced by SRS in this region.

According to the estimates in the previous section, the SBS intensity threshold for our parameters is about $10^{14}\,\mathrm{W\,cm^{-2}}$, and the growth rate exceeds $1\,\mathrm{ps^{-1}}$. One can thus expect the Brillouin scattering to grow almost immediately, when the rising edge of the laser pulse penetrates into the plasma. This is indeed confirmed in our simulations. The temporal evolution of the k-spectrum of the ion density fluctuations recorded in region 2 (in figure 3) is shown in figure 5(*a*). The density in region 2 is about 1/16th of the critical density and the ion acoustic wave number at this density should be $k_i \approx 1.9k_0$. It is thus possible to conclude that the k-spectrum shows two significant spikes corresponding to SBS at the time of about 7 and 10 ps. Taking into account the propagation of light wave to the left boundary of the simulation box, the SBS peaks in the k-spectrum correspond to the two biggest peaks in the reflectivity in figure 2(*b*). However this is a transient phenomenon and the Brillouin scattering at later times is rather weak.

Raman scattering takes place near the quarter critical density; its threshold, according to equation (6), is about $10^{14}\,\mathrm{W\,cm^{-2}}$ and its growth rate is about $0.1\,\mathrm{ps^{-1}}$, ten times higher than that of Brillouin scattering. The Raman instability may start to grow only after the laser penetrates up to the quarter critical density, which takes about 3 ps. The temporal evolution of the k-spectrum of the electron density fluctuations recorded at the quarter critical density (region 1 of figure 3) is shown in figure 5(*b*). The wave number of the electron plasma wave excited by the Raman scattering process is the same as the wave number of the light wave at this plasma density, i.e. $k_e \approx 0.87k_0$. The signal with this wave number is clearly observed in figure 5(*b*) appearing at about 5 ps and disappearing later at about 7 ps. The small wave number part of the k-spectrum is not included in the figure because the signal in this region is related to the deformation of the plasma density profile. Taking into account the propagation of the scattered light out of the target, the signal due to SRS should appear in figure 2(*b*) at about 8 ps and it probably contributes to the early peak in the reflectivity.

Electron acceleration into the target in the electron plasma wave excited by Raman scattering is also observed in our simulations around the quarter critical density at this time. However, the strong Raman scattering takes place at the quarter critical density only for a relatively short time and therefore the accelerated electrons do not play a significant role in the overall energy balance and we do not discuss this process in more detail here.

The fact that the backward Raman scattering is suppressed by Landau damping below the quarter critical density and it takes place only in a small region around this density has important

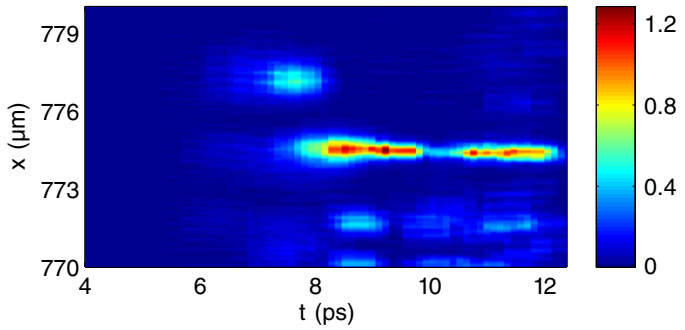

Figure 6. The temporal evolution of the transverse electric field energy density around the quarter critical point. The energy density units are MJ cm^{-3}. The transverse field grows significantly in time locally, which is a clear significance of absolute instability.

consequences. The scattered light spectrum is strongly peaked around $0.5\omega_0$ and the energy absorption into electron plasma waves in the quarter critical region may be relatively high (up to 50% of the incident laser pulse energy). Moreover, the Raman scattering instability is absolute at the quarter critical point, which means that the perturbations induced by this instability grow in time locally.

The absolute nature of the SRS instability is indeed confirmed by the temporal evolution of the transverse electric field energy density around the quarter critical point, which is plotted in figure 6. The electromagnetic field energy density at the point $x = 775\,\mu$m grows very strongly for about 1 ps and at the time of 9 ps it reaches 1.2 MJ cm^{-3}. This energy density is equal to the kinetic energy density of the plasma itself at this point. In such a case, the ponderomotive force of the electromagnetic wave expels electrons from the resonance point and then the ions experience the Coulomb explosion. This process manifests itself by the appearance of a cavity in the density profile. It is observed at the quarter critical density at the time of about 9 ps. This time is not included in the k-spectrum in figure 5(b) because the strong modification of the density profile obscures any other signals. (A small part of the cavity signal can be seen in the upper left corner of figure 5(b).)

Similarly to the cavity formation in the process of Brillouin scattering [29], it requires that the electromagnetic field pressure becomes higher than the thermal pressure of the plasma in that region. This can be expressed approximately as

$$\frac{\varepsilon_0}{2}E_y^2 \gtrsim \frac{1}{4}n_c T_e, \tag{7}$$

where E_y is the amplitude of transverse electric field. Under the ponderomotive pressure the electron density rapidly decreases and the electromagnetic field finds itself trapped inside. Then the amplitude of the electromagnetic field and the cavity size adjust self-consistently in order to establish the pressure balance. The field trapped inside the cavity can accelerate particles to high energies and the cavity can be a source of significant absorption. The cavity, which is observed in our simulation at the quarter critical density, however, disappears after several picoseconds and does not contribute much to the overall absorption of the laser pulse. However, it initiates the second cascade of Raman instability. Very likely the burst of Brillouin scattering in 7 and 10 ps in the underdense plasma (figure 5(a)) is due to the cavity formation in the quarter critical density and the corresponding temporal suppression of the backscattered signal.

As the cavity disappears, the light scattered from the quarter critical density propagates back along the density profile, and as long as its intensity is not very high it leaves the plasma.

However, when the intensity of this light overcomes the SRS threshold, it may be scattered again on its way back at 1/16th of the critical density, which is its own quarter critical density. For our parameters, the intensity threshold for the absolute SRS of the $0.5\omega_0$ light at 1/16th of n_c is 7×10^{13} W cm^{-2}, according to equation (6).

Thus, when the light at $0.5\omega_0$ is sufficiently intense and it propagates down the density profile, it may be scattered again, when it encounters its own quarter critical density at 1/16th of the critical density for the incident laser pulse. The scattered light can only propagate down the density profile and if its intensity is still sufficient, the process may proceed the same way by the next stage in the cascade at 1/64th of the critical density. Our simulations do not have sufficient resolution to include the processes at such a low density, but it is likely that Landau damping will suppress the development of this instability.

The Raman scattering at 1/16th of the critical density can be identified in the k-spectrum at the time of about 14 ps. The spectrum is, however, quite noisy with strong signals due to the density profile modification and thus we do not show it here. The Raman cascade explains the signal at $0.25\omega_0$ in figure 2(a). The partial rescattering of the backscattered light in the cascade explains the spectral broadening of the peak around $0.5\omega_0$. The temporal evolution of the frequency spectrum of the reflected light in figure 4 confirms the temporal sequence of the discussed processes. The Brillouin scattering is very strong initially but its intensity decreases in time, apparently because the strong density perturbations in the $1/16n_c$ destroy the resonance conditions. The Raman scattered signal around $0.5\omega_0$ appears a few picoseconds later. It is followed by the signal around $0.25\omega_0$ with a 5 ps delay.

The absolute Raman instability at 1/16 of the critical density results in a local electric field growth and cavitation similar to the process at the quarter critical density discussed above. However, multiple cavity generation was not expected. As shown in figure 7, many cavities appear in a relatively wide region around 1/16 of critical density. They are relatively stable and exist more than 15 ps up to the end of the simulation. The cavitation process shows some regularities. The spatial separation of cavities is about 5 μm and the cavities at higher densities appear at later times. Very likely, this process of spreading and multiplication of cavities is due to the spectral spreading of the backscattered light in the self-sustained resonator formed between $(1/4)n_c$ and $(1/16)n_c$.

The stable character of density cavities is probably an artifact of our one-dimensional simulation. Our previous studies of the plasma cavitation due to the Brillouin scattering [13] show that the cavity lifetime in two spatial dimensions is in the picosecond scale. They disappear and reappear leading to the temporal fluctuations and the spectral broadening of the backscattered signal. However, the average reflectivity level remains the same as in the one-dimensional simulations.

One can also see in figure 7 the ions expelled symmetrically on both sides at the stage of cavity formation. At a later time the accelerated ions merge into a few relatively dense bunches, which propagate into the target. According to the propagation velocity of the bunches of about $v_i \approx 10^6$ m s^{-1} the energy of the accelerated ions is in the 10 keV range.

Up to this point, we have mentioned and discussed three processes related to parametric instabilities—SBS, SRS and cavitation—and contributing to laser energy absorption in our simulations. The importance of these processes changes in time, but on the global scale one can conclude from figure 8 that the large absorption of about 73% observed in our simulation is connected in particular with the cavitation process at 1/16th of the critical density. Figure 8(a) shows the kinetic energy density in units of MJ cm^{-3}. The significant kinetic energy density increase with time in the low density region around $x \approx 0.2$–0.4 mm corresponds to the light absorption in the cavities. The same is observed for the electromagnetic field energy density plotted in figure 8(b) in the same units MJ cm^{-3} (the field energy density is spatially averaged

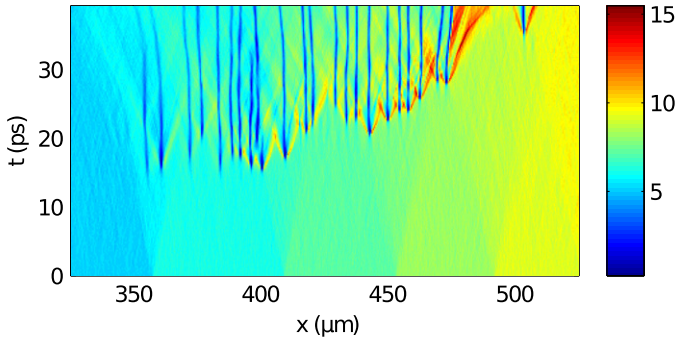

Figure 7. The temporal evolution of the density in region 2 of figure 3 (around 1/16th of n_c). The density represented by the color is measured in percent of critical density. The cavities, which develop in this region, are clearly seen as well as the ion waves launched during the cavity formation. The cavities are quite stable in our 1D simulations.

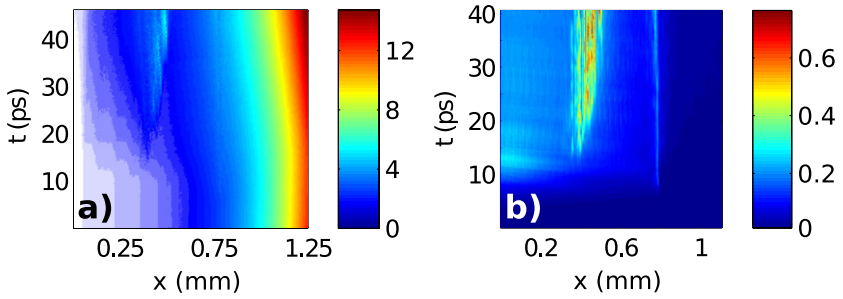

Figure 8. (*a*) The temporal evolution of the kinetic energy density (in MJ cm^{-3}). (*b*) The temporal evolution of the electromagnetic field energy density (MJ cm^{-3}, spatially averaged). The field energy peak at quarter critical density and later in the region of cavities. The cavities accumulate significant amount of energy.

and its amplitude is almost an order of magnitude higher in the region of the cavities). This is in agreement with the reflectivity data plotted in figure 2(*b*) and the temporal evolution of the cavitation process plotted in figure 7, where one can see a temporal coincidence between the decrease in the reflectivity and the appearance of cavities.

From the temporal evolution of the kinetic energy in figure 8 one can also conclude that the cavities accumulate some energy during their creation, but the energy in the region containing cavities does not significantly increase in time after the end of the transient phase at $t \approx 30$ ps, even though the laser pulse is still on. Thus the energy absorbed after this time is transported by electrons into the denser part of the target at the rear boundary, where the energy density significantly increases. The kinetic energy density distribution shown in figure 8(*a*) comes from the simulation without the thermalization region at the rear boundary. Therefore, the kinetic energy density of the plasma significantly increases in this region. As discussed in section 2, the heating at the rear boundary has an influence on the distribution of the return current electrons. Nevertheless, it can be seen that a significant heating at the rear boundary starts at about 32 ps and the propagation of electrons with the temperature of 10–20 keV (observed in the simulation) over the distance of about 1 mm takes more than 10 ps. Thus, the energy distribution of the electrons reflected from the rear boundary does not influence the results of this simulation significantly before 45 ps.

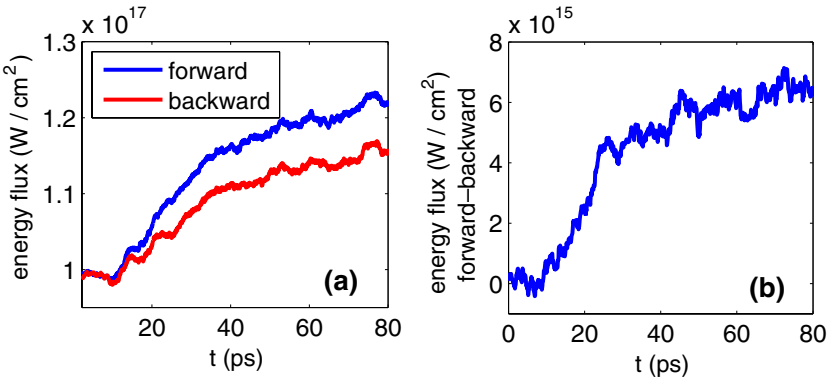

Figure 9. (*a*) The temporal evolution of the kinetic energy flux recorded at the coordinate $x = 1.1$ mm of figure 3. The forward flux increases due to laser absorption, the backward flux rise is due to the return current. (*b*) The temporal evolution of the difference between the forward and the backward kinetic energy flux saturates at a nearly constant value corresponding to the absorbed laser energy flux.

The quasi-steady state is established in the interaction domain because of coupling between the two resonance regions at the quarter and at 1/16th of the critical density. Apparently this is a stable self-organized structure. Would the cavities disappear at 1/16 of the critical density, the absorption in this region drops down, the laser pulse may penetrate up to quarter critical density and induce the absolute instability there. Then the scattered light will in turn produce the absolute instability at 1/16th of the critical density and will reinstall the cavitation.

4.3. Particle energy distribution and the energy flux

Most of the absorbed energy in our simulations is contained in electrons. The increase in the total kinetic energy of electrons is five times higher than the increase in the energy of ions. The energy distribution of electrons propagating into the target and their energy flux are necessary for further simulations of the electron transport in the dense shell, where the shock wave is formed. Although under the quasi-stationary conditions the absorbed energy flux can be evaluated from the laser reflectivity coefficient, it is instructive to confirm it directly from the electron energy distribution function. To obtain the appropriate value for the energy flux, it is, however, necessary to simulate the boundary condition at the rear side of the simulation box correctly. The simulation results presented in this section were all calculated with the thermalization layer at the rear boundary as discussed in section 2.

The energy distribution of electrons and ions and the energy flux are recorded at the check layer located at $x = 1.1$ mm in figure 3 in our simulations. The layer is sufficiently deep inside the plasma, where the density $n_{\mathrm{cl}} = 0.67 n_{\mathrm{c}}$ and only a negligible part of the laser pulse can penetrate. All the important processes, discussed previously, take place in front of this boundary in the lower density plasma. The temporal evolution of the energy flux through this boundary is plotted in figure 9(*a*) in W cm^{-2} separately for the electrons going to the left (backward—out of the target) and to the right (forward—into the target).

The partial energy fluxes in figure 9(*a*) at the initial time are the same in both the forward (into the target) and the backward (return current) directions. They correspond to the collisionless thermal flux in a plasma with Maxwellian distribution of particles, $q_{\mathrm{th}} = \sqrt{2/\pi} n_{\mathrm{e}} v_{\mathrm{te}} T_{\mathrm{e}}$. It can be seen that the partial thermal fluxes in the overdense plasma

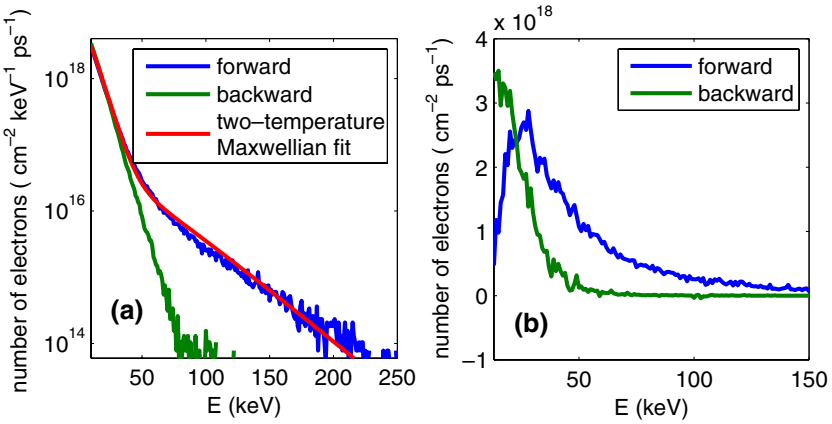

Figure 10. (*a*) The (temporally averaged) energy distribution of the forward and the backward propagating electrons crossing the point $x = 1.1$ mm (normalized per picosecond). The distribution of backward propagating electrons can be fitted by a single Maxwellian, the forward propagating electrons exhibit a two-temperature Maxwellian. (*b*) The function $\varepsilon(f_e(\varepsilon) - f_{e0}(\varepsilon))$, where f_{e0} is the initial distribution function of electrons crossing the coordinate $x = 1.1$ mm during 1 ps and f_e is the energy distribution of electrons crossing the same coordinate temporally averaged over the whole simulation and normalized per picosecond.

at $x = 1.1$ mm are already several times higher than the energy flux of the laser pulse itself. The forward flux starts to grow at about 15 ps, and it is followed also by the increase in the backward energy flux. This is due to the return current that compensates the space charge of hot electrons propagating into the target and maintains the quasi-neutrality of the lower density plasma.

On the time scale of about 50 ps, the partial energy fluxes in both directions saturate and a quasi-steady state with an approximately constant energy flux is reached. This defines the simulation time of the entire laser–plasma interaction. The temporal evolution of the net energy flux—the difference between the partial forward and the backward energy fluxes—is shown in figure 9(*b*). It saturates at a constant level of $\sim 7 \times 10^{15}$ W cm^{-2} after 60 ps. This nicely corresponds to the intensity of the laser pulse itself decreased by the intensity of the reflected light ($(1 - R) \times I_0$) and it demonstrates the consistency of our calculations and the fact that the stationary state is reached.

The energy distribution of electrons crossing the boundary in both directions is plotted in figure 10(*a*). The distribution of electrons propagating backward (the return current) is Maxwellian with a single temperature (about 5.5 keV), which is slightly higher than the initial temperature. This difference is due to the overdense plasma heating by hot electrons. The distribution of forward propagating electrons (into the target) can be fitted with a two-temperature Maxwellian distribution with the lower temperature 5.5 keV and the hot electron temperature $T_h = 26$ keV. The number of hot electrons, n_h, is about 3.2% of the check layer density. The total electron flux $n_h v_{th}$ is thus 2×10^{18} cm^{-2} ps^{-1}, where $v_{th} = \sqrt{T_h/m_e}$.

The energy density contained in hot electrons, $n_h T_h$, constitutes 13.5% of the electron kinetic energy in the critical density. To demonstrate where the energy of the forward and backward propagating electrons is stored, we presented in figure 10(*b*) the electron energy distribution $\varepsilon(f_e(\varepsilon) - f_{e0}(\varepsilon))$, where f_{e0} is the initial distribution function of electrons crossing the coordinate $x = 1.1$ mm during 1 ps and f_e is the energy distribution of electrons crossing the same coordinate temporally averaged over the whole simulation and normalized per 1 ps.

One can see that the energy is transported into the target mainly by electrons with the energies in the range $\varepsilon = 20$–80 keV. The backward propagating electrons have much lower energy.

Finally, we can also estimate the density of hot electrons from the energy conservation principle as $n_h \approx (1 - R) I_0 / v_{th} T_h$, where $R = 27\%$ is the average reflectivity at the end of the simulation. Then one finds that n_h is about 2.14% of critical density. Using this value, one can recalculate the energy flux as $n_h T_h v_{th}$, which agrees well with the flux in figure 9(*b*). To show that the estimate of the beam density is consistent with the number of hot electrons recorded at the check line $x = 1.1$ mm inside the plasma, we note that the density of plasma at the check layer is $0.67 n_c$ and we found there about 3.2% of hot electrons. Thus the beam density calculated at the boundary is consistent with the estimates obtained from the reflectivity, the electron beam temperature and velocity.

5. Conclusions

We presented large scale plasma fully kinetic simulations of the laser–plasma interactions under the SI conditions in one-dimensional geometry. The simulations consider the realistic parameters of the plasma (temperature, density profile and ion mass) and the laser pulse (intensity and wavelength). The simulations are sufficiently long so that a quasi-steady state has been established. Numerical heating is suppressed by using high order particle shapes. Specially designed absorbing boundary conditions at the rear side of the simulation box allowed us to evaluate correctly the number of hot electrons and the energy transported to the denser plasma.

Our results demonstrate that a high temperature, large scale plasma could provide an efficient collisionless absorption of high intensity laser radiation. The laser energy is absorbed in density cavities that are created and maintained by two coupled SRS processes forming a self-organized resonator between the zones of 1/4th and 1/16th of the critical density. This particular plasma response that was not seen before is due to the high initial plasma temperature that suppresses the SRS development everywhere in plasma with the exception of the resonant point where SRS grows as an absolute parametric instability. This particular combination of strong Landau damping of plasma waves and their localization provokes the plasma cavitation and an efficient laser energy conversion in the flux of moderately energetic electrons.

These results indicate rather favorable conditions of the SI scenario, as a large absorption coefficient exceeding 70% and a Maxwellian spectrum of hot electrons with a temperature less than 30 keV are favorable for the creation of high amplitude shock wave in the fusion target. The first experiments on the SI conducted in the LLE [30] demonstrated a laser absorption coefficient that is in agreement with our simulations.

The results presented in our paper are limited to the one-dimensional model and to a special set of laser and plasma parameters. Although they are pertinent to the SI radiation hydrodynamic simulations [7] it is not clear for a moment what are the margins of the domain of parameters for this particular scenario and how restrictive is the one-dimensional model. Our previous experience with the studies of strongly nonlinear regimes of the SBS [13] allow us to expect that the overall behavior and the quasi-stationary absorption efficiency will not be affected considerably, although the detailed temporal evolution will be certainly affected. It might be also that a shorter lifetime of cavities and the excitation of the two plasmon decay (which is forbidden in the one-dimensional geometry) will undermine the efficiency of the resonant coupling of SRS processes and its overall performance.

In a more general sense, our simulations demonstrate an importance and a large innovative potential of large scale kinetic modeling. Such a specific regime of interaction cannot be seen in smaller plasmas or in short time simulations. The zone of 1/16th of the critical density needs

to be described in detail as well and the zone of $n_c/4$ and some space need to be reserved in order to make the wave propagation and adjustment of phase resonance conditions possible. Moreover, the synergy between two SRS processes is accompanied by their destructive effect on the SBS performance. Intricate details of these processes need to be studied in the near future.

Acknowledgments

The authors are grateful to G Schurtz and X Ribeyre for the stimulating discussions. The support from the National Research Agency under project No ANR-07-BLAN-004 and the Centre National de la Recherche Scientifique is acknowledged. This work was also partly supported by the Aquitaine Region Council and performed within the framework of the HiPER project (EC FP7 project number 211737). The support by the Czech Ministry of Education, Youth and Sports under Project Nos LC528 and LA08024 is also gratefully acknowledged. The authors are grateful to the French national computational center GENCI for the support within the framework of the project KITSI, number x2009056129.

References

[1] Atzeni S and Meyer-ter-Vehn J 2004 *The Physics of Inertial Fusion* (Oxford: Oxford University Press)
[2] Lindl J 1995 *Phys. Plasmas* **2** 3933
[3] Besnard D 2007 *Eur. Phys. J.* D **44** 207
[4] Basov N G, Guskov S Y and Feokistov L P 1992 *J. Russ. Laser Res.* **13** 396
[5] Tabak M *et al* 1994 *Phys. Plasmas* **1** 1626
[6] Betti R *et al* 2007 *Phys. Rev. Lett.* **98** 155001
[7] Ribeyre X *et al* 2009 *Plasma Phys. Control. Fusion* **51** 015013
[8] Kruer W 1988 *The Physics of Laser Plasma Interactions* (New York: Addison-Wesley)
[9] Kolber T, Rozmus W and Tikhonchuk V T 1993 *Phys. Fluids* B **5** 138
[10] Vu H X, DuBois D F and Bezzerides B 2001 *Phys. Rev. Lett.* **86** 4306
Vu H X, DuBois D F and Bezzerides B 2002 *Phys. Plasmas* **9** 1745
Vu H X, DuBois D F and Bezzerides B 2007 *Phys. Plasmas* **14** 012702
[11] Cohen B I *et al* 2006 *Phys. Plasmas* **13** 022705
[12] Weber S, Riconda C and Tikhonchuk V T 2005 *Phys. Plasmas* **12** 043101
[13] Riconda C *et al* 2006 *Phys. Plasmas* **13** 083103
[14] Albrecht-Marc M *et al* 2007 *Phys. Plasmas* **14** 072704
[15] Yin L *et al* 2007 *Phys. Rev. Lett.* **99** 265004
Yin L *et al* 2008 *Phys. Plasmas* **15** 13109
[16] Hüller S *et al* 2006 *Phys. Plasmas* **13** 022703
[17] Johnston T W *et al* 2009 *Phys. Plasmas* **16** 042105
[18] Langdon A B and Hinkel D E 2002 *Phys. Rev. Lett.* **89** 015003
[19] Masek M and Rohlena K 2010 *Eur. Phys. J.* D **56** 79
[20] Klimo O, Limpouch J and Zhavoronkov N 2006 *J. Phys. IV* **133** 1181
[21] Lichters R, Pfund R E W and Meyer-ter Vehn J 1997 *Technical Report No* 225 Max-Planck Institute für Quantenoptik, Garching
[22] Kemp A J, Pfund R E W and Meyer-ter-Vehn J 2004 *Phys. Plasmas* **11** 5648
[23] Ribeyre X 2009 private communication concerning simulations published in [7]
[24] Hockney R W and Eastwood J W 1988 *Computer Simulation using Particles* (London: Taylor and Francis)
[25] Liu C S, Rosenbluth M N and White R B 1974 *Phys. Fluids* **17** 1211
[26] Pesme D 1993 *La Fusion Thermonucleaire Inertielle par Laser* partie 1, vol 1 ed R Dautray and J P Watteau (Paris: Eyrolles)
[27] Kruer W L *et al* 1980 *Phys. Fluids* **23** 1326
[28] Estabrook K and Kruer W L 1983 *Phys. Fluids* **26** 1892
[29] Lontano M *et al* 2006 *Laser Part. Beams* **24** 125
[30] Theobald W *et al* 2009 *Plasma Phys. Control. Fusion* **51** 124052

Laser plasma interaction studies in the context of shock ignition—Transition from collisional to collisionless absorption

O. Klimo,[1,2,a)] V. T. Tikhonchuk,[2] X. Ribeyre,[2] G. Schurtz,[2] C. Riconda,[3] S. Weber,[2] and J. Limpouch[1]
[1]*Czech Technical University in Prague, FNSPE, Brehova 7, Prague 11519, Czech Republic*
[2]*Centre Lasers Intenses et Applications, University Bordeaux 1-CEA-CNRS, Talence 33405, France*
[3]*TIPS/LULI, Université Paris 6, CNRS, CEA, Ecole Polytechnique, Ivry-sur-Seine 94200, France*

(Received 7 June 2011; accepted 26 July 2011; published online 26 August 2011)

The shock ignition concept implies laser pulse intensities higher than 10^{15} W/cm^2 (at the wavelength of 351 nm), which is the commonly accepted limit where the inverse bremsstruhlung absorption dominates. The transition from collisional to collisionless absorption in laser plasma interactions at higher intensities is studied in the present paper with the help of large scale one-dimensional particle-in-cell simulations. The initial parameters are defined by the hydrodynamic simulations corresponding to recent experiments. The simulations predict that a quasi-steady regime of laser plasma interaction is attained where the total laser energy absorption stays on the level of ~65% in the laser intensity range 10^{15}–10^{16} W/cm^2. However, the relation between the collisional and collisionless processes changes significantly. This is manifested in the energy spectrum of electrons transporting the absorbed laser energy and in the spectrum of the reflected laser light. © *2011 American Institute of Physics*. [doi:10.1063/1.3625264]

I. INTRODUCTION

Shock ignition (SI)[1,2] is considered as a relatively robust way to achieve efficient fuel burn in inertial confinement fusion (ICF). The phases of fuel assembly and ignition are separated and additional energy to ignite the target is supplied to the central hot spot by a strong converging shock. This shock is launched by increasing the power of radiation impinging on the surface of compressed shell to several hundreds of terawatt. As the diameter of the shell at that time is (at the critical surface) of the order of a few hundred μm (approximately half of the initial target size[3]), the necessary ignition laser pulse intensity is in the domain where nonlinear phenomena in the laser plasma interaction play an important role. When these nonlinear processes become strong, the laser absorption mechanism changes both qualitatively and quantitatively and it is important to take it into account in the calculations used to design ICF targets with high energy gain.

Among the nonlinear processes, parametric instabilities and especially the stimulated Raman scattering and stimulated Brillouin scattering (denoted SRS and SBS, respectively) play an important role.[4,5] These instabilities are responsible for scattering of the laser light and in the case of SRS also for partial absorption, which is usually accompanied by generation of hot electrons. Hot electrons produced by SRS are dangerous in the conventional direct drive hot spot ignition concept, because they preheat the fuel and prevent its sufficient compression.[6] However, in SI scheme hot electrons with moderate energy of order of tens of keV do not necessarily have detrimental effect. The areal density of the compressed shell may be sufficiently high to prevent these electrons to penetrate into the hot spot as noted in Refs. 1 and 2. These hot electrons may deposit their energy at the outer surface of the imploding shell and contribute to the shock pressure.[7] This implies that SRS may be acceptable or even desirable in SI if it provides sufficient collisionless absorption into hot electrons with moderate energy. On the other hand, SBS has more deleterious effect as it does not contribute to the laser absorption and it may be responsible for reflection of a large fraction of the laser light.

The maximum laser irradiance (the product of the intensity and the square of the wavelength, $I\lambda^2$) in the classical hot spot ignition concept of the direct drive ICF is limited to about 10^{14} W/cm$^2 \times \mu$m^2. Below this limit, the growth of parametric instabilities is reasonably slow, scattering of light is suppressed, and a large fraction of the incident laser pulse energy is absorbed due to inverse bremsstrahlung. For higher irradiances on the other hand, the efficiency of inverse bremsstrahlung decreases as the oscillatory velocity of electrons in the laser wave becomes relatively high. At the same time parametric instabilities are excited more rapidly, resulting in stronger scattering and reflection of laser light. However, for the laser irradiance of the order 10^{15} W/cm$^2 \times \mu$m^2, which is an order of magnitude above the limit, SRS may also induce efficient collisionless absorption mechanisms as demonstrated in Ref. 8. The aim of the present paper is to study the transition of the laser plasma interaction regime dominated by inverse bremsstrahlung into the regime dominated by collisionless absorption processes induced by parametric instabilities.

The laser plasma interaction is studied here for the conditions close to those of current SI experiments.[9,10] First, a linear gain analysis of SRS and SBS instabilities is presented and discussed. However, this simple theoretical model does not reflect the full complexity of the parametric processes and their mutual interplay in the laser plasma interaction

a)Electronic mail: ondrej.klimo@fjfi.cvut.cz.

region. Moreover, the gain analysis can provide information only about the overall absorption of the laser pulse but not about the energy and angular distributions of particles transporting the energy from the interaction region deeper into the target. Such information can be obtained in numerical simulations, and it is very important to properly determine the parameters of the final shock launched into the target.

In this paper, the laser plasma interaction is studied by means of fully kinetic numerical simulations. These simulations are performed in one spatial dimension in a plasma with realistic size, density scale, temperature, and expansion velocity. The initial parameters are taken from hydrodynamic simulations.[11] Our kinetic simulations are performed for laser irradiances in the range 10^{14}–10^{15} W/cm^2 × μm^2. In the case of the lowest irradiance, the results of simulations with and without collisions are compared to demonstrate the effect of inverse bremsstrahlung absorption. We show that it helps to suppress the growth of parametric instabilities and the most of absorbed energy is contained in thermal electrons. When collisions are not taken into account, the parametric processes are overestimated, which results in higher reflectivity.

Collisional simulations for higher irradiances demonstrate the transition from collisional to collisionless absorption. In this case SRS becomes strong enough to provide an efficient transformation of the laser energy into hot electrons. This absorption mechanism has been studied in Ref. 8 for the case of a higher temperature ($T_e = 5$ keV), large scale ($L = 300$ μm) plasma irradiated by the laser pulse with the irradiance of 1.2×10^{15} W/cm^2 × μm^2. It has been demonstrated that the laser energy is absorbed in density cavities, which are created and maintained by two coupled SRS processes forming a self-organized resonator between the zones of 1/4th and 1/16th of the critical density. This particular plasma response was attributed to the high initial plasma temperature, which results in strong Landau damping of SRS induced electron plasma waves. The SRS development is thus suppressed everywhere in plasma with exception of the resonant points, where SRS is growing as an absolute parametric instability. The localization and temporal growth of plasma waves provokes the plasma cavitation and an efficient laser energy conversion in the flux of moderately energetic electrons. This absorption mechanism takes place also in the simulations presented in this paper, which are performed for a lower temperature and lower laser irradiances than in Ref. 8. The two dimensional phenomena were studied separately in a plasma of reduced size due to computational constraints.[12] They essentially confirm the results of one dimensional simulations, although in a shorter time scale.

The initial conditions used in the simulations throughout this paper are presented in Sec. II. In Sec. III, we discuss the linear gain of parametric instabilities (SBS and SRS) for the conditions of Sec. II. Our simulation model is introduced in Secs. IV and in Sec. V, we present simulation results. The most important results are summarized in Sec. VI together with our concluding remarks.

II. INITIAL CONDITIONS FOR THE LASER PLASMA INTERACTION—HYDRODYNAMIC PROFILES

The laser plasma interaction that is studied in this paper corresponds to the time of the laser spike arrival, when the spherical target shell has already been accelerated by the main laser pulse and partially imploded. We consider the realistic plasma conditions, which are taken from the hydrodynamic simulations[11] of recent shock ignition experiments on Omega laser facility (spherical target irradiation experiments) at the laser wavelength of 351 nm.[10] The profiles resulting from the simulations 100 ps after the beginning of the shock pulse are plotted in Fig. 1. Only the parts important for the laser plasma interaction are included and the analytical approximations used in our study are shown as well. The velocity and density profiles change only weakly during the

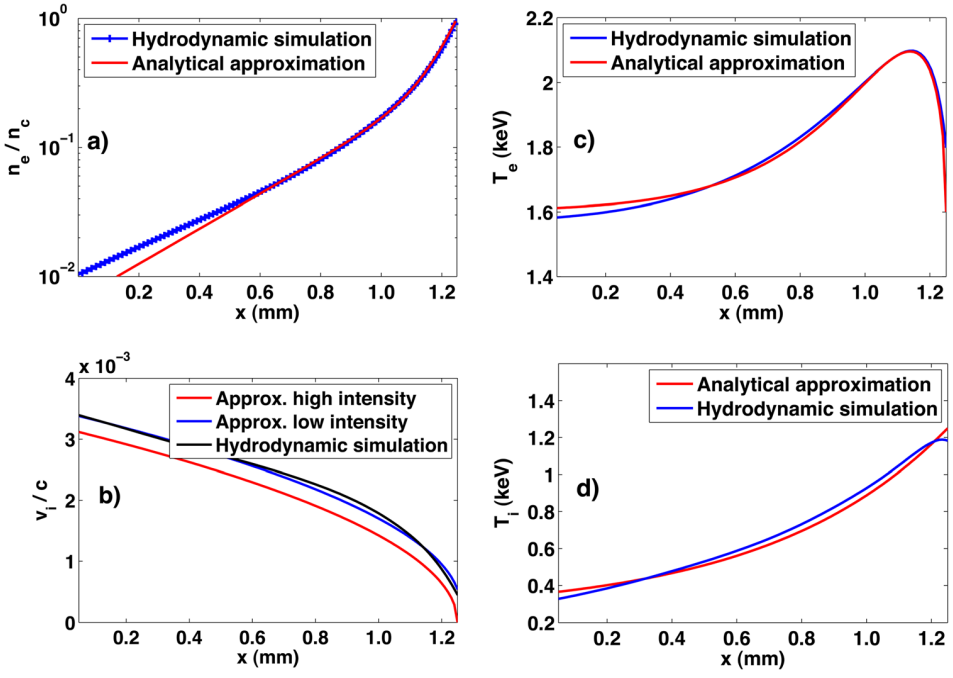

FIG. 1. (Color online) The results of hydrodynamic simulations of a recent shock ignition experiment (Ref. 10) and their analytical approximations used as the initial conditions in our study of the laser plasma interaction.

interaction with the ignition pulse in the hydrodynamic simulations (in the interaction region plotted in Fig. 1). The electron temperature profile changes more significantly during the interaction, nevertheless a precise value of the initial temperature is not important in the simulations, which will be presented here, as the plasma in usually significantly heated on the simulation time scale.

All the approximations of hydrodynamic profiles are relatively accurate with exception of the hydrodynamic velocity, shown in Fig. 1(b). In the case, where we study ignition pulse with high intensity, we subtract the velocity of about 150 km/s from the analytical approximation to keep the high density part of the profile at rest and avoid propagation of the whole target in the simulation box. This allows us to simulate the interaction for longer time before the front boundary can significantly influence the results.

However, such approach is not fully applicable for lower intensities. The cut off of the hydrodynamic velocity and the plasma density behind the critical surface and extension of the density profile by a plateau with zero hydrodynamic velocity are not consistent with full hydrodynamic simulations. We observe a partial deformation of the profile in this part at later times. Namely, a small and shallow hole emerges there on the time scale of a few tens of picoseconds. It will be shown that in the case of high intensity (above 4×10^{15}–5×10^{15} W/cm^2), the profile modification close to the critical surface is not important because the absorption is essentially collisionless and it takes place below the quarter critical density. In the case of low intensity ($\sim(1 \times 10^{15}$–2×10^{15} W/cm^2), the collisional absorption close to the critical density may be important and therefore, the density profile in this part should be more realistic. For this reason, we use another approximation for the hydrodynamic velocity in the low intensity case and let the whole target propagate. With this new velocity profile, we do not observe any significant modification of the density profile in front of critical density during our simulations.

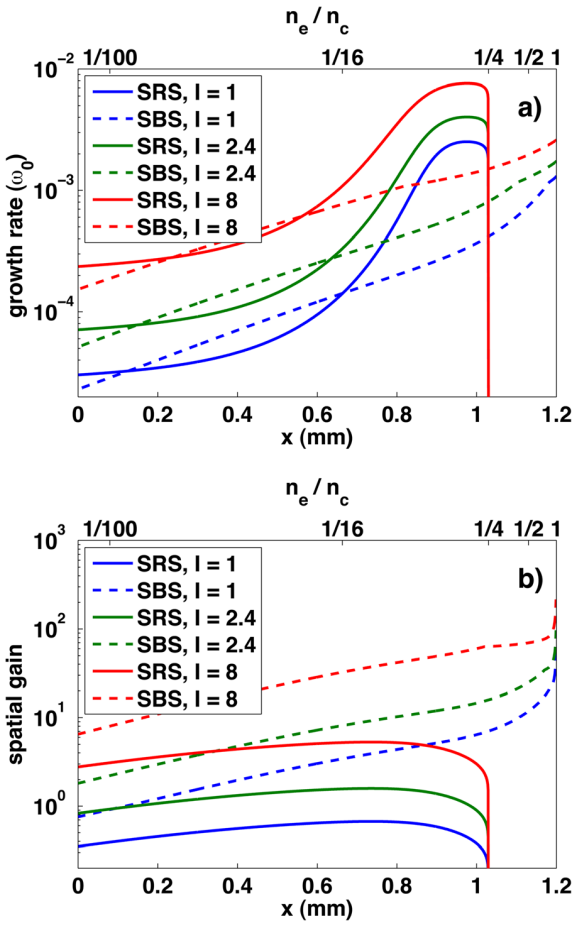

FIG. 2. (Color online) The growth rates (a) and the gains (b) of SBS and SRS backscattering versus the spatial coordinate along the density profile (the corresponding density is shown in the upper axis). The intensity in the graph legend is in the units of 10^{15} W/cm^2. The parameters of plasma are taken from the analytic approximations in Fig. 1. In panel (a), Landau damping of the electron and ion plasma waves and the collisional damping of the electron plasma wave are considered. In panel (b), the gain Eq. (1) is limited by the wavenumber mismatch, which is due to inhomogeneity in the hydrodynamic velocity (in the case of SBS) or in the plasma density (in the case of SRS).

III. LINEAR SBS AND SRS GAINS

The parametric instabilities in laser plasma interactions are characterized by their growth rates and spatial gains. The growth rates give the temporal amplification of the most unstable mode in homogeneous plasma and in the case of SBS and SRS, they are highest for backscattering. This justifies our one-dimensional approach, which is used to study these instabilities. The instability growth rates should be compared with the rates of damping of the daughter waves, which include collisional and Landau damping. In Fig. 2(a) we show the growth rates for SRS and SBS backscattering with the damping rates (both collisional and Landau) of the daughter plasma waves accounted for. The rates are calculated using the analytical approximations of the hydrodynamic profiles shown in Fig. 1.

As can be seen in Fig. 2(a), the SRS growth rates are relatively high in the plasma in front of the quarter critical density. All the curves attain their maximum in a relatively broad region at about 0.95 mm, which corresponds to plasma density of 0.19 critical density. In the lower density plasma, the growth of backward SRS is strongly reduced by linear Landau damping of the electron plasma wave due to a relatively high $k\ \lambda_D$ parameter (here k is the plasma wave number and λ_D is the electron Debye length). Thus, from Fig. 2(a), one would expect a strong SRS scattering in front of the quarter critical density. The growth rates for SBS are not so high as for SRS. The ion acoustic waves are mainly damped by the collisionless Landau damping as the ion-ion and ion-electron collision frequencies are relatively low. Collisional damping of the light wave originating from SBS is not taken into account but it may have a significant effect on the growth of SBS in the plasma close to the critical surface.

The spatial amplification of daughter waves induced by stimulated scattering during their propagation in an inhomogeneous plasma is described by the gain factor G.[13] The wavenumber matching conditions can be satisfied only locally and the propagation of daughter waves in inhomogeneous plasma induces a mismatch, which eventually quenches the amplification. Whereas, the inhomogeneity in plasma density governs

the convective amplification of SRS wave, the spatial amplification of SBS wave is usually limited by the inhomogeneity in the hydrodynamic velocity,[4] which is also the case in this paper. The spatial gain factor is defined as follows:

$$G = \frac{\pi\gamma_0^2}{|\kappa' v_{g1} v_{g2}|}. \quad (1)$$

In this equation, γ_0 is the growth rate in homogeneous plasma, κ' is the spatial derivative of the wave number mismatch, and v_{g1} and v_{g2} are the group velocities of the daughter waves. This gain is plotted in Fig. 2(b) for SRS and SBS backscattering. The convective amplification of SRS seems to be very low at low intensities but it might be quite significant at higher intensities if Landau damping does not strongly suppress the growth of electron plasma waves. The SBS gains are much higher especially in denser plasma.

The linear gain analysis thus indicates that convective amplification of the Brillouin scattered wave in a dense plasma should be very significant unless there is some other mechanism, which will limit this amplification or deplete the pump before it reaches the denser part of the plasma. The growth rate analysis, on the other hand, suggests that SRS may be considerably strong in front of the quarter critical density and that the growth of this instability will be localized to a small part of the density profile. As the SRS takes place in the lower density plasma and its growth is faster than that of SBS, it may influence the growth and amplification of SBS. Thus, it is not clear what will result from the mutual interplay of these two instabilities. To answer this question and one has to resort to numerical simulations.

IV. SIMULATION MODEL

The fully kinetic collisional simulations are performed using our massively parallel relativistic electromagnetic particle-in-cell (PIC) code in one-dimensional geometry. The simulations are sufficiently long (several tens of picoseconds) so that a quasi-steady state may be established in the interaction. The minimum and the maximum values of the density in the density profile are 2% and 100% of the critical density. The relatively high initial temperature results in the minimum Debye length in the simulation box of about 4 nm. We are thus using the computational cells of the size $\Delta x = 5$ nm. The computational time step Δt is about 0.017 fs (i.e., magic time step $\Delta x = c\Delta t$). Numerical heating is suppressed by using smooth high order shapes for particles, which extend over three simulation cells each.[14] Due to this particle shape, the effective number of particles per cell is much higher and the number of particles required for a given noise level can be significantly reduced. We are thus using 100 particles per cell at critical density and all particles in the simulation box have equal numerical weight.

The simulation box is about 1.25 mm long and it contains 50–100 μm of empty space at the front side of the density profile to enable expansion of plasma. The boundary of the simulation box at the laser side of the profile is reflecting particles. Specially designed absorbing boundary condition at the rear side of the simulation box described in Ref. 8 allows us to evaluate correctly the number of hot electrons and the energy transported to denser plasma. This boundary condition is used to absorb the increased flux of kinetic energy due to laser absorption and provide the return current with a constant temperature equal to the initial one. This is realized by thermalizing (assigning velocity sampled from Maxwellian distribution with initial temperature) of all particles in a boundary region of the simulation box with a given probability. However, such boundary condition is somewhat artificial and it may bring problems in some cases. Namely, thermalizing of particles with very high probability results in significant emission of a white electromagnetic noise. This mechanism is similar to bremsstrahlung emission, but it is unphysically strong in our case. The noise intensity might even be comparable to the laser pulse intensity. Therefore, it must have been suppressed in the simulations presented here. This is done by simply zeroing the component of the electromagnetic field at the border of the absorption region.

Relativistic Coulomb collisions (both intra- and interspecies, i.e., e-e, e-i, i-i) are included in our code using the Monte Carlo algorithm[16] similar to Ref. 17. The scattering angle describing multiple small angle Coulomb collisions is sampled from the distribution given in Ref. 18. The accuracy of the collisional algorithm has been checked in simulations of inverse bremsstrahlung absorption of the laser pulse in a homogeneous underdense plasma. The density of plasma (10% of critical density) and the laser pulse irradiance (10^{13} W/cm^2 $\times$ μm^2) are chosen to be low enough in this test case so that parametric instabilities are not induced on the simulation time scale. The laser pulse energy is relatively low and thus the increase of electron temperature during the simulation is negligible. The results are compared with a simple theoretical model (e.g., Ref. 15) in Fig. 3. The target parameters (length 125 μm, electron and ion temperature 200 eV, deuterium ions) and the laser pulse (wavelength 350 nm, temporal length FWHM 20 fs) are the same in all these simulations and the collision frequency is changed by increasing or decreasing the Coulomb logarithm, which is otherwise constant in our numerical model. Our simulation results are in a good agreement with the theory in a broad range of collisional frequencies. For the sake of completeness, we give the

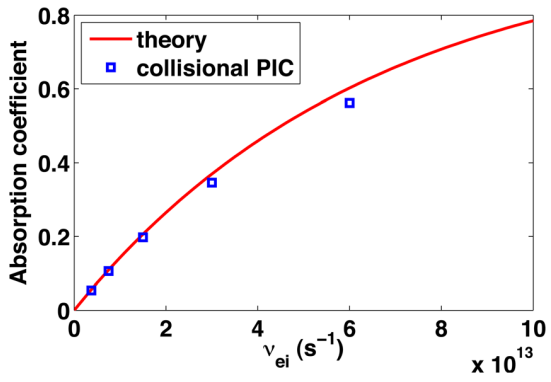

FIG. 3. (Color online) Comparison of the theoretical collisional absorption model of the laser pulse (Ref. 15) with the results of our collisional PIC simulations. The dependence of the absorption coefficient on the electron-ion collision frequency is plotted.

value of the electron-ion collision frequency in the vicinity of critical surface that is about 3×10^{13} s^{-1} (which is 5.6×10^{-3} ω_0, where ω_0 is the laser frequency) in our SI simulations.

In the simulations presented in the following part, the laser pulse intensity is 1×10^{15}, 2.4×10^{15}, or 8×10^{15} W/cm^2 and the wavelength is 350 nm. The laser pulse has a 5 ps long linear ramp at the beginning and then it stays on the maximum intensity. The simulation includes only one species of ions with the charge and the mass of 3.5 and $7 \times$ the proton mass, respectively. In the collisionless part of the algorithm, this corresponds to the average ion in the fully ionized deuterated plastic (CD) shell. The collision frequency is calculated using a constant Coulomb logarithm $\ln \Lambda = 10$.

V. SIMULATION RESULTS AND DISCUSSION

A. Lower intensity—the effect of collisions

This section is devoted to the description of collisional effects on the laser plasma interaction at lower laser intensity (10^{15} W/cm^2). It follows from the growth rate and the gain presented in Fig. 2 that the SRS instability may take place in the vicinity of the quarter critical density but its convective amplification is rather low ($G < 1$) at the intensity of 10^{15} W/cm^2. The SBS, on the other hand, may be convectively amplified everywhere inside the target, but its growth is significantly higher in the denser plasma close to the critical surface.

When the SBS instability becomes sufficiently strong at some place to backscatter significant part of the incident radiation, intensity of radiation propagating further into the target and thus also the SBS growth rate will be reduced. Hence by taking into account the pump depletion one would expect that the maximum of SBS and SRS will shift toward the lower density part of the plasma for higher laser pulse intensity.

Nevertheless, it will be shown below that at the laser pulse intensity of 10^{15} W/cm^2 pump depletion takes place only in the higher density plasma close to the critical surface. In this part of the density profile, the electron ion collision frequency is already relatively high (of order of 10^{-3} ω_0) and the collisional absorption of the electromagnetic wave becomes important. Namely, the absorption coefficient can be calculated as

$$\alpha_{abs} = 1 - \exp\left(- \int \frac{\nu_{ei}(n_c)}{c} \left(\frac{n_e}{n_c}\right)^2 \left(1 - \frac{n_e}{n_c}\right)^{-1/2} \mathrm{dx} \right), \quad (2)$$

where $\nu_{ei}(n_c)$ is the electron-ion collision frequency evaluated at critical density (n_c), n_e is the local electron plasma density, and c is the speed of light in vacuum. The integral taken between the quarter critical density and the critical density for the density and temperature profiles shown in Fig. 1 gives the absorption coefficient $\alpha_{abs} = 0.6$. Thus, there should be a significant difference in laser absorption between the collisional and the collisionless simulation.

The temporal behavior of the total reflectivity and the reflectivity in the SRS frequency domain calculated in the collisional and collisionless simulations are presented in Fig. 4.

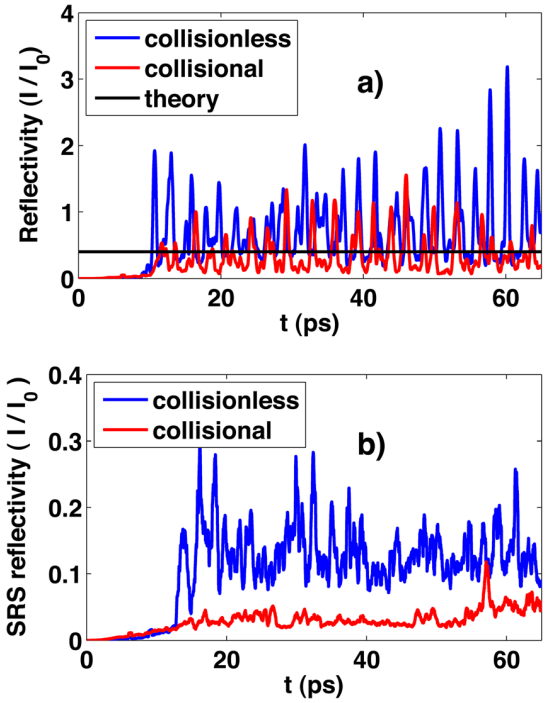

FIG. 4. (Color online) The temporal evolution of the reflectivity in the whole frequency range (a) and in the frequency range corresponding to SRS ($\omega < 0.9\ \omega_0$) b) in the collisional and collisionless simulation of laser plasma interaction at the intensity 10^{15} W/cm^2. The theoretical reflectivity obtained as $1-\alpha_{abs}$ is included in panel (a) for comparison.

The theoretical value obtained as $1-\alpha_{abs}$ is included for comparison. This should correspond to the level of reflectivity in standard hydrodynamic simulations. The overall reflectivity in the collisionless case is more than 60% and it can be seen that the reflected light comes in a series of intense bunches. As will be shown later, these bunches originate from the convectively amplified SBS waves. On the time scale of our simulation one cannot see any trend toward saturation of the instability and drop of the reflectivity. In the collisional case, the situation is qualitatively similar, but the bunches of the reflected light are much less intense and the overall reflectivity is little less than 30%. Similarly like in the collisionless case, there is no significant trend in the temporal evolution of the reflectivity.

Panel (b) of Fig. 4 shows the reflectivity in the SRS frequency range ($\omega < 0.9\ \omega_0$). The reflectivity due to SRS is quite steady and it stays below 5% level in the collisional simulation. This is in agreement with experimental measurements at Omega laser facility for similar ignition laser pulse intensity.[10] From the time of about 12 ps on, the reflected signal due to SRS is about 3 times stronger in the collisionless simulation. The time of 7 ps (taking into account the initial 5 ps rise time of the laser pulse intensity) roughly corresponds to 2 mm of light propagation, which is approximately the distance from the front boundary of the simulation box to the quarter critical density. The characteristic growth time (growth rate^{-1}) of SRS close to the quarter critical density is on the other hand much shorter, of the order of tens of fs.

The temporally resolved spectra of the reflected light in Figs. 5(a) and 5(b) exhibit quantitative and qualitative differences between the collisional and collisionless simulation.

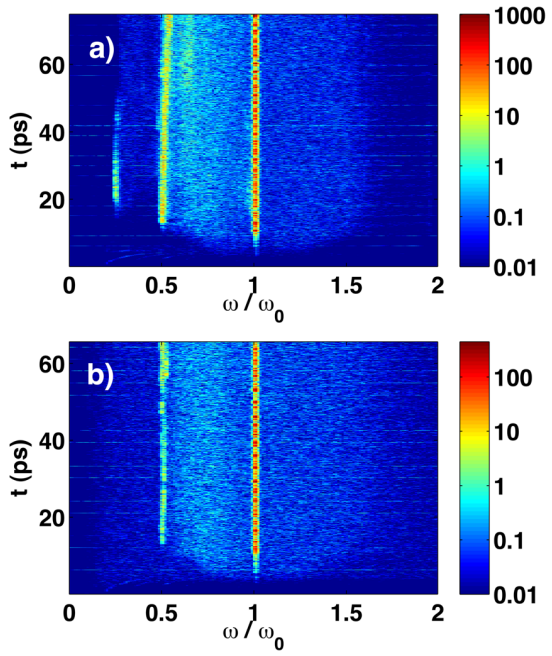

FIG. 5. (Color online) The temporal evolution of the spectra of the reflected light in the collisionless (a) and the collisional (b) simulation of laser plasma interaction at the intensity 10^{15} W/cm^2.

The spectra in the frequency range from 0.5 ω_0 to ω_0 are qualitatively similar in both cases and they show three distinct features: the narrow signal around ω_0 due to SBS, the broad spectrum around 0.7 ω_0 due to convective SRS, and a strong signal around 0.5 ω_0 due to absolute SRS at quarter critical density. In the collisional case, the whole signal is weaker because of the lower reflectivity. The spectra start to differ also qualitatively in the lower frequency part. In the collisionless case, one can observe a strong narrow signal at 0.25 ω_0, which is absent in the collisional case. This signal comes from the secondary SRS process, which is induced by the Raman scattered light (coming from the absolute SRS at 1/4th of critical density) at 1/16th of critical density. It has been already observed and described in details in Ref. 8.

The spectra of the reflected light provide information about the processes taking place during the interaction and their temporal evolution can tell us about their growth and possibly also about the interplay between individual processes. The temporal behavior in Fig. 5 panel (a) demonstrates that the light at 0.25 ω_0 comes later in time after the strong SRS at quarter critical density. This is in agreement with our interpretation that this signal originates from the secondary SRS process.

It is also interesting that the signal at 0.25 ω_0 is clearly visible only for a finite time interval between 20 and 40 ps and it disappears afterwards. We explain this temporal behavior by the density profile modification around the 1/4th and the 1/16th of critical density. As demonstrated in our recent paper,[8] the absolute SRS is accompanied by cavitation and acceleration of electrons. These processes result on a longer time scale in the density profile modification, which will be shown later in this section in the collisionless case. The absolute SRS may be suppressed in the modified density profile, which is in fact observable also in Fig. 5(a), where the strength of the signal at 0.5 ω_0 decreases at the expense of the signal in the higher frequency part around 0.6 ω_0 for t > 50 ps.

There is no significant signal in the low frequency part of the spectrum (around 0.25 ω_0) in the simulation with Coulomb collisions. As can be seen in Fig. 5(b), only the SBS and the convective and absolute SRS at quarter critical density are present. It is also noticeable that all the signals in Fig. 5 panel (b) are much weaker than in panel (a), if one compares the color scales. The absolute SRS at quarter critical density is not strong enough and the scattered light cannot induce the secondary absolute SRS process at 1/16th of the critical density.

To demonstrate the origin of SBS scattered light and its propagation and amplification, we plot the temporal evolution of the electromagnetic field energy density versus the spatial coordinate along the density profile in Fig. 6. In both cases, the collisional and the collisionless, one can clearly see the origin of the first strong burst of SBS, which is seen in the reflectivity in Fig. 4(a) at about 11 ps. SBS starts at about 1.1 mm in both cases corresponding to the density (0.4–0.6) n_c (n_c being the critical density), which is in agreement with the relatively high growth rate plotted in Fig. 2(a). The scattered light gains most of its energy during the first 0.3 mm of propagation to the density of about 0.1 n_c.

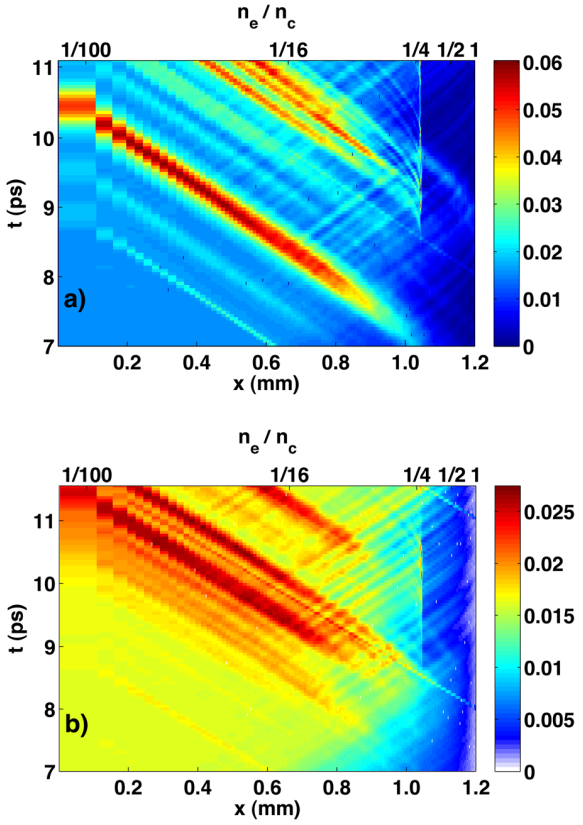

FIG. 6. (Color online) The temporal evolution of the electromagnetic field energy density versus the spatial coordinate along the density profile in the collisionless (a) and the collisional (b) simulation of laser plasma interaction at the intensity 10^{15} W/cm^2. The energy density is in arbitrary, but same units in both panels.

The pulsating behavior of the SBS signal has been reported in many publications.[19–25] It is explained by a strong convective gain of the scattered wave, which depletes completely the pump on its way out of plasma. The SBS pulse duration is of the order of the inverse temporal growth rate–less than 0.5 ps according to Fig. 2(a). The interval between the pulses is defined by the time needed for the pump to penetrate into plasma after the scattered pulse is gone. It is about 3 ps for our 1 mm plasma.

The strength of the light pulse scattered by SBS is much weaker in the collisional case (panel (b)) as the collisional damping of both, the incident and also the scattered light wave near the critical density is comparable to the SBS growth rate. The SBS growth is significantly reduced and the SBS amplification zone shifts in a less dense plasma below the quarter critical density, where the collisional absorption plays less important role. Consequently, collisions play an important role in suppressing SBS instability in the low intensity case. Nevertheless, the plasma reflectivity is still higher than one would expect from the inverse bremsstrahlung–the only dissipation process that is included in most hydrodynamic codes.

The absolute SRS at quarter critical density, which is at about 1 mm, is also clearly visible in both panels of Fig. 6 at the time of about 10 ps. In fact, these figures confirm the absolute nature of SRS instability, as the field energy density is localized in a narrow region and slowly varies with time. The transverse field energy density due to the absolute SRS reaches its maximum at about 10 ps and if one takes into account its propagation out of the target (about 3.5 ps), it coincides with the appearance of the signal at 0.5 ω_0 in Fig. 5(a). At this laser intensity, the SRS does not make a significant contribution to the reflectivity and the overall absorption. Namely, the reflectivity due to SRS is about 5 times lower than the reflectivity due to SBS as can be deduced from Figs. 4(a) and 4(b).

We have demonstrated that the laser pulse absorption is more efficient in the collisional case, while the parametric instabilities are more strongly excited in the collisionless case. To provide more insight into the absorption mechanisms, the spatial profile of the effective electron temperature ($T_{eff} = \frac{2}{3n}\int E f_e d^3p$, where E is the kinetic energy and f_e is the electron distribution function) is plotted in Fig. 7(a). In comparison with the initial time, there is a mild increase in the effective electron temperature in the low density part of the profile with a sharp maximum at about 0.7 mm in the collisionless case. The sharp maximum corresponds to the region at 1/16th of the critical density, where the cavities develop. It has been demonstrated in our previous paper[8] that a significant part of energetic electrons is coming from the domain of cavities induced by SRS. This is confirmed also in present collisionless simulation with a smaller laser pulse intensity 10^{15} W/cm^2. Panel (c) shows the density profile with the cavities developing in the zone of 1/16th n_c in the collisionless case. A weak cooling of electrons can be observed in the high density part of the profile in the collisionless simulation. There is no absorption of the laser pulse energy in this region, and we have checked in a separate test simulation without the laser pulse that the electrons cool down due to ion acceleration during the expansion of plasma in this part of the profile.

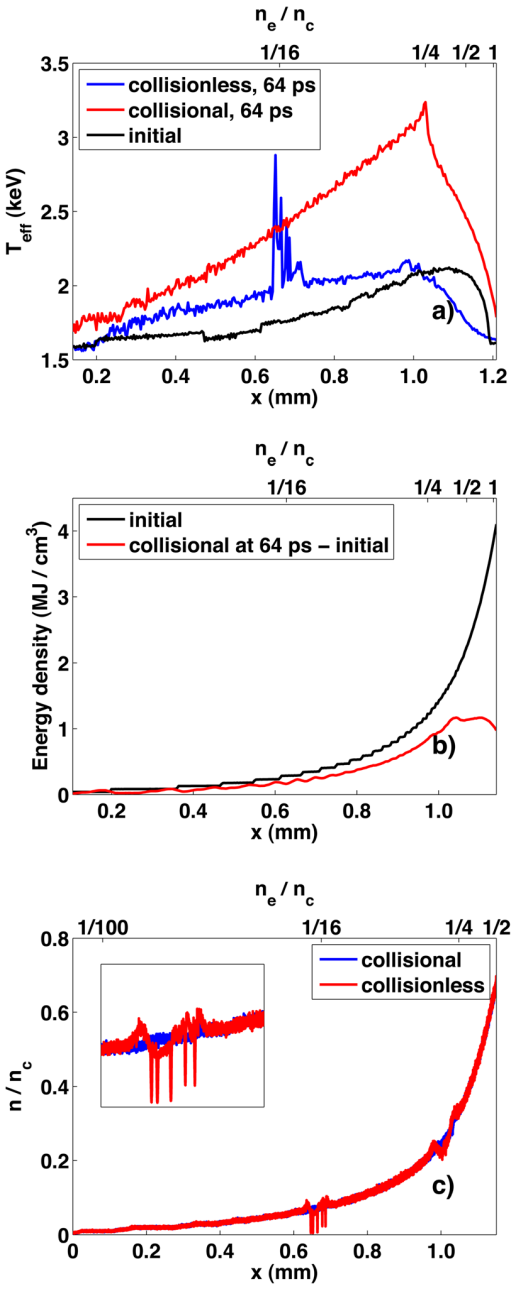

FIG. 7. (Color online) (a) The spatial profile of the effective electron temperature in the initial time and at the time 64 ps for the collisionless and the collisional cases. (b) The spatial profile of the initial kinetic energy density and the energy density increment during the 64 ps in the collisional simulation. (c) The density profiles in the collisional and the collisionless simulation at 64 ps. The inset shows enlarged density profile near $n_c/16$ to better demonstrate the cavities and profile modification.

Electrons along the whole profile are significantly heated in the collisional simulation. In comparison with the initial time, the maximum electron temperature is slightly shifted to the lower density plasma (~1 mm), because of competition of the collisional and collisionless processes. The sharp temperature maximum coincides with the quarter critical density, where the absolute SRS is excited in a

narrow region and contributes to the laser energy absorption. The maximum contribution of SRS to laser absorption can be estimated from the intensity of SRS signal scattered by the target. The energy of plasmons excited by SRS attains its maximum at the quarter critical density and it is equal to the energy of the scattered photons. Thus SRS may be responsible for absorption of at most 5% of the incident laser pulse. Although this corresponds to less then 10% of the total absorption, it makes a significant contribution to the temperature because of its localization. Another reason for the shift of the temperature maximum to the lower density may be related to the inverse bremsstrahlung absorption and SBS, which result in diminution of the laser wave intensity with the coordinate.

The effective electron temperature T_{eff} in Fig. 7(a) should not be confused with the kinetic energy density, $W = \frac{3}{2} nT_{eff}$. The initial energy density of plasma, $W_0 = \frac{3}{2} n_0 T_0$, is plotted in Fig. 7(b) and the other curve shows the increment in the energy density at time 64 ps in the collisional simulation, i.e., $W(t) - W_0$. The curve $W(t)$ demonstrates a broad peak localized in a higher density plasma, where the collisional absorption of the laser pulse takes place. When integrated along the density profile, we obtain the energy increase of 43 kJ/cm^2. This is in agreement with the average absorption coefficient and the laser energy fluence, $F(t) = \int I(t)dt$, which is about 64 kJ/cm^2 during the first 64 ps.

Fig. 7(c) shows the lower density part of the density profiles in the collisional and the collisionless simulation at the time 64 ps. The whole density profile in the collisional case is smooth and without cavities. Only weak profile modification near the quarter critical density can be seen, which maintains the SRS activity on a certain quasi-stationary level. On the other hand, there are significant density perturbations around the quarter critical density and cavities around 1/16th of critical density in the collisionless simulation. These density perturbations come from the absolute SRS instability and they are due to the ponderomotive force exerted by the excited plasma waves on the ion density distribution as described e.g., in Refs. 26 and 27. The profile modification leads to gradual suppression of the SRS and/or pulsations on the time scale of tens of picoseconds.

To answer the question, which particles contain and transport the absorbed laser pulse energy, we plot the energy distributions of electrons and ions obtained in the collisional simulation in Fig. 8. The results from the collisionless simulation are not included here. The energy distributions of electrons in the simulation box in the initial and final times (64 ps) are shown in panel (a). Both distributions are essentially Maxwellian with temperatures of about 2 keV (the initial one) and 2.5 keV (the final one in the collisional simulation). This clearly demonstrates efficient heating of the bulk population of electrons due to the collisional absorption process. Subtracting the initial energy distribution from the final one and integrating, we find the amount of absorbed energy which is contained in thermal electrons. It is about 60% of the absorbed laser pulse energy.

The higher energy electrons ($E > 20$ keV) are fast enough ($v > 0.27c$, where c is the velocity of light) so that they can cross the whole simulation box in less than 15 ps. It is thus clear that the instantaneous energy distribution recorded at time 64 ps does not contain all of these fast electrons, because most of them can quickly leave the box. To quantify the energy transported by these higher energy electrons, we record the forward and the backward electron flux differential in energy 40 μm behind the quarter critical density. It is shown in panel (b) of Fig. 8. Subtracting the

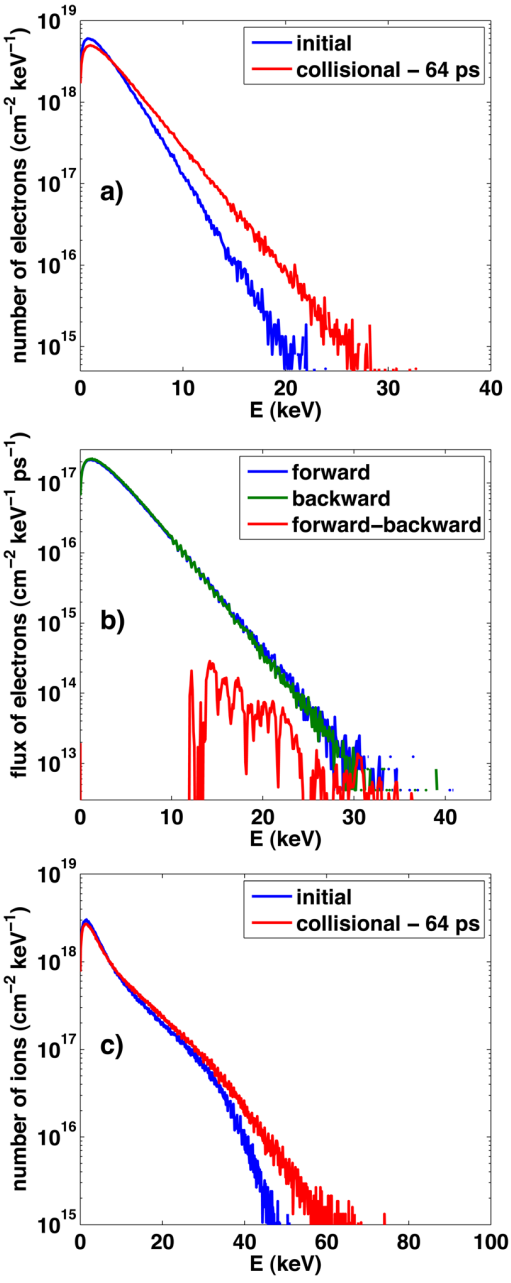

FIG. 8. (Color online) (a) The electron energy distributions in the simulation box at the beginning and at the end of the collisional simulation. (b) The temporally averaged (over 64 ps) electron flux differential in energy pointing into in the target (forward) and in the opposite direction (backward) recorded inside the target at spatial location 1.08 mm (i.e., behind 1/4 n_c) in the collisional simulation. The subtraction of the forward and the backward flux demonstrates forward moving electrons in the high energy tail. (c) The ion energy distributions in the simulation box at the beginning and at the end of the collisional simulation.

backward (opposite to the laser propagation direction) going electrons from the forward going ones we obtain the flux due to higher energy electrons transporting the absorbed energy into the target. As can be seen in panel (b), the energy of these electrons extends from 10 to 30 keV. Integrating this flux over the energy, we estimate the energy transported by these higher energy electrons to about 20% of the absorbed laser pulse energy (i.e., about 13% of the total laser pulse energy). This is more than what can be produced by SRS, because the absorption due to SRS is limited to value of about 5% (the SRS reflectivity) in the collisional simulation. The energy of these hot electrons is however only 4–12 times higher than the bulk electron temperature. It is thus clear that the electrons heated by inverse bremsstrahlung can contribute to this hot electron population. This result is also in agreement with the theory of collisional electron energy transport which states that the electron thermal energy is transported in particular by electrons with energy between about 5 and 16 times the thermal energy in a laser produced plasma e.g., Refs. 4–6.

The remaining 20% of the absorbed energy is spent for ion acceleration as can be seen in the energy distribution of ions in panel (c) of Fig. 8. The rate of ion energy gain can be theoretically estimated as

$$\frac{m_i}{2}\partial_t \int_0^L n_i v^2 dx \approx \int_0^L v \partial_x P_e dx. \tag{3}$$

Substituting the hydrodynamic velocity and the electron thermal pressure from the analytical approximations used as initial conditions in our simulations, we find that the ions may contain energy corresponding to about 14% of the incident laser pulse energy. This is in reasonable agreement with the 20% found in our simulation taking into account that the pressure and the velocity profiles change during the simulation time.

To summarize this section, the Coulomb collisions are essential to describe correctly the interaction of laser pulses of intensity $\sim 10^{15}$ W/cm^2 with plasma in the conditions of SI. They largely suppress the Brillouin scattering, which originates from the higher density part of the profile and also the Raman scattering. The most of laser pulse energy ($\sim$60%) is absorbed due to Coulomb collisions. The contribution from the Raman scattering is relatively minor and does not exceed 5%.

If collisions are not taken into account, the scattering instabilities are stronger and they may enter into the self-organized regime described in our previous paper,[8] in which there is a strong interplay between absolute SRS in different resonance points along the density profile. The energy absorption decreases to less than 30% and the deposited energy is stored in energetic electrons between the resonance regions of 1/4th and 1/16th of critical density. This self-organized regime may be temporally suppressed by density profile modification, which may follow from strong plasma evolution in the resonance regions.

Collisionless absorption processes are suppressed at this relatively low intensity due to Coulomb collisions. The energy distribution of electrons remains Maxwellian with a single temperature, which depends on the absorbed energy and the heat transport inside the target. A relatively minor part of the absorbed energy is due to the SRS and this process produces hot electrons with energies in the range 10–30 keV.

B. Higher intensities-transition to collisionless absorption

The importance of parametric processes increases with increasing laser pulse intensity while the collisional processes become less important. We demonstrate this transition by changing the laser pulse intensity from 10^{15} W/cm^2 to 8×10^{15} W/cm^2 through the intermediate case at 2.4×10^{15} W/cm^2, while keeping the same initial temperature and density profiles. The collisionless absorption mechanisms will be described in details in a separate publication. Here, we just demonstrate that after a transient stage of interaction, the collisionless absorption at a high intensity becomes as efficient as the collisional one in the lower intensity case, but the absorbed energy is transported into the dense target by hot electrons.

The temporal evolution of the reflectivity is plotted in Fig. 9(a). After a transient stage of variable length, which is characterized by strong SBS scattering, the reflectivity in both cases saturates at the level of about 35%. If the laser pulse is much longer than this transient stage, about 65% of its energy can absorbed in the target. Close inspection of the absorbed energy distribution shows that for the higher intensity 8×10^{15} W/cm^2, this absorption is mostly due to a cascade of two SRS processes accompanied by the self-organized resonator between 1/4th and 1/16th of critical density described in Ref. 8. The transient stage is longer when the laser pulse intensity is reduced, because it takes longer time for the parametric processes to grow and set up the resonator.

The spectra of the temporally integrated reflected light in Fig. 9(b) show the features similar to the spectrum for the lower intensity case of 10^{15} W/cm^2, which can be seen in Figs. 5(a) and 5(b). This indicates that the physics of interaction is still governed by the same processes. Although the repartition between the collisional and collisionless processes changes with laser intensity, the overall absorption remains approximately at the same level of $\sim$65%. From the energy distributions of electrons, we are able to estimate that the fraction of energy absorbed by collisionless processes increases from 5 to 70 and 93% when the laser pulse intensity is raising from 1×10^{15} to 2.4×10^{15} W/cm^2 and then to 8×10^{15} W/cm^2, respectively.

The time averaged energy spectra of electrons crossing a boundary located at 1.08 mm (i.e., behind $1/4\ n_c$) in the direction into the target is calculated from the data recorded in the simulation. This time averaged differential (in energy) electron flux $\Psi(E)$ is related to the time averaged electron distribution function $\langle f_e \rangle$ as

$$\Psi(E) = \int \langle f_e \rangle p^2 d\Omega, \tag{4}$$

where p is the momentum of electrons and the integral is over a hemisphere and it includes electrons going into the

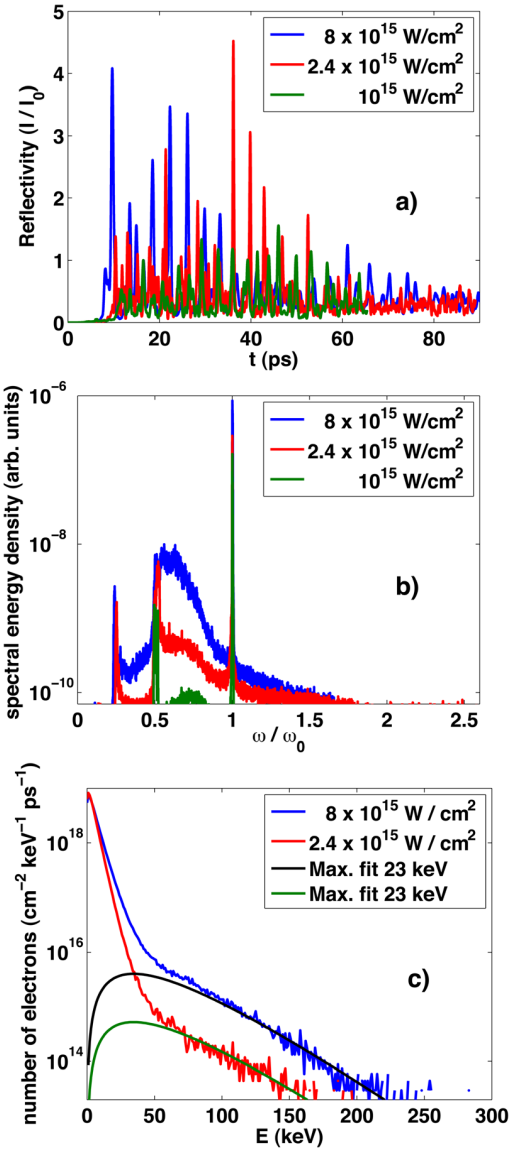

FIG. 9. (Color online) The temporal evolution of the reflectivity (a) and the temporally integrated spectrum of the reflected light (b) in the collisional simulations of laser plasma interaction with the laser pulse intensity 2.4×10^{15} and 8×10^{15} W/cm^2. The results of the collisional simulation performed at the lowest intensity 10^{15} W/cm^2 is plotted for comparison. (c) The temporally averaged flux of electrons flying into the target differential in energy (recorded in the dense plasma close to the target rear side). The differential electron flux is related to the distribution function (see text) and the fits of the high energy tails with Maxwellian functions can be performed.

target. The functions $\Psi(E)$ for the higher intensity laser plasma interactions are shown in Fig. 9(c) together with the approximations of the high energy tails by $p^2 f_{Max}$, where f_{Max} is the Maxwellian distribution function with temperature 23 keV. This hot electron temperature is comparable with the hot electron temperature of 30 keV reported in our previous paper[8] for the laser intensity of 10^{16} W/cm^2 and initial temperature of 5 keV. The differential electron flux plotted in Fig. 9(c) can be compared with the forward flux of electrons plotted in Fig. 8(b). The temperature of thermal electrons increases with the laser intensity (for the same simulation time) from 2.5 keV at the lowest intensity to 3 keV for the intensity 2.4×10^{15} W/cm^2 and to 4 keV at the maximum intensity. This temperature increase cannot be explained by collisional absorption, as the efficiency of this absorption mechanism significantly decreases (from about 60% to 20% and then to 5%) with increasing laser intensity. It follows that there must be a certain thermalization of fast electrons generated by SRS either due to collisions of fast electrons or due to the collisionless heating. This mechanism will be further studied in our following publication.

The collisionless processes lead to formation of hot electrons. Their energy distributions are fitted by a Maxwellian function with a good precision. However, electrons generated in the SRS process are not fully thermalized and their number depends on laser intensity. Our results show that the effective temperature remains almost the same (23 keV) while the number of hot electrons increases about 8 times when the laser pulse intensity is increased from 2.4×10^{15} to 8×10^{15} W/cm^2. This order of magnitude difference in the hot electron number cannot be explained only by the higher laser pulse intensity and the more efficient absorption into hot electrons (this gives only a difference by a factor of about 5). The remaining factor of 1.5 results from the difference in the temporal duration of the quasi-steady state, in which the hot electrons are produced.

There are virtually no hot electrons at the lowest laser intensity, while at higher intensities an increasing fraction of the absorbed energy is transported into the target with the electrons having the average energy of about 40 keV (maximum of the function $E\Psi(E)$, where $\Psi(E)$ is the differential (in energy) electron flux as described above). The energy transported into the target by hot electrons ($E > 30$ keV) is calculated from $\Psi(E)$ and it is about 0.44 MJ/cm^2 when integrated over the simulation time for the highest intensity, in which case the laser pulse fluence is about 0.72 MJ/cm^2. The hot electrons thus carry about 62% of the incident laser pulse energy. For the laser pulse intensity of 2.4×10^{15} W/cm^2, the energy carried by hot electrons ($E > 30$ keV) is only about 29%. A close inspection of the energy distribution in this case shows that there could be a third Maxwellian component with an intermediate temperature of about 10 keV. These mildly hot electrons (20 keV $< E <$ 30 keV) carry a similar amount of the absorbed laser pulse energy like the hot electrons with temperature 23 keV.

VI. CONCLUSIONS

We study the physical processes in the parameter domain relevant for shock ignition by using PIC kinetic simulations, which include Coulomb collisions. These one-dimensional simulations are carried out in a large volume corresponding to the actual size of plasma corona found in hydrodynamic simulations.[11] The ignition pulse considered here, which should launch the shock into the target, has intensity in the range of 1×10^{15}–8×10^{15} W/cm^2 and the wavelength of 351 nm (third harmonic of the Nd:glass laser). In the lower end of the intensity range, the parametric instabilities are playing a secondary role, which is manifested in a relatively weak overall reflectivity and efficient electron heating. The electron collisions largely suppress the SBS

reflectivity to the level of less than 30% and shift the SBS amplification zone into a less dense plasma. About 70% of the laser pulse energy is absorbed due to Coulomb collisions, which is consistent with the theoretically predicted collisional absorption coefficient calculated for the plasma density and temperature profiles. The SRS is also strongly limited by both electron collisions and high electron temperature, and the reflectivity in the SRS frequency range remains below 5%.

On the contrary, at the upper boundary of the intensity domain, the collisional effects are insignificant and the collective effects dominate. The interaction begins by a transient stage of variable duration, which is characterized by strong SBS resulting in a series of strong bursts of scattered light with the average reflectivity of more than 80%. During this stage, the two step absolute SRS develops in the resonance points near 1/4th and 1/16th of the critical density[8] and it forms a self-organized resonator. This is due to the high initial plasma temperature that suppresses SRS development in the lower density plasma, while a weak plasma collisionality does not limit the growth of absolute instability at quarter critical density. The duration of the transient stage (30 and 50 ps in the case of our simulations with higher intensity) is given by the rise time of the resonator and it is decreasing with laser intensity.

The transient stage is followed by a quasi-steady stage, where the average reflectivity drops down to about 35% and remains almost constant. The strong absolute SRS near the quarter critical density suppresses collisional absorption and SBS, and the laser plasma interaction is dominated by collective processes, which take place in the low density plasma in front and at the quarter critical density. The energy absorption occurs in the density cavities developing in the resonance zones near 1/4th and 1/16th of the critical density and the deposited energy is stored in energetic electrons with characteristic temperature of about 25 keV. This temperature does not show significant variation with the laser pulse intensity in our simulations, while the number of hot electrons increases with the intensity.

Our results are thus indicating rather favorable conditions for SI. A relatively large absorption coefficient of about 65% remains on the same level for the laser pulse intensity in the range 1×10^{15}–8×10^{15} W/cm^2 studied here (taking into account only the absorption in the quasi-steady stage in the case of higher intensities). In the lower intensity range, the absorption is dominated by inverse bremsstrahlung and the absorbed energy is transported into the target by electron thermal conduction. A higher energy Maxwellian components appear in the electron energy distributions in the intensity range above 2.4×10^{15} W/cm^2. In this case, collective effects play the dominant role in the laser pulse absorption and more than 70% of the absorbed energy is carried into the dense plasma by hot electrons with temperature <30 keV. In this case, the non-local electron transport becomes important. Nevertheless, the resulting Maxwellian spectra of thermal or hot electrons with a moderate temperature are favorable for creation of high amplitude shock wave in the fusion target.[7]

As the initial (transient) stage of interaction depends strongly on the initial conditions, the quantities calculated at the quasi-steady stage are more appropriate for comparison with experiments. In the low intensity case, the total reflectivity and the reflectivity in the SRS frequency range are in good agreement with the results measured at Omega laser.[10] The absence of hot electrons in the simulation is also consistent with experiments.[10] In the higher intensity domain, the reflectivity during the quasi-steady stage of the interaction in our simulation and the hot electron temperature are both in a relatively good agreement with the experiments[10] too.

The comparison with the measured spectra of SRS is less satisfactory, in particular, in what concerns the signal at the half-harmonic of the laser frequency. This issue needs further more detailed analysis. Our recent two-dimensional PIC simulations[12] performed for downscaled plasma parameters (the density scale length is 3 times smaller than in this paper), shorter time scale, and higher laser pulse intensity confirm the important role of collective absorption. They show that the two-plasmon decay (TPD) is developing in concomitance with SRS. Both these instabilities are active only during the first picosecond of interaction, and then they are rapidly saturated due to plasma cavitation. The hot electron spectrum created by SRS and TPD is relatively soft, limited to energies below one hundred keV, which should not be a danger for the fuel core preheat in the SI scenario.

ACKNOWLEDGMENTS

The support to O.K. by the Czech Science Foundation, project P205/11/P660 is acknowledged. This work was partially supported by EURATOM within the "Keep-in-Touch" activities, the Aquitaine Region Council, and it is performed within the framework the European Union's Seventh Framework Program: the HiPER project # 211737 and the Marie Curie project #230777. The partial support to J.L. by the Czech Ministry of Education, Youth, and Sports (projects LC528 and MSM6840770022) is gratefully acknowledged.

[1]R. Betti, C. D. Zhou, K. S. Anderson, L. J. Perkins, W. Theobald, and A. A. Solodov, Phys. Rev. Lett. **98**, 155001 (2007).
[2]X. Ribeyre, G. Schurtz, M. Lafon, S. Galera, and S. Weber, Plasma Phys. Controlled Fusion **51**, 015013 (2009).
[3]M. Lafon, X. Ribeyre, and G. Schurtz, Phys. Plasmas, **17**, 052704 (2010).
[4]W. Kruer, *The Physics of Laser Plasma Interactions* (Addison-Wesley, New York, 1988).
[5]H. A. Baldis, E. M. Campbell, and W. L. Kruer, *Laser Plasma Interactions*, in Handbook of Plasma Physics Vol. 3, edited by M. N. Rosenbluth, R. Z. Sagdeev, A. M. Rubenchik, and S. Witkowski (North-Holland, Amsterdam, 1991), pp. 361–434.
[6]S. Atzeni and J. Meyer-ter-Vehn, *The Physics of Inertial Fusion* (Oxford University Press, Oxford, 2004).
[7]A. Bell and M. Tzoufras, Plasma Phys. Controlled Fusion **53**, 045010 (2011).
[8]O. Klimo, S. Weber, V. T. Tikhonchuk, and J. Limpouch, Plasma Phys. Controlled Fusion **52**, 055013 (2010).
[9]W. Theobald, K. S. Anderson, R. Betti, R. S. Craxton, J. A. Delettrez, J. A. Frenje, V. Yu. Glebov, O. V. Gotchev, J. H. Kelly, C. K. Li, A. J. Mackinnon, F. J. Marshall, R. L. McCrory, D. D. Meyerhofer, J. F. Myatt, P. A. Norreys, P. M. Nilson, P. K. Patel, R. D. Petrasso, P. B. Radha, C. Ren, T. C. Sangster, W. Seka, V. A. Smalyuk, A. A. Solodov, R. B. Stephens, C. Stoeckl, and B. Yaakobi, Plasma Phys. Controlled Fusion **51**, 124052 (2009).
[10]W. Theobald, R. Betti, K. S. Anderson, O. V. Gotchev, D. D. Meyerhofer, C. Ren, A. A. Solodov, C. Stoeckl, V. A. Smalyuk, J. A. Delettrez, V. Yu. Glebov, F. J. Marshall, J. F. Myatt, T. C. Sangster, W. Seka, B. Yaakobi, J. A. Frenje, and R. D. Petrasso, LLE Review, Quarterly Report No. 119,

p. 117, 2009; "Shock-ignition experiments on OMEGA at NIF-relevant intensities," Phys. Rev. Lett. (unpublished).
[11]X. Ribeyre and M. Lafon, private communication concerning hydrodynamic simulations of Omega experiments (Ref. 9) (2010).
[12]S. Weber, C. Riconda, O. Klimo, A. Heron, and V. T. Tikhonchuk, "Fast saturation of the two-plasmon-decay instability for shock-ignition conditions," Phys. Rev. Lett. (unpublished).
[13]C. S. Liu, M. N. Rosenbluth, and R. B. White, Phys. Fluids **17**, 1211 (1974).
[14]C. K. Birdsall and A. B. Langdon, *Plasma Physics via Computer Simulation* (Institute of Physics, Bristol, England, 1991).
[15]S. Eliezer, *Interaction of High Power Lasers with Plasmas* (Institute of Physics Publishing, Bristol, 2002).
[16]T. Takizuka and H. Abe, J. Comp. Phys. **25**, 205 (1977).
[17]Y. Sentoku and A. J. Kemp, J. Comp. Phys. **227**, 6846 (2008).
[18]K. Nanbu and S. Yonemura J. Comp. Phys. **145**, 639 (1998).
[19]S. Weber, C. Riconda, and V. T. Tikhonchuk, Phys. Rev. Lett. **94**, 055005 (2005).
[20]C. Labaune, H. Bandulet, S. Depierreux, K. Lewis, P. Michel, A. Michard, H. A. Baldis, S. Hulin, D. Pesme, S. Hüller, V. Tikhonchuk, C. Riconda, and S. Weber, Plasma Phys. Controlled Fusion **46**, B301 (2004).
[21]S. Wilks, P. E. Young, J. Hammer, M. Tabak, and W. L. Kruer, Phys. Rev. Lett. **73**, 2994 (1994).
[22]P. Young, E. A. Williams, and K. G. Estabrook, Phys. Rev. Lett. **73**, 2051 (1994).
[23]A. B. Langdon and D. E. Hinkel, Phys. Rev. Lett. **89**, 015003 (2002).
[24]H. X. Vu, D. F. DuBois, and B. Bezzerides, Phys. Plasmas **14**, 012702 (2007).
[25]L. Yin, B. J. Albright, K. J. Bowers, W. Daughton, and H. A. Rose, Phys. Plasmas **15**, 013109 (2008).
[26]S. Weber, C. Riconda, and V. T. Tikhonchuk, Phys. Plasmas **12**, 043101 (2005).
[27]M. Lontano, M. Passoni, C. Riconda, V. T. Tikhonchuk, and S. Weber, Laser Part. Beams **24**, 125 (2006).

Plasma Phys. Control. Fusion **55** (2013) 095002 (12pp) doi:10.1088/0741-3335/55/9/095002

Laser–plasma interaction studies in the context of shock ignition: the regime dominated by parametric instabilities

O Klimo[1] **and V T Tikhonchuk**[2]

[1] Faculty of Nuclear Sciences and Physical Engineering, Czech Technical University in Prague, Brehova 7, 11519, Prague, Czech Republic
[2] Univ. Bordeaux-CEA-CNRS, Centre Lasers Intenses et Applications, UMR 5107, 33405 Talence Cedex, France

E-mail: ondrej.klimo@fjfi.cvut.cz

Received 22 January 2013, in final form 28 April 2013
Published 4 July 2013
Online at stacks.iop.org/PPCF/55/095002

Abstract
The shock ignition concept for inertial confinement fusion includes launching a strong shock with a high-intensity laser spike into an imploding shell. The laser intensity in the plasma corona is above the threshold for parametric instabilities, thus providing conditions for strong non-linear effects. Here we present a series of one-dimensional kinetic simulations of laser–plasma interactions in such a regime. After a transient period of strong non-stationary scattering, the laser–plasma interaction enters an asymptotic regime where a significant part of the incident laser flux is absorbed in the plasma and is transformed into hot electrons. The repartition of the absorbed energy and spectral characteristics of the scattered radiation are presented for laser intensities in the range 2.4–24 PW cm^{-2}. For a laser intensity of 8 PW cm^{-2}, the total absorption is 69%; about 50% of absorption takes place at quarter critical density and the remaining 19% at 1/16th of the critical density. 52% of the total laser pulse energy are absorbed due to stimulated Raman scattering, which produces electrons with a temperature of about 30 keV, and 17% is absorbed due to cavitation, which produces a more isotropic distribution of hot electrons with a temperature of about 10 keV.

(Some figures may appear in colour only in the online journal)

1. Introduction

The shock ignition (SI) concept of inertial confinement fusion relies on the ability to launch a strong converging shock into a pre-assembled fuel [1, 2]. Ignition and high gain may be achieved if the shock would bring the hot spot at the target center to a pressure of the order of 1 Tbar (for a standard hot spot radius of 20–30 μm). To launch such a strong ignition shock in the late stage of target implosion, it is necessary that the plasma corona absorbs a few hundred terawatts of the laser power (depending on the target configuration and the compression pulse energy) and that this energy is efficiently transported to the ablation layer, where the shock is created. For most of the target configurations under investigation [3–6], the ignition laser pulse at the wavelength of 351 nm must be focused to intensities in the range 1–10 PW cm^{-2} for a few hundred picoseconds. At the lower boundary of this intensity range, the laser–plasma interaction is dominated by collisional absorption, and laser–plasma instabilities (LPIs) are of minor importance [7, 8]. On the other hand, the laser intensity is not homogeneous everywhere, but it usually shows some pattern of high-intensity speckles [9]. The space–time distribution of speckles depends on the applied beam smoothing techniques (random-phase plate (RPP) and smoothing by spectral dispersion (SSD)) [10, 11] and on the laser–plasma interaction itself via filamentation and self-focusing. Even if the average intensity is around 1 PW cm^{-2}, the intensity in the speckles can be several times higher and LPIs may develop locally.

In the higher intensity domain, the collisional processes turn over and the interaction is dominated by collective effects. The temporal behavior of the laser–plasma interaction

depends on the development of non-linear processes and their mutual coexistence in the interaction region. This regime of interaction is less predictable due to the stochastic behavior of the fields excited by the instabilities. Nevertheless, a quasi-stationary state may develop after some characteristic period of time. In this quasi-steady state, absorption becomes quite steady as the flux of energy goes deeper into the target. In the case of collective processes, this energy flux consists partially of suprathermal electrons. The results of recent experiments [4–6] and simulations [7, 8] for SI-relevant conditions indicate that these electrons are 'not-too-hot', having temperatures of a few tens of kiloelectron volts. Such electrons may not be dangerous in the SI concept concerning the fuel preheat, if they come in the late stage of target compression and are stopped in the dense shell, which surrounds the hot spot [12]. Furthermore, these hot electrons may be beneficial because their non-local transport smooths out the non-uniformities due to the inhomogeneous target irradiation pattern. It has recently been demonstrated theoretically that these 'not-too-hot' electrons (30 keV) can efficiently drive the ignition shock wave if their flux is sufficiently high [13]. If the absorption of an intense laser pulse is reasonably high and the absorbed energy goes into these 'not-too-hot' electrons, one may think about the possibility of using a smaller number of higher intensity beams or even about a longer laser wavelength to launch the ignition shock. Finally, the beam smoothing techniques such as RPP or SSD may become unimportant. The overall efficiency of converting the laser energy to the shock pressure may be comparable or higher due to the production of hot electrons of moderate energy as compared with the inverse bremsstrahlung absorption alone. Smoothing techniques, which tamp down the parametric instabilities, may thus lower the overall laser–shock coupling under certain conditions. On the other hand, high-intensity spikes may help to drive parametric instabilities and the energy deposition modulations will be smoothed while the electrons propagate from the corona to the ablation zone. The higher intensity regime of LPI under SI conditions is addressed by the simulations presented in this paper.

The simulations consider the realistic time and spatial scales but are limited to the one-dimensional (1D) geometry. Two-dimensional (2D) simulations in a smaller sized computational box [14, 15] demonstrate that major features of 1D simulations are reproduced in 2D runs, although the laser beam filamentation makes the coupling processes more complicated. Extended 2D and 3D simulations of parametric instabilities were conducted by the US research groups [16–20]. However, they correspond to the parameters different from the SI conditions. Either they are focused on a small part of the entire density profile where the competition between the stimulated Raman scattering (SRS) and the two plasmon decay (TPD) takes place [16–18], or they consider the SRS in speckles in large homogeneous plasmas [19, 20] modeling the laser beam propagation in indirect drive hohlraums. These extended simulations show a complicated dynamics and competition of several non-linear processes. At the moment it is difficult to make a full comparison. Nevertheless, at these intensities long time behavior seems to favor the SRS and filamentation, while TPD is more active on the transient stage of a few picoseconds. This also agrees with the experiments [5, 21], where a correlation between the hot electron production and the SRS emission was observed.

Our 1D collisional particle-in-cell (PIC) simulations of laser interaction with HiPER relevant target have been described in [7]. In this case, the plasma profile was approximated by the exponential density dependence with the scale length 300 μm and the homogeneous electron and ion temperatures of 5 keV and 1 keV, respectively. The laser pulse intensity was 10 PW cm^{-2} at the wavelength 351 nm. It was found that a large fraction of the laser pulse energy (70%) is absorbed in density cavities, which develop as a consequence of the localized absolute SRS near the quarter critical density. The goal of this paper is to clarify the mechanisms of non-linear absorption and their dependence on the laser intensity. We analyze, in detail, the spatial localization of the zones of non-linear coupling, their mutual interaction, spectral characteristics of the reflected light, the energy repartition and the angular distribution of different groups of accelerated electrons. The parameters used in this paper are also more realistic than in our previous studies [7, 8]. Plasma density, temperature and velocity profiles are obtained from the hydrodynamic simulations with the code CHIC [22] of recent experiments on the Omega laser facility [6]. The laser pulse intensity is varied in the range 2.4–24 PW cm^{-2}, and it is shown that the laser pulse absorption becomes relatively steady after the initial transient stage. Similarly to the case of HiPER target [7], it reaches the level of about 69% (including both inverse bremsstrahlung and hot electron generation) and it is independent of the laser intensity. The energy flux into the target is due to fast electrons with a temperature of about 30 keV, which also depends weakly on the laser intensity. Simulations with a reduced part of the density profile at an intermediate intensity of 8 PW cm^{-2} indicate that 50% of absorption takes place at the quarter critical density, 38% absorption is due to the SRS, which produces directional distribution of electrons with a temperature of about 30 keV and 12% of absorption is due to cavitation, which produces a more isotropic distribution of hot electrons with a temperature of 10 keV. Such conditions may be favorable for driving the SI by hot electrons.

In spite of the fact that the overall time behavior of laser–plasma interactions is dominated by the absolute SRS and cavitation, our simulations show that convective SRS may coexist with them. The convective SRS is induced by intense laser pulses in a low-density plasma in the inflationary regime. However, the increase in plasma temperature during the interaction pushes the domain of convective SRS toward higher densities. During the quasi-steady stage of interaction, this process exists in the region between the cavities at 1/16th and quarter of the critical density. During the transient stage of interaction, the convective SRS may be induced even by short intense pulses of light scattered by the stimulated Brillouin scattering (SBS). The SBS reflectivity during this stage shows a series of strong spikes with intensity several times higher than that of the incident laser pulse. In the high-intensity regime at the level of 10 PW cm^{-2}, these SBS spikes are

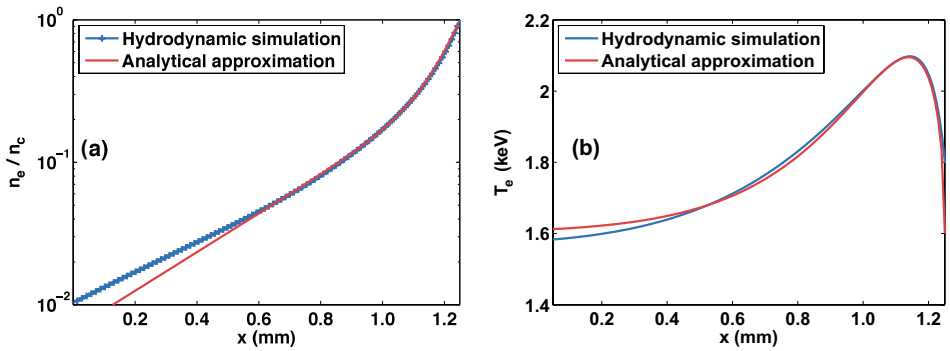

Figure 1. Profiles of electron density (*a*) and temperature (*b*) from hydrodynamic simulations of the SI experiment [6] and their analytical approximations used as the initial conditions in our studies of laser–plasma interaction. n_c is the critical density, which is 9×10^{21} cm^{-3}.

so intense that they induce convective Raman backscattering while propagating outside the target. This Raman scattered light thus propagates into the target and it may be more efficiently absorbed. This process is partially responsible for the saturation of SBS reflectivity at high laser pulse intensities.

This paper is organized as follows. The initial conditions used in the simulations are presented in section 2 together with the simulation model. Section 3 contains the results of our simulations and their discussion. In section 3.1, we present a comparison of reflectivities for three particular laser intensities in the range from 2.4 to 24 PW cm^{-2} and discuss two stages of the laser–plasma interaction. The time behavior of SBS and SRS during the transient and the quasi-steady stage of interaction is discussed in section 3.2. The simulations with a reduced density profile dedicated to a detailed analysis of the absorption process are presented in section 3.3. The most important results are summarized in section 4 together with our concluding remarks.

2. Simulation model and initial conditions

We simulate the interaction of the ignition laser pulse with the plasma expanding from a partially imploded target in the reference frame of the moving shell. It is important to consider the realistic laser and plasma conditions to examine all non-linear processes and observe the result of their mutual interplay. This is obviously a multidimensional problem because the laser pulse has a finite focal spot size and the scattered waves can propagate, in general, in any direction once they satisfy the k-vector matching condition. However, long and large-scale multidimensional simulations consume too much computational time, and it is difficult to understand the interplay of all the processes, which take place there. Therefore, we restrict our attention to the 1D problem in this paper. The 2D simulations of LPI in the SI context have been presented in [14, 15] and for other interaction conditions in [16–20]. Other results are now being prepared for publication. The 1D approach is also justified by the fact that the two parametric processes of special interest, SBS and SRS, have the largest growth rates for backscattering, which is accurately described by our simulations and which was observed in the experiment [6].

The realistic plasma conditions are taken from the hydrodynamic simulations of recent SI experiments at the Omega laser facility [6]. The simulations were performed with the code CHIC [22] in the spherical geometry. The profiles of electron density and electron temperature are plotted in figure 1 together with their analytical approximations used in our simulations. It should be pointed out that the electron temperature in our simulations increases. The initial temperature is not an important parameter unless it is very low and the plasma is highly collisional inhibiting parametric instabilities. The density scale length at quarter critical density is 150 μm. The ion temperature and hydrodynamic velocity profiles have almost linear shapes (the temperature decreasing and the velocity increasing with the distance from the target). The ion temperature ranges between 0.4 and 1.2 keV and the expansion velocity varies between 150 and 1050 km s^{-1}. The density profile steepening near the critical density due to the spike beam reported in the DRACO simulations [6] was not accounted for.

The simulations are performed using a massively parallel relativistic electromagnetic PIC code. The code uses smooth high-order shapes for particles, which suppress numerical heating and allows us to reduce the number of particles required for a given level of noise. The number of (equally weighted) particles per cell at the critical density is 100 in all simulations. The simulation cell size is $\Delta x = 5$ nm, which is similar to the minimum Debye length in the simulation box (4 nm). The computational time step is about 17 as. The simulations contain up to 4.7×10^6 steps and require about 50 000 core CPU hours on the Intel XEON Harpertown CPUs of the JADE cluster of CINES. This simulation time is sufficiently long (several tens of picoseconds) so that a quasi-steady state may be established in the laser–plasma interaction. In the case of simulations with high intensity ($\gtrsim$10 PW cm^{-2}), the simulation time is limited by the evolution of the density profile in the region of intense cavitation. The ions accelerated from the density cavities produce a significant density modulation, which may not be realistic, because the cavitation is a 3D effect. The density modulation may be overestimated in 1D geometry and the simulation should be stopped before this modulation becomes too large (in our case, the run is stopped at 60 ps for the intensity of 8 PW cm^{-2} and at 40 ps for 24 PW cm^{-2}).

The simulation box is about 1.25 mm long with about 100 μm of free space added at the laser side. The front simulation boundary is reflecting particles. The rear boundary is specially designed to absorb the energy flux carried by

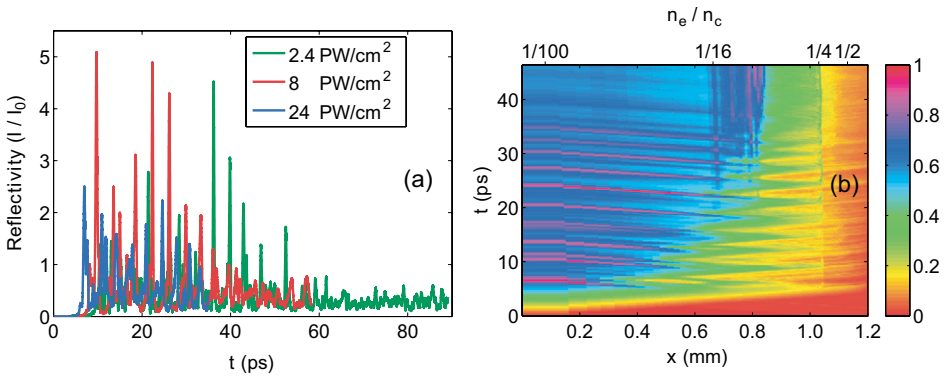

Figure 2. (*a*) Temporal evolution of reflectivity in the simulations of laser–plasma interaction with laser pulse intensities 2.4, 8 and 24 PW cm^{-2} (green, red and blue, respectively). The simulations with higher intensity are stopped at an earlier time because the density profile is more strongly modified. (*b*) Temporal evolution of the electromagnetic field energy density inside the target in the simulation with 8 PW cm^{-2}. The color scale is in arbitrary units.

accelerated particles [8]. Relativistic Coulomb collisions (both intra- and inter-species, that is, electron–electron, electron–ion and ion–ion) are included in our code using the Monte Carlo algorithm [23]. The presented simulations are collisional, but the collisions do not play an important role here, because most of the laser absorption and backscattering takes place in an underdense plasma in front of the quarter critical density. The collision frequency is calculated using a constant Coulomb logarithm $\ln\Lambda = 10$. The simulations include only one species of ions with charge 3.5 and mass seven times the proton charge and mass, respectively, thus modeling a CH plasma in the average ion approximation. According to [24], one may expect a reduced level of SBS reflectivity due to Landau damping of ion acoustic waves if the simulation includes two ion species. However, this is impractical from the computational point of view, as we would have to use higher number of particles for both ion species to have enough statistics for the distribution function in the vicinity of the acoustic wave velocity. As the ion acoustic waves do not play an important role in the SRS excitation and the cavitation scenario, including the second ion species will have no effect on laser–plasma interaction in the quasi-steady stage. The laser pulse intensity in our simulations is 2.4, 8 and 24 PW cm^{-2} and the wavelength is 351 nm. The laser pulse has a 5 ps long linear ramp at the beginning and then it stays on the maximum intensity.

3. Simulation results

3.1. Reflectivity dependence on the laser intensity

The laser–plasma interaction in a higher intensity domain studied in this paper proceeds through two subsequent stages demonstrated in figure 2(*a*). The first stage is transient with a variable duration, which is usually a few tens of picoseconds in our simulations. This transient stage is characterized by a high reflectivity of the order of 80% dominated by SBS. This convective parametric instability has much higher gain than SRS [8] for the conditions used here, and thus the backscattered light can be efficiently amplified during its propagation down the density profile. As there are no processes that can suppress SBS initially, this instability can backscatter most of the pump wave energy and the reflectivity shows strong short spikes with an intensity several times higher than the laser pulse intensity. SBS pulsations during the transient phase is described in more details in section 3.2. This transient stage is partially due to a steep laser pulse front in our simulations. It will probably show a different evolution in experiments with the characteristic pulse rise time of the order of 100 ps.

The temperature of the plasma is relatively high in the low-density part of the target and the electron plasma waves associated with SRS are efficiently damped by strong Landau damping in this region. SRS has thus a lower gain than SBS [8] and it plays only a secondary role during the transient stage. At the quarter critical density, however, SRS is an absolute instability. It has a relatively high growth rate [8, 15] and it also grows during the initial stage of interaction dominated by SBS. The SRS scattered field grows locally in time at the quarter critical density until the field pressure becomes comparable to the kinetic pressure of the surrounding plasma [7]. At this point, the ponderomotive force expels electrons from the unstable region and the subsequent Coulomb explosion of ions produces a density cavity, which partially traps the scattered light. This trapped light cannot escape in the 1D simulation, and it is gradually converted into the kinetic energy of electrons. This cavitation process has already been described in [7] and the existence of cavities has also been confirmed in 2D simulations in smaller scale plasmas [14, 15].

The absolute SRS at the quarter critical density, where the plasma frequency is equal to the half of the laser frequency, $\omega_{pe} = 0.5\,\omega_0$, produces a strong scattered light at the frequency

$$\omega_{SRS} \simeq \omega_0 - \omega_{pe}. \qquad (1)$$

The frequency of the scattered light is also equal to the half of the laser frequency, $0.5\,\omega_0$ and this light is rescattered at the region of 1/16th of the critical density. This second region corresponds to the resonance where the scattered light can excite another absolute SRS on its way out of the target. This rescattering may also result in cavity formation. In our 1D simulations, the cavities are first produced at the quarter critical density and later at 1/16th of the critical density. Once they

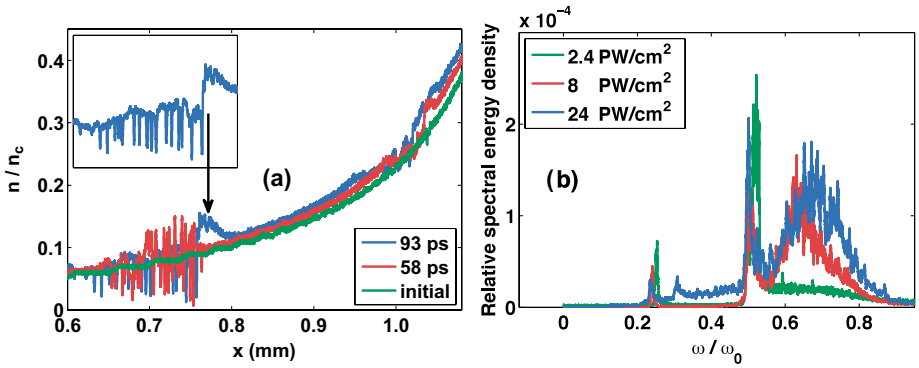

Figure 3. (*a*) Density profile in the simulation with the laser pulse intensity 8 PW cm^{-2} at times of 0, 58 and 93 ps. The inset shows the enlarged density profile near 1/16th of the critical density to better demonstrate the profile modification at 93 ps. (*b*) Spectra of reflected light in the simulations of laser–plasma interaction with laser pulse intensities 2.4, 8 and 24 PW cm^{-2} (green, red and blue, respectively).

develop, the cavities efficiently suppress SBS because they interrupt its spatial amplification. At this time, the first stage of interaction terminates. This can be seen in figure 2(*b*), where the temporal evolution of the electromagnetic field energy density is plotted for the simulation with the intensity 8 PW cm^{-2}. The flashes due to SBS (propagating out of the target to the left) are clearly observed during the transient stage, which lasts for about 35 ps. The cavities around 1/16th of the critical density start to develop at about 30 ps. They can be clearly observed in the figure as vertical strips as they trap a significant electromagnetic energy.

The duration of the transient stage depends, in general, on the laser pulse intensity, as can be seen in figure 2(*a*). It is given by the time necessary to grow the absolute SRS to a sufficiently high level so that the cavities can develop at the quarter and 1/16th of the critical density. This time depends on the laser pulse intensity and its temporal profile via the SRS growth rate and also on the temperature of the surrounding plasma as the local field pressure is equal to the kinetic pressure at the moment of cavity formation. The higher the laser pulse intensity and the lower the temperature, the faster may be the appearance of cavities and the shorter the transient stage. On the other hand, the electron temperature cannot be much lower than the temperature considered in this paper (that is, about 2 keV), because this may allow a strong convective SRS amplification in the low-density plasma and suppression of the absolute SRS due to pump depletion. The dependence of the laser–plasma interaction regime on the electron temperature is, however, not the subject of this paper.

At the end of the transient stage of interaction, a positive feedback is established between the SRS at different locations and the cavitation processes. The cavities at 1/16th of the critical density suppress SBS amplification thus enabling propagation of the incident light up to the quarter critical density. The quasi-steady stage is thus dominated by the SRS and cavitation. It is also characterized by a relatively high absorption coefficient of about 69%, as can be seen in figure 2(*a*). In the 1D simulations at a high intensity we follow the interaction through the quasi-steady stage until the density profile flattens in the region of cavities (at 1/16th of the critical density) due to successive Coulomb explosions of ions in multiple cavities. The cavitation and the subsequent density profile modification are observed on the ion density profile in figure 3(*a*) for the laser pulse intensity 8 PW cm^{-2}. The coupling between the SRS processes in the quarter and 1/16th of the critical density might be overestimated in our 1D simulations. This issue needs further studies.

3.2. SBS and SRS dynamics

The dynamic equilibrium between SRS at different locations is demonstrated in figure 3(*b*), which shows the spectra of reflected light in the SRS domain ($\omega < 0.9\omega_0$). These spectra demonstrate three distinct features: two narrow peaks at 0.5 and $0.25\omega_0$ and a broad peak between 0.6 and $0.8\omega_0$. The narrow peaks, according to equation (1), correspond to the absolute SRS at the quarter and 1/16th of the critical density, respectively. The relative strength of these peaks, which corresponds to the reflectivity due to these processes, decreases only slightly with the laser intensity. On the other hand, the strength of the signal in the frequency range 0.6 and $0.8\omega_0$ increases strongly with the intensity in the domain below 10 PW cm^{-2}, but in the high-intensity domain, $\gtrsim$10 PW cm^{-2}, it does not change significantly.

This broad peak is due to the convective SRS. The frequencies 0.6 and $0.8\,\omega_0$, according to equation (1), correspond to scattering from the plasma with the density ranging between 14% and 2% of the critical density. The plasma wave number, k_e, thus varies from 0.25 to $0.65\,\lambda_D^{-1}$, respectively, where λ_D is the local Debye length. For $k_e\lambda_D \gtrsim 0.3$, the convective SRS would be strongly Landau damped in a Maxwellian plasma. Nevertheless, the convective SRS may exist in the inflationary regime when the velocity distribution of electrons becomes non-Maxwellian [25]. The lowering of SRS threshold due to the fast electrons was demonstrated in [20] even at lower laser intensities. For the higher intensities used in our simulations, the velocity distribution of electrons is modified, and the convective SRS can be induced even in a less dense plasma. The departure of electron velocity distribution from the Maxwellian due to Landau damping of electron plasma waves is demonstrated in figure 4(*a*). The distributions include electrons in an about 100 μm long region in the underdense plasma centered around 4% of the critical density in the time 11.5 ps. The convective SRS originates

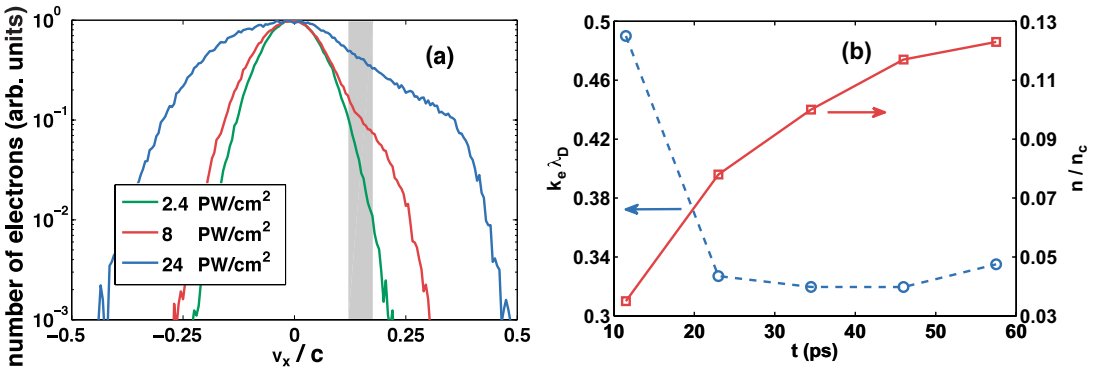

Figure 4. (*a*) Velocity distributions of electrons in the underdense plasma in the region (about 100 μm long) around 4% of critical density in the early stage of interaction. The distribution is taken in the region, where the convective SRS is strongest according to the spectrum of reflected light taken at the same time (11.5 ps). The gray area corresponds to the phase velocity in the region of strongest SRS scattering deduced from the spectra of the reflected light. (*b*) Plasma density, where the maximum convective SRS takes place, and the corresponding $k_e\lambda_D$ parameter as a function of the simulation time for the laser pulse intensity 8 PW cm^{-2}.

from this region in the given time according to the spectrum of the backscattered light. The corresponding range of phase velocities of SRS excited electron plasma waves is included as a gray area in the background.

The temporal behavior of the convective SRS can be understood from figure 4(*b*), which is plotted for the laser intensity 8 PW cm^{-2}. It shows the density, where maximum convective SRS takes place, and the corresponding $k_e\lambda_D$ parameter (which also includes the temporal evolution of the plasma temperature in the simulation) as a function of time. The convective SRS starts first in the inflationary regime in a very low density plasma, where $k_e\lambda_D \approx 0.5$ (as seen in figure 4(*a*)). However, the plasma is significantly heated by the laser pulse in this region and the parameter $k_e\lambda_D$ increases more than two times at a later time. The convective SRS cannot exist here even for relatively high laser intensities and it shifts toward higher densities, where $k_e\lambda_D \approx 0.33$. The shift of convective SRS toward higher densities (and thus lower frequencies of the scattered light) is also observed in the temporal evolution of the reflected light spectrum plotted in figure 5(*a*). The spectra shown in figure 3(*b*) are integrated over the whole simulation time. As the convective SRS shifts with time toward lower frequencies, one cannot directly compare the positions of the peaks in the spectra and conclude about the dependence of the location of SRS activity on the laser pulse intensity. Nevertheless, it is observed that most of the convective SRS is located between quarter and 1/16th of the critical density. Thus, the convective SRS has its own domain of existence. It does not directly interfere with the absolute instabilities at the resonance points of absolute SRS and cavitation.

However, there might be an indirect interaction between the convective and absolute SRS. If the convective SRS is very strong for a long time, the feedback loop between the quarter and 1/16th of the critical density will be destroyed, and this may allow SBS to come into play again and suppress the convective SRS because of pump depletion. This regime of coexistence of convective and absolute SRS instabilities was indeed observed in our simulations. This might also explain the experimental observation of SBS activity being displaced to a denser plasma as the laser intensity increases [6].

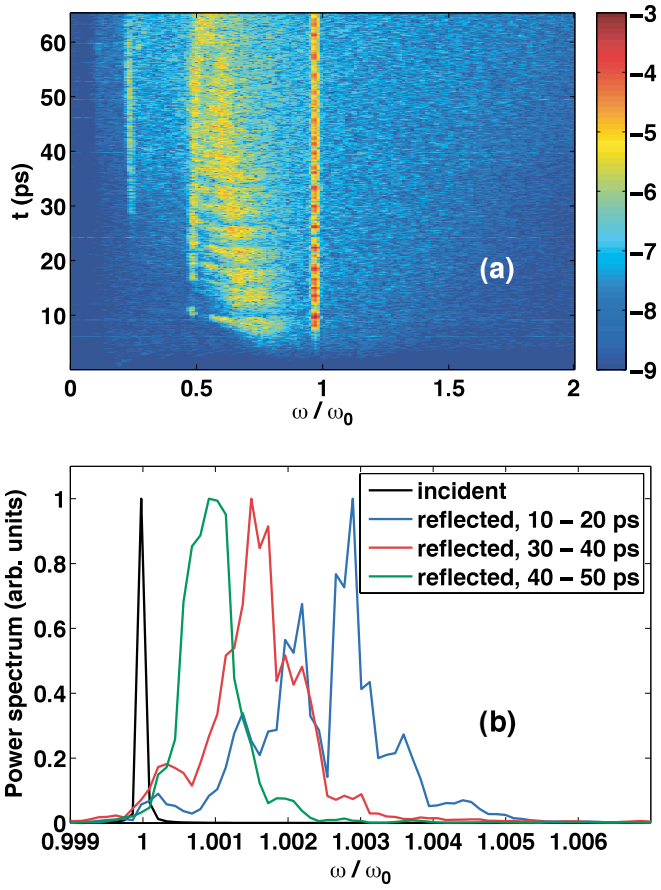

Figure 5. (*a*) Temporal evolution of the spectrum of the reflected light recorded at the vacuum boundary of the simulation box for the laser pulse intensity 8 PW cm^{-2}. The color represents a decadic logarithm of the power spectral density in the respective time in arb. units. (*b*) Spectrum of the reflected light in the SBS domain in three time intervals: 10–20 ps (blue), 30–40 ps (red), 40–50 ps (green). The incident light spectrum is shown in black. The spectra are recorded in the simulation with the laser pulse intensity 8 PW cm^{-2}.

The transient phase of laser–plasma interaction is characterized by strong pulsations of the reflectivity shown in figure 2. Most part of the reflectivity is due to SBS. This can also be seen in the temporal evolution of the spectra of

reflected light for the intensity 8 PW cm^{-2} shown in figure 5(*a*), where the strongest spectral component is at about ω_0. As can be seen in figure 2(*b*), the SBS amplification zone is in a less dense plasma, below the quarter critical density in the beginning of the transient phase of interaction (e.g. 10–20 ps for the laser pulse intensity 8 PW cm^{-2}). As time proceeds, the SBS amplification zone gradually shifts toward a denser part of the target.

In the later part of the transient stage (e.g. 20–40 ps for the laser pulse intensity 8 PW cm^{-2}) the SBS operates, in particular, in the region between the quarter and 1/16th of the critical density. This agrees qualitatively with the observations [6]. During this time, the reflected light comes out in a train of regular 0.3 ps long pulses, which are separated from each other by about a 3.8 ps time interval (see also figure 2). The behavior is similar for all laser intensities, only the pulse separation and the pulse length are not so regular in the case of the lowest and the highest intensity. The time separation between SBS pulses is given by the pump depletion effect and the time necessary for amplification of another ion acoustic wave. From figure 2(*b*) we see that the amplification length is about 0.4 mm, which corresponds to about 1.3 ps of time for the pulse traveling at the speed of light. The pump is almost depleted at this distance. Before the next SBS pulse may start up, the pump must travel the same distance into the target. By subtracting twice the pump depletion time from the pulse separation time, we obtain 1.2 ps for the SBS amplification. This is consistent with the growth rate of SBS, which is about 0.2 ps^{-1} (see figure 2(*a*) in [8]) in the region $x \simeq 1.0$ mm, where SBS is seeded.

The spectrum of the reflected light in the SBS domain in the simulation with the laser pulse intensity 8 PW cm^{-2} can be seen in figure 5(*b*) in three different time intervals. In comparison with the incident light, the spectrum of backscattered light is shifted and broadened. The frequency shift,

$$\omega_{\mathrm{SBS}} - \omega_0 = -2\,k_0(c_\mathrm{s} + u), \tag{2}$$

is caused by two effects—the acoustic wave frequency and the Doppler shift. The acoustic wave frequency is $2\,k_0 c_\mathrm{s}$, where $k_0 = (\omega_0/c)\,(1 - n_\mathrm{e}/n_\mathrm{c})^{1/2}$ is the incident laser wave number and c_s is the ion acoustic velocity. The Doppler effect $2\,k_0 u$, accounts for the blueshift as the plasma expansion velocity u is negative.

The ion acoustic velocity in the plasma corona varies in the range (0.9–1) $\times\ 10^{-3}c$, where c is the velocity of light. The plasma expansion velocity increases from $-0.5 \times 10^{-3}c$ in the dense plasma close to critical density to $-3.5 \times 10^{-3}c$ in the low-density plasma. Thus, according to equation (2), the blue-shifted light originates from the underdense plasma. This is observed in figure 5(*b*), where the SBS frequency shift is always positive and approximately in the range 1–2.5 $\times$ $10^{-3}\omega_0$. The frequency shift is larger in the early phase of interaction indicating scattering from the lower density plasma, where the hydrodynamic velocity is high. This is consistent with our previous discussion of figure 2(*b*). The frequency shift in the quasi-steady phase of interaction discussed above does not significantly depend on laser intensity. This is not the case of the average SBS reflectivity during the quasi-steady stage of interaction, which increases from 13% for the laser intensity 2.4 PW cm^{-2} to about 21% for the intensity 8 PW cm^{-2}. In the case of the highest intensity 24 PW cm^{-2}, the SBS reflectivity was not measured as the quasi-steady stage of interaction lasts only for a short time before the end of the simulation.

The width of the spectrum is also largest initially. This is partially caused by the competition of the effects mentioned above, namely the redshift due to SBS and the blueshift due to the Doppler effect, and the fact that scattering takes place in a large region of plasma with different temperatures and velocities. However, there is another important effect, which contributes to the width of the spectra, that is, the pulsation of SBS reflectivity. As already discussed above, the pulses of SBS are relatively short and well separated from each other. These short pulses must have a spectrum width, which is equal to or larger than the width of a Fourier transform limited pulse. For a 0.3 ps long Gaussian pulse with wavelength $\lambda_0 = 351$ nm, the width of the transform limited pulse is $\Delta\lambda = 1.7 \times 10^{-3}\lambda_0$. This is consistent with the width of the spectra in figure 5(*b*), where the width is about $2 \times 10^{-3}\omega_0$ in the early time of 10–20 ps and it decreases with time to less than $10^{-3}\omega_0$ in the quasi-steady phase, when the reflectivity is much less pulsating.

The propagation of SBS pulse and other pulses induced by SRS can also be seen in the k-spectrum of the electromagnetic field inside the target. This spectrum is plotted in figure 6 for the laser pulse intensity 8 PW cm^{-2} at three subsequent time instants. In panels (*a*), (*b*) and (*c*) one can see the laser light propagating into the target (the strongest signal, which starts on the left at $k = k_0$) and several distinct pulses induced by the parametric instabilities and marked by numbers. Number 1 denotes the SBS pulse. The frequency shift of the scattered light is very small and thus the SBS pulse merges with the incident laser pulse in these k-spectra. The relative strength of the electromagnetic field at a given position inside the target can be seen at the bottom line of the figure and the white arrow shows the position of this strongest signal in the k-spectrum. One can see that the signal denoted by 1 corresponds to the strongest field. This is the SBS pulse, which comes out of the target at about 9 ps in figure 2(*b*). The SBS pulse is about 100 μm long, which corresponds to a pulse duration of about 0.3 ps. It is also observed that the strong SBS pulse has much wider spectrum than the incident laser pulse.

Number 2 denotes the convective SRS induced in the lower density plasma. It is observed that this process is responsible for the wide peak in the SRS spectrum in figure 3(*b*). The convective SRS exists only in front of the SBS pulse. The field of the SBS pulse is much stronger than that of the incident laser pulse (about five times as can be seen in figure 2(*a*) and thus the SBS pulse may destroy the resonance coupling between the incident laser wave and the electron plasma wave in the low-density plasma. Number 3 in figure 6 denotes the light scattered by the absolute SRS at the quarter critical density. Finally, number 4 also denotes the light coming from the convective SRS backscattering. However, in this case the convective SRS backscattering is not induced by the incident laser wave but by the SBS pulse. It is clearly observed that this pulse starts at the position of the SBS pulse and propagates into the target in the time sequence of the k-spectra. This

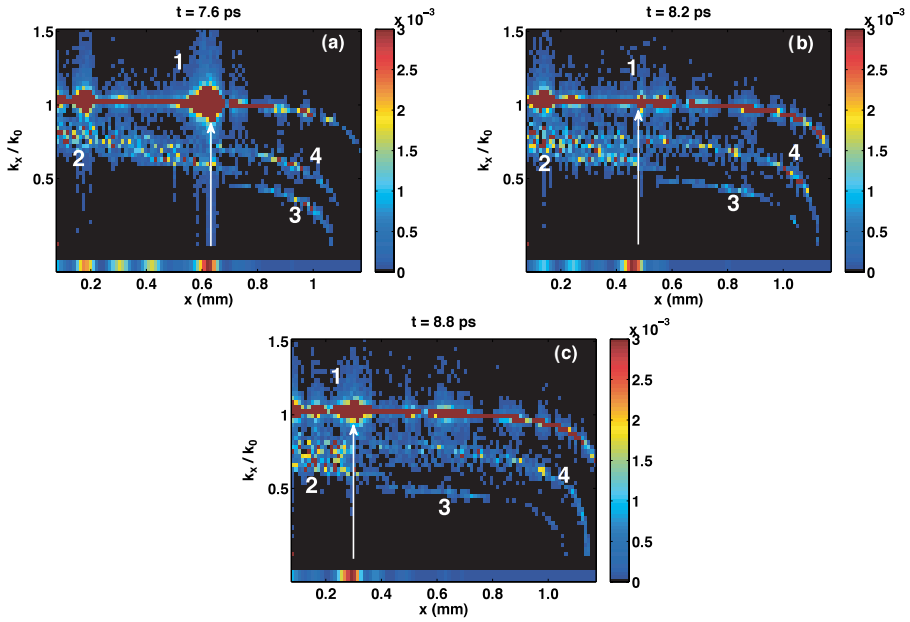

Figure 6. Wave number spectra of the transverse electric field in the simulation with the intensity 8 PW cm^{-2} at times 7.6 ps (*a*), 8.2 ps (*b*) and 8.8 ps (*c*). The white numbers point to the flash of SBS (1), convective backward SRS (2), absolute SRS from the quarter critical density (3) and the Raman backscattered from SBS pulse propagating into the target (4). The very bottom strip of the figure includes the normalized spectral integral of the transverse electric field amplitude at a given position and thus it shows how strong the transverse electric field at a given position is. The arrow points to the position of this strongest signal in the k-spectrum. The figure is color-saturated and the units are arbitrary. In reality, the incident laser pulse and the SBS pulse are order of magnitude stronger than the pulses induced by SRS.

SRS pulse has a broader spectrum than the incident laser pulse and the central frequency of about $0.75\,\omega_0$. It can thus propagate up to about 0.56 critical density without being significantly scattered by parametric instabilities, and it can be more efficiently absorbed by collisions.

This process of SBS rescattering is observed in the case of simulations with a higher intensity ($\gtrsim$8 PW cm^{-2}) and it does not depend on the plasma temperature so strongly like the convective SRS induced by the laser pulse, because it is induced in a denser plasma. This rescattering contributes to the overall absorption but only by a few percent in the case of simulations presented in this paper. Nevertheless, the importance of this process increases with the laser pulse intensity and it is partially responsible for the saturation of amplitude of the SBS pulses at the highest intensity of 24 PW cm^{-2}. Namely, in figure 2(*a*), one can see that the maximum intensity of SBS pulses exceeds by about 4.5–5 times the incident laser intensity for two simulations with lower intensities. For the simulation with the highest intensity, the maximum amplitude of SBS pulses exceeds the incident laser intensity only by a factor of 2.5.

3.3. Hot electron generation

It follows from the reflectivity plotted in figure 2(*a*) that the laser energy absorption in the quasi-steady stage is quite efficient (∼69%), and the average absorption coefficient does not depend on the laser intensity. This agrees rather well with the observations [6]. The efficiency of collisional absorption decreases with the laser intensity because the electron collision frequency decreases with the temperature. Thus, enhanced absorption indicates the role of non-linear collisionless processes. The most important processes in this context in the 1D geometry are electron acceleration in the SRS generated plasma waves and in the trapped electromagnetic field inside the cavities. In all these processes, the energy is transferred to a relatively small group of suprathermal electrons.

The importance of collisionless absorption mechanisms is confirmed by the differential energy electron flux plotted in figure 7(*a*). This function is obtained from the electron energy flux $q_x = \int \mathrm{d}\vec{v}\, v_x \varepsilon\, f_\mathrm{e}(\vec{v})$ by analyzing its distribution on the electron energy, $\varepsilon = m_\mathrm{e} v^2/2$. It is defined as follows:

$$\frac{\mathrm{d}q_x}{\mathrm{d}\varepsilon} = \frac{1}{2}\int \mathrm{d}\vec{\Omega}\, v_x v^3 f_\mathrm{e}(\vec{v}), \tag{3}$$

where $\vec{\Omega}$ is the unitary vector in the direction of electron velocity. The function $\mathrm{d}q_x/\mathrm{d}\varepsilon$ is calculated at the end of simulation in a dense plasma behind the quarter critical density. We dump all electrons crossing a virtual boundary located at 1.1 mm and we calculate the electron energy flux averaged over the time interval of a few picoseconds for each energy bin. Only the forward flux can be seen in the figure, the backward flux of return current electrons, which dominates at low energies, is not shown.

Figure 7(*a*) also shows that the high-energy tail of the differential electron energy flux can be fitted by a sum of several Maxwellian functions

$$\frac{\mathrm{d}q_x^\mathrm{M}}{\mathrm{d}\varepsilon} = 2\sqrt{\frac{2}{\pi}} n_\mathrm{h} \sum_{k=1}^{n} f_k \sqrt{\frac{T_{\mathrm{h}k}}{m_\mathrm{e}}} \left(\frac{\varepsilon}{T_{\mathrm{h}k}}\right)^2 \exp\left(-\frac{\varepsilon}{T_{\mathrm{h}k}}\right), \tag{4}$$

where n_h is the total hot electron density. The respective fractions of hot electron populations with different

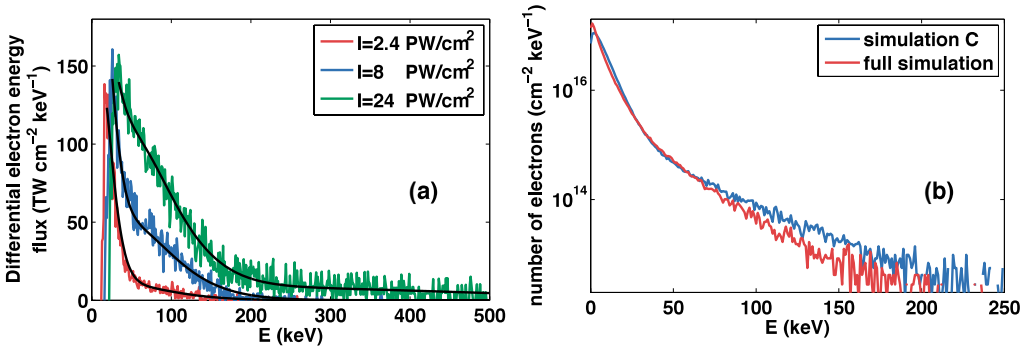

Figure 7. (*a*) Temporally averaged energy flux of electrons differential in electron kinetic energy $\mathrm{d}q_x/\mathrm{d}\varepsilon$ as given by (3) recorded in a dense plasma close to the target rear side and obtained at the end of simulation for laser intensities 2.4 (red), 8 (blue) and 24 PW cm^{-2} (green). Only the positive flux pointing into the target is plotted, the negative part pointing toward the vacuum is located at a low energy. The energy flux can be fitted by the flux corresponding to several Maxwellian distributions; the temperatures and number of electrons are given in table 1. (*b*) Electron energy distribution obtained after the cavitation starts in the simulation with the laser intensity 8 PW cm^{-2} for the full or reduced density profile (simulation C) as specified in table 2.

temperatures $T_{\mathrm{h}k}$ are denoted by f_k and they are normalized such that $\sum_{k=1}^{n} f_k = 1$. The temperatures T_{hk} and the respective fractions f_k are given in table 1. It can be seen in the figure that the approximation (4) is correct only above a minimum energy. Below this energy, the flux drops to zero and becomes negative due to the return current. This minimum energy is denoted by $\varepsilon_{\min}$ and it is also given in table 1. Thus, even if f_1 is much higher than f_2, the number of hot electrons with temperature T_1 can be lower than the number of electrons with temperature T_2. This is because $T_1 < \varepsilon_{\min}$. For example, the number of electrons n_k with the temperature $T_{\mathrm{h}k}$ is calculated as follows:

$$n_k = \sqrt{\frac{2}{\pi}} n_{\mathrm{h}} f_k \int_{\varepsilon_{\min}}^{\infty} \sqrt{\frac{\varepsilon}{T_{\mathrm{h}k}^3}} \exp\left(-\frac{\varepsilon}{T_{\mathrm{h}k}}\right) \mathrm{d}\varepsilon. \qquad (5)$$

The number of hot electrons with temperature T_2 normalized to the total number of hot electrons is also given in table 1.

As can be seen in table 1, we can identify three groups of hot electrons. One group of hot electrons has the temperature of 7–8 keV and it dominates at low laser intensities of a few PW cm^{-2}. It will be demonstrated later that this group of electrons is likely due to acceleration in the cavities and their angular distribution is isotropic. The second group, which has already been described in previous publications, has a temperature of about 28 keV and it is responsible for the transport of most of the absorbed laser pulse energy deeper into the target at intensities $\gtrsim$5 PW cm^{-2}. Strictly speaking, electrons with temperature 28 keV carry 33%, 76% and 72% of the electron energy flux into the target for the laser intensities 2.4 PW cm^{-2}, 8 PW cm^{-2} and 24 PW cm^{-2}, respectively. These are the electrons accelerated in the backward SRS generated plasma waves and they form a directional beam into the target. Finally, at high laser intensities of a few tens of PW cm^{-2} there appears a third group of hot electrons with a relatively high temperature above 100 keV. These high-energy electrons originate from the forward SRS, which develops close to the quarter critical density at the end of the simulation when the density profile starts to flatten there, as in the inset of figure 3(*a*).

The phase velocity of the plasma wave excited in the forward SRS, v_{pf} is close to 60% of the velocity of light in this region, thus the energy of resonantly accelerated electrons $m_{\mathrm{e}} v_{\mathrm{pf}}^2/2$ corresponds well to the temperature T_3 found in the simulation as in [26]. As the density profile modification is likely due to the 1D geometry of the simulation and indeed was not observed in 2D simulations [14, 15], the generation of this highest energy electron component needs to be further verified. It was not reported in the experiment [6]. Concerning the other hot Maxwellian components, the temperature of hot electrons thus stays almost constant, while the number of hot electrons with the moderate temperature of about 28 keV increases almost linearly with the absorbed laser pulse energy. This value of the hot electron temperature agrees well with the experiment.

The fraction of laser energy converted into hot electrons measured in the recent experiments on the Omega facility [27] with planar targets at a laser intensity of 5 PW cm^{-2} was 5%, much smaller than that calculated in our simulations. However, this conversion efficiency was evaluated from the K-α emission in the molybdenum layer placed behind the 50 μm plastic target. It is possible that the plastic layer stopped the hot electrons with the energies below 50 keV before they reach the molybdenum layer. This issue needs to be clarified in future.

3.4. Laser absorption mechanisms

The absorption takes place, in particular, in front and in the vicinity of the quarter critical density in the case of higher laser pulse intensities studied here. This is confirmed by the electromagnetic field energy density plotted in figure 2(*b*). Namely, the field energy density is quite low behind the quarter critical density. Therefore, we restricted our attention to the lower density part of the target, when studying the most important absorption mechanisms. Three simulations with a reduced density profile and the laser intensity 8 PW cm^{-2} were performed to separate the contributions of SRS and cavitation to the overall absorption balance sheet, and to define the location, where the absorption takes place. The reduced simulations have the same initial parameters, only the volume

Table 1. Temperatures of hot electrons T_{hk} used in (4) to fit the distributions plotted in figure 7(*a*) and the fraction of hot electrons with the given temperature f_k. The energy, above which the approximation (4) is valid, is denoted by ε_{min}. The relative number of hot electrons with temperature T_2 is denoted by n_2 and it is normalized to the total number of hot electrons n_h.

Laser intensity	T_1	f_1	T_2	f_2	T_3	f_3	ε_{min}	n_2/n_h
2.4 PW cm^{-2}	7 keV	0.9690	28 keV	0.031			19 keV	0.137
8 PW cm^{-2}	7 keV	0.8915	28 keV	0.1085			26 keV	0.552
24 PW cm^{-2}	8 keV	0.7109	28 keV	0.2793	135 keV	0.0099	34 keV	0.795

Table 2. Density range of reduced simulations with the laser intensity 8 PW cm^{-2} used to describe the absorption process. The last column shows the regions with the absolute SRS and cavities that are contained in the simulation.

Simulation	Minimum density	Maximum density	Contains
A	0.01 n_c	0.30 n_c	1/4th and 1/16th of n_c
B	0.01 n_c	0.16 n_c	1/16th of n_c
C	0.16 n_c	0.30 n_c	1/4th of n_c

of the plasma is restricted to the low-density part, as shown in table 2.

The first reduced simulation A includes the density profile from 0.01 to 0.3 n_c, that is, it includes both resonance regions at the quarter and 1/16th of the critical density. The absorption coefficient of 69% obtained in this simulation is in good agreement with the full-scale simulation discussed above. This confirms that the absorption takes place in front of or around the quarter critical density.

The second simulation B includes only the region from 0.01 to 0.16 n_c with the cavities around 1/16th of the critical density. This simulation is realized from simulation A by removing the denser part (0.16–0.3 n_c) of the profile after the cavities have already developed (i.e. about 25 ps after the beginning of the simulation). This simulation thus includes the cavities, but does not include the part of the density profile producing the scattered light at the frequency $0.5\omega_0$, which can resonantly interact with these cavities. The reflectivity and transmissivity obtained in this simulation are plotted in figure 8(*a*). The overall reflectivity is below 10% in this case, while the transmissivity is above 80%. The initial short transient evolution observed in figure 8(*a*) corresponds to the light already reflected or transmitted at the end of simulation A before the denser part of the density profile has been removed. From the reflectivity and transmissivity obtained in this run we can deduce that the low-density part of the profile including the cavities at 1/16th of the critical density does not significantly influence the intensity of laser light propagating into the target. The laser light with frequency ω_0 does not strongly interact with density modulations (cavities) induced in this very low density plasma.

The spectra of reflected and transmitted light in simulation B are plotted in figure 8(*b*). The spectrum of reflected light shows only a broad peak with central frequency about $0.6\omega_0$ corresponding to the convective SRS and the peak around ω_0 corresponding to SBS. The spectrum of the transmitted light includes only the laser light at the fundamental frequency ω_0 and a weak noise. Consequently, we can say that the light propagating into the target is not significantly influenced by the low-density part of the profile, and the light trapping inside the cavities at 1/16th of the critical density is efficient only for the backscattered light with the frequency $\sim 0.5\ \omega_0$.

The third reduced simulation C includes only the region around the quarter critical density (0.16–0.3 n_c). The energy distribution of electrons is compared with the distribution taken from the full-scale simulation in figure 7(*b*). The high-energy tail of the distribution has a similar slope indicating the same hot electron temperature. This simulation confirms that the restriction of the density profile does not change the laser energy absorption process significantly. The transmissivity is 12% and the reflectivity is 38% in this case, as can be seen in figure 9(*a*). The transient phase of interaction is very short in this simulation because SBS does not have enough space for a significant amplification. The absorption during the quasi-steady stage is 50%. The behavior of the reflectivity changes at the end of this simulation because of the evolution of the density profile.

The spectrum of the reflected light is concentrated around $0.5\omega_0$ in the reduced simulation C. According to the Manley–Rowe relation, the absorbed energy in this case should be equal to the one backscattered by SRS. Therefore, SRS is responsible for 38% of the laser pulse absorption at the quarter critical density. The remaining 12% of the laser pulse energy absorbed in this simulation can be attributed to trapping of electromagnetic waves in the cavities. Similar processes take place at 1/16th of the critical density with the light reflected from the quarter critical density, which has the resonant frequency $0.5\omega_0$. Thus, 50% of the reflected light is absorbed, 38% due to SRS and 12% due to cavitation. Taking into account both absorption regions, 1/4th and 1/16th of the critical density, we arrive at the overall absorption of about 69%. This is in very good agreement with the absorption observed in the full-scale simulations.

The electron plasma waves generated by SRS propagate and accelerate electrons only along the density gradient in the 1D case considered here. On the other hand, the strong electromagnetic fields trapped inside the cavities may accelerate electrons also obliquely. This acceleration of electrons is of a stochastic nature because each electron can be accelerated in multiple cavities, it can enter the cavity already with a non-negligible initial velocity and in any phase of the field trapped inside. The electrostatic fields induced inside the cavities also influence the electron trajectory, its energy gain and the final ejection angle. Thus, the acceleration of electrons inside cavities is more isotropic. This approximately isotropic acceleration of electrons in cavities has already been observed in 2D PIC simulations [14, 15].

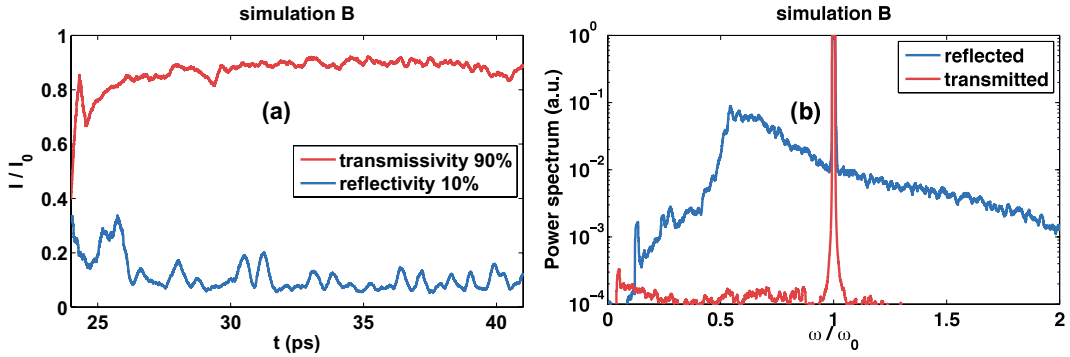

Figure 8. (*a*) Temporal evolution of the reflectivity (blue) and transmissivity (red) in the reduced simulation B. The values given in the legend are the temporal averages. (*b*) Spectrum of reflected (blue) and transmitted (red) light in simulation B.

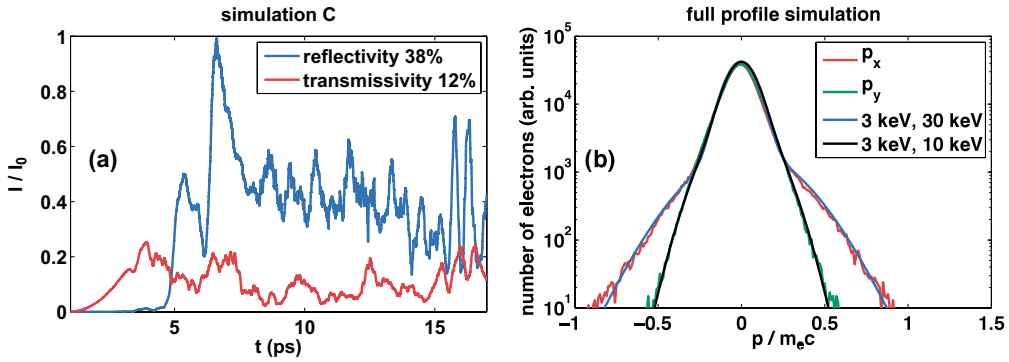

Figure 9. (*a*) Temporal evolution of the reflectivity (blue) and transmissivity (red) in the reduced simulation C. The values given in the legend are the temporal averages. (*b*) Momentum distributions of electrons in the simulation with the full density profile and the intensity 8 PW cm^{-2} and their fits with two-temperature Maxwellian distributions with the cold electron temperature 3 keV (black) and the hot electron temperatures of 10 (black) and 30 keV (blue). The momentum p_x (red) is the direction parallel and p_y (green) perpendicular to the density gradient.

The asymmetry in the momentum distribution can be used to find the temperatures of hot electrons due to SRS and due to cavitation. The momentum distributions of electrons in the directions parallel and perpendicular to the density profile are shown in figure 9(*b*). These distributions can be fitted by two-temperature Maxwellian distributions and the corresponding temperatures of cold and hot electrons can be found. The high-energy tail of the distribution in the parallel direction can be fitted by the Maxwellian distribution with the temperature of about 30 keV. This temperature can be attributed to SRS-accelerated electrons. The high-energy tail of the momentum distribution in the perpendicular direction can be fitted by the Maxwellian distribution with a temperature of about 10 keV.

These temperature estimates are in good agreement with the temperatures deduced from the Maxwellian fit to the differential electron energy flux given in table 1. Namely, the temperature of the SRS-accelerated electrons (30 keV) is very close to T_2 and the temperature of electrons accelerated in the cavities (10 keV) is close to T_1. Moreover, we can find the relative intensity of the electron beam produced by SRS from the absorption. We recall that 38% of the laser pulse energy is absorbed due to SRS at the quarter critical density and the total absorption is 50%. It results that 76% of the absorbed energy is transported into the target by hot electrons with a temperature of about 30 keV. This is consistent with the value calculated from the Maxwellian fit to the differential electron energy flux, which is also 76% for the simulation with the same laser intensity (i.e. 8 PW cm^{-2}). On the other hand, if we attribute the electrons with temperature T_1 to the cavitation and the electrons with temperature T_2 to the absolute SRS, we observe that at lower intensities (2.4 PW cm^{-2}) cavitation dominates, while at higher intensities (8 and 24 PW cm^{-2}) SRS becomes more important.

4. Conclusions

We studied the physical processes in laser–plasma interaction in the parameter domain relevant for shock ignition and for the laser intensities in the range 2.4–24 PW cm^{-2} at the wavelength 351 nm. We have used fully kinetic PIC simulations with Coulomb collisions in one-dimensional geometry. The simulations are carried out in a large plasma volume with the initial profiles of density, temperature and velocity obtained from hydrodynamic simulations for the experimental conditions [6]. The laser–plasma interaction proceeds through two subsequent stages.

During the first, transient stage the average reflectivity is as high as 80% and the reflected light comes out from the target in a train of short (about 0.3 ps) intense pulses. The reflectivity is dominated by SBS and the transient stage lasts for a few tens of picoseconds. The absolute SRS develops in the meantime in the resonance points near the quarter and

1/16th of the critical density, and it forms a self-organized resonator. The growth of the local field amplitude due to these absolute SRS instabilities is saturated due to creation of density cavities when the field pressure equals the kinetic pressure of the plasma. The cavities are created in both resonance regions, they interrupt an efficient convective amplification of SBS, and the SBS reflectivity drops. This transient stage was not seen in the experiment because the pulse rise time was longer than its duration.

The reflectivity is about 30% during the second quasi-steady stage of interaction. The absorption coefficient during this stage is almost independent of the laser intensity in the studied laser intensity range. The laser pulse absorption is dominated by collective processes and it takes place, in particular, at the quarter critical density (about 50%) and at 1/16th of the critical density (about 19%). The larger part of absorption (52% of laser pulse energy) is due to SRS. This process produces hot electrons with a temperature of about 30 keV accelerated along the density profile. The rest of the absorption (17% of laser pulse energy) is due to trapping of light in cavities and the subsequent conversion of this light into kinetic energy of hot electrons. Hot electrons accelerated in cavities have a temperature of about 10 keV and an approximately isotropic momentum distribution in the interaction plane. The temperature of hot electrons produced during the laser–target interaction does not significantly depend on the laser intensity in the studied domain, while the number of hot electrons scales linearly with the absorbed laser pulse energy. These simulation results are in rather good agreement with the experimental observations [6], showing similar constant absorption fraction and the hot electron temperature. Albeit, two-dimensional simulations are needed for evaluation of the role of effects such as filamentation, laser beam speckled structure, TPD and cavitation.

At high laser intensities, the convective SRS also becomes important. During the quasi-steady stage of interaction, it exists in the inflationary regime in the domain between the quarter and 1/16th of the critical density and thus it does not directly interact with the absolute SRS and cavitation. During the transient stage of interaction, the convective backward SRS can be induced by intense SBS pulses. The light coming from this process is observed in our simulations and this rescattering of SBS pulses results in their saturation at high laser intensities. It may also partially contribute to laser absorption, as the rescattered light propagates into the target. It has a broader spectrum, so it is less influenced by the parametric processes.

In summary, our results indicate rather favorable conditions for shock ignition. The absorption is relatively high and it goes, in particular, into hot electrons, which are however 'not-too-hot' to preheat the fuel inside the hot spot. Recent studies indicate that these hot electrons can contribute to or even drive themselves strong ignition shock wave [13]. If this would be confirmed in experiments and in two-dimensional simulations, it may completely change the point of view on the role of parametric instabilities and weaken our endeavor to suppress them as much as possible. In such a case, one may think, for example, of using longer wavelength lasers, higher intensities or removing the beam smoothing techniques.

Acknowledgments

The authors are grateful to X Ribeyre for the stimulating discussions and for providing data from hydrodynamic simulations. This work was performed within the framework of the HiPER project EC FP7 #211737. It is partly supported by the EURATOM within the 'Keep-in-Touch' activities and the Aquitaine Regional Council. The support by the Czech Science Foundation, project P205/11/P660 is acknowledged. The numerical simulations were conducted on the HPC resources of CINES under the allocation 2013-056129 made by GENCI and on the Scientific Cloud CERIT.

References

[1] Shcherbakov V A 1983 *Sov. J. Plasma Phys.* **9** 240
[2] Betti R *et al* 2007 *Phys. Rev. Lett.* **98** 155001
[3] Ribeyre X *et al* 2009 *Plasma Phys. Control. Fusion* **51** 015013
[4] McCrory R L *et al* 2008 *Phys. Plasmas* **15** 055503
[5] Theobald W *et al* 2009 *Plasma Phys. Control. Fusion* **51** 124052
[6] Theobald W *et al* 2012 *Phys. Plasmas* **19** 102706
[7] Klimo O *et al* 2010 *Plasma Phys. Control. Fusion* **52** 055013
[8] Klimo O *et al* 2011 *Phys. Plasmas* **18** 082709
[9] Emery M H *et al* 1982 *Phys. Rev. Lett.* **48** 253
Kato Y *et al* 1984 *Phys. Rev. Lett.* **53** 1057
[10] Skupsky S *et al* 1989 *J. Appl. Phys.* **66** 3456
[11] Berger R L *et al* 1999 *Phys. Plasmas* **6** 1043
[12] Betti R *et al* 2008 *J. Phys. Conf. Ser.* **112** 022024
[13] Guskov S Yu *et al* 2012 *Phys. Rev. Lett.* **109** 255004
[14] Riconda C *et al* 2011 *Phys. Plasmas* **18** 092701
[15] Weber S *et al* 2012 *Phys. Rev.* E **85** 016403
[16] Vu H X *et al* 2010 *Phys. Plasmas* **17** 072701
[17] Yan R *et al* 2012 *Phys. Rev. Lett.* **108** 175002
[18] Vu H X *et al* 2012 *Phys. Plasmas* **19** 102703
Vu H X *et al* 2012 *Phys. Plasmas* **19** 102708
[19] Yin L *et al* 2012 *Phys. Plasmas* **19** 056304
[20] Yin L *et al* 2012 *Phys. Rev. Lett.* **108** 245004
[21] Regan S P *et al* 2010 *Phys. Plasmas* **17** 020703
[22] Maire P H *et al* 2007 *SIAM J. Sci. Comput.* **29** 1781
[23] Takizuka T and Abe H 1977 *J. Comput. Phys.* **25** 205
[24] Neumayer P *et al* 2008 *Phys. Rev. Lett.* **100** 105001
[25] Vu H *et al* 2001 *Phys. Rev. Lett.* **86** 4306
Vu H *et al* 2002 *Phys. Plasmas* **9** 1745
[26] Estabrook K *et al* 1980 *Phys. Rev. Lett.* **45** 1399
[27] Hohenberger M *et al* 2012 *54th Annual Meeting of the APS Division of Plasma Physics* (*Bulletin of the American Physical Society, Providence, RI, Oct. 29–Nov. 2*) vol 57 BAPS.2012.DPP.GO5.1

Fast saturation of the two-plasmon-decay instability for shock-ignition conditions

S. Weber,[1] C. Riconda,[1,*] O. Klimo,[2] A. Héron,[3] and V. T. Tikhonchuk[4]
[1]*LULI, Université Pierre et Marie Curie, Ecole Polytechnique, CNRS, CEA, F-75252 Paris, France*
[2]*FNSPE, Czech Technical University in Prague, CR-11519 Prague, Czech Republic*
[3]*CPHT, Ecole Polytechnique, CNRS, F-91128 Palaiseau, France*
[4]*CELIA, Université Bordeaux, CNRS, CEA, F-33405 Talence, France*
(Received 17 March 2011; revised manuscript received 19 December 2011; published 20 January 2012)

Two-plasmon-decay (TPD) instability is investigated for conditions relevant for the shock-ignition (SI) scheme of inertial confinement fusion. Two-dimensional particle-in-cell simulations show that in a hot, large-scale plasma, TPD develops in concomitance with stimulated Raman scattering (SRS). It is active only during the first picosecond of interaction, and then it is rapidly saturated due to plasma cavitation. TPD-excited plasma waves extend to small wavelengths, above the standard Landau cutoff. The hot electron spectrum created by SRS and TPD is relatively soft, limited to energies below 100 keV, which should not be a danger for the fuel core preheat in the SI scenario.

DOI: 10.1103/PhysRevE.85.016403 PACS number(s): 52.35.Mw, 52.38.Bv, 52.57.−z, 52.65.Rr

I. INTRODUCTION

Parametric instabilities in laser-plasma interaction are collective processes operating in the under-critical density domain. They generate energetic electrons and compete with collisional absorption, which is particularly important for inertial confinement fusion. Two-plasmon-decay (TPD) [1–3] instability was identified as a source of hot electrons, which could induce preheat of the fuel and inhibit strong compression and hot-spot creation [4]. In this process an incoming laser photon (ω_o) decomposes into two plasmons (ω_{p1}, ω_{p2}) in the vicinity of the quarter-critical density $n = \frac{1}{4}\, n_c$, with $n_c \approx 10^{21}/\lambda_o^2$ cm^{-3} and λ_o the laser wavelength in microns. The plasmon frequency is determined by the dispersion relation for electron plasma waves, $\omega_p \approx \omega_{pe}(1 + 3k_p^2\lambda_D^2)^{1/2}$, and by the matching conditions $\omega_o = \omega_{p1} + \omega_{p2}$ and $\mathbf{k}_o = \mathbf{k}_{p1} + \mathbf{k}_{p2}$. Here, $\omega_{pe} = (4\pi ne^2/m_e)^{1/2}$ is the electron plasma frequency, k_p the plasma wave vector, k_o the laser wave number at the quarter critical density, $\lambda_D = v_e/\omega_{pe}$ the Debye length, and $v_e = (T_e/m_e)^{1/2}$ the thermal velocity.

The shock-ignition (SI) approach to inertial confinement fusion [5,6] consists in direct drive fuel compression to undercritical conditions and boosting of the central hot spot to ignition with a secondary strong shock. This scheme appears to be more robust and efficient than the conventional direct and indirect drive scenarios. It is one of the candidates for the European inertial fusion energy project HiPER [7]. As the ignition shock is launched by an intense laser spike, parametric instabilities are of primary concern for the SI scheme. The expected intensities of the laser spike amount to values of 10^{15-16} W/cm^2 at a wavelength of 350 nm, which are far above the threshold for the TPD instability. In particular, this instability has been considered a potential danger for the SI scheme, being a source of hot electrons: indeed, there is experimental evidence of hot electrons produced by TPD [8]. However, it is not possible to infer a direct conclusion on the destructive role of TPD for SI from the above-mentioned results, as the experimental conditions [8] did not match the conditions for SI [5,6].

In fact, TPD develops in the same spatial plasma domain as stimulated Raman scattering (SRS) and stimulated Brillouin scattering (SBS), and their mutual interaction for SI conditions corresponding to large scales and high temperatures is not known. SRS-SBS competition was investigated with one-dimensional (1D) particle-in-cell (PIC) simulations [9]. Plasma cavitation under the ponderomotive pressure of SRS-excited plasma waves was identified as the prime mechanism of strong suppression of SBS and efficient laser energy absorption. However, the 1D geometry excludes the possibility of TPD. The present work presents the first two-dimensional (2D) PIC simulations for SI relevant conditions. It is shown that the TPD instability develops in concurrence with SRS around $n_c/4$, and it is rapidly saturated due to plasma transverse modulations and cavitation close to the quarter critical density. This effect strongly limits hot electron production.

II. SIMULATION SETUP

The 2D full PIC simulations were performed with the code EMI2D [10]. The laser and plasma parameters are motivated by hydrosimulations of SI [6] and 1D PIC simulations [9]. In the following we present the results of a representative run for SI [11]. The simulated plasma region extends 160 μm in the laser propagation direction (x) and 103 μm in the transverse direction (y). The exponential plasma profile has a scale length of $L_n = (d \ln n/dx)^{-1} \approx 60$ μm, extending from 0.04 n_c up to 0.4 n_c, with 60 particles per cell for the highest density value. The plasma is surrounded by vacuum in the parallel direction with open boundary conditions. In the transverse direction boundary conditions are periodic. Limiting the maximum plasma density to 0.4 n_c allows one to diagnose the frequency-upshifted transmitted light. Corresponding 1D PIC simulations of the complete plasma profile up to n_c have shown that very little of the incident laser penetrates beyond the quarter critical density for up to ~100 ps. Electron and ion temperatures are $T_e = 5$ keV and $T_i = 1$ keV, respectively. The ion-to-electron mass ratio is $m_i/m_e = 3672$ and the ion charge is $Z = 1$. The laser beam of p polarization has a

*caterina.riconda@upmc.fr

normal incidence, with an intensity $I_o = 5 \times 10^{16}$ W/cm^2 and a wavelength $\lambda_o = 0.35$ μm. It is emphasized that simulations at a lower intensity [11] confirm the scenario described in the following regarding TPD and SRS around $n_c/4$. The transverse profile of the laser intensity corresponds to a full speckle with a full width at half-maximum FWHM ≈ 24 μm. The intensity was ramped up over a short time, of the order of 50 ω_o^{-1} or 9.4 fs. Simulation times extend up to 2.5×10^4 ω_o^{-1}, which corresponds to 4.7 ps. The characteristic electron-ion collision time at the density $\frac{1}{4}$ n_c is of the order of ~7 ps. For the present conditions collisions play no role in the saturation process. The plasma scale length is about a factor of 3 smaller, and the intensity about a factor of 2–3 higher, than anticipated for the SI scenario. This choice of parameters allows us to reduce the CPU time requirements while retaining the dominant physical processes. This was confirmed by extensive full-scale 1D PIC simulations. The threshold for TPD in an inhomogeneous profile is given as $I_{16}^{\mathrm{TPD}} \simeq 0.5\, T_e L_n^{-1} \lambda_o^{-1}$ [12,13], where T_e is in units of kilo–electron volts, I_{16} is the laser intensity (in units of 10^{16} W/cm^2), and L_n and λ_o are in units of microns. This value is exceeded in our simulations by a factor of 5 or more. Moreover, for the chosen parameters the threshold of the SRS instability near the quarter critical density [4,14] $I_{16}^{\mathrm{SRS}} \simeq 12\, L_n^{-4/3} \lambda_o^{-2/3}$ is of the same order as TPD. Both instabilities develop very rapidly and their competition is determined by their respective growth rates and localization.

III. TEMPORAL EVOLUTION

A standard signature of TPD is considered to be the generation of $\frac{3}{2}$ ω_o light [15,16]. However, the SRS-created plasma wave can also contribute to this process. A more distinctive signature that provides an unambiguous interpretation follows from the k_y spectra of the electrostatic field in the transverse direction [1,2] as displayed in Fig. 1. At an early time [$t = 3000\ \omega_o^{-1}$; Fig. 1(a)], two distinct branches can be seen: a parabolic one extending from the quarter critical density down the density gradient describes the TPD activity, and an almost-straight line of very small k_y values stems from the SRS under a small opening angle. Approaching $\frac{1}{4}$ n_c, the transverse component k_y of the plasma wave becomes very small, such that TPD and SRS are basically indistinguishable. The parametric excitation of plasma waves near the quarter critical density is manifested in the transmitted light by a spectral component at $\frac{3}{2}$ ω_o (Fig. 2; see below concerning the spatial structuring of the signal). Although the threshold values in the vicinity of $\frac{1}{4}$ n_c for SRS and TPD are very close, the simulation shows that the SRS branch in the k_y spectrum is established before TPD at $t = 2600\ \omega_o^{-1}$ when the laser pulse just arrives at $\frac{1}{4}$ n_c. The growth rate for both instabilities [12–14] is roughly given as $\gamma \simeq 35\, I_{16}^{1/2}$ ps^{-1}, which corresponds to a characteristic growth time of $\gamma^{-1} \approx$ 13 fs. During this time the laser light propagates a distance of ~60 k_o^{-1}, which is much smaller than the zone of coexistence of TPD and SRS shown in Fig. 1. Consequently, SRS is excited before TPD.

At intermediate times [3400 and 4000 ω_o^{-1}; Figs. 1(b) and 1(c)], the k_y spectrum starts to change structure: electron

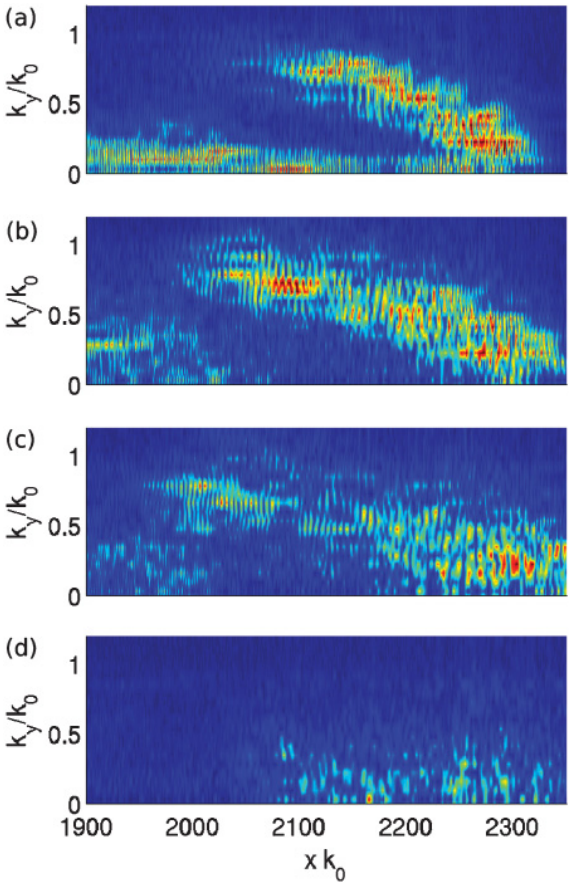

FIG. 1. (Color online) Perpendicular spectrum of the electrostatic field $E_x(k_y)$ as a function of the parallel coordinate at time (a) 3000 ω_o^{-1}, (b) 3400 ω_o^{-1}, (c) 4000 ω_o^{-1}, and (d) 9400 ω_o^{-1}. The quarter critical density is located at $x \approx 2300\ k_o^{-1}$. Spectra were evaluated over a representative spatial region of width ~100 k_o^{-1} in the center of the speckle.

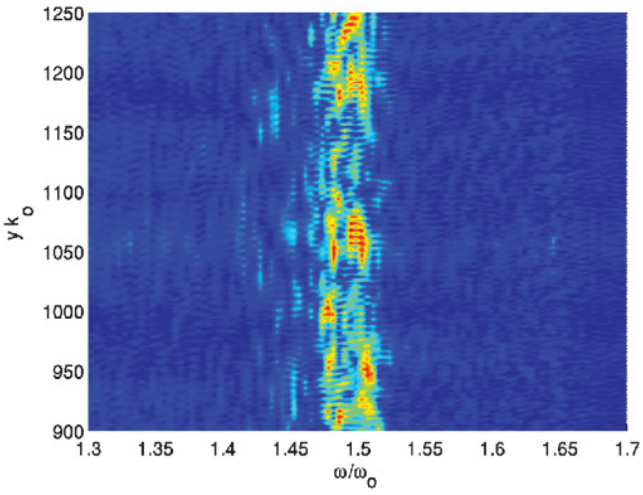

FIG. 2. (Color online) Frequency spectrum of the transmitted light as a function of the transverse location (central part of the speckle only). The spectrum is integrated in time from 4607 ω_o^{-1} to 6073 ω_o^{-1}, accounting for the distance of ~1300 k_o^{-1} the light has to travel to reach the boundary of the simulation box where the diagnostic is located.

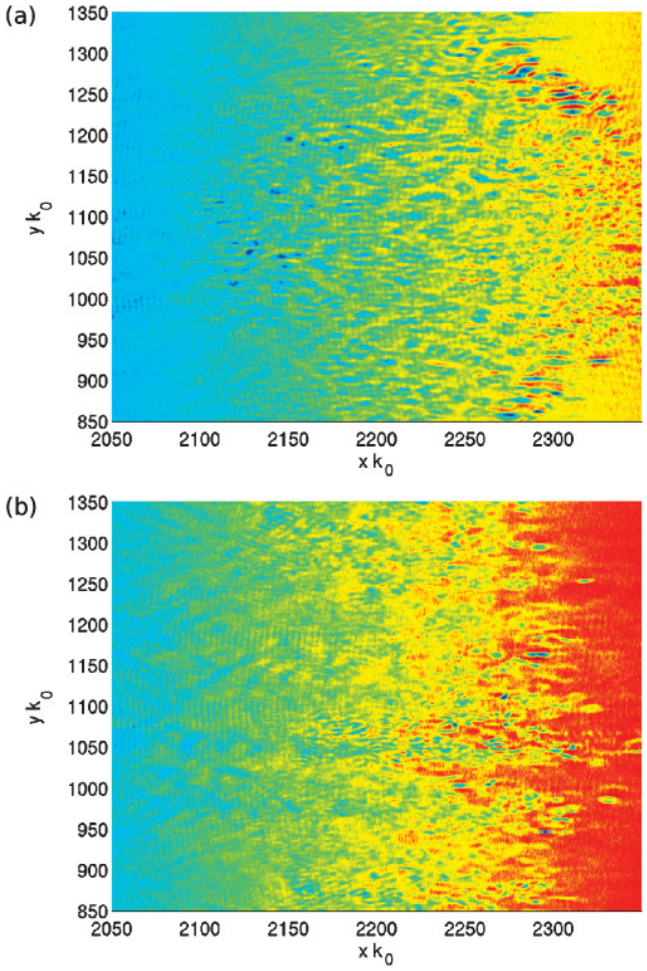

FIG. 3. (Color online) Continuity of cavitation. Ion density after TPD activity ceases at 9400 ω_o^{-1} (a) and at the end of PIC simulation at $t = 2.5 \times 10^4\ \omega_o^{-1}$ (b) in the vicinity of $\frac{1}{4}\ n_c$.

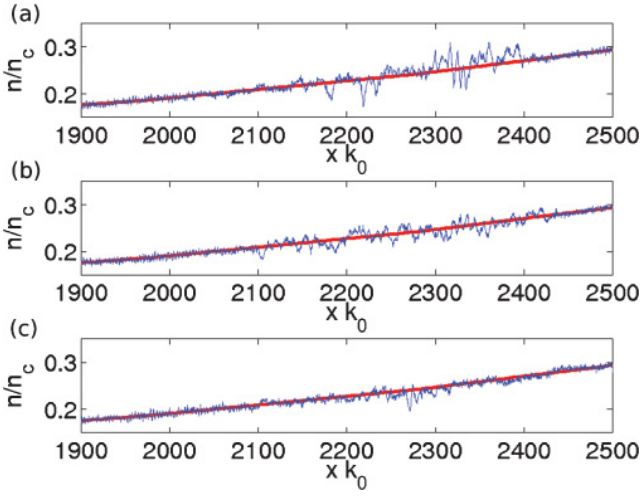

FIG. 4. (Color online) Lineouts of the ion density at different times: (a) 7000 ω_o^{-1}, (b) 9000 ω_o^{-1}, and (c) 25 000 ω_o^{-1}. The fluctuating ion density [thinner (blue) curve] is superimposed on the initial smooth profile [thick (red) curve] for comparison.

plasma waves related to the SRS signal between 2000 and 2200 k_o^{-1} are quenched first, followed at a later time by electron plasma waves due to TPD in the same spatial zone. Beating of the TPD decay products provides a quasineutral density modulation at $k \sim 2k_y$ of the plasmon, which serves as seeding for the subsequent cavitation: modulations and cavities start to appear around 3400 ω_o^{-1}, immediately affecting the backscattered SRS at small opening angles. By the time the cavities are fully established at 4500 ω_o^{-1}, SRS has been quenched completely and TPD is affected as well. At a later time [9400 ω_o^{-1}; Fig. 1(d)], the k_y spectrum broadens and completely loses its structure. At this time we observe the ion density cavities to be evenly distributed as shown in Fig. 3.

Modulations at $k \sim 2k_y$ of TPD decay products have been observed before [17,18]. However, only the large spatial scales in both dimensions as well as the long time scale of the present simulation allow us to show the outcome of the initial modulation. As a result, the originally observed profile steepening reveals itself in fact to be a layer of cavities statistically distributed in two dimensions, as visible in Figs. 3(a) and 3(b). To emphasize this result, we reproduce in Fig. 4 the lineout of the density profile taken at the center of the speckle ($y = 1100\ k_o^{-1}$) at three times: 7000, 9000, and 25 000 ω_o^{-1}. The lineouts are superimposed for comparison to the original density profile. Figure 3 is representative of the density inside the speckle, although the exact value of the fluctuations' amplitude, as well as their location, varies with time and transverse coordinate.

Cavity formation is evident from very early on in the simulations ($\sim$4500ω_o^{-1}) until much later, as shown in Figs. 3(a) and 3(b). Following the time evolution of the cavities, we see no evidence of its being affected by the recirculation of hot electrons from the back of the plasma, which starts around $\sim$7000 ω_o^{-1} for our plasma conditions.

A similar behavior was found for cavitation driven by SBS [19], leading to quenching of the instability. It is conjectured that the SRS instability is important, as it provides the electromagnetic contribution for the soliton formation that drives cavitation [11]. This is in contrast to Ref. [20], where only electrostatic 1D solitons were considered in relation to TPD. This conclusion agrees with 1D simulations, where the creation of the cavities is attributed to SRS only [9]. Figure 5 shows that the SRS component in the reflected signal ceases at a time around $10^4\ \omega_o^{-1}$, coming back near the end of the simulation. The SBS instability, which has a much lower growth rate and develops in the low-density part of the plasma profile, appears as the SRS and TPD activity are fading. It is responsible for most of the reflectivity and has a bursty behavior as observed in previous studies [19]. SBS is not implicated in the saturation of SRS in the region close to $\frac{1}{4}\ n_c$. A lower intensity simulation [11] shows exactly the same cavity-induced saturation scenario while having SBS reflectivities which are much smaller and come up much later, therefore excluding the possibility that SBS-driven pump depletion plays any role.

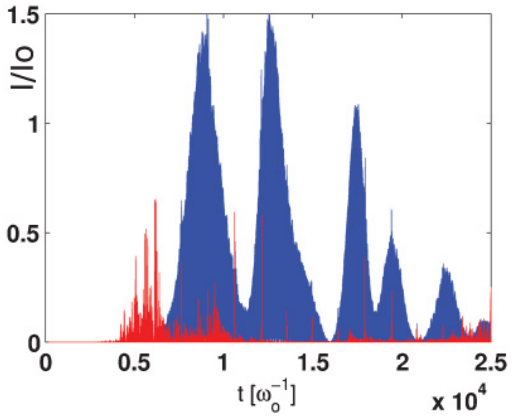

FIG. 5. (Color online) Frequency-resolved reflectivity for the backscattered intensity I/I_o at the center of the speckle [dark gray (blue), SBS-like 0.9–1.1 ω_o; light gray (red), SRS-like 0.0–0.9 ω_o]. From about 5000 ω_o^{-1} onward the laser light transmission is at a relatively steady level of 15%–20%.

IV. SPATIAL LOCALIZATION

The competition between SRS and TPD is corroborated by the phase-space structure as shown in Fig. 6. According to Ref. [13], the fastest-growing TPD modes correspond to the plasma wave vectors related by the following condition: $k_{1y} = -k_{2y} = k_y$, $k_{1,2x} = \frac{1}{2}k_o \pm \Delta k$, and $\Delta k^2 = \frac{1}{4}k_o^2 + k_y^2$. The spatial localization of the decay defines the value of k_y. The smallest $k_y \approx 0$ is realized very close to $\frac{1}{4}\,n_c$. It corresponds to the position $x \approx 2300\ k_o^{-1}$ in Fig. 1. There $\Delta k \approx 0.5\ k_o$, and consequently, the moduli of the plasma wave vectors are $k_1 \approx k_o$ and $k_2 \approx 0$. As the resonance condition moves toward lower densities, k_y increases. This is represented by the broad band in Fig. 1 that ends near $x \approx 2000$–$2100\ k_o^{-1}$, where $k_y \approx k_o$ and $\Delta k \approx 1.1\ k_o$. Consequently, the plasma wave numbers are $k_1 \approx 1.9\ k_o$ and $k_2 \approx 1.6\ k_o$. Large values of k are considered to be forbidden because the plasma waves are strongly damped. For the present plasma parameters the cutoff of the TPD band corresponds to the largest k_1, giving $k_1\lambda_D \approx 0.42$. This is quite a large number. It is commonly thought that Landau damping suppresses the instability for $k_p\lambda_D > 0.3$–0.35. The phase-space activity at time 3100 ω_o^{-1} [Figs. 6(a) and 6(b)] extends from 1500 to 2300 k_o^{-1} and it is mainly due to SRS, showing a very small opening angle around 2180 k_o^{-1} and electron acceleration essentially in the forward direction. For the later time, 4000 ω_o^{-1} [Figs. 6(b) and 6(d)], additional features are present, related to TPD, which swamp the SRS signature in the perpendicular phase space. High-amplitude plasmons created close to $\frac{1}{4}\,n_c$ accelerate electrons mainly in the forward direction at a small angle in a similar way as SRS: these forward-traveling plasmons have $k_p\lambda_D$ values of <0.22, which is below the strong linear damping limit. The corresponding backward-traveling plasmons have a very high phase velocity and interact with very few particles.

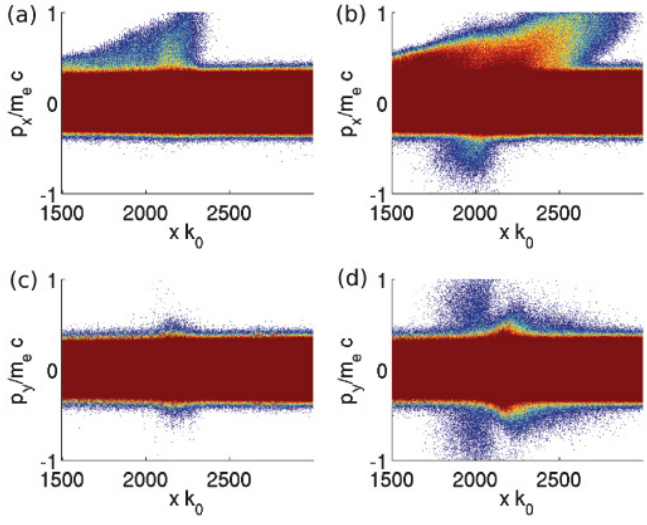

FIG. 6. (Color online) Blowup of the parallel $p_x - x$ (a, b) and perpendicular $p_y - x$ (c, d) electron phase space at times 3100 ω_o^{-1} (a, c) and 4000 ω_o^{-1} (b, d). Figures are color-saturated for low energies in order to enhance fine structures at a higher energy.

The lifetime of plasmons in this area and their efficiency in heating the electrons are limited by the appearance of the cavities. Electrons accelerated in the positive and negative direction around 2000 k_o^{-1} are related to the TPD plasmons' having a large opening angle. Plasmons propagating in the backward direction have a $k_p\lambda_D$ value limited to $\sim$0.26, enabling large electron acceleration. Plasmons propagating in the forward direction have larger $k_p\lambda_D$ values, up to $\sim$0.42, and give acceleration of a larger number of electrons, but for a shorter time, since they are damped faster (as observed in the simulations). The excitation of TPD well above the conventional Landau cutoff was reported by other authors [1,2], and this is in contrast to recent experimental data, which stipulate that TPD is strongest in the vicinity of the Landau cutoff [21].

V. CAVITIES

Figure 3 shows the ion density distribution some time after TPD has ceased [Fig. 3(a)] and close to the end of the simulations [Fig. 3(b)]. Cavities are clearly visible and create strong density perturbations, inhibiting any renewed TPD and SRS activity. A similar process of cavity formation has been reported before, induced by SBS instability [19]. Their formation is explained by the trapping of intense electromagnetic and electrostatic fields in the density depletions created by the ponderomotive force of the wave packets. Their size is of the order of 1–2 λ_o and the depth $\sim$30%–50%. Neither secondary Langmuir wave decay instability [16,22] nor modulational Langmuir instability [23] is observed in our simulations in the cavitation region, and therefore these processes do not participate in the saturation of TPD. The reasons are the hot plasma and the high laser intensity, which favor cavity formation before Langmuir wave decay instability has time to establish itself. The transmitted $\frac{3}{2}\ \omega_o$ light (Fig. 2) shows a structure in the transverse direction that can be related to the formation of filaments of size 5—6 λ_o. Inspection of the Poynting vector [11] shows that around time 5000 ω_o^{-1}, the laser speckle having an initial size of 100 λ_o experiences filamentation in the low-density part of plasma, $n < 0.2\ n_c$.

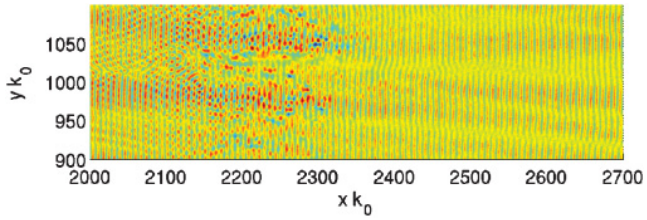

FIG. 7. (Color online) Transverse electromagnetic field E_y in the region of $n_c/4$ and beyond at the end of the simulation, showing the randomization of the phase front. Only the central part of the speckle is shown.

First, it breaks into four or five large filaments of size $\sim 30\,\lambda_o$, which is in agreement with the expected optimum value $k_y \simeq 0.022\,k_o$ for our parameters [24]. The laser light is further filamented as it traverses the cavitation region around $\frac{1}{4}\,n_c$. The size of the small laser speckles is determined by secondary scattering over the plasmons and the density cavities. These small speckles are stationary over the time window selected for integration ($\approx$1500 ω_o^{-1}) and show up in the transmitted light.

SBS is due to laser light scattering on ion acoustic waves. It grows much more slowly, with the characteristic time $\sim$2000–3000 ω_o^{-1} and it appears once SRS and TPD are saturated (Fig. 5). Moreover, the strongly cavitated region around the quarter critical density does not support the resonant interaction [19,25], and SBS is first excited in the low-density region, below $0.2\,n_c$. The presence of the strong density perturbations in a layer of width $\sim$200 k_o^{-1} below $\frac{1}{4}\,n_c$ thereby acts like a dynamic random phase plate [25], which destroys the coherence of the laser beam and enables plasma-induced smoothing [26]. This scrambling effect is clearly shown in Fig. 7. Later in time, around $2.4 \times 10^4\,\omega_o^{-1}$, the cavities gradually disappear and the laser starts to penetrate beyond $\frac{1}{4}\,n_c$. Transmission increases, and in due time SBS will develop in the region above $\frac{1}{4}\,n_c$.

The long-time behavior of density cavities is difficult to predict because of the limited computation time. Two possible scenarios can be expected: either the cavities close on a characteristic ion-acoustic time scale and the SRS and TPD repeat themselves periodically or some quasistationary state will be established as seen in 1D simulations [9]. The latter scenario of plasma-induced smoothing was observed for the case of SBS [26].

VI. HOT ELECTRONS

The temporal evolution of the plasma density also affects the electron distribution function shown in Fig. 8. It is symmetric in the perpendicular (p_y) momentum, while in the parallel (p_x) momentum a hot tail forms first at 3100 ω_o^{-1} in the positive direction. This indicates the dominant role of SRS for electron acceleration in the initial stage of evolution. The slower time evolution of the perpendicular distribution function is attributed to heating by TPD and cavitation. In agreement with the phase space shown in Fig. 6, TPD is not the dominant process in producing hot electrons. Also, TPD and SRS are both quickly saturated. The hot tail can be attributed

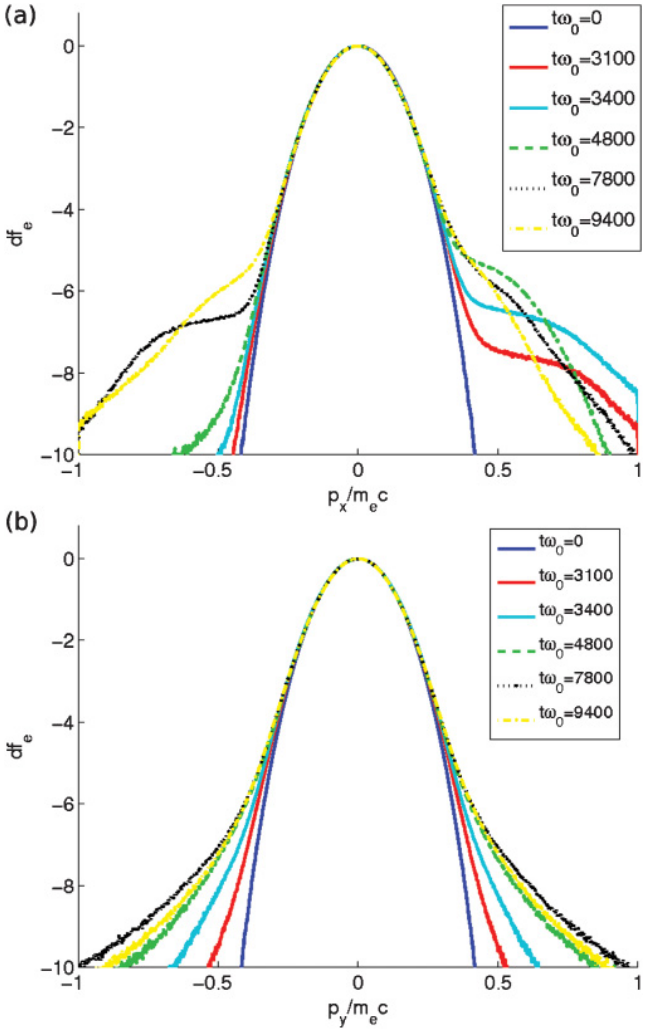

FIG. 8. (Color online) Parallel (a) and perpendicular (b) electron distribution function for various times. Particles start to recirculate from $\sim$7000 ω_o^{-1} onward due to the electrostatic field at the rear plasma-vacuum interface. The electron distribution was integrated in the parallel direction from $x = 2000$ to 2350 k_o^{-1} (covering the density range from 0.2 to 0.25 n_c) and over all transverse space.

a temperature of about 30–50 keV, which is in agreement with 1D simulations [9].

VII. CONCLUSION

By using large-scale 2D PIC simulations it is shown that TPD and SRS instabilities are both rapidly saturated by plasma cavitation in the vicinity of the quarter critical density. It is expected that for realistic SI conditions the density scale length close to $\frac{1}{4}\,n_c$ will be $\sim$3 times larger than in the present simulations. This will result in a decrease in the SRS threshold compared to the TPD one and, consequently, will reinforce the dominant role of SRS over TPD for SI conditions. SRS-driven hot electrons propagate essentially in the forward direction and have energies below a hundred kilo–electron volts. According to hydrodynamic simulations, such hot electrons do not present a danger for fuel preheat, as they will be stopped in the compressed imploding shell.

Moreover, they can play a positive role in energy transport to the compressed shell by increasing the ablation pressure as demonstrated by kinetic simulations in Ref. [27]. It is a noteworthy outcome of these simulations that, for the time scales considered, the absorption of the incoming laser takes place at or below the quarter critical density. This is contrary to hydrodynamic simulations which assume that absorption is predominantly by inverse Bremsstrahlung at the critical density [6].

ACKNOWLEDGMENTS

The authors thank D. Pesme for helpful discussions. This work was partially supported by EURATOM within the "Keep-in-Touch" activities, Aquitaine Region Council, and it is performed within the framework of the HiPER project (EC FP7 Project No. 211737). Use of the computing center CCRT of the CEA and support of O.K. by the Czech Science Foundation, Project No. P205/11/P660, are acknowledged.

[1] R. Yan, A. Maximov, C. Ren, and F. Tsung, Phys. Rev. Lett. **103**, 175002 (2009).
[2] R. Yan, A. Maximov, and C. Ren, Phys. Plasmas **17**, 052701 (2010).
[3] H. Vu, D. DuBois, D. Russell, and J. Myatt, Phys. Plasmas **17**, 072701 (2010).
[4] W. Kruer, *The Phsics of Laser Plasma Interactions* (Addison Wesley, New York, 1988).
[5] R. Betti, C. Zhou, K. Anderson, L. Perkins, and A. Solodov, Phys. Rev. Lett. **98**, 155001 (2007).
[6] X. Ribeyre, G. Schurtz, M. Lafon, S. Galera, and S. Weber, Plasma Phys. Control. Fusion **51**, 015013 (2009).
[7] High Power Laser Energy Research facility; http://www.hiper-laser.org.
[8] C. Regan, N. Meezan, L. Suter, D. Strozzi, W. Kruer, D. Meeker, S. Glenzer, W. Seka, C. Stoeckle, V. Glebov, T. Sangster, D. Meyerhofer, R. McCrory, E. Williams, O. Jones, D. Callahan, M. Rosen, O. Landen, C. Sorce, and B. MacGowan, Phys. Plasmas **17**, 020703 (2010).
[9] O. Klimo, S. Weber, V. Tikhonchuk, and J. Limpouch, Plasma Phys. Control. Fusion **52**, 055013 (2010).
[10] Code developed by A. Héron and J.-C. Adam, CPHT, Ecole Polytechnique.
[11] C. Riconda, S. Weber, V. Tikhonchuk, and A. Heron, Phys. Plasmas **18**, 092701 (2011).
[12] C. Liu and M. Rosenbluth, Phys. Fluids **19**, 967 (1976).
[13] A. Simon, R. Short, E. Williams, and T. Dewandre, Phys. Fluids **26**, 3107 (1983).
[14] C. Menyuk, N. El-Siragy, and W. Manheimer, Phys. Fluids **28**, 3409 (1985).
[15] P. Young, B. Lasinski, W. Kruer, E. Williams, K. Estabrook, E. Campbell, R. Drake, and H. Baldis, Phys. Rev. Lett. **61**, 2766 (1988).
[16] D. Russell and D. DuBois, Phys. Rev. Lett. **86**, 428 (2001).
[17] A. Langdon, B. Lasinski, and W. Kruer, Phys. Rev. Lett. **43**, 133 (1979).
[18] A. Langdon and B. Lasinski, Phys. Fluids **26**, 582 (1982).
[19] S. Weber, C. Riconda, and V. Tikhonchuk, Phys. Rev. Lett. **94**, 055005 (2005).
[20] H. Chen and C. Liu, Phys. Rev. Lett. **39**, 881 (1977).
[21] W. Seka, D. Edgell, J. Myatt, A. Maximov, R. Short, V. Goncharov, and H. Baldis, Phys. Plasmas **16**, 052701 (2009).
[22] C. Labaune, H. Baldis, B. Bauer, V. Tikhonchuk, and G. Laval, Phys. Plasmas **5**, 234 (1998).
[23] H. Rose and L. Yin, Phys. Plasmas **15**, 042311 (2008).
[24] B. Cohen, L. Divol, A. Langdon, and E. Williams, Phys. Plasmas **12**, 052703 (2005).
[25] C. Riconda, S. Weber, V. Tikhonchuk, J.-C. Adam, and A. Heron, Phys. Plasmas **13**, 083103 (2006).
[26] M. Grech, G. Riazuelo, D. Pesme, S. Weber, and V. Tikhonchuk, Phys. Rev. Lett. **102**, 155001 (2009).
[27] A. Bell and M. Tzoufras, Plasma Phys. Control. Fusion **53**, 045010 (2011).

IOP Publishing

Plasma Physics and Controlled Fusion

Plasma Phys. Control. Fusion **56** (2014) 055010 (7pp)

doi:10.1088/0741-3335/56/5/055010

Two-dimensional simulations of laser–plasma interaction and hot electron generation in the context of shock-ignition research

O Klimo[1], J Psikal[1], V T Tikhonchuk[2] and S Weber[3]

[1] Czech Technical University in Prague, Faculty of Nuclear Sciences and Physical Engineering, Brehova 7, 11519 Prague, Czech Republic

[2] Univ. Bordeaux-CEA-CNRS, Centre Lasers Intenses et Applications, UMR 5107, 33405 Talence Cedex, France

[3] ELI-Beamlines project, Institute of Physics, ASCR v.v.i., Na Slovance 2, 18221 Prague, Czech Republic

E-mail: ondrej.klimo@fjfi.cvut.cz

Received 10 December 2013, revised 20 February 2014
Accepted for publication 26 February 2014
Published 25 April 2014

Abstract

Laser–plasma interaction and hot electron generation play a crucial role in the context of inertial confinement fusion and in particular in the shock-ignition concept. Here we present a fully kinetic large-scale two-dimensional simulation studying laser–plasma interaction and hot electron generation in a relatively long and hot coronal plasma. The simulation shows saturation of the reflectivity of an intense spike pulse and absorption taking place close to a quarter critical density in particular, due to cavitation and stimulated Raman scattering. The signatures of steady two-plasmon decay are observed, but the hot electron number produced by this instability is low in comparison with the other two processes. The spectral and angular distribution of the back-scattered light is presented and the energy and angular characteristics of hot electrons due to individual absorption processes are studied.

Keywords: laser plasma interaction, stimulated Raman scattering, hot electrons, particle-in-cell simulation

S Online supplementary data available from stacks.iop.org/PPCF/56/055010/mmedia

(Some figures may appear in colour only in the online journal)

1. Introduction

The ignition of a precompressed fusion pellet can be achieved by using a strong shock wave [1, 2]. This concept of inertial confinement fusion (ICF) is called shock ignition (SI). The shock wave has to raise the pressure in the target hot spot to the order of 0.5 Tbar (for the standard hot spot radius of 20–30 μm). About 200–300 TW of laser power have to be absorbed to create sufficient pressure in the ablation layer to launch the strong shock wave. The nonlinear collective processes play an important role in the laser–plasma interaction physics in this context. These processes are currently being investigated in experiments in several laboratories [3–9].

Among the nonlinear collective processes, stimulated Brillouin and Raman scattering (SBS and SRS, respectively), filamentation instability (FI) and two-plasmon decay (TPD) are widely studied. These processes are considered as detrimental for ignition for two reasons. The first reason is that they may scatter or reflect a significant part of laser pulse energy, thus reducing laser absorption. Usually, SBS is considered to be the most dangerous in this respect, as it has a high gain and has been identified as a source of significant reflectivity

in many ICF-relevant experiments. The second reason for avoiding nonlinear processes is the production of hot electrons due to electron plasma waves excited by these instabilities. Hot electrons may penetrate into the dense shell and deposit their energy there, thus inhibiting compression. It has been demonstrated that electrons with energy below about 100 keV may be stopped in the dense shell surrounding the hot spot in the late phase of compression, when the intense spike of the laser pulse reaches the target [10]. These 'not-too-hot' electrons may partially contribute to driving the shock wave, as demonstrated in [11]. The electrons produced by TPD have a higher temperature than electrons produced by SRS (with the exception of the forward SRS, which is less likely to play a role) due to the smaller wave number and thus higher phase velocity of associated waves. As a result, in the case of SI it is desirable to suppress SBS and TPD in particular.

The competition between backward SRS and SBS has been studied in the one-dimensional geometry in our previous works [12–14] for plasmas with the density scale length at a quarter critical density 150 and 300 μm, initial electron temperatures of about 2 and 5 keV and the laser pulse intensity in the range of 1–24 PW cm^{-2}. In these simulations, it has been found that the reflectivity (initially dominated by SBS) stabilizes after a transient stage around the value of 35% and SBS is suppressed by density cavities, which develop at around a quarter and 1/16 of critical density. The absorbed laser pulse energy goes in particular into hot electrons with a temperature of about 30 keV, but the absorption into hot electrons seems to be overestimated in one-dimensional simulations in comparison with recent experiments [9]. Fully kinetic particle-in-cell (PIC) simulations aiming to study the competition of nonlinear processes in two-dimensional geometry have been performed for a reduced plasma volume in [16, 17]. They have shown that TPD is excited before SRS and the existence of cavities at around a quarter of critical density in two-dimensional geometry has been confirmed. The formation of cavities was associated with the beating of TPD electron plasma waves as this process is excited faster than SRS. The two-dimensional simulations have also demonstrated the generation of 'not-too-hot' electrons, but the boundary conditions (reflecting at the rear side and periodic at the lateral sides) did not allow to follow the interaction on a long time scale and estimate the hot electron temperature and absorption because of hot electron recirculation.

The two-dimensional simulation presented in this paper is performed for similar parameters like in [16, 17], but it overcomes the problem of hot electron recirculation by using a special boundary condition absorbing the hot electron flux. This allows us to follow the interaction for a longer time and distinguish hot electron sources. The overall reflectivity of the target for the set of laser and plasma parameters specified below in section 2 is about 36%. This value is similar to that reported in one-dimensional simulations [12–14], but it should not be generalized to other SI configurations. The cavitation at one quarter critical density is also observed and the cavities are identified to be responsible for significant absorption into hot electrons with a temperature of about 13 keV. Hot electrons produced by SRS with a temperature of 31 keV are less important, while TPD electrons with a temperature of 63 keV are negligible as this instability saturates due to cavitation on a rather low and steady level. The hot electrons due to SRS and cavitation propagating into the target have relatively wide angular distribution with full width at half maximum (FWHM) of about 72°. The TPD hot electrons propagate out of the target in a direction of about ±135° with respect to laser incidence. Clear density channels in the low-density plasma and light filaments are also observed, and the maximum light intensity reaches up to nine times the incident pulse intensity.

This paper is organized as follows. The initial conditions used in the simulation are presented in section 2 together with the simulation model. Section 3 contains the results of our simulation and their discussion. In section 3.1, we present the reflectivities and the properties of reflected and transmitted light, while in section 3.2, we discuss the properties of hot electrons and the flux of kinetic energy into the target. The most important results are summarized in section 4 together with our concluding remarks.

2. Simulation model and initial conditions

The simulation is performed using a massively parallel relativistic electromagnetic PIC code in the two-dimensional geometry. The code was developed from the one previously used in [12–14]. It uses smooth high order shapes for particles and current assignment using the zig-zag algorithm [18], which suppresses numerical heating and allows a reduction in the number of particles while keeping a low level of noise. The Maxwell's equations are solved using the standard finite-difference time-domain (FDTD) scheme on the Yee mesh [19], and the absorbing boundary conditions for fields are done similarly to [20]. The boundary conditions for particles are reflecting on the front side, and thermalizing to the initial temperature on the lateral sides. A special boundary condition to absorb the kinetic energy flux into the target due to hot electrons is used at the rear side similar to the one-dimensional simulations [12]. As demonstrated later in figure 4(*c*), the effect of this boundary condition is to keep the energy distribution of particles forming the return current Maxwellian with the initial temperature.

The collisions of plasma particles are not accounted for as the electron–ion collision frequency ν_{ei} (evaluated at one quarter critical density for the initial electron temperature of 5 keV) multiplied by the simulation time (assuming the laser wavelength $\lambda = 351$ nm) is about 1.5. The time between two collisions ($1/\nu_{ei}$) around a quarter critical density is thus much longer than the onset of kinetic processes described in this paper and thus collisions play no role in their saturation. The collisional absorption coefficient calculated for the initial conditions of our simulation is about 0.01 (assuming $\lambda = 351$ nm) and the contribution of collisions to absorption can be neglected. The fact that the simulation is collisionless allows us to rescale the results to another laser wavelength. This may be useful for comparison with other SI experiments performed at laser wavelengths other than 351 nm [3, 6].

The simulation cell size is the same in both directions $\Delta x = \Delta y = 0.03\lambda$ and it is similar to the minimum Debye

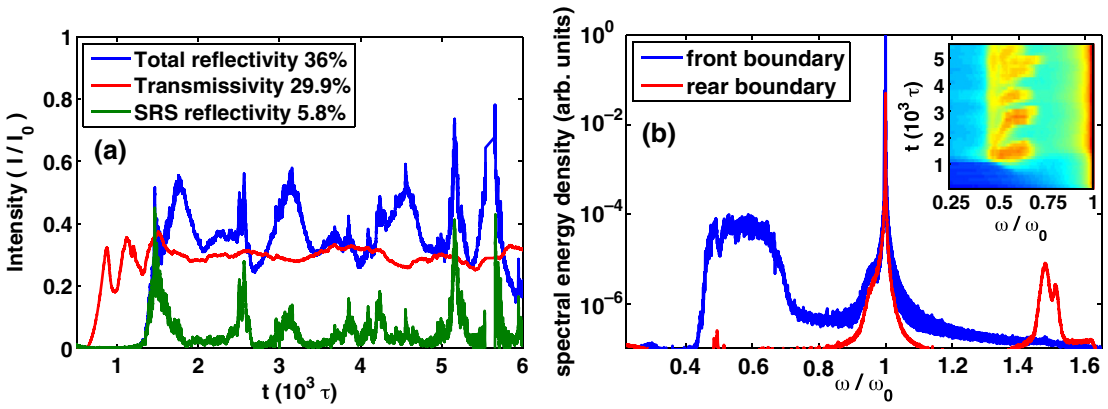

Figure 1. (*a*) Temporal evolution of the reflectivity and transmissivity in the simulation and the reflectivity in the SRS domain (0–0.9ω_0, where ω_0 is the laser pulse frequency). The numbers in the legend give the average values during the interaction. Time is measured in thousands of laser periods (τ). (*b*) Spectral energy density calculated from the magnetic field perpendicular to the interaction domain at the front and at the rear side of the simulation box. The inset shows the temporal evolution of the reflected light spectrum calculated at the front boundary.

length in the simulation box. The computational time step is about 0.02τ to fulfil the Courant–Friedrichs–Lewy condition, where τ is the laser period. The number of (equally weighted) particles per cell is such that each particle (electron or ion) represents 1% of critical density (e.g. 25 electrons per cell at one quarter critical density). The simulation domain contains in total 1.2×10^8 cells and 2.3×10^8 particles. About 2.5×10^5 time steps are performed and the computational time required is about 400 000 core CPU hours on the Intel XEON Harpertown CPUs of the JADE cluster of CINES. The simulation time (7 ps assuming $\lambda = 351$ nm) is short in comparison with the length of a real ignition laser pulse and it is currently limited by the computational resources. Nevertheless, the time is long enough to study the competition between different nonlinear processes at least in the initial stage of interaction.

The simulation box is about $600\lambda \times 228\lambda$. It contains quasi-neutral deuterium plasma with an exponential density profile and the scale length $L = 142\lambda$. Extensive preparatory one-dimensional simulations confirmed that while the density scale length is about three times smaller than in the previous one-dimensional simulations (and in a real SI scenario), the dominant physical processes are retained. The minimum plasma density is 1% and the maximum is 40% of critical density (n_c). The temperatures are constant throughout the target and they are 5 keV for electrons and 1 keV for ions. The target is initially at rest without any macroscopic hydrodynamic motion. The laser pulse is propagating along the y direction and its maximum dimensionless potential a_0 ($I\lambda^2 = a_0 \times 1.37 \times 10^{18}\,\mathrm{W}\mu\mathrm{m}^2\,\mathrm{cm}^{-2}$, where I is the laser pulse intensity) is $a_0 = 0.06$. This corresponds to maximum intensity $40\,\mathrm{PW\,cm}^{-2}$ for $\lambda = 351$ nm. Such intensity is higher than that used in current experiments and that expected for the spike pulse in the SI scheme. Nevertheless, it has been demonstrated in one-dimensional simulations [14] that the laser pulse absorption and hot electron distribution do not significantly change with the laser pulse intensity. The laser pulse has a 430τ long linear ramp at the beginning and then it stays at the maximum intensity for the rest of the simulation. The transverse laser intensity profile is Gaussian with FWHM 85λ. This spot size is larger than the speckle size in experiments with smoothed laser beams. It corresponds to the size of a tightly focused interaction beam in interaction experiments [6]. It also enables comparison with one-dimensional simulations while retaining the important two-dimensional processes like FI, TPD and side-scattering. The laser pulse is linearly polarized with the electric field component lying in the interaction plane.

3. Simulation results

3.1. Reflected and transmitted light

The electric and magnetic fields are recorded ten times per period at the front and the rear side of the simulation box (in front of absorbing boundary conditions). These fields are used to find the temporal evolution of reflectivity and transmissivity in the simulation. The Poynting flux component along the laser pulse propagation direction averaged over one laser period and over the transverse size of the simulation box is shown in figure 1(*a*).

The overall temporally averaged reflectivity is about 36%, but the instantaneous one shows intense spikes reaching up to 70%. Moreover, according to figure 2(*a*), the reflected light intensity can even be much higher locally. Comparing the overall reflectivity with the reflectivity due to SRS only (in the frequency range 0–0.9ω_0, where ω_0 is the laser pulse frequency), it can be seen that SRS is excited earlier than SBS, but SBS is amplified over a larger region and it dominates the interaction as in the initial transient phase of interaction in one-dimensional simulations [14]. The overall transmissivity of the particular target used in this simulation is stabilized at the level of 30%. It demonstrates how much light can propagate through the quarter critical density deeper into the target. The resulting laser absorption in the target is less than 34% if we do not take into account weak side-scattered radiation, which leaves the simulation box through lateral boundaries. In comparison with one-dimensional simulations [14], the reflectivity saturates at the same level but the absorption is significantly lower.

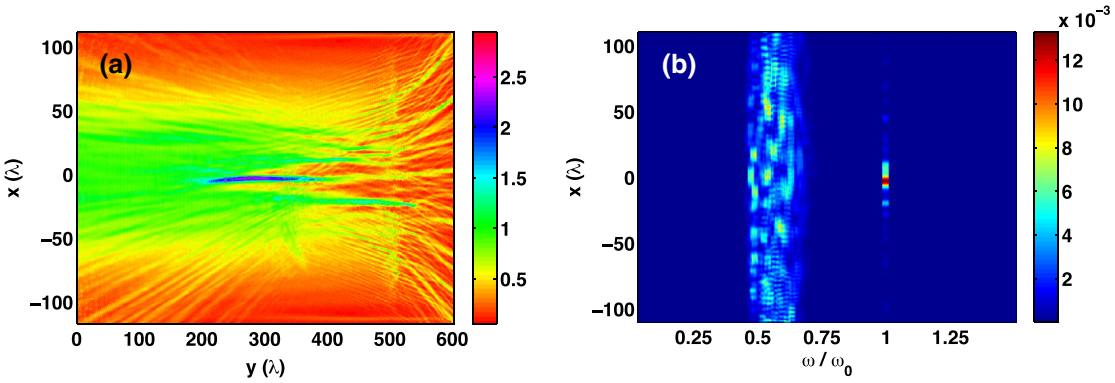

Figure 2. (*a*) Electromagnetic field amplitude in the simulation box at the time 5300τ. The laser pulse is incident from the left and quarter critical density is at $\sim 500\lambda$. The units are normalized to the maximum field of the incident laser pulse. (*b*) The spatially resolved power spectral density of the reflected light recorded at the front boundary and integrated over time 1000–5000τ. We assume plane waves to be able to distinguish between the incident and the scattered light. The color scale is linear and the units are arbitrary. The signal in the frequency range 0–$0.9\omega_0$ has been multiplied by 20 to fit in the same color scale as the signal close to ω_0.

Figure 1(*b*) demonstrates the spectrum of light calculated from the B_z field component at the front and the rear side of the target. The signal at the front side of the target combines both the incident and the back-scattered light. Besides the laser pulse itself and the SBS scattered light (both located in a narrow interval around ω_0), there is quite a broad peak due to SRS with a central frequency of $0.58\,\omega_0$. It comes from plasma with a density in the range of $1/10$ to a quarter of critical density and it is generated by both the absolute and the convective SRS. In the temporal evolution of the spectrum shown in the inset of figure 1(*b*), it is observed that SRS starts at one quarter critical density and propagates toward the lower density plasma, where it is quenched due to strong Landau damping. The spectrum of transmitted light shows only the transmitted laser light and the signal at $3/2\,\omega_0$, which is a signature of TPD. The signal at $3/2\,\omega_0$ is quite steady during the whole simulation with the exception of the initial phase of interaction (where it is higher). The relative importance of TPD in comparison with SRS is estimated below from the electron energy distribution.

The snapshot of the electromagnetic field amplitude normalized to the amplitude of the laser field itself is shown in figure 2(*a*). Here, a significant amount of light scattered by SBS can be seen in one of the filaments. The filamentation of the incident laser beam sets in at the simulation time of about 1400τ and it is clearly observed behind $y = 300\lambda$ corresponding to the density of about 8% of the critical density. The laser power in this region is already above the threshold for the relativistic self-focusing. The light pulse in figure 2(*a*) is about 200λ long, which is slightly shorter than the length of SBS scattered pulses in one-dimensional simulations [14]. This is perhaps due to the shorter density scale length and thus shorter region for the instability amplification. The width of the filament is about 7λ and the electromagnetic field intensity is about nine times higher than that of the incident pulse. This is a significant amplification and energy concentration of the incident laser pulse. It is almost two times higher than the maximum reflectivity in one-dimensional simulations because the intensity of the SBS scattered pulse is further enhanced by FI. The normalized vector potential of the scattered field in the filament is well below the relativistic potential ($a_0 \simeq 0.18 \ll 1$). However, for a higher laser intensity or longer wavelength, the scattered pulse may already accelerate electrons via $\boldsymbol{v} \times \boldsymbol{B}$ force.

Most of the light scattered by SBS propagates in a relatively narrow cone of about 4°. This can be estimated from figure 2(*b*), where the spatially resolved power spectrum density of the scattered light is shown at the front side. In this estimate we further assume the point source of scattered light located about 450λ from the front boundary, which is the point where most of the SBS scattered light originates. The narrowness of the cone of SBS scattered light justifies our approach of collecting the scattered light only at the front boundary of the simulation domain and neglecting scattering on the lateral boundaries. On the other hand, SRS scattering, which is responsible for a smaller part of the reflectivity, is not confined to a narrow cone. As we do not have the diagnostic for scattered light at lateral boundaries, we can only give the minimum value of the width of the angular distribution of SRS scattering. This is estimated in a similar way as for SBS (assuming the point source is located 450λ from the front boundary) and the minimum value is 27°. The temporal evolution of the electromagnetic field amplitude in the simulation box is shown in the online movie similarly to figure 2(*a*)(stacks.iop.org/PPCF/56/055010/mmedia). One can see there a very strong interaction at one quarter critical density in the beginning ($\approx 900\tau$), and later on strong pulses due the SBS scattering and FI. Weak pulses of back-scattered light propagating with a wide angular distribution before the times 1500, 2600, 3200 and 5700τ are observed and they correspond to the strong SRS reflectivity in figure 1(*a*).

The cone in which the transmitted light propagates is also relatively broad - about 30°, as can be estimated directly from figure 2(*a*). The intensity of the transmitted light shows a pattern of small filaments, which start in the region around one quarter of critical density. The pattern changes in time as can be seen in the online movie and thus the quarter critical density region works like a dynamic random phase plate as pointed out in [16].

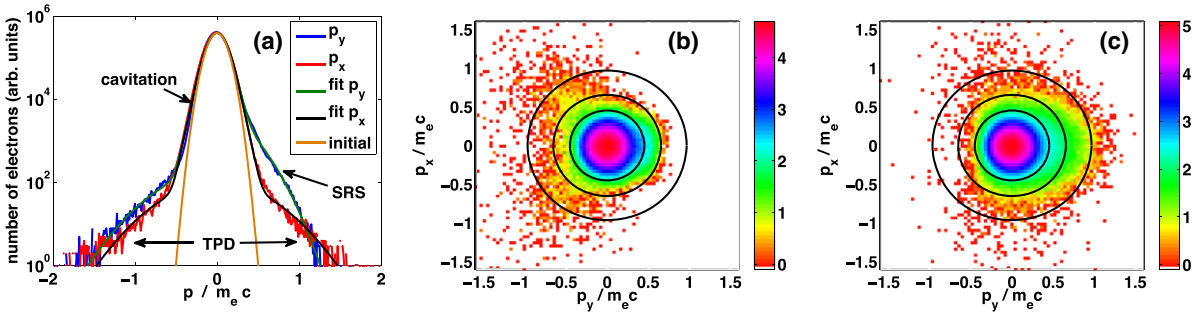

Figure 3. (a) The parallel, p_y, and the perpendicular, p_x, components of the momentum distribution of all electrons in the simulation domain ($t = 4000\tau$). The initial distribution is shown for comparison. The distributions are fitted with three Maxwellian functions with temperatures of 13, 31 and 63 keV. The groups of hot electrons with these energies are described in the text. Panels (b) and (c) show the $p_x \times p_y$ phase space density at the time 6000τ. They are recorded in the region $380\lambda < y < 470\lambda$ corresponding to the density range 11–23% n_c and the region $470\lambda < y$ corresponding to density above 23% n_c, respectively. The circles correspond to electron kinetic energies of 50, 100 and 200 keV. The color scale is logarithmic and the units are arbitrary, but the same in both panels.

3.2. Hot electrons

Our simulation shows approximately round density cavities near one quarter critical density similarly to [17]. Their typical size is of the order of one laser wavelength and they are first induced at about the time of 900τ by TPD and later by SRS similarly to [16]. Unlike in one-dimensional simulations, the cavities continuously disappear and other cavities are induced. Later in the simulation when the filamentation of the incident laser beam becomes significant at one quarter critical density, the cavities are merged within the light filaments. The cavities together with TPD and SRS are responsible for laser absorption and acceleration of hot electrons. The sources of hot electrons and their properties are analyzed below.

Figure 3(a) shows the momentum distribution of all electrons in the interaction domain at the time 4000τ in the direction parallel (p_y) and perpendicular (p_x) to the laser propagation direction. These distributions can be fitted by a sum of several Maxwellian distributions. The initial (isotropic) distribution of electrons is included for comparison. The departure from this distribution shows electron heating in three distinct regions. In the region $p < 0.5 m_e c$, the heating of the electron distribution is almost isotropic. The temperature of these electrons is relatively low and we ascribe them to the cavitation process. The second group of electrons in the region $0.5 m_e c < p_y < m_e c$ is accelerated along the laser propagation direction. They can thus be ascribed to electron plasma waves produced by SRS. The last group of hot electrons forms the hot tail, which is clearly observed in the perpendicular and the backward directions. These electrons are likely accelerated by electron plasma waves induced by TPD. The TPD plasmons have higher phase velocity and wider angular spread compared to SRS.

The distribution function of electrons in the time 6000τ is shown figures 3(b) and (c). In the lower density part, where the density is below 23% n_c, the dominant process producing hot electrons is TPD. These electrons have relatively high energies (>150 keV), and they propagate backward and obliquely with respect to the incident laser pulse. The acceleration of hot electrons in the higher density part close to one quarter critical density is dominated by SRS. The accelerated electrons mostly have an energy below 200 keV and propagate in a forward direction into the target.

The angular distribution of electrons is demonstrated in figure 4(a) for the high energy tail. The electrons accelerated by SRS form the forward propagating beam ($\theta = 0°$) and the half width at half maximum (HWHM) of the distribution decreases with increasing the minimum energy from 36° ($E > 50$ keV) to 23° ($E > 150$ keV). Otherwise, the angular distribution is almost isotropic for lower energy electrons and it is dominated by electrons accelerated in cavities. For energies above 150 keV, the electrons produced due to TPD dominate and form a second broad peak in the distribution around the angle $\theta = 135°$. This is consistent with the momentum distribution in figure 3(a), where the high energy tail has a similar temperature for the backward and the transverse part of the distribution, and the backward part has an amplitude about two times higher.

The energy distributions of all electrons inside the simulation box are shown in figure 4(b). The least square fit using a sum of four Maxwellian distributions to the distribution corresponds to the time 3000τ. The first Maxwellian function describes thermal electrons and the other three components represent hot electrons. The largest number of hot electrons has a temperature of about 13 keV, which is in good agreement with the temperature (10 keV) of hot electrons accelerated in cavities in one-dimensional simulations [14]. The second group of hot electrons has a temperature of about 31 keV. These electrons are accelerated by SRS and their temperature is again in good agreement with one-dimensional simulations [14]. The last group of electrons with a temperature of about 63 keV was not observed in one-dimensional simulations as they originate from TPD. The fractions of hot electrons in the figure indicate that cavitation may be a more important hot electron source than SRS. This is different from one-dimensional simulation results [14].

The instantaneous electron energy distribution cannot give a clear answer on the importance of different processes. The hot electrons originate from different locations and they propagate in various directions with the velocity given by their kinetic energy. For example, the electrons produced by cavitation most probably have a velocity of about 0.23 times

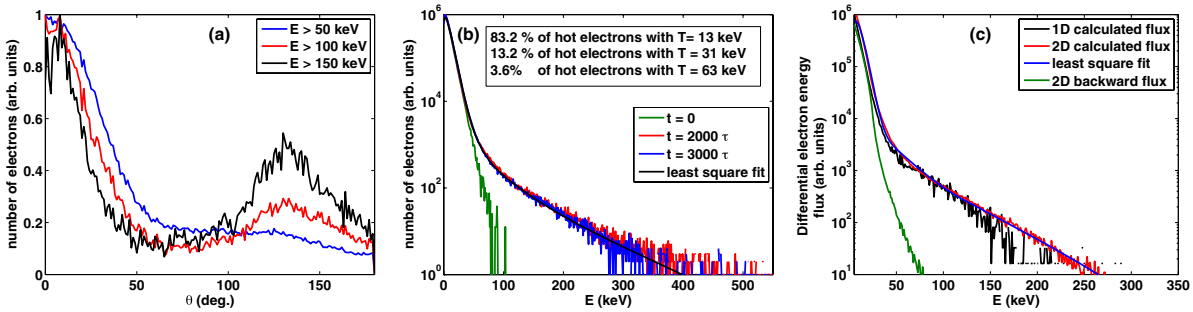

Figure 4. (*a*) The angular distribution in the simulation box at 6000τ for electrons with kinetic energy above 50 keV (blue), 100 keV (red) and 150 keV (black). The angle θ is measured with respect to the laser incidence direction. (*b*) The electron energy distribution in the whole simulation domain for the time 0, 2000 and 3000τ and the least square fit using a sum of four Maxwellian functions to the distribution at 3000τ. The temperatures of hot electrons and the respective fractions of these electrons are in the textbox included in the figure. (*c*) The differential electron energy flux into the target (in the positive y direction) recorded at the end of simulation and averaged over about 200τ. The flux is recorded in the dense part of the target at the spatial position of about 550λ. For comparison, we also include a least square fit to the flux assuming an electron distribution with several Maxwellian components as described in the text and a rescaled flux from the one-dimension simulation with laser pulse intensity 8×10^{15} W cm^{-2} published in [14]. The backward flux is included to demonstrate the effect of the absorbing boundary condition.

the velocity of light, while the electrons from TPD have a velocity more than two times higher. If they have to propagate the same distance before leaving the simulation box through the boundary, the instantaneous electron energy distribution would contain proportionally two times more hot electrons from cavitation than from TPD in comparison with the number of hot electrons produced by the source.

To get a better understanding of the flux of hot electrons into the target, we record the particles crossing the cells at $y = 545\lambda$, which is located well behind the quarter critical density and close to the rear boundary of the simulation box. This gives us the electron energy flux differential in electron kinetic energy. Provided that the source of hot electrons is quasi-stationary and the electrons do not leave the simulation box through another boundary, this diagnostic describes the source of hot electrons. Hot electrons do not accumulate inside the simulation box but some of them (namely those from TPD) leave the simulation box through the lateral boundaries. Therefore, this diagnostic characterizes the source of hot electrons due to SRS and partially due to cavitation but not due to TPD.

The differential electron energy flux pointing into the target recorded at the end of simulation is plotted in figure 4(*c*). It is compared with the same flux taken from the one-dimensional simulation [14] with a laser pulse intensity of 8 PW cm^{-2}. Although the laser pulse intensities are different, the energy distributions are quite similar in one- and two-dimensional simulations. An exception is the higher energy part, where the statistics are very poor in the one-dimensional simulation. The dominant source of hot electrons in the energy range 50–150 keV is SRS in both simulations, and the temperature of these electrons is also similar – given by the phase velocity of SRS-induced waves close to the quarter critical density. The rescaled flux of electrons is thus similar in this energy range.

The differential electron flux from the two-dimensional simulation has been fitted with a sum of several Maxwellian electron distributions. This fit gives temperatures similar to the ones shown in figure 4(*b*) (namely 12.8 and 31.4 keV) with the exception of the highest temperature component due to TPD. As already explained, the TPD electrons leave the simulation box mostly through the lateral boundaries, and they are not recorded in this diagnostic. Integrating the corresponding Maxwellian functions, we are able to find the energy transported into the target by hot electron components. The result is that 78.5% of hot electron energy is transported by electrons with the temperature 12.8 keV and 21.5% of energy is transported by hot electrons with the temperature 31.4 keV. To demonstrate the effect of the absorbing boundary condition, we also include the differential electron energy flux of the return current. This flux is similar to the initial one and does not contain any significant high energy tail due to hot electron recirculation.

4. Conclusions

We have studied the nonlinear processes in laser–plasma interaction in the parameter domain relevant to current experiments in the context of SI research using PIC simulations in two-dimensional geometry. The set of initial parameters corresponds to higher laser intensity and smaller plasma scale length due to the large computational demands of the simulation. For this set of initial parameters, the overall laser pulse reflectivity is about 36%, which is quite similar to our previous one-dimensional simulation results [14]. Nevertheless, it is necessary to study more realistic parameters and longer time scales to draw general quantitative conclusions about laser–plasma interaction relevant to the SI scenario. Our results instead demonstrate the qualitative behavior of laser–plasma interaction that may be expected when the interaction is dominated by parametric instabilities.

The reflectivity in our simulation is dominated by SBS, with the reflected light propagating backward in a narrow cone (4°) and formed by a train of spatially separated intense spikes. SRS emission also comes in a series of bunches, which are separated by a significant time delay, and the angular distribution of the scattered radiation is much wider (opening angle >27°). Laser pulse absorption is dominated by density

cavities, which develop at around one quarter critical density. Unlike in the case of one-dimensional simulations [13, 14], the cavities at 1/16 of critical density, which may further reduce the SBS reflectivity, are not observed here. It is likely that the simulation time is not sufficient or that the scattered light in two-dimensional simulations is not intense enough to induce this process.

The cavities play four important roles. They suppress SBS and TPD, they work as a dynamic random phase plate for the transmitted light and they are also a significant source of laser energy absorption. Hot electrons accelerated in the cavities have a temperature of about 13 keV and despite their almost isotropic angular distribution, they are the dominant group of hot electrons transporting the energy deeper into the target. The hot electrons due to SRS have a temperature of about 31 keV and originate in the region close to one quarter critical density. They propagate into the target in a cone with an opening angle FWHM of 72°. A significant SRS is also observed in a less dense plasma, where it is excited in the inflationary regime. The least important source of hot electrons is due to TPD. The temperature of electrons produced in this process is about 63 keV and these electrons propagate in the backward direction in a cone with a wide opening angle. The electron temperature is in a good agreement with one-dimensional simulations [12–14] and also with experiments demonstrating hot electrons due to SRS [9] and TPD [7, 15].

Acknowledgments

The support of OK by the Czech Science Foundation, project P205/11/P660 is acknowledged. This work was performed within the framework of the HiPER project EC FP7 #211737. It is also partly supported by EURATOM within the 'Keep-in-Touch' activities and the Aquitaine Regional Council. The PIC code has been partially modified by JP in the frame of the Czech Science Foundation project P205/12/P366. Support of SW by the ELI-Beamlines (CZ.1.05/1.1.00/483/02.0061) and OPVK (CZ.1.07/2.3.00/20.0279) projects is acknowledged. The numerical simulations were conducted on the HPC resources of CINES under the allocation 2013-056129 made by GENCI.

References

[1] Shcherbakov V A 1983 *Sov. J. Plasma Phys.* **9** 240
[2] Betti R *et al* 2007 *Phys. Rev. Lett.* **98** 155001
[3] Depierreux S *et al* 2009 *Phys. Rev. Lett.* **102** 195005
[4] Baton S D *et al* 2012 *Phys. Rev. Lett.* **108** 195002
[5] Antonelli L *et al* 2011 *Acta Tecnica* **56** T57
[6] Batani D *et al* 2011 *Plasma Phys. Control. Fusion* **53** 124041
[7] Hohenberger M *et al* 2014 *Phys. Plasmas* **21** 022702
[8] Theobald W *et al* 2009 *Plasma Phys. Control. Fusion* **51** 124052
[9] Theobald W *et al* 2012 *Phys. Plasmas* **19** 102706
[10] Betti R *et al* 2008 *J. Phys.: Conf. Ser.* **112** 022024
[11] Guskov S Yu *et al* 2012 *Phys. Rev. Lett.* **109** 255004
[12] Klimo O *et al* 2010 *Plasma Phys. Control. Fusion* **52** 055013
[13] Klimo O *et al* 2011 *Phys. Plasmas* **18** 082709
[14] Klimo O *et al* 2013 *Plasma Phys. Control. Fusion* **55** 095002
[15] Yaakobi B *et al* 2012 *Phys. Plasmas* **19** 012704
[16] Riconda C *et al* 2011 *Phys. Plasmas* **18** 092701
[17] Weber S *et al* 2012 *Phys. Rev.* E **85** 016403
[18] Umeda T *et al* 2003 *Comput. Phys. Commun.* **156** 73
[19] Yee K 1966 *IEEE Trans. Antennas Propag.* **14** 302
[20] Umeda T *et al* 2001 *Comput. Phys. Commun.* **137** 286

IOP Publishing | International Atomic Energy Agency Nuclear Fusion
Nucl. Fusion **54** (2014) 054009 (29pp) doi:10.1088/0029-5515/54/5/054009

Special Topic

Physics issues for shock ignition

D. Batani[1], S. Baton[2], A. Casner[3], S. Depierreux[3], M. Hohenberger[4], O. Klimo[5], M. Koenig[2], C. Labaune[2], X. Ribeyre[1], C. Rousseaux[3], G. Schurtz[1], W. Theobald[4] and V.T. Tikhonchuk[1]

[1] University Bordeaux-CNRS-CEA, Centre Lasers Intenses et Applications, UMR 5107, 33405 Talence, France
[2] LULI, CNRS-CEA-École Polytechnique-UPMC, 91128 Palaiseau, France
[3] CEA, DAM, DIF, F-91297 Arpajon, France
[4] Laboratory for Laser Energetics, University of Rochester, Rochester, NY 14623, USA
[5] Czech Technical University in Prague, FNSPE, 11519, Prague, Czech Republic

E-mail: tikhonchuk@celia.u-bordeaux1.fr

Received 9 January 2013
Accepted for publication 23 July 2013
Published 17 April 2014

Abstract
The paper presents theoretical analysis and experimental results concerning the major physical issues in the shock-ignition approach. These are the following: generation of a high amplitude shock in the imploding target, laser–plasma interaction physics under the conditions of high laser intensities needed for high amplitude shock excitation, symmetry and stability of the shock propagation, role of fast electrons in the symmetrization of the shock pressure and the fuel preheat. The theoretical models and numerical simulations are compared with the results of specially designed experiments on laser plasma interaction and shock excitation in plane and spherical geometries.

(Some figures may appear in colour only in the online journal)

1. Introduction

Shock ignition is a relatively new scenario in inertial confinement fusion. It was Shcherbakov [1] who proposed to ignite a spherical target compressed to a high density with a converging shock wave. In that scenario the initial temperature of the compressed fuel was less than 1 keV, and essentially the all energy needed for ignition was brought by the shock. However, no current laser is capable of generating the required shock pressures. A more realistic scenario of *shock-assisted* ignition has been proposed by Betti *et al* [2]. In this approach, a hot spot is created during the compression phase, but with a temperature below the ignition threshold (about 2–3 keV). The converging shock, amplified in a collision with the rebound shock near the inner shell surface, brings the remaining part of the ignition energy to the hot spot [3, 4]. This scheme called *shock ignition* has been applied to the target design in [5–8]. A more detailed review of the shock-ignition scheme can be found in [9].

The attractiveness of shock-ignition scheme relies first of all on a relatively simple and robust implosion scheme and on the ignition shock that can be realized on the existing laser installations. The implosion implies a rather conservative laser temporal profile with the intensities of the order of a few tenths of PW cm^{-2}, where the laser–plasma interactions proceed essentially in a classical collisional regime, which is well known theoretically and is confirmed in many experiments. The laser radiation is absorbed in a plasma corona, most efficiently near the critical density where the laser frequency is equal to the electron plasma frequency. The absorbed energy is transported to high densities with the heat flux of thermal electrons where it creates ablation, and the pressure of ablated vapours pushes the solid shell forwards. The shell acceleration and implosion velocity are significantly lower than in the common central ignition scheme. In combination with a longer laser pulse the shell implosion is expected to be more stable providing access to relatively large fuel areal densities at laser pulse energies of a few hundred kJ. However, a hot-spot temperature in the range of 2–3 keV is insufficient for self-ignition.

The ignition is achieved with a strong shock which is launched at the end of implosion phase by raising abruptly the laser intensity by one or two orders of magnitude. Laser–plasma interactions at this stage are strongly nonlinear and are not sufficiently investigated experimentally at the moment, but it is expected that the quality of absorption would be sufficient to create the required ablation pressure. The physics of laser spike absorption and ablation pressure enhancement are the major unknowns in the shock-ignition scenario. These issues are discussed in this paper.

The ablation pressure $p_{\rm abl}$ in the regime of classical collisional absorption is proportional to the laser intensity and inversely proportional to the laser wavelength in the power 2/3. In the quasi-stationary regime of laser–plasma interaction it is described by the following scaling law [10–12]:

$$p_{\rm abl} \approx 57\,(\eta_{\rm abs} I_{\rm L}/\lambda_{{\rm L}\mu{\rm m}})^{2/3}\,{\rm Mbar}, \qquad (1)$$

where $\eta_{\rm abs}$ is the laser absorption coefficient, $I_{\rm L}$ is the laser intensity in units of PW cm^{-2} and $\lambda_{\rm L}$ is the laser wavelength in micrometres. For $\lambda_{\rm L} = 0.35\,\mu$m, $I_{\rm L} = 0.3$ PW cm^{-2} and $\eta_{\rm abs} \simeq 0.7$, the ablation pressure at the implosion stage is about 40 Mbar leading to a relatively slow and hydrodynamically stable implosion at velocities of the order of 250 km s^{-1} (or 250 μm ns^{-1}). It creates a central hot spot with parameters somewhat below the ignition curve. Ignition is boosted with a specially designed *ignition shock* that is launched just before the stagnation. It should have a rather high amplitude of the order of 300 Mbar to bring to the hot spot an entropy necessary for ignition. According to (1), the corresponding laser intensity exceeds 5 PW cm^{-2} (assuming $\lambda_{\rm L} = 0.35\,\mu$m and $\eta_{\rm abs} \simeq 0.6$), and the laser power needed for the ignition shock launch is at the level of 200–400 TW, which is within the operational domain of the existing laser installations—National Ignition Facility (NIF) [13] and Laser MegaJoule (LMJ) [14]. Because of lower energy invested in fuel assembly compared with the classical hot-spot ignition scenario, shock ignition promises higher energy gain of the order of 100 or more, which is the crucial point for a future power plant.

The fact that the laser parameters requested for shock ignition are available today makes it much different from other alternative schemes discussed in this issue, which require for their demonstration construction of new installations with an operational power that exceeds many petawatts and with an energy of the order of hundred kilojoules. That is by itself a formidable engineering challenge. However, the plasma and laser parameters needed for the ignition shock are in a 'dangerous' zone where the nonlinear effects in laser–plasma interaction manifest themselves in enhanced scattering and generation of energetic electrons. The laser intensities above 1 PW cm^{-2} demonstrate increasing reflectivity levels [15] related to the stimulated Raman scattering (SRS) and Brillouin (SBS) scattering, laser beam filamentation (FI), two-plasmon instability (TPD) and other parametric processes. All these effects are not included in standard versions of hydrodynamic codes and thus may be easily underestimated or overlooked. Moreover, this range of laser intensities was not studied experimentally as all other ignition schemes considered previously avoided it. Since the experiments performed around 1980 and later demonstrated an increasing level of SRS that is correlated with production of high energy electrons [16], no other results in this parameter domain have been reported for many years. Only recently the correlations between the hot-electron production and SRS have been reported in the NIF experiments [17].

However, the specificities of the shock-ignition scheme may allow one to mitigate undesirable nonlinear effects and even to benefit from their presence. In difference from the standard implosion schemes, the shock-ignition target is accelerated for a longer time at lower intensities, so that, at the moment of intense ignition spike arrival the shell radius is reduced by a factor of two. It is already compressed and its areal density is increased by a factor of ten or twenty approaching a level of about 10 mg cm^{-2}. This value is comparable to the range of 100 keV electrons [18]. For this reason the electrons generated in the corona with lower energies may not present a danger for the fuel compression. They may be even beneficial when propagating to the solid shell and smoothing the inhomogeneities of the laser intensity in corona and increase the ablation pressure while depositing their energy at the outer shell surface. Moreover, at the moment of laser spike arrival the corona has a larger scale and a higher temperature than in conventional target designs. This changes considerably the conditions of excitation of parametric instabilities and their competition. As will be shown in this paper, the recent numerical simulations and some experiments are showing the laser absorption coefficient in the range of laser intensities interesting for shock ignition remains at the acceptable level of $\eta_{\rm abs} \simeq$ 60–70%. As laser intensity increases, more absorbed energy is transported by hot electrons, but their average energy remains at the acceptable level of 30–50 keV if the interaction is restricted to isolated beams and overlapping of the spike laser beams is avoided.

Importance of issues related to the laser–plasma interaction and fast electron transport in the context of shock ignition has been recognized a few years ago and were studied analytically, numerically and experimentally. Many problems are not yet resolved, but significant progress has been made that shows promising features of the shock-ignition approach. A brief summary of these studies is presented in this review. Three major questions are addressed first theoretically and then experimentally.

- What are the specificities of the laser–plasma interaction under the conditions of shock ignition? What is the role of collisional processes and parametric instabilities and how do they compete? What are the characteristics of hot electrons generated in the corona? What are their energy and number and how do they transport their energy into the dense plasma? Although the interaction physics is rather complicated, the responses to these questions are encouraging indicating good absorption and relatively low hot-electron energies seen in numerical simulations and in experiments.
- How is the ignition shock generated in the target and what laser intensities are needed to achieve the pressures required for ignition? How are the collisional and collective effects in the hot-electron transport competing and what would be the optimal condition for the shock launch? The possibility of the generation of shock pressures above 100 Mbar is not yet demonstrated experimentally, while the theory and simulations provide positive estimates if the hot-electron transport is taken into account.
- How does the electron transport affect the symmetry of the implosion? Because of a sufficiently large distance between the zone of electron generation and the ablation surface, hot electrons may smooth out small scale inhomogeneities thus improving the shell stability and suppressing the fuel mix with the hot-spot material at the internal surface of the shell. Moreover, it might be that the hot-electron generation need not be very symmetric. Thus

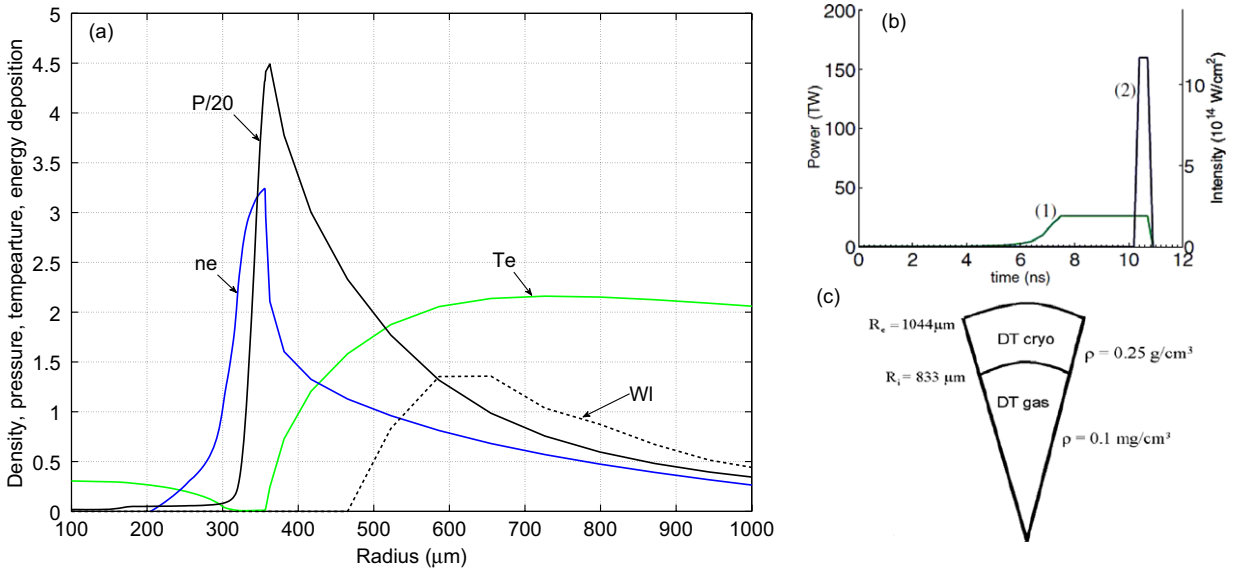

Figure 1. (*a*) Profiles of the plasma density, $\log(n_e/n_c) + 1$ (in blue), the electron temperature T_e in keV (solid line, green), laser energy deposition W_L (dashed line) and the pressure p in Mbar divided by 20 (solid line, black) as a function of the radius of an imploding shell at the time 10.1 ps of the spike arrival. The simulations were conducted with the radiation hydrodynamic code CHIC [20] for the laser wavelength of 0.35 μm. (*b*) Temporal shape of the main laser pulse (1) and the laser spike (2). (*c*) Scheme of the baseline all-DT HiPER target.

a relatively small number of laser beams may be needed for driving the shock. This would agree rather well with the polar irradiation geometry of NIF and LMJ designed for indirect-drive ignition.

Direct-drive ignition experiments on these installations will be rather complicated because of the necessity of repointing and refocusing laser beams in order to equilibrate irradiation over the spherical target surface. The polar direct-drive (PDD) scheme proposed by the scientists from the LLE, Rochester [19], requires some significant modifications in the NIF focusing system that will affect the target design and its robustness. In that aspect shock ignition might have also some advantages compared with the standard direct-drive PDD approach as the implosion velocity is lower and it thus might impose less stringent conditions on the implosion symmetry.

The paper is organized as follows: section 2 is dedicated to the laser–plasma interaction physics and numerical simulations of the laser absorption. Section 3 presents studies related to the hot-electron transport, ablation pressure and the shock symmetry. The experiments on laser–plasma interaction and the shock excitation are discussed in section 4 of this review.

2. Laser–plasma interaction

This section provides the reader with the necessary theoretical background related to the physics of laser–plasma interaction under the conditions relevant to shock ignition and with a review of results of numerical simulations. In the shock-ignition scheme, the laser spike intensity is above the threshold of parametric instabilities. Thus the collisional absorption of laser light becomes inefficient and nonlinear processes play an important role. Section 2.1 recalls the basic results of the inverse bremsstrahlung process and the major characteristics of the laser-driven parametric instabilities.

The progress in numerical computing over last ten years makes a direct kinetic modelling of laser–plasma interaction possible on the relevant temporal and spatial scales. We discuss in sections 2.2 and 2.3 the results of particle-in-cell simulations in one and two spatial dimensions for the shock-ignition conditions. These simulations that were not possible ten years ago can be readily compared with experiments and provide important information for the target design.

2.1. Theoretical estimates of interaction conditions

2.1.1. Inverse bremsstrahlung absorption of laser light. The particularity of shock ignition lies in the fact that the strong shock needs to be launched at a late time of implosion when the shell radius is reduced already by a factor of two. The shell is already compressed by a factor of ten or more. The characteristic profiles of the density, temperature, pressure and laser energy absorption rate are presented in figure 1(*a*). They are calculated for laser pulse profile shown in panel b at the moment of the laser spike arrival $t = 10.1$ ps. The target is shown schematically in figure 1(*c*). This is the baseline HiPER target designed in [5] for shock ignition.

The plasma corona has at that time a large extent of the order of 800 μm, the characteristic density scale length in the absorption zone near the critical density is $L_n \sim 200\,\mu$m, the distance between the absorption zone and the ablation surface is about 150 μm, and the distance between the critical and quarter-critical densities is about 300 μm. The electron temperature of the corona is rather homogeneous and it exceeds the value of 2 keV. The ion temperature is 2–3 times lower, at the keV level. The standard linear mechanism of laser absorption in the plasma corona is due to the inverse bremsstrahlung. It is described by the relation

$$\mathrm{d}I_L/\mathrm{d}z = -\kappa_{IB} I_L, \qquad (2)$$

where $\kappa_{IB} = (\nu_{ei}^c/c)\,(n_e/n_c)^2\,(1-n_e/n_c)^{-1/2}$ is the absorption coefficient, n_e is the electron density, ν_{ei}^c is the electron–ion collision frequency at the critical density $n_c = \epsilon_0 m_e \omega_0^2/e^2$, e and m_e are the elementary charge and the mass of electron, ϵ_0 is the permittivity of free space, $\omega_0 = 2\pi c/\lambda_L$ is the laser frequency, and z is the coordinate along the laser ray trajectory. The optical plasma thickness, $\tau_c = \nu_{ei}^c L_n/c$, defines the efficiency of collisional absorption. It is of the order of unity under the conditions of interest. This corresponds to the absorption $\eta_{abs} \sim 70\%$ for the case of normal incidence. However, for the PDD irradiation geometry, a large part of laser rays arrives at the oblique incidence and the total collisional absorption does not exceed 50–60%. Moreover, the nonlinear processes may significantly decrease this value.

2.1.2. Parametric instabilities under shock-ignition conditions. The laser intensity required for launching the ignition shock wave exceeds the threshold of several parametric instabilities (such as SRS, TPD and SBS) that may reflect a significant portion of the laser light, filament laser beams creating high-intensity spots, redistribute the laser energy over the absorption zone due to the cross-talk between the overlapping beams arriving from different directions. These processes may generate large amounts of energetic electrons due to the resonance absorption near the critical density and the parametric instabilities near or below the quarter-critical density (SRS and TPD) [21]. The interaction parameter that is defining the efficiency of nonlinear processes is proportional to the quivering electron energy in the laser field, $\varepsilon_{osc} = e^2 E_L^2/m_e\omega_0^2$, where E_L is the laser pulse amplitude. In practical units, the quiver energy scales as the product $I_L\lambda_L^2$. The qualitative estimates and experiments indicate that the parametric instabilities manifest themselves in enhanced light scattering and hot-electron generation starting from the values of the interaction parameter above the level as low as $10\,\mathrm{TW}\,\mu\mathrm{m}^2\,\mathrm{cm}^{-2}$. However, they become the dominant effect in the laser energy absorption for the intensities above $1\,\mathrm{PW\,cm}^{-2}$ for the $3\,\omega$ laser radiation (the wavelength of $0.35\,\mu$m). The inverse proportionality of the parametric instability thresholds with the laser wavelength explains an interest of using the short wavelength lasers for suppressing the nonlinear processes and enhancing the collisional absorption.

Self-focusing is an important process that can modify the propagation of a high power beam in a lower density part of plasma located in front of the absorption region. The technique of laser beam smoothing employed at high energy laser facilities by the random phase plates and smoothing by spectral dispersion [22] allows one to suppress the global beam self-focusing by splitting the whole beam into multiple mutually incoherent beamlets with much smaller power. Self-focusing of the smoothed laser beam takes place in a focused beamlet (laser speckle) if the average speckle power $\langle P\rangle$ exceeds the critical power of the ponderomotive self-focusing [23, 24]

$$P_c = 34\,T_{keV}(n_c/n_e)\sqrt{1-n_e/n_c}\,\mathrm{MW}, \qquad (3)$$

which is of the order of a hundred MW for the conditions of interest. For the typical focusing optics of the large scale installations $f/8$, the speckle radius is rather small about $2.5\,\mu$m, nevertheless the average speckle power $\langle P\rangle \simeq 1\,\mathrm{GW}$ exceeds the critical power by a factor of 4 for the laser intensity $I_L = 5\,\mathrm{PW\,cm}^{-2}$ in front of the absorption region. The effect of self-focusing on the laser beam energy deposition under such conditions implies that strong intensity enhancements may take place, but this was not yet studied in detail for the particular conditions of shock ignition.

The SBS is the parametric instability corresponding to the decay of the incident electromagnetic wave into another electromagnetic wave and ion acoustic wave. Because of smallness of the ion acoustic frequency compared with the laser frequency, $\omega_s/\omega_0 \sim c_s/c \ll 1$, the SBS develops in whole plasma corona up to the critical density. Two processes—SBS in near forward and in backward or near backward directions, are equally important. The forward SBS may develop even below the self-focusing threshold leading to strong beam spraying [25, 26]. Similarly to self-focusing, this is a non-stationary process resulting in reduced local laser intensity inside the plasma and reduced collisional absorption. These considerations indicate that some strategy must be identified to control self-focusing and beam spraying, such as using a shock laser pulse with a smaller f-number or a smaller wavelength. The use of a broadband laser smoothing through spectral dispersion and multiple polarizations has been shown to be efficient and should be taken in consideration [27].

The SBS in the backward direction is one of the principal laser energy losses in the plasma corona. Its performance depends strongly on the velocity and temperature profiles in expanding plasmas and on the spatial and temporal structure of the laser beam. It develops in high-intensity laser speckles and manifests itself in periodic bursts of reflectivity.

The SRS corresponds to the decay of the incident electromagnetic wave into another electromagnetic wave and an electron plasma wave. The frequency of the SRS light, ω_{SRS}, is red shifted with respect to the laser light by the local plasma frequency, ω_{pe}, that is, $\omega_{SRS} = \omega_0 - \omega_{pe}$. That provides a relation between the SRS wavelength and the plasma density

$$\lambda_{SRS} \simeq \lambda_L\,[1-(n_e/n_c)^{1/2}]^{-1}. \qquad (4)$$

Thus the spectral shift of the SRS light provides information about the plasma density.

In a homogeneous plasma the SBS and SRS instabilities are characterized by their growth rates. They depend on the direction of the propagation of the scattered wave, and they attain the maximum values for the backward scattering. This justifies a one-dimensional (1D) approach, which is often used to study these instabilities. The instability growth rates are shown in figure 2(*a*). In reality, the growth rates could be smaller if the damping of the daughter waves is accounted for. The SRS growth rates are relatively high in the plasma in front of the quarter-critical density. They attain their maximum in a 0.1 mm wide region, which corresponds to the range of plasma densities from 0.2 to $0.25\,n_c$. In the lower density plasma, the growth of backward SRS is strongly reduced by the Landau damping of the electron plasma wave. This is a particular feature of a high temperature plasma where the kinetic parameter, $k_p\lambda_D$, is relatively high. Here, k_p is the plasma wave number and λ_D is the Debye wavelength.

Although SRS is strongly suppressed in high temperature Maxwellian plasma, it may reappear under non-equilibrium conditions where the electron distribution function is modified by the plasma waves creating a plateau in the velocity domain

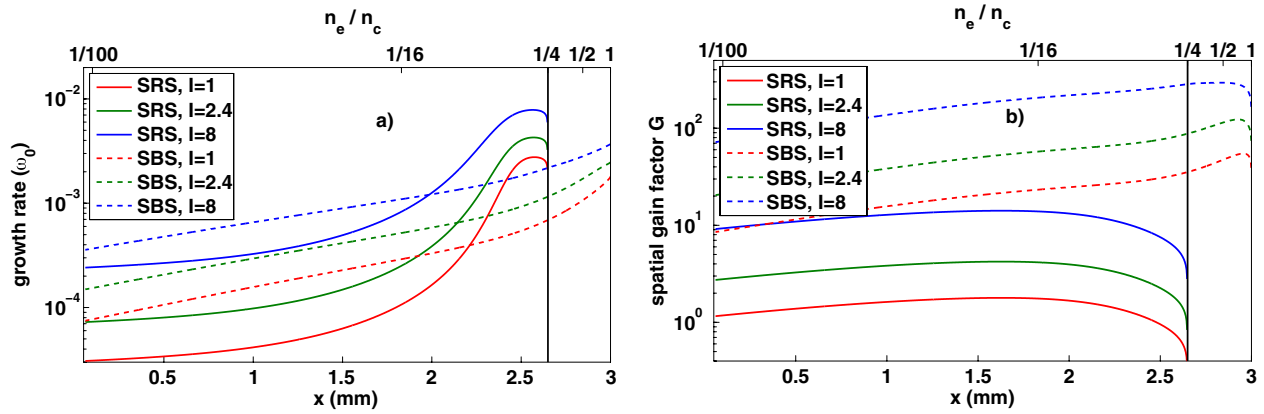

Figure 2. Growth rates (a) and gains (b) for SBS and SRS backscattering versus the spatial coordinate along the density profile (the corresponding density is shown in the upper axis). The intensity in the legend is in the units of PW cm^{-2}. The parameters of plasma correspond to the profiles shown in figure 1(a). The gain equation (5) is limited by the wavenumber mismatch, which is due to inhomogeneity in the hydrodynamic velocity (in the case of SBS) or in the plasma density (in the case of SRS).

corresponding to the resonance interaction with SRS-excited plasma waves. Then the growing SRS further suppresses the Landau damping leading to the explosive evolution of the scattering process. This effect called 'inflationary SRS' [28] has been discussed in application to the indirect drive experiments. However, it is also important under the shock ignition conditions where a high-intensity laser spike interacts with a hot plasma corona.

The growth rates for SBS are not as high as for SRS. It is partially related to the fact that ion acoustic waves in the underdense plasma are suffering the collisionless Landau damping. Nevertheless, at the transitional stage of interaction strong SBS spikes may be generated near the critical density. They are propagating all over the plasma and carrying out large amounts of the laser energy.

In an inhomogeneous plasma the resonance conditions are fulfilled in a spatially localized zone. Its width depends on the gradient length and the scattered wave frequency. Due to this fact the SRS and SBS instabilities lead to a finite convective amplification of the daughter waves in plasma, except the zone of quarter-critical density, that is discussed separately. The spatial amplification of daughter waves induced by stimulated scattering in an inhomogeneous plasma is described by the Rosenbluth gain factor [29]:

$$G = \frac{\pi \gamma_0^2}{|\Delta k' v_{g1} v_{g2}|}, \tag{5}$$

where γ_0 is the temporal growth rate in a homogeneous plasma, $\Delta k'$ is the spatial derivative of the wave numbers of three interacting waves in the resonance point $\Delta k = 0$, and $v_{g1,2}$ are the group velocities of the scattered and daughter plasma waves. Whereas the inhomogeneity in plasma density governs the convective amplification of SRS wave, the spatial amplification of the SBS wave is usually limited by the inhomogeneity in the hydrodynamic velocity. The SRS and SBS gains are plotted in figure 2(b). The SBS gain is rather high but it takes place at high plasma densities that may be screened by the SRS. The convective amplification of SRS might be quite significant at intensities above 5 PW cm^{-2} if Landau damping does not suppress the growth of electron plasma waves.

Special attention is required in the zone of quarter-critical density where, in addition to SRS, the TPD can be excited.

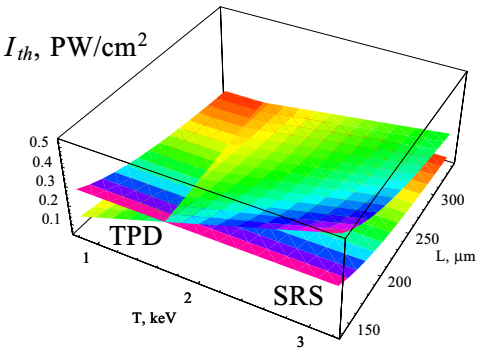

Figure 3. Thresholds of the SRS and TPD instabilities as a function of the plasma scale length and the temperature for the shock-ignition conditions at the wavelength of 0.35 μm.

It corresponds to the decay of the incident laser photon in two plasma waves with approximately equal frequencies. The threshold for TPD in an inhomogeneous plasma has been obtained in [30, 31]. In the high-β regime which corresponds to the shock-ignition conditions, the threshold laser intensity reads [31]

$$I_{\mathrm{thTPD}} \simeq 8.2\, T_{\mathrm{keV}} L_n^{-1} \lambda_{\mathrm{L}}^{-1}\ \mathrm{PW\,cm^{-2}}, \tag{6}$$

where the electron temperature in the quarter-critical density is in keV, and L_n and λ_{L} are in micrometres. For the plasma scale lengths of more than 100 μm and the temperatures of a few keV, the threshold intensity is below the level of 1 PW cm^{-2}. Thus, it could be detrimental at both, the implosion and ignition phases, by creating a large number of energetic electrons [32].

Moreover, SRS also becomes an absolute instability in the quarter-critical density as it develops near the turning point of the scattered wave [33–35]. Its threshold [36]

$$I_{\mathrm{thSRS}} \simeq 99.5\, L_n^{-4/3} \lambda_{\mathrm{L}}^{-2/3}\ \mathrm{PW\,cm^{-2}} \tag{7}$$

is comparable to the TPD threshold in the parameter range relevant for the shock ignition.

Figure 3 demonstrates the dependence of the thresholds of both instabilities on the plasma temperature and the density scale length. Both thresholds are in the intensity range

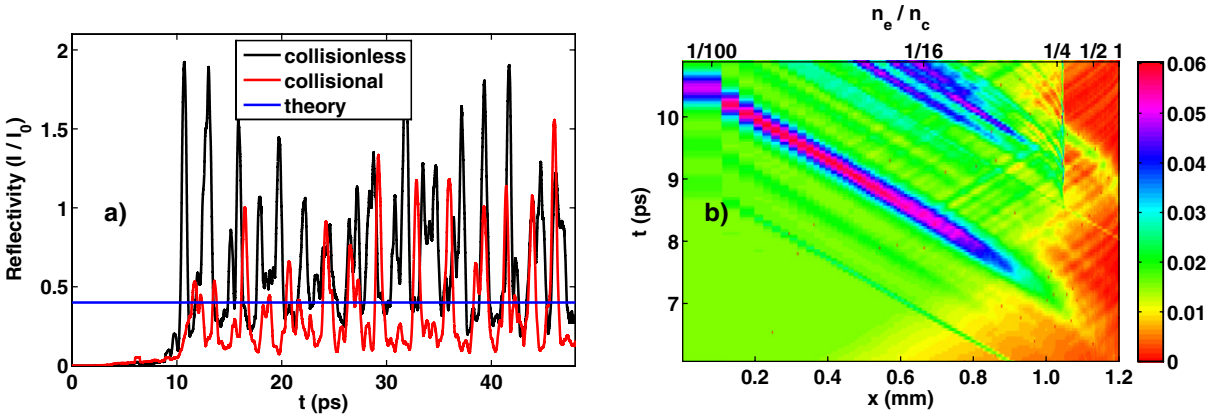

Figure 4. (*a*) Temporal evolution of reflectivity in the collisional and collisionless simulations of laser–plasma interaction at the intensity $1\,\mathrm{PW\,cm^{-2}}$. The reflectivity calculated from the inverse Bremsstrahlung theory is included for comparison. (*b*) Temporal evolution of the electromagnetic field energy density (in arbitrary units) inside the target in the collisionless simulation with $1\,\mathrm{PW\,cm^{-2}}$.

0.1–$0.5\,\mathrm{PW\,cm^{-2}}$. Moreover, the TPD threshold increases with the temperature, while the SRS does not depend on it. Correspondingly, TPD dominates at the temperatures below 1.5 keV, and SRS is more important at higher temperatures. In the temperature range 1–2 keV the parametric instability at the quarter-critical density evolves in a hybrid mode that combines both SRS and TPD as the limiting cases [37, 38]. In the transient domain and near the threshold, the direction of maximal growth depends on the plasma temperature and the scale length. However, the maximum growth rate well above the threshold is the same for both instabilities, $\gamma_{\max} \simeq 11\, I_{\mathrm{L}}^{1/2}$ ps [39], where I_{L} in the units of $\mathrm{PW\,cm^{-2}}$.

Numerical studies of the competition between SRS and TPD require multi-dimensional simulations [39–42]. The simulations by the American group [40–42] were performed with laser intensities below $1\,\mathrm{PW\,cm^{-2}}$ typical in the compression phase, for temperatures lower than 2 keV where the TPD dominates. Only the simulations [39] were performed for the intensities corresponding to the shock-ignition conditions. They demonstrate that the TPD is effective on the transient stage of a few ps. This was evidenced by the spectral distribution of the plasma waves and the energy and the number of hot electrons, see section 2.3. Later in time the SRS dominated the plasma response. Similar conclusion has been reported in the experimental paper [43], where a correlation between the hot-electron production and the generation of the $3\omega/2$ harmonic (the signature of TPD) was reported in the very beginning of the laser pulse when the plasma was sufficiently cold, while a correlation of hot-electron production with the SRS emission was seen later in time.

In the following section we present the results of a series of numerical simulations with PIC codes in one and two spatial dimensions dedicated to the studies of the effect of parametric instabilities under the shock-ignition conditions.

2.2. Numerical simulations of laser–plasma interaction: SRS and SBS competition

Fully kinetic collisional simulations are performed using a massively parallel relativistic electromagnetic PIC code in 1D geometry [44, 45]. The simulations are sufficiently long (several tens of picoseconds) so that a quasi-steady state may be established in the interaction. Specially designed absorbing boundary conditions at the rear side of the simulation box allow us to evaluate the number of hot electrons and the energy transported to denser plasma. This boundary condition is used to absorb the increased flux of kinetic energy due to laser absorption and provide the return current with a constant temperature equal to the initial one. Numerical heating is suppressed using the higher order shape forms for the particles.

The plasma conditions are taken similarly as in [45] from the hydrodynamic simulations of recent shock-ignition experiments on the Omega laser facility [46]. The profile of electron density is approximately exponential in the underdense part of plasma with the scale length of about $150\,\mu$m. The electron density ranges from 0.01 to $1.1\,n_{\mathrm{c}}$. The electron temperature varies between 1.6 and 2.1 keV with the maximum at about $0.3\,n_{\mathrm{c}}$. The ion temperature and hydrodynamic velocity profiles have almost linear shapes (the temperature decreasing and the velocity increasing with the distance from the target). The ion temperature ranges between 0.4 and 1.2 keV and the expansion velocity between 150 and $1050\,\mathrm{km\,s^{-1}}$.

In simulations, the laser pulse intensity was 1, 2.4 or $8\,\mathrm{PW\,cm^{-2}}$ at the wavelength of 350 nm. The laser pulse had a 5 ps long linear ramp at the beginning and then it stayed on the maximum intensity. The ion charge and the ion mass were assigned values of $Z = 3.5$ and $m_{\mathrm{i}} = 7\,m_{\mathrm{p}}$, respectively, where m_{p} is the proton mass. That corresponds to the average ion in a fully ionized CD shell. The simulations were performed with relativistic Coulomb intra- and inter-species collisions, which have been tested in simulations of laser absorption in a homogeneous plasma [44].

2.2.1. Lower intensity domain—1 PW cm^{-2}. The collisional effects are important in the low intensity domain. The simulations were performed also with the collisional algorithm turned off to demonstrate the effect of collisions in this case. The temporal behaviour of overall reflectivity in the collisional and collisionless simulations is presented in figure 4(*a*). The theoretical value obtained as $1 - \eta_{\mathrm{abs}}$, where η_{abs} is the inverse bremsstrahlung absorption coefficient calculated according to (2), is included for comparison. The average reflectivity is larger than 60% in the collisionless case and the reflected

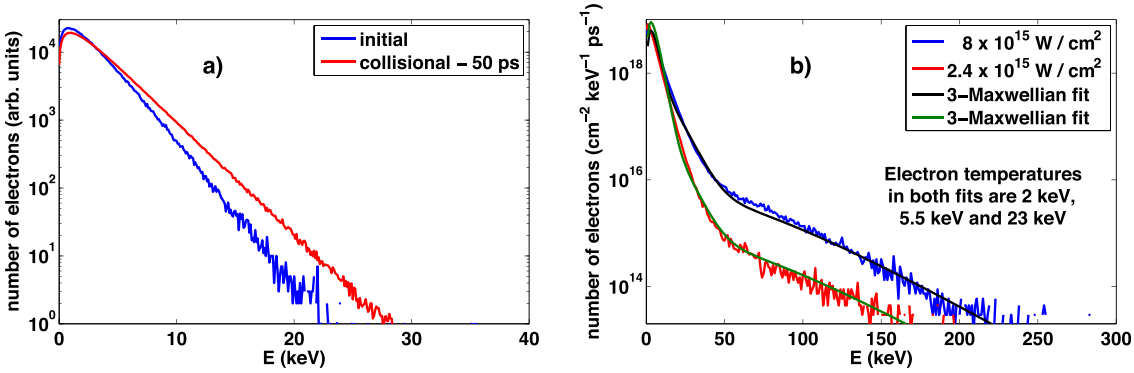

Figure 5. (*a*) Electron energy distributions in the simulation box, $\ln(\mathrm{d}n_\mathrm{e}/\mathrm{d}\varepsilon)$, at the beginning and at the end of the collisional simulation with the laser pulse intensity 1 PW cm^{-2}. (*b*) Differential flux of electrons flying into the target for the laser pulse intensity 2.4 (red) and 8 PW cm^{-2} (blue) recorded close to the rear side of the target in simulations with higher intensity and averaged over the whole simulation time. The distributions are interpolated as a sum of three Maxwellian distributions with the temperatures 2, 5.5 and 23 keV. Note the different energy scales in (*a*) and (*b*).

light comes in a series of intense pulses, which originate from the convectively amplified SBS waves. The amplitude of reflectivity is much smaller and the average value is little less than 30% in the collisional case comparable to the reflectivity expected from the inverse bremsstrahlung theory.

The origin and amplification of SBS in the collisionless simulation are clearly seen in the temporal evolution of electromagnetic field energy density inside the target as shown in figure 4(*b*). This figure demonstrates the first strong pulse, which is observed in the reflectivity at about 11 ps. This SBS pulse starts at about 1.1 mm corresponding to the density of about 0.4–0.6n_c and it is strongly amplified during the first 0.3 mm of propagation to the density of about 0.1 n_c. The pulsating behaviour of SBS has been reported in [47] and it is explained by a strong convective gain of the scattered wave which depletes completely the pump on its way out of plasma. The strength of the light pulses scattered by SBS is much weaker in the collisional case as the collisional damping of both, the incident and also the scattered light wave in the denser plasma, is comparable to the SBS growth rate.

An efficient heating of the bulk population of electrons due to collisional absorption of the incident laser pulse is confirmed by analysis of the energy distributions of electrons, $\mathrm{d}n_\mathrm{e}/\mathrm{d}\varepsilon$, in the simulation box. Figure 5(*a*) presents the electron distribution function averaged over the angles

$$\frac{\mathrm{d}n_\mathrm{e}}{\mathrm{d}\varepsilon} = \frac{p^2}{v}\int \mathrm{d}\vec{\Omega}\, f_\mathrm{e}(\vec{p}) \tag{8}$$

in the initial time and the time of 50 ps. Here $\vec{\Omega} = \vec{p}/p$ is the unitary vector in the momentum direction, $v = p/\gamma_\mathrm{e} m_\mathrm{e}$ is the electron velocity, γ_e is the electron relativistic factor, $\varepsilon = m_\mathrm{e}c^2(\gamma_\mathrm{e} - 1)$ is the electron energy and $f_\mathrm{e}(\vec{p})$ is the electron distribution function. The electron energy distribution has an exponential profile corresponding to a Maxwellian function. The initial temperature is 2 keV, while the temperature at 50 ps is increased to about 2.4 keV. Thus, the laser plasma interaction at 1 PW cm^{-2} is dominated by collisions. The laser pulse is efficiently absorbed due to inverse bremsstrahlung in the higher density plasma (above 1/4 n_c). The collisions suppress the SRS instability, and the resulting reflectivity (which is less than 30%) is largely dominated by SBS.

2.2.2. Higher intensity domain—2.4 and 8 PW cm^{-2}. Importance of parametric processes increases with increasing laser pulse intensity, while the collisional processes become less important. This transition manifests itself by the appearance of a hot-electron tail in the energy distribution function and it is observed while changing the laser pulse intensity from 1 to 8 PW cm^{-2} through the intermediate case at 2.4 PW cm^{-2} and keeping the same initial temperature and density profiles [45]. The time averaged differential (in energy) electron flux is defined as follows:

$$\Psi(\varepsilon) = \frac{p^2}{v}\int \mathrm{d}\vec{\Omega}\, v_x f_\mathrm{e}(\vec{p}), \tag{9}$$

where the integral is taken over the hemisphere $v_x > 0$. This function Ψ is shown in figure 5(*b*) for the laser intensities of 2.4 and 8 PW cm^{-2}. It is recorded in the simulations at the position $x = 1.2$ mm, close to the target rear side and averaged over the whole simulation time. This flux can be interpolated with Maxwellian-like components representing the bulk and the hot electrons. The temperature of the bulk electron population increases slowly with the laser intensity from 2.5 keV at the end of the simulation with the intensity 1 PW cm^{-2} to 3 keV at the intensity 2.4 PW cm^{-2}, and to 4 keV at the highest intensity of 8 PW cm^{-2}. Such a slow increase in the bulk temperature is explained by a dramatic decrease in the bremsstrahlung absorption from about 60% at the lowest intensity to 20% in the intermediate case, and to 5% at the highest intensity case. The remaining part of the absorbed laser energy is transmitted to the hot electrons having an effective temperature of 25–30 keV.

It is important to note that the temperature of hot-electrons is virtually independent of the laser intensity in the range considered here, while the hot electron number increases linearly with the absorbed laser pulse energy. There are virtually no hot-electrons at the lowest laser intensity as is shown in figure 5(*a*), while at higher intensities an increasing fraction of the absorbed energy is transported into the target with the electrons having approximately the same effective

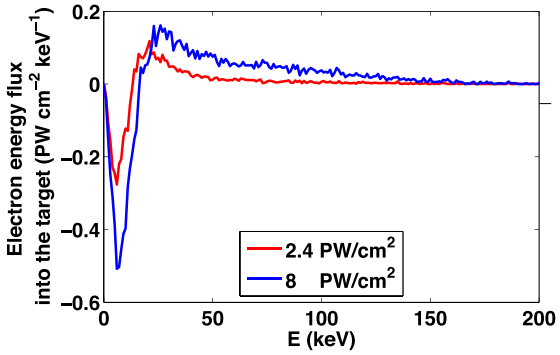

Figure 6. Temporally averaged differential energy flux of electrons in the collisional simulations of laser–plasma interaction with the laser pulse intensity 2.4 (red) and 8 PW cm^{-2} (blue).

temperature. The collisionless mechanisms of the laser energy absorption and the characteristics of hot-electron population in the laser intensity range extending from 1 to 24 PW cm^{-2} have been studied in more detailed numerical simulations recently [48]. It is confirmed that the number of hot electrons increases with the laser intensity, but not their temperature. This is explained by the fact that the electron acceleration and heating are dominated by the resonant interaction with the SRS-driven electron plasma wave. The phase velocity of this wave is fixed by the SRS resonance conditions, and it depends effectively on the plasma density. For the density range from 0.2 to 0.25 n_c, where we observe the SRS activity it varies in the range from 0.3 to 0.55 of the light velocity. The electron energy corresponding to this plasma wave phase velocity range varies from 25 to 100 keV. This corresponds to the energy range of accelerated electrons.

The distribution function of the electrons carrying energy in the dense plasma can be characterized by the differential energy flux that is described by the function

$$\frac{\mathrm{d}q_x}{\mathrm{d}\varepsilon} = \varepsilon \frac{p^2}{v} \int \mathrm{d}\vec{\Omega}\, v_x f_e(\vec{p}), \qquad (10)$$

where the integral is taken over the unit sphere. This function is shown in figure 6 for the laser intensities of 2.4 and 8 PW cm^{-2}. This function was time averaged over the last 15 ps of the simulation time. The energy in the dense plasma is carried out with the electrons having energies above ∼15 keV. The energy of electrons carrying the maximum energy increases from 21 to 25 keV in the considered range of laser intensities. Taking into account only electrons with energies above 30 keV, the part of energy transported by hot electrons found in our simulations is about 25% and 70% of the laser pulse energy for the intensities 2.4 PW cm^{-2} and 8 PW cm^{-2}, respectively. However, a significant part of this energy flux is compensated with the return current of colder electrons. For example, the total electron energy flux through the right boundary in the latter case is 2.3 PW cm^{-2}, or only 28% of the incident laser energy. This is partially due to the fact that the electron energy flux is measured in the laboratory frame, but the plasma has a significant hydrodynamic velocity. The return current energy flux thus accounts also for the energy transfer due to plasma expansion.

Thus the 1D simulations indicate that the average laser absorption coefficient remains approximately constant through the intensity range from 1 to 24 PW cm^{-2}. However, the quality of absorption changes dramatically from the collisional-dominated absorption at the lower end to the fully collisionless—at the higher end. This is manifested in the change in the electron distribution function from a single Maxwellian distribution at the lower end to a three-temperature distribution at the higher end. It could be that 1D simulations overestimate the role of the parametric absorption and hot-electron generation. As is shown in the next section, the cavitation process is weaker in two-dimensional (2D), and the effects such as self-focusing and FI modify the interaction dynamics.

Laser–plasma interaction in the higher intensity domain proceeds through two successful steps, which are demonstrated in the temporal evolution of reflectivity in figure 7(*a*). The first one is a transient stage with a high reflectivity (80%) dominated by the SBS. It is followed by a quasi-steady stage with a higher absorption (70%) dominated by the SRS and cavitation. For our initial conditions, SBS has much higher gain than SRS and its growth is not suppressed significantly during the initial transient stage. Therefore, this instability backscatters most of the pump wave energy and the reflectivity is rather high. The SRS is an absolute instability at $1/4\ n_c$ and it is growing in the meantime. When the local field induced by this instability becomes high, it expels electrons and the subsequent Coulomb explosion of ions produces density cavities, which partially trap the light and accelerate the particles [44]. The cavities are first produced at $1/4\, n_c$.

The inset in figure 7(*a*) contains the power spectra of reflected light in the SRS domain. One can distinguish here three different signals. In the spectral range 0.6–0.8 ω_0, the signal is due to convective SRS from lower density plasma (below $1/4\, n_c$). It is observed that the signal in this domain strongly depends on laser intensity. As already noted, this convective SRS is strongly suppressed by Landau damping. Therefore, it is not observed at lower intensities, while at higher intensities the electron distribution function is strongly modified and SRS can take place in the inflationary regime [28]. Two other signals at 0.5 ω_0 and 0.25 ω_0 are due to absolute SRS at 1/4 n_c and its Raman cascade, which is explained below.

The light scattered from the quarter-critical density (with frequency 0.5 ω_0) propagates back along the density profile, and if its intensity is not very high it leaves the plasma. However, when the intensity of this light overcomes the SRS threshold, it may be scattered again on its way back at $1/16\, n_c$, which is its own $1/4\, n_c$. The scattered light can only propagate down the density profile and if its intensity is still sufficient, the process may proceed the same way by the next stage in the Raman cascade at $1/64\ n_c$. The absolute SRS taking place at $1/16\ n_c$ also results in cavitation, which is even stronger than at $1/4\ n_c$ at later times $t > 30$ ps for 8 PW cm^{-2}.

During the second quasi-steady part of interaction, the reflectivity is reduced due to the cavitation in lower density plasmas as the cavities discontinue the spatial amplification of SBS waves. This can be seen in figure 7(*b*) where the temporal evolution of electromagnetic field energy density is plotted. The flashes due to SBS (propagating out of the target to the left) are clearly observed during the transient stage, which lasts for about 35 ps. The cavities around $1/16\ n_c$ start to develop

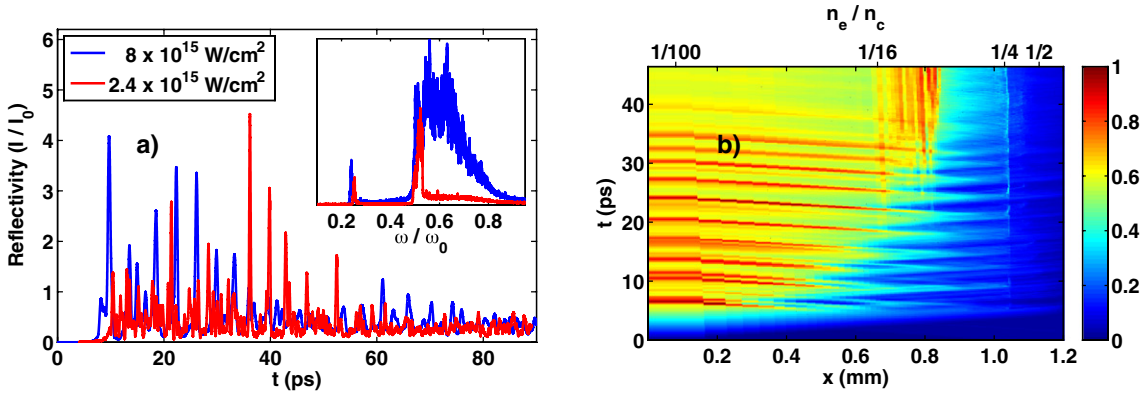

Figure 7. (*a*) Temporal evolution of the reflectivity in the collisional simulations of laser plasma interaction with the laser pulse intensity 2.4 and 8 PW cm^{-2}. The inset contains the temporally integrated spectra of the reflected light in the SRS domain. (*b*) Temporal evolution of the electromagnetic field energy density inside the target in the simulation with the intensity 8 PW cm^{-2}. The energy density is in arbitrary units.

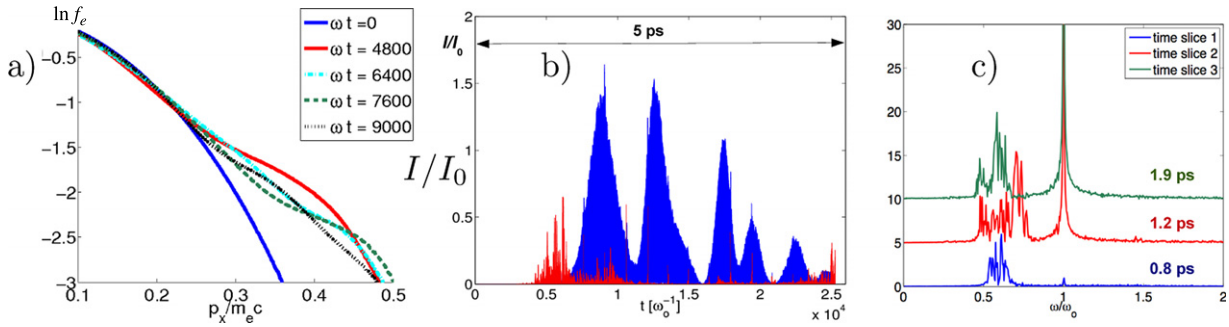

Figure 8. 2D simulation of interaction of the laser speckle with the intensity 40 PW cm^{-2} with an inhomogeneous plasma: (*a*) electron distribution function in the simulation box at the time moments of 0 (blue), 0.80 (red), 1.05 (dashed light blue), 1.3 (dashed green) and 1.5 ps (dashed black). The blue line corresponds to the Maxwellian distribution with the temperature of 5 keV. (*b*) Temporal evolution of the reflectivity [39]. The SBS component ($>0.9\,\omega_0$) is shown in blue, the SRS part ($<0.9\,\omega_0$—in red. (*c*) Three snapshots of the electromagnetic field spectrum emitted from the centre of speckle. (*a*) Reprinted from [39] with permission from the American Physical Society. Copyright 2012, APS Publishing LLC. (*b*) Reprinted from [49] with permission from the American Institute of Physics. Copyright 2011, AIP Publishing LLC.

at about 30 ps. They can be clearly observed in the figure as vertical strips as they trap a significant electromagnetic energy.

The absorption of the laser pulse becomes quite efficient (70%) in the quasi-steady stage of interaction after the cavities develop. Most of the absorbed energy goes into hot electrons with a temperature in the 20–30 keV range as shown in figure 5(*b*). The absorption takes place in particular in a low-density plasma, and it is due to the convective SRS that is developing in the inflation regime and the absolute SRS around the 1/4 and the 1/16 of n_c, that is trapping strong electromagnetic fields in cavities.

2.3. 2D simulations of laser–plasma interaction

Plasma cavitation under the ponderomotive pressure of SRS-excited plasma waves is identified as the prime mechanism of strong suppression of SBS and efficient laser energy absorption in 1D simulations with higher laser intensities. However, the 1D geometry excludes the possibility of the TPD, SRS side scattering, FI and self-focusing and also cavity expansion in the transverse directions. The 2D PIC simulations of the laser–plasma interaction were performed to understand the importance and the interplay of these processes [39, 49]. The results of 1D simulations indicate that the most important processes in laser–plasma interaction at higher intensities take place in a lower density plasma $n_e \lesssim 1/4\,n_c$. This enables one to restrict the volume of plasma in the 2D case, which in turn enables one to treat time scales of several ps.

The 2D full PIC simulations were performed with the code EMI2D, which was developed by A. Heŕon and J.-C. Adam at École Polytechnique, France. The laser and plasma parameters are similar to that discussed in the previous section. The simulated plasma region extends 160 μm in the laser propagation direction and 103 μm in the transverse direction. The exponential plasma profile has a scale length of $L_n \approx 60\,\mu$m, extending from 0.04 n_c up to 0.4 n_c, with 60 particles per cell for the highest density value. Electron and ion temperatures are 5 keV and 1 keV, respectively. The case that is discussed here corresponds to the laser intensity of 40 PW cm^{-2}, which are higher than in the 1D case, as the simulations are modelling a single laser speckle with a full-width at half-maximum (FWHM) of 29 μm.

The 2D simulations [49], similarly to the 1D case, show a fast development of the SRS and SBS instabilities manifesting themselves in strong reflectivity bursts, see figure 8(*b*), during initial few ps of interaction. The SBS dominates the reflectivity starting from the first picosecond as it is less sensitive to the density inhomogeneity and high temperatures. However,

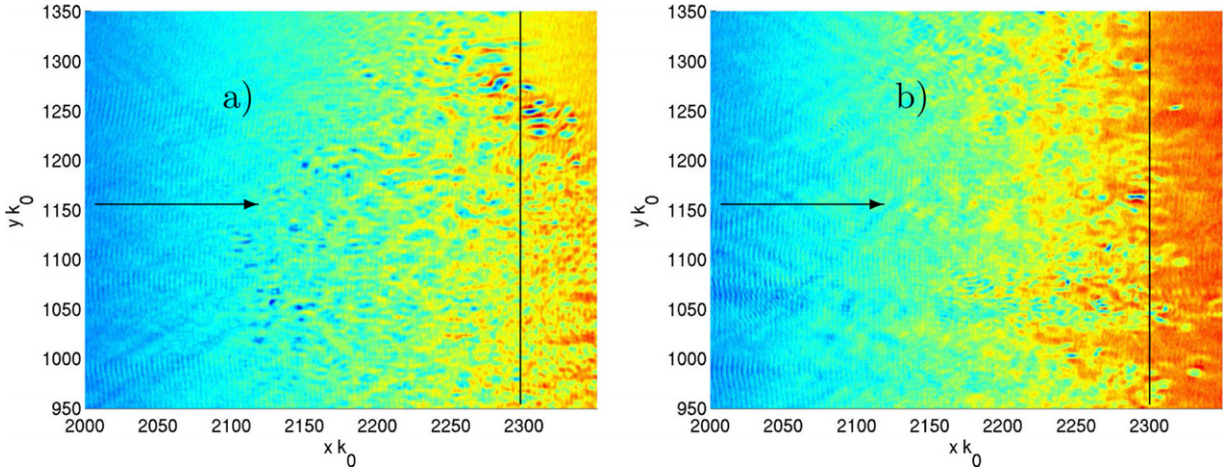

Figure 9. Density modulations in the zone $1/4\,n_c$ at the time moments of 0.9 (left) and 2.4 ps (right) [39]. The cavity's size is much smaller than the speckle size and they are elongated parallel to the density gradient (horizontal axis) due to the TPD seeding. The laser comes from the left. The picture size is $20 \times 22\ \mu m^2$. The vertical line shows the initial position of the quarter-critical density. The speckle axis is indicated by the arrow. The maximum depth of cavities is about 50% of the average density. Reprinted from [39] with permission from the American Physical Society. Copyright 2012, APS Publishing LLC.

as time goes on, the SBS bursts become less violent as the amplification is inhibited by the cavitation process developing in $1/4\,n_c$.

Before the SBS has time to grow up, the spectrum in figure 8(*c*) shows that the SRS from the $1/4\,n_c$ dominates the response. However, later in time the SRS spectrum broadens significantly indicating SRS contribution from a low-density plasma $n_e \sim 0.22$–$0.05\ n_c$. This is manifestation of inflationary SRS, which corresponds to scattering from short wavelength plasma waves that were initially strongly damped because of their low phase velocity ($k_p\lambda_D \lesssim 0.7$). The fast electrons generated in the near $1/4\,n_c$ region decrease the damping of a broad spectrum of plasma waves as they spread over the plasma and facilitate the SRS excitation. The light scattered by the inflationary SRS has a wide angular distribution with opening angles up to 45°.

Destabilization of the SRS in a low-density plasma can be seen in the electron distribution function in figure 8(*a*). Flattering of the electron distribution in the velocity range 0.2–0.3 *c* (the electron energies 10–25 keV) corresponds to the reduction of Landau damping for the plasma waves with phase velocities 2–3 times the electron thermal velocity. These are the waves that are responsible for the late time SRS. A similar scenario of SRS destabilization by hot electrons has been discussed in large scale multi-speckle simulations [50, 51]. In their case of a large, homogeneous, low-density ($n_e/n_c \sim 0.12$–0.14) plasma the electrons produced in the SRS process in a high-intensity speckle destabilized smaller neighbour speckles with intensities even below $1\ PW\,cm^{-2}$. It is quite possible that the SRS will also develop at lower intensities under the shock-ignition conditions if one considers a multi-speckle laser beam.

The specificity of 2D simulations is in the simultaneous excitation of the absolute SRS and TPD. As their growth rates under the shock-ignition conditions are comparable, according to section 2.1, both instabilities are excited as soon as the laser radiation attains the quarter-critical zone [39]. They can be clearly distinguished in the wave spectrum as the TPD plasma waves have larger wave vector components perpendicular the density gradient that depend on the frequency detuning between the half of laser frequency and the local plasma frequency.

The TPD instability was studied separately in the full PIC [41] reduced PIC 2D simulations [40, 42] for plasma with the density close to the quarter-critical density. Although the parameters in these studies do not correspond completely to those expected in shock ignition, the conclusions are in a qualitative agreement with the simulations made with more appropriate parameters [39]. Both the absolute SRS and TPD are quickly saturated in the time scale of a few picoseconds. The saturation of the TPD is due to the formation of the electrostatic [42] or electromagnetic cavities [39]. In 2D simulations, compared with the 1D case, the interference of electron plasma waves induced by the TPD facilitates the cavitation. Because of symmetry of plasma wave excitation in the plane perpendicular to the density gradient, the oppositely travelling pairs of plasma waves interfere thus creating quasi-static modulations with the scale equal to a half of their perpendicular wavelength [39, 42]. These forced coherent electron density modulations shown in figure 9 are inducing the ion motion and seeding the cavities. Thus cavitation spans over a large region of plasma below $1/4\ n_c$ producing small-scale density depressions filled with high-intensity electromagnetic waves. Thus the TPD in 2D simulations reinforce the cavity formation and enhance the efficiency of laser energy absorption. However, unlike in 1D simulations, the cavitation in 2D is unstable. After trapping the light, the cavities transfer their energy to electrons and ions, expand and disappear on the characteristic time scale of a few ps. The cavitation-induced density perturbations in the vicinity of $1/4\ n_c$ have the function of a dynamic random phase element, which affects spatial and temporal coherence of the electromagnetic waves in plasma. In particular, it inhibits the SBS amplification and reduces strongly the plasma reflectivity.

In the initial stage of the laser–plasma interaction, laser absorption takes place around $1/4\ n_c$ due to absolute SRS,

TPD and cavitation. Later in time the inflationary SRS at the densities around $0.1\,n_c$ contributes to the formation of hot tail in the electron energy distribution. As is shown in figure 8(*a*), the hot-electron temperature is about 30–50 keV and the electron energy distribution is cut at energies less than 150–200 keV, which is in agreement with 1D simulations. Thus the presence of SRS, TPD and cavitation does not seem to be detrimental to the shock-ignition scenario as far as the preheating of the compressed fuel is concerned. However, the laser–plasma interaction in 2D simulations is dominated by SBS on the longer time scales of several ps resulting in a rather high reflectivity exceeding 50%. Although the SBS activity seems to be decreasing with time, a long-term behaviour of reflectivity and SBS saturation in relation to the dynamic cavitation need further studies.

The cavitation mechanism of parametric instability saturation seems to be quite robust and takes over other processes as soon as the laser intensity is sufficiently high, above a few times the level of PW cm^{-2}. In contrast, very close to the TPD threshold, the level of plasma wave turbulence is relatively low and the cavitation was not observed [41].

In summary, starting from the laser intensities of several PW cm^{-2}, the laser–plasma interaction is ruled by the collective effects, which dominate the laser energy absorption and substitute the bremsstrahlung absorption that operates at lower intensities. After the initial transient period of several picoseconds, the plasma cavitation develops due to absolute SRS and TPD at 1/4 n_c and interaction enters into the quasi-steady phase. The collisional absorption at lower intensities is substituted by the parametric processes. The laser light is absorbed due to inflationary SRS and cavitation. Both these processes accelerate electrons to suprathermal velocities thus producing hot electrons with approximately Maxwellian energy distribution with the temperature in the range 25–30 keV and the cut-off near 150–200 keV. Increasing the laser pulse intensity, the absorption and the hot-electron temperature remain the same, while the number of hot electrons correspondingly increases.

Although these conclusions are encouraging for the shock-ignition scenario, they are rather preliminary and limited by the present computer performances. While the 1D simulations are sufficiently detailed and extended to a whole range of relevant laser intensities and plasma parameters, the 2D simulations are limited to relatively short plasmas, the simulation time of less than 10 ps, and the laser intensities above 10 PW cm^{-2}. The 2D simulations did not reach yet the quasi-stationary state, which is seen in 1D simulations with the lapse time of 30–50 ps, depending on the laser intensity. The longer plasmas are also interesting for more detailed studies of the SRS and TPD competition, the effects of the laser beam FI and SBS on the processes taking place near the quarter-critical density.

3. Ablation physics

The laser energy absorbed in the plasma corona is transported to the dense target with electrons. We distinguish three types of electrons in the energy transport: (i) the thermal electrons with the mean free path smaller than the distance between the energy deposition zone and the dense shell; (ii) the fast electrons that penetrate the shell, but have the mean free path smaller than the shell thickness, and (iii) very energetic electrons that cross the shell and depose their energy homogeneously. Figure 1 obtained in the simulations of shock ignition with the laser wavelength of $0.35\,\mu$m shows that the shocked region where the pressure is maximal, ~100 Mbar, is located at the distance of about $200\,\mu$m from the energy deposition zone. The maximal density rises by a factor ~400 compared with the critical density. The shell density is exceeding 10 g cm^{-3} and its thickness is ~30 μm.

3.1. Hot-electron transport and preheat

The electron thermal transport in ICF hydrodynamic simulation codes is described commonly with the flux-limited model [52]. The electron energy flux in such a model is calculated as a minimum between the Spitzer–Härm heat flux [53], $q_{SH} = -\kappa_{SH}\nabla T_e$, proportional to the electron temperature gradient, and a fraction $f < 1$ of the free-streaming limit: $q_f = -n_e T_e v_{the}\nabla T_e/|\nabla T_e|$, where $v_{the} = (T_e/m_e)^{1/2}$ is the electron thermal velocity. The typical value used to simulate the direct-drive implosion is $f = 0.06$. Although the value of flux limiting factor does not affect directly the ablation pressure, it affects the corona temperature and thus the laser absorption efficiency and the role of parametric processes.

The ablation pressure driven by the thermal electrons can be estimated from equation (1) that was derived in [10]. In this model, the laser energy flux is deposited near the critical density $\rho_c = m_i n_c$. Here, the expansion plasma velocity is equal to the local sound velocity c_s, and the absorbed laser energy flux $I_{L\,abs}$ is related to the energy flux carried with the plasma flow as: $\eta_{abs} I_L \simeq 4\rho_c c_s^3$, where $c_s = (T_e/m_i)^{1/2}$ is the ion acoustic speed. Thus the corona temperature scales as $T_e \simeq m_i(\eta_{abs} I_L/4\rho_c)^{2/3}$ and the ablation pressure reads

$$p_{abl} \simeq 0.4\,\rho_c^{1/3}(\eta_{abs} I_L)^{2/3}. \qquad (11)$$

This formula in practical units corresponds to equation (1). However, it does not account for fast electrons that have the mean free path comparable to the size of heat conduction zone and need to be considered separately.

A shock pressure of more than 300–400 Mbar is needed to achieve ignition. Assuming the laser wavelength $\lambda = 0.35\,\mu$m and the absorption $\eta_{abs} = 60\%$, the scaling law (1) indicates that laser intensities higher than 7–10 PW cm^{-2} are necessary. These values are evidently well above the threshold of parametric instabilities. Hot-electron transport in corona cannot be described with the standard flux-limited model as their angular distribution could be strongly anisotropic and their mean free path could be comparable to or even more than the distance to the ablation layer. Thus such hot electrons may modify the spike pressure significantly.

The role of hot electrons in the shell implosion has been studied in the 1980s in the experiments with the CO_2 laser [54–56]. Because of a long wavelength of $10.6\,\mu$m, the laser interaction parameter $I_L\lambda_L^2$ was very large and the nonlinear effects dominated the interaction already at the intensities below 0.1 PW cm^{-2}. Copious hot electrons generated in the corona were crossing the target and preventing the shell from an efficient implosion. This effect was the main reason of abandoning the CO_2 lasers in the ICF research. However, it was already noted at that time that energetic electrons or ions

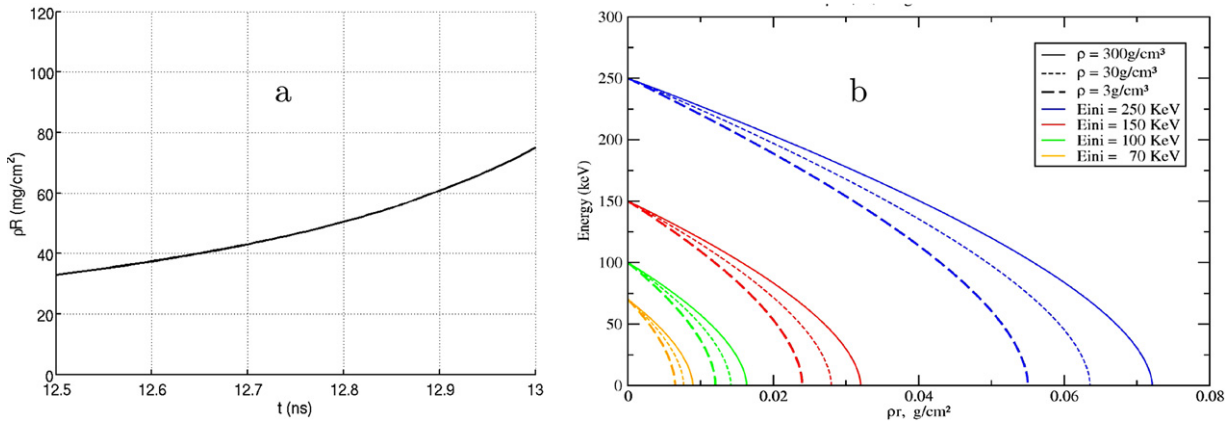

Figure 10. (*a*) Time evolution of the shell areal density during the implosion of a DT target of the NIF-LMJ scale. (*b*) Stopping power of electrons with the energies of 70, 100, 150 and 250 keV in a DT plasma with the density 3, 30 and 300 g cm^{-3}.

could generate a high ablation pressure if stopped in the target [56–59].

The situation with the hot-electron population in the context of shock ignition is different from that with the CO_2 lasers. Figure 10(*a*) shows the areal density of the shell during the laser spike interaction with the DT target of the LMJ-NIF scale. It varies in the range from 30 to 80 mg cm^{-2}. As can be seen in figure 10(*b*), the areal density of 30 mg cm^{-2} corresponds to the range of electrons with energies ∼150 keV. Thus the electrons with energies below 100 keV will be stopped in the shell and will not preheat it. Instead they may contribute to the ablation pressure as was suggested in [2, 5, 60].

It was discussed in sections 2.2 and 2.3 that there are two hot-electron sources in the corona related to the SRS and TPD instabilities. The hot electrons generated by the SRS are expected to have a quasi-Maxwellian distribution with the characteristic temperature ∼30 keV. They may carry up to 70% of the absorbed laser energy. In contrast, the TPD electrons are more energetic and they may contribute to the target preheat. However, according to studies of SRS–TPD competition presented in section 2.3, the TPD instability is excited at the transient stage of evolution and then it is suppressed by the caviton formation. The energy carried by such electrons with energies above 200 keV does not exceed a few per cent of the total energy flux.

3.1.1. Ablation pressure created by hot electrons. The, hot electrons in the shock-ignition scenario may provide a useful contribution to the shock pressure. However, this issue is not yet studied in detail. The pressure formation by hot electrons in a dense plasma was described by the Fokker–Planck kinetic equation coupled to cold fluid ions in [61]. It was found that non-local effects are significant in the heat front regime and might lead to formation of high pressures of a several hundred Mbar. However, the heat front regime corresponds to very short times before the shock formation. One has to consider longer electron beams for evaluation of their efficiency for the shock drive.

The particularity of hot-electron energy deposition is that their stopping distance λ_e depends only on the hot-electron energy ε_e and the electron density n_e [62, 63]:

$$\lambda_e \simeq 4\pi\psi\epsilon_0^2\varepsilon_e^2/e^4 n_e \ln\Lambda \qquad (12)$$

where ψ is a numerical factor of the order of 1 in a DT plasma and $\ln\Lambda$ is the Coulomb logarithm. Consequently, the areal mass of the target heated by fast electrons depends only on their energy. Assuming that the shell areal density is larger than $\rho_s\lambda_e$, the electrons will heat a small part of the shell launching a shock inside and a rarefaction wave outside. The dynamics of the shock launched by a beam of energetic particles in a dense solid shell was considered in [58, 64, 65].

The characteristic time needed to create a pressure and to launch a shock is defined by the time the rarefaction wave crosses the heated region, $t_h \simeq \lambda_e/c_s$. For a given electron beam energy flux I_b, this time reads $t_h \simeq \lambda_e\rho_s^{1/3}I_b^{-1/3}$. At that time the maximum pressure is created in the shell. Later in time the shock pressure decreases as $t^{-1/2}$ [65], as the remaining part of the electron beam energy is absorbed in the expanding plasma. Therefore, the time of the order of t_h presents the optimal time of shock excitation by the beam of hot electrons. The pressure at that moment can be evaluated as [58, 64]

$$p_h \simeq I_b t_h/\lambda_e \simeq 0.4\,\rho_s^{1/3}I_b^{2/3}. \qquad (13)$$

Although this pressure scales with the intensity in the same way as the one created with thermal electrons (1) and (11), this pressure is much higher since the fast electrons deposit their energy in a much denser plasma. For example, in a shell with the density $\rho_s = 10\,\mathrm{g\,cm^{-3}}$ an electron beam with intensity of 1 PW cm^{-2} creates a pressure of the order of 400 Mbar. That is ten times higher than the ablation pressure created by a laser beam with the same intensity at the critical density of $\rho_c = 10\,\mathrm{mg\,cm^{-3}}$. For electrons with the characteristic energy of 70 keV, the stopping power in DT shell is $\rho_s\lambda_e \simeq 8\,\mathrm{mg\,cm^{-2}}$, see figure 10. Then, the thickness of hot electron ablated layer is 8 μm and the heating time $t_h \simeq 80$ ps. The efficiency of shock excitation by fast electrons could be of the order of 10%.

3.1.2. Target preheat by hot electrons. Very energetic electrons with the ranges comparable or larger than the shell areal density at the time of spike launch are harmful as they provide a homogeneous shell heating thus degrading the fuel compression during the both the implosion and the shock launch phases. According to figure 10, these are the electrons with the energies above 150–200 keV that are created near the quarter–critical density due to the TPD instability. However,

even less energetic electrons could be dangerous at the earlier implosion phase, when the shell areal density is lower.

The preheat effect can be illustrated as follows. The shell heating by fast electrons can be considered as an isobaric process, $p_s \simeq$ const. The shell pressure, $p_s \propto \alpha\rho_s^{5/3}$ is proportional to the adiabat parameter α and the shell density ρ_s. The shell internal energy $\mathcal{E}_s \propto \alpha M_s \rho_s^{2/3}$, is proportional to the shell mass, M_s, and the ratio of p_s to ρ_s. Thus, the shell density variation, $\Delta\rho_s$ is proportional to the hot-electron energy deposited in the shell, $\mathcal{E}_{hot}$:

$$\Delta\rho_s/\rho_s = -5\Delta\alpha/3\alpha = -\mathcal{E}_{hot}/\mathcal{E}_s.$$

The areal density of compressed shell ρR is proportional to the square of the compression factor $C = R_s/R_{min}$, which itself is proportional to the square root of the ratio of the shell kinetic energy to its internal energy. Thus the areal density variation is directly proportional to $\mathcal{E}_{hot}$:

$$\Delta(\rho R)/\rho R = -\mathcal{E}_{hot}/\mathcal{E}_s.$$

In the context of the HiPER shock-ignition target [5], a shell with the mass of 0.5 mg, the adiabat parameter $\alpha = 2$ and the density 10 g cm^{-3} has the internal energy of 1.6 kJ. Thus the energy deposition of 0.5 kJ hot electrons will reduce the areal density more than 30% while increasing the adiabat parameter by 50%. These numbers could be considered as the upper limits for the acceptable hot electron preheat level in the shock-ignition fuel assembly.

For example, for the shell radius of 200 μm, the corresponding hot-electron energy flux is $\sim$100 kJ cm^{-2}. Then, supposing the spike duration of 300 ps, the maximum intensity for the electrons with the energies above 150 keV should not be higher than $\sim$0.3 PW cm^{-2}, or $\sim$5% of the total energy carried with the hot electrons. Supposing a Maxwellian distribution of hot electrons, the maximum temperature should not exceed 30 keV. This number is comparable to the results of numerical simulations presented in section 2.2.

3.1.3. Efficiency of shock ignition. Efficiency of shock excitation by the laser energy deposition is defined as the ratio between the energy of the shock $\mathcal{E}_{sh}$ and the laser absorbed energy $\mathcal{E}_{abs}$. The deposited laser energy can be estimated as follows: the laser intensity that is needed to produce a pressure $p_h = 300$ Mbar is defined from the scaling law (1). The absorbed laser intensity is $\sim$4 PW cm^{-2} for a wavelength of 0.35 μm. Considering that the target is compressed by a factor of 2 at the time of launching the spike, the radius of the ablation surface is $r_{abl} \simeq 350\,\mu$m, [5], see also figure 1. Then the radius of the critical surface is almost twice larger, $r_c \simeq 550\,\mu$m, which corresponds to the critical surface of 3 mm^2. Then the absorbed spike power is $\sim$125 TW and the laser spike absorbed energy is $E_{abs} = 62$ kJ for the spike duration $t_{spike} = 500$ ps. That corresponds to about 100 kJ of the incident laser energy assuming an absorption efficiency of 60%.

The energy in the shock wave can be estimated from knowing the shock pressure p_h and the thickness of the shock front Δr_{sh}. Assuming the ideal gas equation of state (EOS) with the polytrope parameter 5/3, the shock enthalpy is $5/2\ p_h$ and the shock energy $E_{sh} = 10\,\pi r_a^2 \Delta r_{sh} p_h$. The shock thickness can be estimated as a product of the sound speed in the ablation zone and the spike duration, $\Delta r_{sh} \simeq c_s t_{spike} \simeq 50\,\mu$m assuming the acoustic speed of 100 μm ns^{-1}. Then the shock-wave energy is about 3 kJ, that is the efficiency of shock drive is about 3% under the shock-ignition conditions. The problem of shock hydrodynamic efficiency is one of the main issue in shock-ignition physics.

The hot-spot energy at the ignition threshold, $E_{hs} = 3\,M_{hs}T_{ig}/m_i$, depends on the hot-spot mass M_{hs} and the ignition temperature T_{ig}, which is approximately 5–6 keV for the case of the HiPER shock-ignition target design [5]. The hot-spot mass can be estimated as $M_{hs} = (4\pi/3)\,(\rho R)^3/\rho^2 \simeq 3\,\mu$g for the hot-spot density $\rho = 100$ g cm^{-3} and the hot-spot areal density of 0.2 g cm^{-2}. Then the hot-spot energy needed for ignition is approximately 2 kJ. Moreover, the hot-spot is already heated during the implosion stage up to the temperature about 2 keV. Thus, the shock needs to contribute of about 40% of the total energy, that is, $\simeq$1 kJ. This estimate shows that the converging shock has to leave about 30% of its energy in the hot spot. This value is in agreement with the calculations of the converging shock energy deposition given in [66, 67].

Concluding this section, we note that the overall efficiency of the shock ignition scheme turns out to be rather low—less than 2% of the laser spike energy is deposited in the hot spot. However, the sequence of processes of energy transfer from the laser pulse to the hot spot is understood and controlled. The parametric instabilities and laser FI can affect the efficiency of laser spike coupling to the target. The laser power of 200 TW required for the shock launch is already available on the NIF facility. That opens the possibility for full scale experimental test of the shock-ignition scheme.

3.2. Symmetry of the ignition shock

The symmetry presents a serious challenge for shock-ignition similarly for all inertial confinement schemes, although a relatively low implosion velocity provides a better control of the implosion process. Traditionally, the small scale and large scale perturbations are considered separately. This is motivated by the difference in the origin of initial perturbations and in their theoretical and numerical analysis. As the perturbations for a spherical target can be developed in spherical harmonics, they are characterized by the mode number l that corresponds to the number of perturbation wavelengths over the shell perimeter $\lambda = 2\pi R/l$. The low modes, $l \lesssim 10$, are due to the inhomogeneity of laser irradiation and the final number of incident laser beams. The high modes are due to the laser beam and target small-scale inhomogeneities.

3.2.1. Low mode irradiation asymmetry. The particularity of shock ignition is that the shock pressure is rather insensitive to the spike illumination asymmetry. This can be explained by the fact that at the moment of spike arrival the plasma corona is well developed, the distance between the absorption and ablation zones is about 200 μm, which allows an efficient smoothing of even low mode perturbations. To illustrate this effect, we consider here the extreme case of the spike bipolar illumination [5]. The shock is launched by two laser beams arriving on the target along the polar axis. Figure 11 obtained in the 2D CHIC

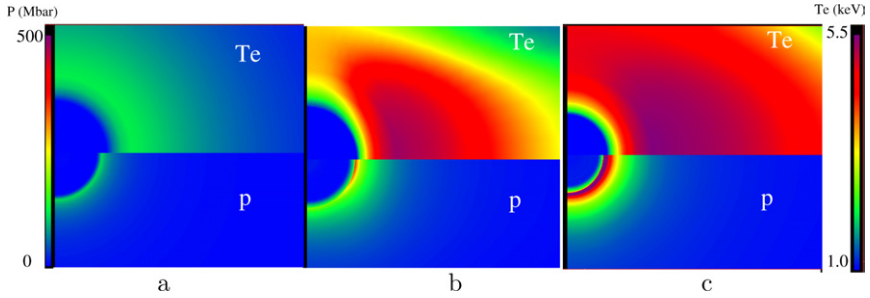

Figure 11. Temperature (upper) and pressure (lower), before the power spike (*a*), during the spike laser rising up and 200 ps (*b*) and after the maximum of power spike (*c*). Simulation results are obtained with the radiation hydrodynamic code CHIC.

simulations shows the temperature and pressure distributions at three consequent stages. Just before the spike arrival, the temperature and pressure are uniform (figure 11(*a*)). The temperature maximum corresponds to the radius of the critical surface and the pressure maximum indicates the position of the ablation layer. Figure 11(*b*) corresponds to the rising part of the spike (∼200 ps). The temperature and the pressure increase at the poles. That corresponds to a strong asymmetry with excitation of the Legendre mode $l = 2$. However, 200 ps later the lateral electron thermal conduction re-establishs the temperature and pressure symmetry (figure 11(*c*)). The relative amplitude of the mode 2 at this moment is reduced to the level of less than 10%. Thus even with a high irradiation laser asymmetry, the thermal smoothing allows one to enhance the spike shock symmetry and ignite the hot spot.

The thermal smoothing of laser induced pressure perturbations can be evaluated qualitatively using the 'cloudy day' model [68]. It assumes, by analogy with the diffusion of the light in clouds, that the amplitude of the mode with the wave number k decreases exponentially on a distance between the layer of critical density and the ablation surface due to the electron thermal conduction. The pressure perturbation at the ablation front $\delta p_{\rm abl}^{(l)}$ corresponding to the mode l, according to equation (11), is proportional to the laser intensity perturbations $\delta I_{\rm L}^{(l)}$. Moreover, it is smoothed out by the electron thermal transport in the heat conduction zone by a factor $\exp[-l\,(1 - r_{\rm abl}/r_c)]$:

$$\delta p_{\rm abl}^{(l)}/p_{\rm abl} = (2/3)(\delta I_{\rm L}^{(l)}/I_{\rm L})\,{\rm e}^{-l\,(1-r_{\rm abl}/r_{\rm c})}. \qquad (14)$$

In the case of bipolar spike illumination $l = 2$, $r_{\rm c} = 500\,\mu$m and $r_{\rm abl} \simeq 300\,\mu$m [5]. Then for a laser intensity perturbation of ∼50%, equation (14) predicts the ablation pressure perturbation of ∼15%. This is in agreement with the 2D CHIC simulations shown in figure 11. Such a pressure perturbation does not prevent the hot-spot ignition. However, the smoothing effect of the heat conductivity may be overestimated in these simulations as they did not account for the effect of self-generated magnetic fields on the electron transport. As the temperature and the density gradient are not collinear, a magnetic field in corona is generated, and it can modify the thermal conduction smoothing effect.

The hot electrons with energies below 100–150 keV can also contribute to the ablation pressure symmetrization. As the distance between the critical surface and the ablation front ∼200 μm is comparable to the shell radius, the hot electrons generated in corona in high-intensity laser spots may spread over the shell surface and smooth out the intensity perturbations. However, this issue is not yet studied in application to shock ignition. This would require implementation of a model of an anisotropic hot-electron transport into a radiation hydrodynamic code.

3.2.2. High mode hot-spot asymmetry. The high modes are dangerous for the shell integrity. The growth rate of the Rayleigh–Taylor instability increases with the mode number, and the modes with wavelengths comparable to the shell thickness may disrupt the shell. Moreover, the outer shell perturbations are transferred to the inner shell surface and are amplified during the deceleration and stagnation phase of the fuel assembly. These perturbations mix the shell material with the hot fuel inside thus reducing the hot-spot volume and degrading the ignition conditions. The dominant mode number $l_* \simeq \sqrt{\pi N}$ can be estimated by knowing the number of laser beams N and supposing that they are distributed evenly over the target surface $4\pi R^2$. For example, in the HiPER project, where the target is supposed to be irradiated by $N = 48$ laser beams [70], the dominant mode is $l_* = 12$.

The advantage of the shock-ignition scheme is that the Rayleigh–Taylor instability at the stagnation phase can be mitigated by the shock wave generated by the laser spike [5, 69]. Figure 12 shows the effect of the shock on the amplitude of the mode $l = 12$. In the case of standard implosion, figure 12(*a*), the mode is growing to a large amplitude in spite of thermal conduction smoothing. In contrast, the converging spherical shock wave decreases significantly the amplitude of the perturbation, figure 12(*b*). This effect can be explained by the differential acceleration of the inner shell surface. Similarly to the Richtmyer–Meshkov instability, the density valleys experience an acceleration in the shock earlier than the density peaks thus reducing the instability growth rate. In the case of sufficiently strong shock the perturbation would be even reversed. Such a stabilization effect was observed in the planar experiments [71] and in the shock-ignition experiment on the OMEGA facility [72]. In the latter case, it was found that the ratio of the measured neutron yield to the 1D predicted yield does not depend on the shell convergence, see section 4.3.

In summary, this section shows the important role that hot electrons are playing in the shock-ignition scheme. Different from the standard direct-drive scheme, the ignition shock pressures strongly affected by the hot electrons, which play two complementary roles. The electrons with the energies below 150–200 keV are depositing their energy in a thin external layer

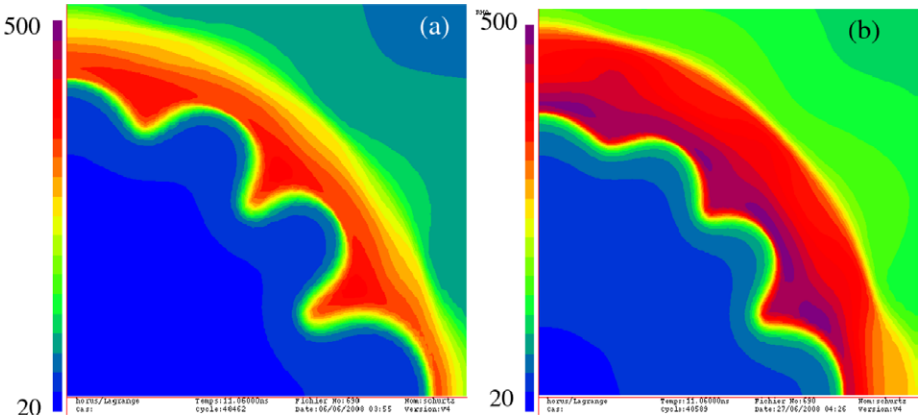

Figure 12. Shell density distribution from the 2D CHIC simulation of the HiPER target at the time moment before stagnation: the mode $l = 12$ for the case (a) without and (b) with the ignition shock (g cm^{-3}). Reprinted from [5] with permission from the IOP Publishing. Copyright 2009, All rights reserved.

of the imploding shell thus making a significant contribution to the ablation pressure. It seems that only due to contribution of hot electrons the pressures of 300–400 Mbar needed for ignition could be achieved. However, the electrons with higher energies are penetrating through the shell and depositing their energy homogeneously thus increasing the adiabat parameter and inhibiting the implosion.

Our estimates show that the former effect dominates for the hot electrons with a Maxwellian distribution if their temperature does not exceed 30 keV. This number agrees with the results of kinetic simulations thus indicating a feasibility of the shock-ignition scheme. However, these predictions need to be validated in the experiments. While the implosion experiments in the spherical geometry presented in the next section confirm the value for the hot-electron temperature, the experiments in a planar geometry indicate higher electron energies. This issue needs further analysis.

The shock-ignition scheme is shown to be less sensitive to the hydrodynamic instabilities than the standard central ignition. This is due to the efficient lateral smoothing of the low mode laser intensity perturbations and the stabilizing role of the ignition shock on the shell perturbations at the decelerating phase.

4. Experiments

Several experiments dedicated to studies of shock-ignition physics have been performed over last five years. The results are presented below. However, some earlier experiments on laser plasma interaction, which were not related to shock ignition, correspond to expected parameters and provide some useful and important results. We start this sections with the analysis of the results on laser–plasma experiments performed in a planar geometry at LULI, PALS and OMEGA, following the results of integrated experiments performed on OMEGA in a spherical geometry.

4.1. Laser–plasma interaction experiments

To be relevant to the shock-ignition scheme, laser–plasma interaction experiments must be conducted in long and hot plasmas at high intensity. The plasma must contain all plasma densities up to the critical density with a typical inhomogeneity scale length of a few hundreds of micrometres. The geometry and the crossing beam effects must also be taken into account. These studies require multiple laser beams to produce the plasma independently of the interaction beam(s), in the multi-kilojoule regime. A very limited number of such installations exists now all over the world, so it is necessary to design experiments on smaller laser systems that can address specific questions on the road to success of good laser–plasma coupling for shock ignition. As discussed in the introduction, the main questions concern the propagation and efficiency of the coupling of the shock-ignition pulses in the plasma corona of the compressed targets. Past experiments have identified the most serious problems: FI, spreading and deviation of the laser beam which affect its propagation and intensity distribution, SBS and SRS which can reject a large part of the incident laser energy outside the plasma.

4.1.1. Experimental conditions. To study these effects under complementary conditions, we have set up a program based on three laser installations: the six-beam LULI system (LULI-6F), 1 kJ LULI system (LULI-2000) and the LIL [73]. The first one has the advantages of driving multiple-beam irradiation that can be used to build sophisticated diagnostics and very well controlled laser and plasma conditions with a complete flexibility and a large number of shots. The LULI-2000 system provides a possibility to operate with two laser beams with energies ∼500 J. The LIL system delivers pulses on the 10 kJ level. The targets were chosen to emulate different parts of the density profile of the corona of a compressed target. Plasmas preformed from underdense foams and gas jets by the first laser beam were used to study the long low-density plasma. Their initial density was chosen to produce an electron density above or below quarter-critical density in order to evaluate the importance of mechanisms that can develop in this area, mainly absolute SRS and TPD. Thick foils irradiated with the first laser beam were used to produce electron density profiles with the critical density. This is important for the growth of SBS in the presence of reflected laser light as well as to study collisional absorption with high electronic densities.

Figure 13 summarizes the laser and plasma conditions that were used for these experiments with the LIL and LULI

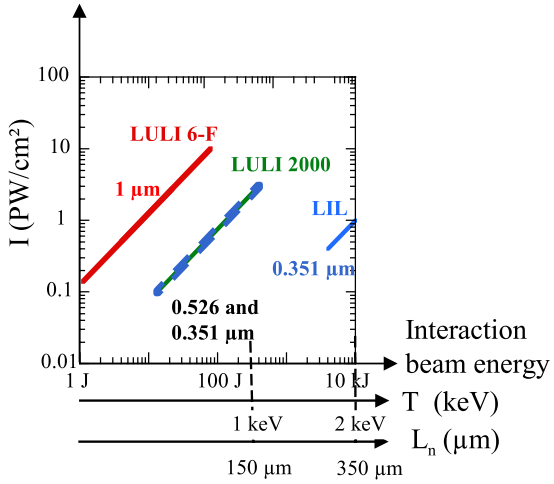

Figure 13. Summary of the laser–plasma conditions for the interaction experiments in the context of shock ignition.

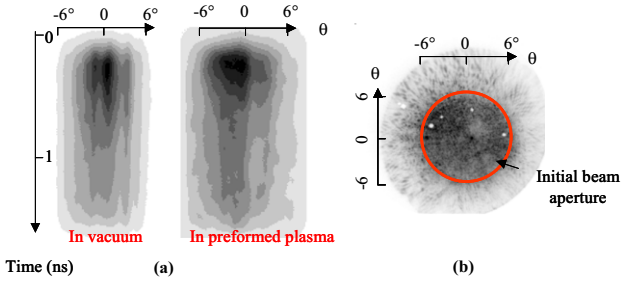

Figure 14. (*a*) Temporal evolution of the angular divergence of the transmitted light through an underdense plasma (right) compared with vacuum (left). (*b*) Gated near field image of the intensity distribution at the output of the plasma at $t = 0.3$ ns.

installations. The electron temperature up to 2 keV, the density gradient scale length up to 350 μm, the laser intensities up to 10 PW cm^{-2} were obtained. Although it is clear that a short laser wavelength will be the most suitable for the shock-ignition pulse, three laser wavelengths, 0.35, 0.53 and 1.05 μm, were used to reach high values of the main interaction parameter $I_L\lambda_L^2$. Different geometries of the laser beams with respect to the target were used to produce the plasma expansion in the direction of the interaction beam or with an angle. This latter case was used to study the effect of beam steering and light deflection that can happen to the shock-ignition pulses that are incident with an angle on the target.

In this section, we present first results from experiments that demonstrate self-focusing, spreading and beam steering of the interaction beam. Reflectivities due to SBS and SRS from long plasmas will then be discussed.

4.1.2. Laser beam propagation. All experiments at LIL and LULI have shown some laser beam spraying and plasma smoothing due to either forward SBS or FI when the laser power approaches the critical power. To illustrate this effect, we recall the six-beam experiments, which had many diagnostics on the beam propagation mechanisms, but the plasma temperature was lower than expected under the shock-ignition conditions. The laser interaction beam was diffraction limited, using a deformable mirror and a diaphragm, with a corresponding spot size measured at half-maximum of 21.5 μm. An example of the modification of the near field image of the laser intensity distribution after propagation through an underdense plasma compared with vacuum is shown in figure 14(*a*) as a function of time. The angular divergence of the incident beam was 6° as observed on the left panel of figure 14(*a*). It is widened by ~50% when going through a preformed plasma as one can see in the right panel of figure 14(*a*). The 2D near field image, integrated over 100 ps, of the laser intensity at the output of the plasma at the time $t = 0.3$ ns is shown in figure 14(*b*). The light scattered outside the initial aperture cone is clearly observed at the rear side of the plasma. Spectral measurements of this light demonstrated that it was due to forward SBS. Broadening of the angular distribution of the forward scattered light was observed to increase with the plasma density but the results of this experiment were limited by the aperture of the collecting optics of the transmitted light.

Plasma beam smoothing, with weak beam spraying, was also observed in the LIL experiments using low-density foam plasmas [74]. These results were obtained in long and hot plasmas but the laser intensity was below what is expected for the shock-ignition pulse. Plasma smoothing may be useful to control the SBS reflectivity to the condition that beam spraying does not affect too much the laser intensity in the critical region which must be high to produce the requested high-pressure shock. This effect must be different in spherical compared with planar geometry as, with multiple beams, the forward scattered energy from one beam could be added to the other beams.

Another important effect in the context of shock ignition is the oblique incidence of the shock pulse with respect to the density and expansion velocity gradients. Not only the laser beam will be reflected at plasma densities lower than the critical one so that the high-density regions could not contribute to collisional absorption, but also beam deflection and FI can happen to the rays that propagate in a flowing plasma [75]. To test these effects, a dedicated experiment was designed on the LULI-6F facility. The experiment used six laser beams with a special configuration to get the interaction beam axis perpendicular to the plasma flow. The plasma was created by two counter propagating 526 nm wavelength laser beams, ablating a 1.2 μm thick, 380 μm diameter CH disc, and heated by a third identical beam delayed by 900 ps with respect to the first two. The total power of the plasma forming beams was 0.2 PW cm^{-2}. The plasma was underdense, expanding rapidly along the preforming beam axis in two directions, backward and forward, with a parabolic density profile and a linear velocity profile. There was no plasma motion only at the top of the density profile. The high-intensity interaction beam, $I_L \simeq 1$ PW cm^{-2}, at the first harmonic, $\lambda_L = 1.053$ μm was sent perpendicular to the principal plasma expansion axis at different positions along this velocity profile [76]. The results are illustrated in figure 15 where far field-gated images of the intensity distribution inside the plasma are shown for various impinging positions on the transverse velocity profile. No breakup of the beam was observed when the laser impinges at the top of the plasma density profile where the flow velocity was almost zero. In contrast, a strong breakup happened in the case where the interaction laser beam propagated in a plasma

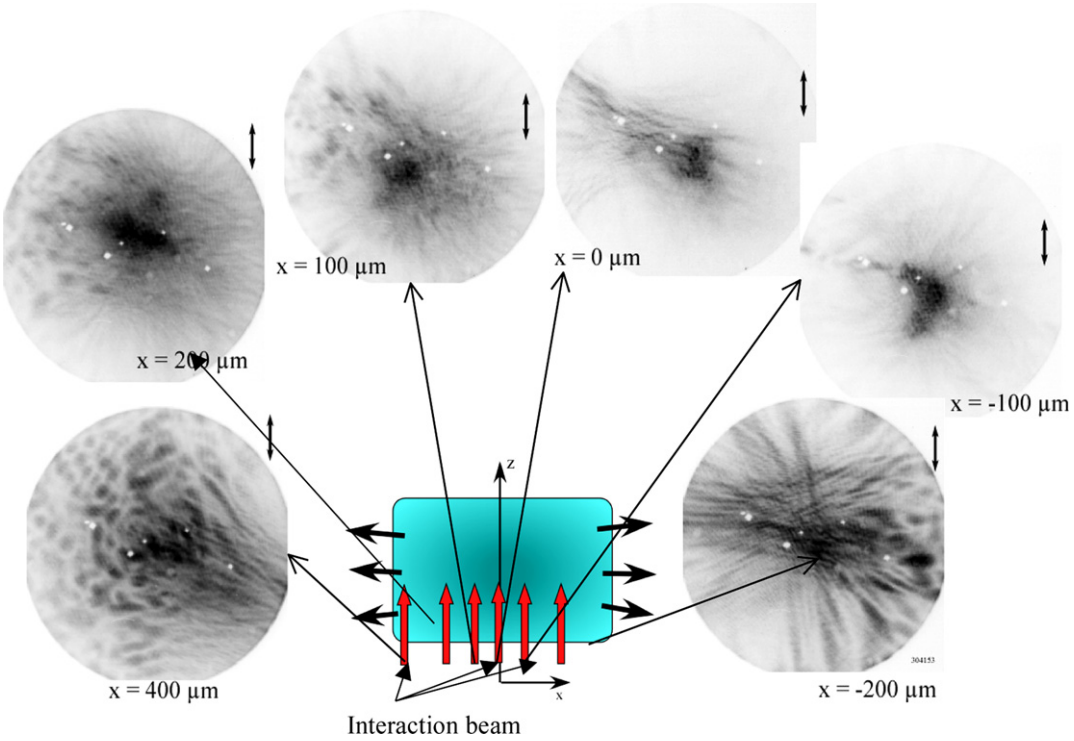

Figure 15. Far field-gated images of the intensity distribution of a laser beam incident at different positions on a transverse velocity profile. The experimental parameters are given in the text.

with high transverse velocities. This is consistent with the modification of the FI threshold as a function of the transverse flow velocity and demonstrates that such an effect could have very deleterious impact on laser beams travelling at an angle in the corona of a compressed target. In the same experiment, beam steering was observed in the near field images.

4.1.3. Stimulated Brillouin scattering. SBS reflectivities have been measured in preformed plasmas for a large set of parameters with temporal and spectral resolution. Specific LULI-2000 experiments were designed to study SBS in long plasmas with two laser beams delivering nanosecond pulses. The plasma was produced by the irradiation of a thick $\sim$50 μm plastic foil with a first laser pulse of 1.5 ns and 300 J. The interaction beam was focused in this plasma, along the normal axis of the target, after a delay of 1.5 ns and a maximum intensity of 3 PW cm^{-2}. The two beams smoothed with the phase plates were at the same wavelength, 0.53 μm in the first part of the experiments and 0.35 μm in the second part. Details on these experiments are reported in [77].

An example of time-resolved spectrum of the SBS light collected in the backward the direction is shown in figure 16 together with its temporal evolution. A broad component that lasts around 150 ps is observed at the beginning of the interaction pulse. It is followed by a narrow component that moves towards shorter wavelengths. The spectra were interpreted by the formation of a velocity plateau in the high-density region early in the interaction pulse, which then moves towards lower densities explaining the blue shift of the SBS spectrum. The plateau formation may result from the increased ablation rate when the interaction beam is fired after the creation phase. This may happen in the case of shock ignition as the shock pulse must have an intensity well above the compression pulses. Most of the SBS spectra were blue-shifted, which combined with hydrodynamics simulations of the density and velocity profiles, gives information about the location of the SBS activity. It indicates that SBS grows in the low-density part of the profile. The absence of SBS activity in the high-density region was interpreted by the effect of FI and self-focusing of the beam in the highest density region with significant beam spray resulting in reduced beam temporal and spatial coherence.

We have studied the backward time-integrated reflectivity as a function of the laser intensity and observed the growth and saturation of SBS. An interesting result was that the saturated backward reflectivity was in the same range, $\sim$10%, both for 0.53 and 0.35 μm laser wavelengths [74]. This 10% level is similar to what was observed previously in 1.05 μm experiments at intensities up to 10 PW cm^{-2} with the LULI-6F facility.

A very quick conclusion would be that the SBS reflectivity does not look to be an issue as one can afford 10% losses. Three important observations complete these results:

- the duration of the SBS emission is shorter than the laser pulse;
- a significant amount of scattered light was collected outside the focusing optics;
- the location and the extension of the plasma area where SBS grows change with the laser intensity.

The near back scattering was measured in an aperture twice the incident optics, and is shown in figure 17. Typically, at high intensities, the same amount of light was scattered outside than inside the focusing optics. This brings already the SBS reflectivity to twice the initial value.

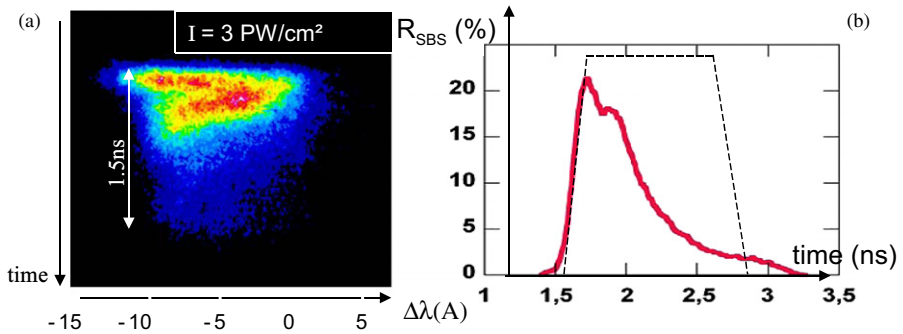

Figure 16. (*a*) Time-resolved spectrum of the backward SBS light in the 2 ω experiment at an intensity of 3 PW cm^{-2}. (*b*) Temporal evolution of the SBS reflectivity. The laser pulse shape is shown with the dotted line.

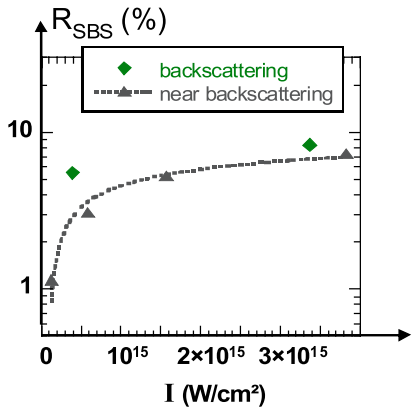

Figure 17. Time-integrated SBS reflectivities measured at 2 ω including backscattering and near backscattering measurements. Reprinted from [77] with permission from the American Institute of Physics. Copyright 2009, AIP Publishing LLC.

In all three experiments, the six-beam, the LULI-2000 and the LIL, we have observed that the SBS reflectivity, at high intensity, is always shorter than the interaction pulse duration and SBS grows at the very beginning of the laser pulse. This is shown in figures 16(*b*) and 18 and it corroborated with the numerical simulations presented in sections 2.2 and 2.3. This means that the average reflectivities measured with laser pulses in the nanosecond range are not meaningful for the shock-ignition pulse which will have a duration of a few hundred of picoseconds. For a SBS duration of one third of the total laser pulse, reflectivities for the few first hundred picoseconds would be ∼3 times larger than the average reflectivities.

In addition to the new experiments conducted recently, one has to reconsider carefully all previous results obtained on the SBS in the last 40 years. Past experiments have demonstrated that the size of the SBS emitting volume increases with the SBS reflectivity [78]. It has also been shown that a few small regions of plasma contribute to SBS and that SBS reflectivity from these regions is ∼50–100 higher than the average SBS reflectivity [79]. This is consistent with the results from [80] where it was observed that the ion acoustic wave saturation amplitude is independent of the density, and the total SBS reflectivity increases with the width of the saturated spectrum thus showing instantaneous values of ∼50%. Seeding SBS may also affect its nonlinear saturation [81]. In the case of crossing beams, SBS may be seeded by reflections or shared ion acoustic waves [82]. Finally, taking everything into account, it is most likely that the SBS reflectivity could be very high for the shock-ignition pulse conditions. To avoid this problem, all possible beneficial effects that could reduce the SBS emission like beam and plasma smoothing, target composition, aperture of the optics must be considered.

4.1.4. Stimulated Raman scattering. In most of our experiments the SRS reflectivity stays at low level, typically below or around a few per cent. The contribution of the quarter-critical density in the Raman spectra has always been negligible compared with SRS coming from lower plasma densities. We have found high levels of SRS only in gas jets where it could grow in the absolute regime until saturation at a level of around 20–25% depending on the plasma electronic density [83]. Three results are of interest in the context of shock ignition as they give tendencies on how the SRS growth could evolve with interaction conditions:

- the effect of the density scale length on the Raman reflectivity;
- the effect of laser intensity on the SRS spectra;
- the effect of plasma length on the SRS reflectivity.

The LIL laser facility, with square pulses of typically 12 kJ of 3 ω light and 2.7 ns duration, was used to produce long and hot plasmas from foam targets with very small (∼1 μm) cell structures. The maximum average intensity on target was 0.8 P W cm^{-2}. Temporal smoothing was achieved by means of the chromatism of the focusing grating, which creates a longitudinal dispersion with a spectral broadening introduced in the laser source by an electro-optic modulator. Various initial foam densities, between 3 and 10 mg cm^{-3} (respectively 10% and 35% of the critical density for 3 ω light), were used. The foams length has been varied from 300 μm to 1 mm. In all cases, because of the long pulse duration, some plasma expanded towards the laser, so that, after a few hundred picoseconds, the density profile displayed two parts: an increasing electron density in the front and a plateau at an electron density determined by the initial foam density in the backward parts of the plasma.

Using relation (4), the time-resolved spectra of the backward SRS light were used to determine the location and the extension of the SRS emitting region of plasma as a function of the interaction conditions. For the foams with

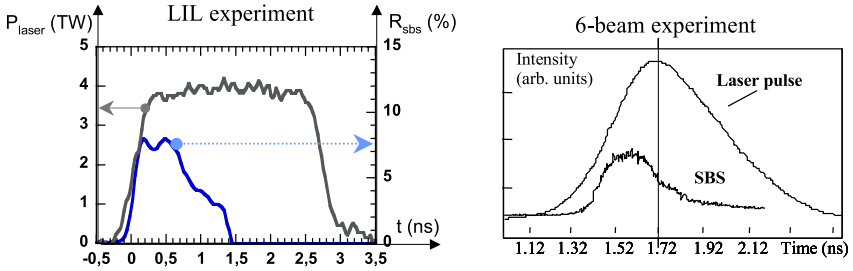

Figure 18. Temporal evolution of the backward SBS reflectivity in the LIL (left) and in the LULI-6F (right) facilities.

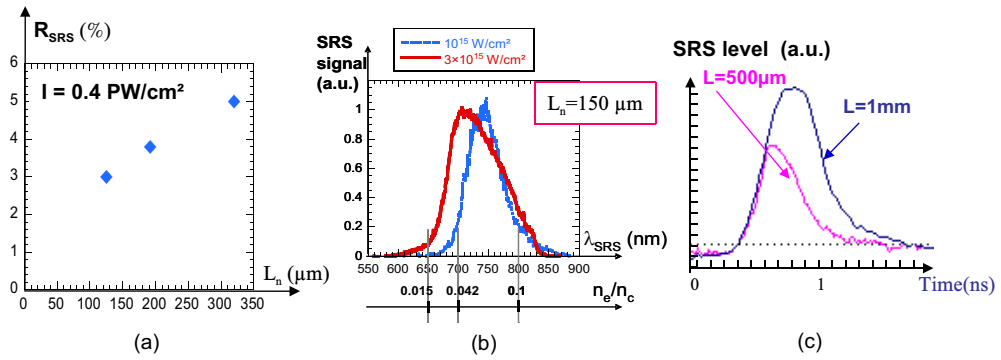

Figure 19. (*a*) SRS reflectivity as a function of the electron density scale length (LIL 3 ω experiment). (*b*) SRS spectra for two laser intensities (LULI-2000 2 ω experiment); (*c*) effect of the plasma length on the SRS reflectivity as a function of time (LIL 3 ω experiment).

the average density 3 mg cm^{-3}, the SRS spectra were quite narrow and limited by the low electron density that could be produced ($\lesssim$0.1 n_c). Using foams with the densities of 7 and 10 mg cm^{-3}, we observed that the width of the SRS spectra increased with the initial foam density showing that Raman instability could grow over a larger density range. The level of SRS reflectivity increased accordingly.

The SRS evolution as a function of the density scale length of the plasma expanding in the front part was deduced from the analysis of the scattered Raman light intensity as a function of time in the foams with the density 10 mg cm^{-3}. The scale lengths were deduced from the hydrodynamic simulations. Results are reported in figure 19(*a*), showing an increase in SRS reflectivity from 3% to 5% for the scale length increasing from 150 to 350 μm for a laser intensity of 0.4 PW cm^{-2}. However, the estimated gain factors (5) for these conditions are rather small. They vary from $G = 0.5$ for the scale length of 150 μm to $G = 2$ for the maximal one. These scale lengths are well in the range of those that will be encountered by the shock-ignition pulses, but the laser intensity is lower so that the low observed SRS levels may not be representative of what could happen under shock-ignition conditions.

The studies of the laser intensity variation on the SRS reflectivity have been performed on the LULI-2000 installation using the same foams as in the LIL campaign. The laser was at 2 ω with 400 J in 1.5 ns. The main result is that the SRS spectra are widened towards shorter wavelength when the laser intensity increased. This means that SRS extends to lower plasma densities at higher intensities, eventually to an area where the Landau damping parameter $k_p\lambda_D$ is quite high. This fact agrees with the numerical simulations presented in section 2.2. An example of such a spectral modification presented in figure 19(*b*) shows that the minimum plasma density relative to critical density where SRS activity is observed extends from 4.2% to 1.5% when the laser intensity is increased from 1 to 3 PW cm^{-2}.

The effect of the plasma length on SRS reflectivity was studied in the LIL experiments. As shown in figure 19(*c*) for the foam with the initial density of 7 mg cm^{-3} and a laser intensity of 0.6 PW cm^{-2}, the SRS reflectivity increases with the initial foam length, from 0.5 to 1 mm, and had a longer temporal duration, demonstrating an effect of the plasma corona extension.

Although the observed SRS characteristics are in general in agreement with the simulations presented in section 2.2, it is too early to draw conclusion on SRS under shock-ignition conditions. The observed tendencies as a function of the density scale length, the laser intensity and the plasma length, indicate some possible problems with Raman losses for interaction conditions of the shock-ignition scheme.

4.2. Planar shock experiments at LULI, PALS and OMEGA

As the shock-ignition scheme is relatively new, only few experiments dedicated to the shock formation have been conducted up to now, while more and more numerical simulations were widely performed recently. In particular, it is important to study the laser plasma interaction and a high-pressure shock formation in the same experiment in order to evaluate the efficiency of hydrodynamic coupling and compare the data with the simulations. This is the key point in validation of the shock-ignition concept. In this context, the experiments have been performed in the planar and spherical geometries. This section presents the results of planar experiments performed at LULI, PALS and OMEGA laser facilities, while the following section will be focused on the spherical implosions conducted at the OMEGA facility.

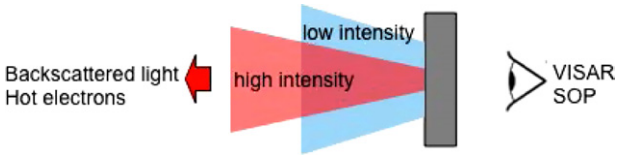

Figure 20. Principle of the experimental set-up for the planar shock experiments.

4.2.1. Experimental parameters. The planar geometry is not completely adequate for studying shock ignition as the convergence effect cannot be reproduced. However, it is extremely favourable for detailed measurements of the spike generated shock correlated with the level of parametric instabilities. The large number of diagnostics, compatible with the planar geometry, turned out to be particularly useful for accurate comparison with numerical simulations and to constrain them, giving confidence in more complex cases where the implementation of diagnostics is more difficult.

While the three laser facilities differ in their capabilities, the experiments performed at LULI [84], PALS [85, 86] and OMEGA [87] are all based on the same principle, as shown in figure 20. The targets were irradiated by a laser pulse consisting of two parts: the first one, the plasma creation pulse, was at low intensity in the range 0.01–0.2 PW cm^{-2}. It launches the first shock into the target and creates a large coronal plasma reminiscent of a shock-ignition environment. The second part provides the high-intensity spike at an intensity of 1–10 PW cm^{-2} that launches a second strong shock into the target. While the principle idea behind the experimental campaigns at each facility was the same, the experimental details were varied.

Both experiments at LULI and PALS employed one laser beam each for the low- and high-intensity part, whereas the experiments at OMEGA comprised a total of 20 beams overlapped at the target to generate the intensity profile. At LULI, the two beams were at $2\,\omega$ (wavelength $0.53\,\mu$m), whereas the wavelength at OMEGA was $0.35\,\mu$m ($3\,\omega$) and at PALS, $1\,\omega$ for the plasma creation beam and $3\,\omega$ for the spike beam. Note that PALS is an iodine laser, so the first and third harmonics correspond to wavelengths $1.33\,\mu$m and $0.44\,\mu$m, respectively. The irradiation at $1\,\omega$ for the first beam was chosen with the goal of maintaining a sufficiently high temperature despite the low intensity available in the creation beam. The pulse durations were 2 ns for each beam at LULI, and 300 ps at PALS. On OMEGA, a succession of three pulses of $\sim$1 ns was used with 0.5 ns temporal overlap between the last two pulses. This created a shaped pulse with a low intensity foot of 1 ns duration, followed by a higher intensity 0.5 ns plateau pulse and a subsequent 0.5 ns high-intensity spike.

In all experiments, to reach the necessary high intensities, the spike beam was focused to a smaller focal spot ($\varnothing \sim 100\,\mu$m for LULI and PALS, and $\varnothing \sim 600\,\mu$m for OMEGA) than the plasma creation beam ($\varnothing \sim 400\,\mu$m for LULI, $\varnothing \sim 900\,\mu$m for PALS and $\varnothing \sim 900\,\mu$m for OMEGA). At PALS and LULI, phase plates were used in the creation beam, in order to produce a large scale and relatively uniform plasma. In contrast, the spike beam was not smoothed in order to get a smaller spot and higher intensities. On OMEGA, polarization smoothing and large-spot distributed phase plates were implemented in 14 pre-plasma generating beams, while small-spot phase plates were implemented in six high-intensity spike beams. The energy contained in the spike beams was varied to give an overlapped spike intensity ranging from 0.5 to 1.5 PW cm^{-2}, while keeping the pre-plasma conditions the same throughout the experiment. The main parameters are summarized in table 1.

Since two beams were totally independent at PALS and at LULI, it was possible to vary the delay between the plasma creation beam and the spike, thus changing the plasma density scale length. By studying the delay dependence of the reflectivity, hot-electron production, and the shock velocity we are able to estimate the influence of the plasma parameters on the level of parametric instabilities and on laser absorption efficiency.

The target design and the suite of diagnostics were very similar at LULI and OMEGA. The targets consisted of multiple layers, with a plastic (CH) layer on the laser side mimicking a low-Z ablator of real ICF pellets. This layer absorbs the incident laser light, while minimizing the x-ray production that might preheat the target. The second layer made of a high-Z material (copper or molybdenum) was used to block x-rays from the front side of the plasma. It also served as a fluorescence layer to diagnose fast electrons that were generated through parametric instabilities, via K_α emission. The third target layer made of an α-quartz was used as a witness layer where the shock dynamics could be observed using the VISAR diagnostic. For the PALS experiment, the third layer was made of aluminum, since only the streaked optical pyrometer (SOP) for shock chronometry was available. The mean shock velocity was measured either with VISAR using targets with a step on the rear side, or with SOP by measuring the time between the laser arrival at the target front (through an optical time fiducial) and breakout at the rear of flat targets.

Although each of these experiments has its specificities and limitations, they are complementary and demonstrate a capacity to launch a strong shock in a large pre-plasma. Relatively small focal spots for the spike beam used at the LULI and PALS installations result in stronger 2D effects, which complicate comparisons with numerical simulations. The OMEGA experiment used significantly larger spots, which mitigates 2D effects, even though they are still present and were taken carefully into account in the data analysis. Although the duration of PALS beam matches well the required spike time, the energy of creation beam is too low to heat the pre-plasma to the keV temperatures expected in fusion targets. Moreover, the shock pressure was decreasing after the spike end, which implies the need for detailed numerical simulations connecting the measured (lower) pressure at shock breakout to the initial one created by the laser pulse. The intensities reached at PALS of up to 10 PW cm^{-2} are also interesting for studying the parametric instabilities under laser and plasma conditions that are not yet well known. A particular effort to diagnose precisely the plasma conditions has been conducted on PALS. This includes the high resolution x-ray spectroscopy [88] measuring the emission lines of chlorine dopant included in the plastic layer, the optical interferometry and a new diagnostics of plasma density based on the x-ray deflectometry [89].

4.2.2. Spike pulse reflectivity. In all experiments, a large set of diagnostics has been implemented (most of them are the same on the three experiments) to estimate, simultaneously

Table 1. Experimental parameters for the planar shock experiments.

	Plasma creation pulse				Spike pulse				Delay
	λ_L (μm)	τ (ns)	$\varnothing$ (μm)	I_L (PW cm^{-2})	λ_L (μm)	τ (ns)	$\varnothing$ (μm)	I_L (PW cm^{-2})	Δt (ns)
LULI	0.53	2.0	400	0.07	0.53	2.0	100	1.0	1–2.4
PALS	1.33	0.3	900	0.01	0.44	0.3	100	10	0–1.2
OMEGA	0.35	1.5	900	0.2	0.35	0.5	600	0.5–1.5	1.5

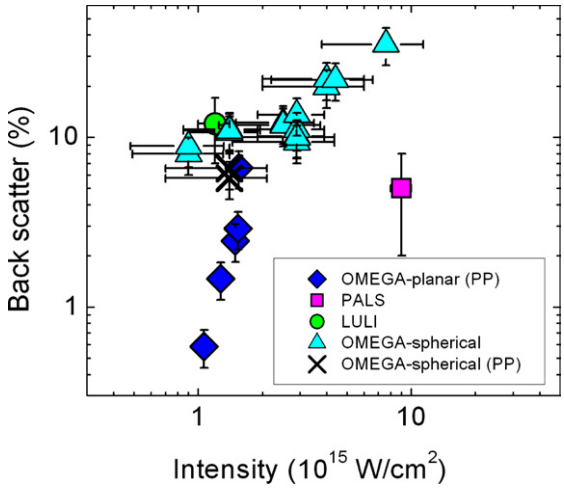

Figure 21. Reflectivities in per cent of the spike beam within the focusing cone as function of the spike intensity. The circle and the square represent the total reflectivity from the LULI and PALS experiments, respectively, while the diamonds (planar targets), the triangles (spherical shells), and the crosses (spherical shells, with phase plates) are from OMEGA. The data from spherical imploded plastic shells are discussed in section 4.3.

- the backscattered energy of the spike (time-resolved SBS and SRS reflectivities as well as time-resolved spectra);
- the hot-electron production;
- the shock velocities.

The reflectivity due to the parametric instabilities driven by the spike beam as it propagates through the large plasma have been measured. Figure 21 summarizes the measured total plasma reflectivity (SRS and SBS) within the laser beam cone obtained from three laser facilities. The backscattered fraction of light is relatively low at LULI (the total reflectivity, corresponding to the SBS and SRS, is limited to 15% at maximum). At PALS, the total reflectivity was even lower (possibly due to the shorter wavelength), always below 5% in all cases and mainly dominated by SBS. The scattered light outside the focusing cone was measured with a few calorimeters and was about of the same order of that within the cone lens, bringing the total reflectivity to $\lesssim$10%. Secondly, variation of the delay between two beams, that is, the plasma density scale length, did not affect the backscattered energy in the PALS and LULI experiments. This appears surprising because the conditions of interaction are expected to change dramatically. In contrast to the PALS and LULI results, a strong increase in the plasma reflectivity with the spike intensity was measured on OMEGA. However, for planar targets and intensities of up to 1.5 PW cm^{-2}, a total reflectivity within the focal cones of up to 6% was measured, which is lower than in the LULI and PALS experiments. This may be explained by multiple overlapping beams equipped with distributed phase plates used on OMEGA. Lower plasma reflectivity and better coupling is expected for smoothed laser beam profiles.

Another set of experiments were performed with spherical targets, which is discussed in more detail in section 4.3. In those experiments, tightly focused beams were directed onto an imploding plastic shell target. Most of the shots were performed without beam smoothing in the spike beams (triangles) and only a couple of shots were performed with small-spot phase plates (cross). As expected, better coupling is achieved with phase plates and a back reflection of a few per cent in the $\sim$1 PW cm^{-2} range was measured for both planar and spherical targets. Without phase plates and intensities reaching $\sim$8 PW cm^{-2}, the reflectivity strongly increased up to 36% (triangles), which is significantly higher than the PALS results. Although a general trend of increasing reflectivity with the spike intensity is seen in figure 21, the differences between the experiments are not fully understood. They may be due to differences in the target geometry and the laser wavelength.

OMEGA experiments showed a strong increase in SRS reflectivity with intensity and SRS dominated the back scatter signal at the highest intensity [46]. Only a modest increase in SBS reflectivity was observed with intensity. The SRS data are in agreement with numerical simulations presented in section 2.2 that also predict a large SRS signal [44]. In the spherical target experiments, almost all of the backscattered light was detected within the cone of the laser beam with very little side-scattering. This is attributed to the strong interaction of single high-intensity beams with the plasma corona creating a channel through the underdense plasma up to the critical density, which guides back reflected laser light within a certain solid angle. In contrast, the planar OMEGA experiments were performed with multiple overlapping beams where channelling is not of importance and side scattering was significantly higher. Preliminary analysis indicates that a few per cent of the laser energy is scattered outside of the laser cone.

Figure 22 shows an example of Raman backscattered spectra obtained at PALS for three delays. According to the formula (4) from the SRS spectral shift, the recorded scattered light spectrum in the range from 680 to 720 nm (FWHM) corresponds to plasma densities between 0.09 and 0.16 n_c. No sign of emission from the layer at $n_c/4$ is obtained, and the spectrum does not depend on the time delay between two laser pulses. These features could either indicate a strong absorption in the plasma corona or the spike beam FI and cavitation as that predicted in [49], see also section 2.3. These processes could partially decouple the spike beam from the dense plasma implying generation of a lower pressure shock.

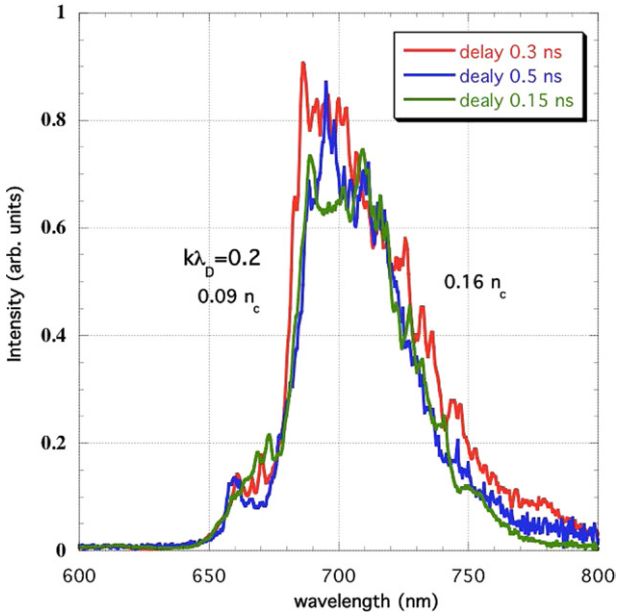

Figure 22. Backscattered Raman spectra obtained at PALS at different pre-pulse delays.

4.2.3. Hot-electron generation. Hot electrons, which are principally generated by parametric instabilities such as SRS and TPD as it discussed in section 2.1, are an important element of the shock-ignition scheme. They might be either beneficial and increase the strength of the shock wave or they are detrimental and lead to preheating of the compressed capsule. This depends essentially on the energy of these electrons and the time when they are generated. Careful characterization of the hot-electron population is therefore required and has been inferred from K_α spectroscopy and x-ray diodes in these experiments. The planar target experiments on OMEGA show a conversion efficiency of 2% of the spike beam energy into hot electrons and temperatures of ~70 keV at the highest intensity [87]. The numbers are inferred from spectroscopy of the Mo K_α emission from a diagnostic layer using an absolutely calibrated spectrograph and a time-resolved multi-channel hard x-ray detector. Both, the hot-electron number and the temperature increase with laser intensity. It is interesting to note that in the spherical OMEGA experiments significantly lower temperatures around 30 keV were measured [46]. Comparison of these data with numerical simulations discussed in sections 2.2 and 2.3 indicates that SRS is the primary generation mechanism and TPD is significantly suppressed.

The results obtained from K_α emission at LULI are partial because only very energetic electrons with the energy higher than 60 keV were able to reach the second layer and to excite K_α emission. The K_α signal was found to be always below the noise level, giving an estimation of a very low laser light fraction converted into hot electrons with energies above 60 keV. This result is consistent with the measured weak value of SRS reflectivity and with the numerical simulations presented in section 2.2.

The results on hot electrons at PALS were obtained from K_α emission using both a single-hit CCD and a K_α imager based on a spherically bent crystal and a CCD detector. The energy of fast electrons was estimated using targets with a plastic layer of different thicknesses. From the dependence of the K_α signal on the target thickness, the average electron energy electron was evaluated to be ~50 keV. The total number of fast electrons was low—the conversion efficiency of laser energy to fast electrons does not exceed 1%. This is consistent with a low measured level of parametric instabilities.

4.2.4. Shock pressure measurements. The measurements of the shock velocity are particularly important because they provide an accurate estimation of the shock pressure and hence of the overall coupling efficiency, that is, the energy conversion from the laser beam to the shock. There are two ways for measuring shock velocity: the instantaneous velocity at the rear side from a VISAR diagnostic (employed at LULI and OMEGA), and the mean velocity, using step targets (PALS) and comparing relative propagation times through the targets of different thicknesses.

The measurements of shock breakout recorded on the three facilities have been compared with 2D hydrodynamic simulations, as well as the instantaneous shock velocity obtained from the VISAR diagnostic at LULI and OMEGA. Pressures are deduced from the measured shock velocity coupled to tabulated Sesame EOS [90]. In all cases, the pressure created by the spike is found to be lower than the expected ablation pressure using the nominal on-target intensity and the formula (1). This emphasizes that knowledge of the absorbed laser energy is crucial in the shock-ignition scheme, and laser coupling with the large pre-plasma has to be studied very precisely. As was discussed in section 3.1, the expression (1) for the ablation pressure is based on simplified assumptions, such as localized collisional laser absorption near the critical density. It is therefore not expected to fully capture the absorption physics. Good agreement between experiment and simulations is obtained for LULI and OMEGA. The experimentally estimated pressure as well as the different events during the propagation of the spike shock (coalescence and shock breakout) are well reproduced in simulations.

Figure 23(*a*) presents a typical image obtained from the VISAR diagnostic on the LULI experiment. On this time-resolved image, one can clearly observe the breakout of the first shock at the Ti–SiO_2 interface and the coalescence between the first shock generated by the plasma creation beam and the strong shock launched by the spike beam. The delay between two beams is 1.7 ns and the coalescence corresponds to the time when the shock driven by the spike beam catches up with the shock of the first beam. The velocity profiles as a function of time obtained from the measured data and numerical modelling are shown in figure 23(*b*). Good agreement between experiment and simulation for the first four nanoseconds allows estimating correctly the pressure of the spike shock, which is, under these conditions, of around 40 Mbar in CH.

The 2D effects arising from the small focal spot size of the spike beam at LULI have been carefully considered. Despite the larger focus in the OMEGA experiments, 2D effects are also important and were considered in the modelling. Concerning the pressure, from the 2D simulations, the pressure of the spike is around 40 Mbar in the LULI experiment, which is in agreement with the shock velocity measured in the experiment [84]. This pressure is in agreement with

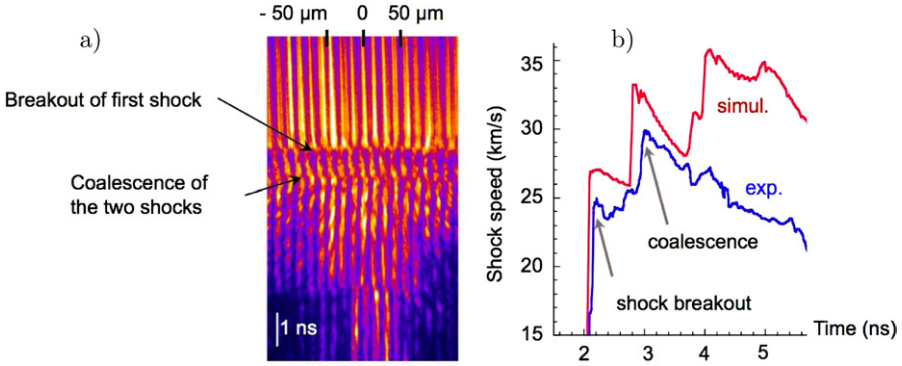

Figure 23. (*a*) VISAR image recorded for a delay of 1.7 ns between the two beams. Laser beams irradiate the target from the top side of the figure and the time goes down. (*b*) Velocity profiles as a function of time corresponding to (*a*) from measured data (blue) and numerical modelling (red).

equation (1) if the absorption coefficient of the order of 60% is accounted for. It is essentially due to the collisional absorption under the LULI conditions. Similar results were obtained on OMEGA. Here, the obtained pressure was higher and reached up to 70 Mbar for a peak intensity of 1.5 PW cm^{-2} in the planar geometry [87]. The pressure was corrected for the impedance mismatch arising from the CH–Mo interface. Excellent agreement, better than 5%, between the measured and predicted shock breakout times was obtained. Based on the comparison of inferred pressure and predicted pressure from a simple model (1), the coupling of the laser energy into the plasma is estimated between 60% and 80%, slightly higher than in the LULI experiment.

Comparisons of experimental data with simulations for the PALS experiment are more difficult due to stronger 2D effects linked to the small focal spot and the short duration of the spike. Both effects are not favourable for maintaining the shock. These factors can contribute to explain a larger discrepancy observed between experimental results and simulations. At PALS, the experimentally observed shock velocity at the rear side of the target is compatible with an initial shock pressure, generated by laser–matter interaction at the target front, of about ∼90 Mbar. Although this is the highest pressure measured in these three experiments, it is significantly lower than what is expected on the basis of equation (1). Such a difference can be explained either as a result of FI taking place in the plasma, spreading the beam and reducing the effective on-target intensity, or due to the collective processes that are governing energy transport and shock formation. These effects have already been discussed in section 4.1.2. The FI threshold [21] is certainly exceeded in all three experiments. A precise evaluation of such a threshold is, however, quite difficult because the spatial quality of the spike beams was not well controlled. When phase plates were not used (in order to achieve the required intensities), the laser beam focal spot contains hot spots with significant variations of intensity from point to point, that are difficult to predict, especially if one considers their evolution during propagation in the plasmas. It is even more difficult to evaluate the impact of FI on beam spreading. Therefore, more experiments with better characterized more energetic laser beams and better beam smoothing are required. Additional modelling efforts are needed to study the impact of hot-electron transport and the self-generated magnetic fields on shock formation.

Nevertheless, the first results from planar experiments are encouraging. Spike generated peak pressures of up to ∼90 Mbar are inferred from the measured shock velocities. Although this is not yet as high as needed for shock ignition, interesting physical effects are emerging. Special efforts to diagnose more precisely the propagation of high-intensity laser beam in the large pre-plasma and a more complete study on fast electron production and transport should be conducted in order to evaluate the validity of shock ignition as a viable ICF alternative scheme.

4.3. Shock-ignition implosions at OMEGA

Shock ignition separates the fuel assembly phase from the ignition phase by compressing a massive capsule on a low adiabat ($\alpha \sim 1$) using a low implosion velocity ($u_{\rm imp} \lesssim 300\,{\rm km\,s^{-1}}$). The ignition phase is initiated by launching a strong (∼300 Mbar) shock in the interaction region. The shock increases in strength while propagating through the imploding and converging shell leading to a non-isobaric hot spot. One way to generate a strong shock is by adding a high power laser spike at the end of the drive pulse. The OMEGA facility has the capability that allows us to investigate important physics issues of the shock-ignition scheme using surrogate implosions. This includes questions of how a power spike at the end of a drive pulse affects the hydrodynamic stability of the shell and what effect it has on the shell compression and the hot-spot compression.

The relative effect of the shock can be investigated by comparing the implosion performance with and without spike. OMEGA spherical shell experiments also address the sensitivity of implosion to laser–plasma instabilities during the high-intensity spike. The experimental campaigns of imploded spherical shells on OMEGA provide first demonstrations of the feasibility and advantages of the shock-ignition scheme. Two approaches have been pursued in the recent years: 60-beam symmetric implosions that use the same pulse shape with a late power spike on all 60 beams (that demonstrated an improvement in the neutron yield and in target compression) and a configuration that uses 40 low intensity beams for compression and 20 high-intensity spike beams for shock generation in laser–plasma interaction studies. The latter approach allows one to increase significantly the single-beam spike intensity and to evaluate

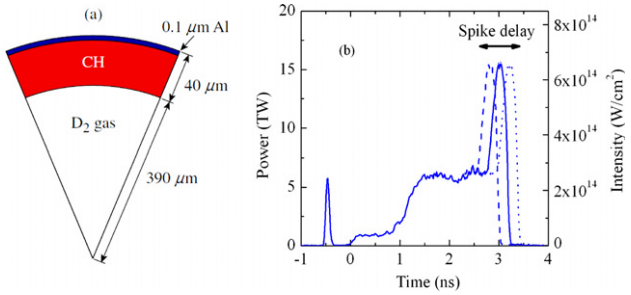

Figure 24. (*a*) Warm plastic shell used on the first shock-ignition 60-beams implosions. (*b*) Typical shock-ignition pulse shape with a variable spike delay.

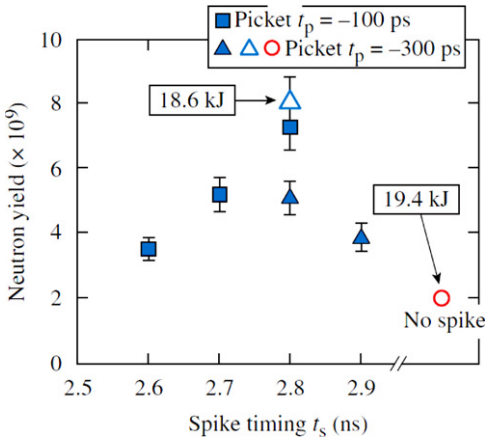

Figure 25. Measured neutron yield as a function of the onset of the spike pulse. Reprinted from [72] with permission from the American Institute of Physics. Copyright 2008, AIP Publishing LLC.

their effect on the hydrodynamic performance and their role on laser–plasma interaction processes at laser intensities that are relevant for shock-ignition. This approach is also relevant for shock-ignition designs on NIF [2, 6] or LMJ [7], where composite irradiation schemes are under study [91, 92].

4.3.1. Symmetric 60-beam implosions. Plastic shell targets filled with deuterium gas, see figure 24(*a*), are convenient to study basic physics issues of the shock-ignition concept in terms of the correct timing of the spike shock wave and the rebound shock wave from the target centre [72]. This is crucial for shock ignition since the concept relies on a proper timing of both shocks in order to obtain a non-isobaric fuel assembly in the core that is necessary for ignition. Experiments were performed with 40 μm thick shells covered with a thin Al layer and with an outer radius of ~430 μm. The shell were filled typically with ~25 atm of D_2 gas. The implosion performance was optimized by varying the timing of the front picket pulse and the late power spike see figure 24(*b*). We concentrate here on the timing of the spike. Figure 25 shows the measured neutron yield for a series of implosion with various spike onset times. Data are included for two picket timings. Most of the shots were performed with ~17 kJ of laser energy and only two shots were performed with higher energy, as indicated in the figure. Maximum yield was obtained with an implosion with a 2.8 ns spike delay and 18.6 kJ of laser energy that performed better than an implosion without spike and laser energy of 19.4 kJ. This demonstrates that with proper timing, shock-ignition implosions lead to significantly improved neutron yield. The neutron and proton yields are, respectively, four and five times higher.

These enhanced performances were not expected based on 1D yield calculations, which only predicted a 30% yield enhancement by the spike for our conditions. A survey study was performed at the optimum timing for a range of convergence ratios of the implosions, which was changed with the shell-fill pressure (from 7 to 30 atm). The convergence ratio is calculated and is defined as the initial inner radius of the target shell divided by the minimum radius of the gas–shell interface at peak compression. The convergence ratio increases with a lower fill pressure. The ratio of the measured to the 1D predicted neutron yield, the yield-over-clean (YOC), is significantly higher in surrogate shock-ignition implosions compared with standard implosions, see figure 26(*a*). In the standard implosions without spike the YOC decreased by a factor of 4 down to ~1%, when convergence ratio was increased from ~11 to ~23, which suggests an increased small-scale mixing for smaller hot-spot radii. In comparison, implosions with spike demonstrate a YOC close to 10% indicating that mixing of cold shell material into the hot spot was mitigated.

The higher stability of the shell implosion is also confirmed by the small standard deviation of areal density measurements from the different lines of sight. Neutron rate averaged areal densities, ρR, of the order of 200 mg cm^{-2} were inferred from individual proton spectra measured from different lines of sight with wedge range filters [93]. Figure 26(*b*) shows the corresponding measured ρR as a function of the convergence ratio and demonstrates that higher areal densities were achieved with increasing convergence ratio in shock-ignition implosions. Up to ~35% higher compression was achieved compared with implosions without the spike. These results again indicate that shock-ignition implosions with optimally timed pulse shapes show an improved performance, suggesting less instability growth.

It is not yet clear why the shock-ignition implosion perform much better than predicted, but there are several possible explanations. Large convergence ratios and the slow assembly make plastic shells inherently Rayleigh–Taylor unstable during the deceleration phase. This gives rise to a substantial mixing of colder plastic shell material into the hot, compressed D_2 gas that quenches fusion reactions and generally results in a low YOC. Mixing is enhanced in these low-velocity implosions because the hot spot is small relative to the target size. The improved performance of shock-ignition implosions suggests that the mixing processes were mitigated for optimal shock wave timing. This might be caused by the impulse acceleration by the spike shock wave shortening the time period for instability growth or by steepening of the density profile at the inner shell surface. It is interesting to note that simulations with spike pulses [5, 69] predict the quenching of Rayleigh–Taylor growth by the spike, which was also measured in Rayleigh–Taylor experiments in the planar geometry [71].

So far, only a handful of cryogenic target 60-beam shock-ignition implosions were performed. The results are encouraging and the imploded shell reach close to the 1D

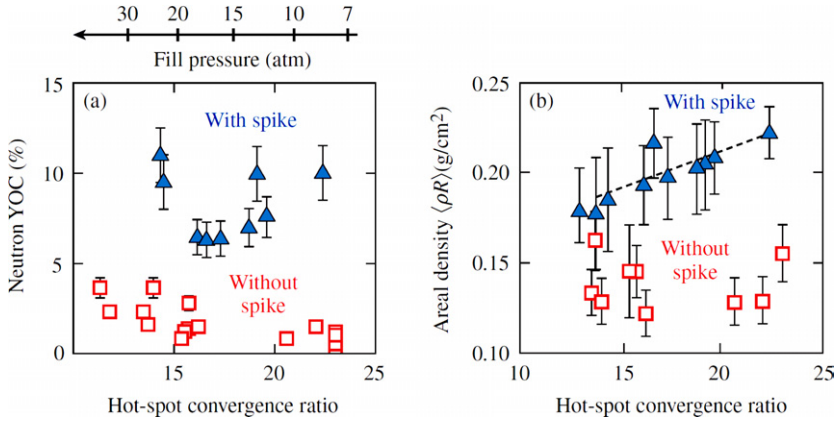

Figure 26. (*a*) The neutron YOC and (*b*) the measured areal density versus 1D calculated hot-spot convergence ratio. Reprinted from [72] with permission from the American Institute of Physics. Copyright 2008, AIP Publishing LLC.

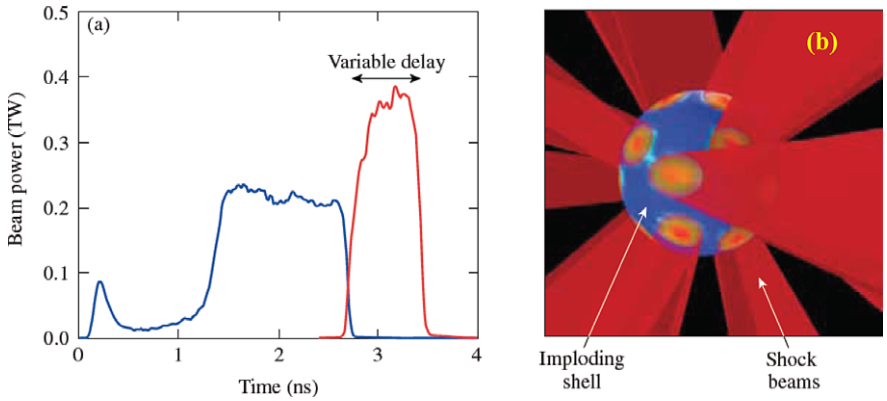

Figure 27. (*a*) The drive-pulse shape (blue) for the 40 beams and the high-intensity pulse (red) for the 20 spike beams. (*b*) Schematics of the 20 delayed spike beams tightly focused onto the critical-density surface.

predicted compression and the measured neutron yields were about 10% of the 1D predictions [72]. Unfortunately, symmetric 60-beam experiments on OMEGA with standard size targets only allow laser intensities of up to ∼0.8 PW cm^{-2} in the power spike, which is almost an order of magnitude lower than what is required [6]. The laser generated pressures are limited to ∼50 Mbar and are much weaker than the required 300 Mbar ablation pressure.

4.3.2. 40+20 beam implosions. In order to overcome the intensity limitation of standard 60-beam implosions, a new platform was developed that uses 40 beams with a low intensity to implode a capsule and the remaining 20 beams at a much higher intensity to interact with the converging shell later in time [46, 94]. Typical pulse shapes for the compression and spike beams are shown in figure 27(*a*). Different focusing options were tested for the spike beams allowing scanning of the single-beam intensity from 0.5 up to 8 PW cm^{-2}. The hydrodynamic performance of plastic shells filled with deuterium gas was studied both in experiments and in 2D hydrodynamic simulations. The experiments indicate a significant energy coupling by the high-intensity spike beams into the capsule that is partially driven by a hot-electron component of a moderate temperature of ∼30 keV and an increased thermal component. It should be mentioned that in these experiments the high-intensity spike beams did not overlap, as indicated in figure 27(*b*), and that the moderate hot-electron temperature is probably the result of an isolated beam interaction. The multiple overlapping high-intensity beams have the capability of producing much hotter electron distributions [95].

The experimental observables indicate that the hot electrons are primarily generated by SRS. The new platform also enables backscatter measurements at single-beam intensities of up 8 PW cm^{-2}. Total reflectivity of up to 36% was measured, see figure 21, and the light is primarily scattered back into the high-intensity beam without significant side scattering.

Hydrodynamic simulations with the 2D DRACO code [96] show the formation of a channel by a tightly focused single high-intensity beam. This channel might be responsible for collimation most of the scattered light back into the focusing lens. The suppression of TPD was observed with increasing laser intensity and a decreasing blue shift of the SBS signal, which is attributed to that the SBS activity shifts to higher plasma densities with increasing spike intensity. At the highest intensity, SBS from around the quarter-critical density was measured. The interaction of driven ion acoustic and electron plasma waves at around quarter-critical density might play a role in the suppression of TPD.

With increasing intensity, a strong reduction in the optical emission at the half-harmonic, $\omega/2$, of the laser frequency was

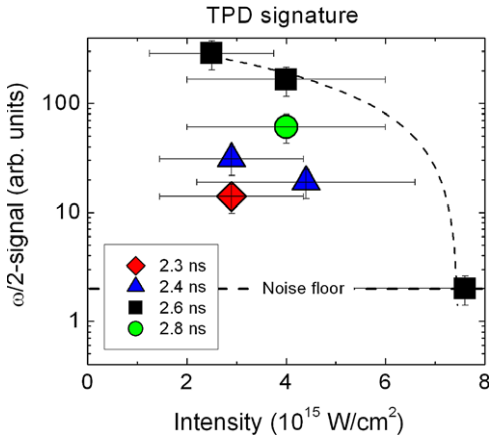

Figure 28. Measured $\omega/2$ signal for various spike intensities and different spike onset times.

observed, see figure 28. The $\omega/2$ signal decreased by more than two orders of magnitude in the experimental intensity range. At the maximum intensity, the $\omega/2$ signal was below the detection threshold, indicating no significant contribution of TPD to the hot-electron production. This and the relatively low hot-electron temperature of ∼30 keV supports the conjecture that SRS plays the dominant role in hot-electron production in these experiments. The strong reduction of $\omega/2$ with intensity, together with the observed shift of the SBS active region to quarter-critical density might indicate that driven ion acoustic waves play a role in the reduction of TPD. Most of the experiments were performed without phase plates in the spike beams and this makes the spike beams vulnerable to FI instabilities that probably disrupted the beams. The 20 spike beams were equipped in a few shots with small-spot phase plates. Encouraging results were obtained, indicating an enhanced coupling despite that a slightly hotter electron population was generated.

Important information was obtained from neutron yield measurements in the 40+20 experiments. It was found that the neutron yield enhancement when adding the 20 spike beams was independent of the single-beam spike intensity. Figure 29(*a*) shows that adding the 20 spike beams, and therefore more energy on target, enhances the yield by a factor of up to 2.3, with a trend of slightly lower yields at later spike onset. The neutron yield shows no significant dependence on the spike intensity. A similar trend is observed in the predicted neutron yield from 1D simulations. There the enhancement is up to a factor of ∼3.5 when adding the spike beams, slightly more than what was measured. A possible explanation why the yield increase is less than predicted might be that the 20 spike beams slightly increased illumination non-uniformities. The YOC was varied from 3% to 5% for these experiments. 2D CHIC [20] simulations show that even if some spike laser imprint in the corona is observed at high intensities, the pressure remains fairly symmetric, independently of the spike intensity on target. Figure 29(*b*) shows electron temperature (top half) and pressure (bottom half) maps obtained from various 2D simulations. Hot electrons were not included in the simulations. Independent of the spike intensity on target the pressure remains symmetric with the same value of ∼75 Mbar. Some slight pressure modulations are observed at the highest intensity. The simulations show that the temperature in the conduction layer is fairly symmetric, which explains why the spike pressure keeps the same values in all the cases and as a consequence also the neutron yield. The neutron measurement therefore might be an indication of a mechanism that provides efficient isotropization of the electron heat flux in the conduction layer of the plasma, as was discussed in section 3.2.1.

4.4. Concluding remarks

Concluding this section, we comment on the current status of comparison of the experimental data with the numerical simulations. Although many particular features in the experiments have been understood and explained qualitatively, complete numerical simulations of the experiment and the diagnostics are not yet available. The laser–plasma interaction physics and the kinetic electron transport need to be included in the radiation hydrodynamic codes in order to describe the laser energy deposition, the hot-electron transport, the shock formation and their effects on the hot-spot formation and ignition self-consistently. The implosion simulations are limited in many cases to spherically symmetric geometry, and the 2D effects are not sufficiently investigated. The implosion experiments conducted on Omega are showing a relatively good agreement with the simulations, but the laser intensities were limited to 5 PW cm^{-2} for single spike beam interaction. The beam quality for the spike has to be improved, as few experiments were carried out with phase plates due to the need to achieve a high laser intensity.

In the 40 + 20 implosions, the shots performed with phase plates for the spike beams evidence an earlier bang time, in correlation with a higher hard x-ray signal [46]. This indicates that the hot-electrons affect the hydrodynamic implosion. The areal-density degradation in SI experiments on OMEGA is well correlated with measurements of hot electrons from the spike [97]. In fact, the areal density on OMEGA is low enough that hot electrons degrade (rather than improve) the implosion performance. This is a subject of current investigations. Another open question is the experimental timing of the spike coalescence in the spherical geometry, as well as a measurement of the spike ablation pressure. Small solid plastic ball targets with diameter of ∼450 μm and doped with a x-ray emitter (such a titanium) have recently been proposed. They can be irradiated with 60 beams equipped with small-spot phase plates in order to reach an overlapping beam intensity of ∼5 PW cm^{-2}. The x-ray flash generated at the shock coalescence time could be used to infer the shock strength. A clear performance enhancement by a spike shock in the case of cryogenic implosions still needs to be demonstrated. The database for cryogenic SI experiments is scarce [72], even if an excellent performance relative to 1D simulations was recently reported [98]. A long-term effort and dedicated resources are required to build a statistical meaningful database of cryogenic SI implosions in order to gain a better understanding of the physics issues of spike beam coupling and its effect on the compression.

In contrast, the planar experiments allow a very good accessibility for diagnostics but they do not account for the convergence effects, which are the essential aspect of all

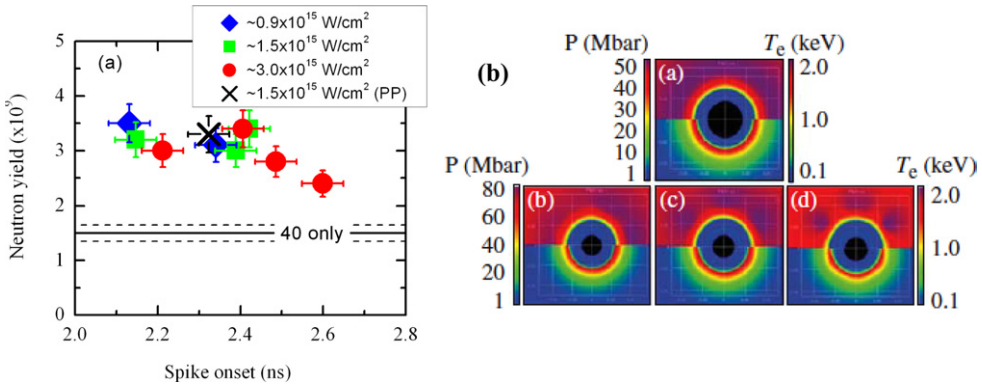

Figure 29. (*a*) Measured neutron yield for various spike onset times and spike intensities. (*b*) 2D CHIC simulations for different spike intensities. Electron temperature (top half) and pressure (bottom half). Reprinted from [46] with permission from the American Institute of Physics. Copyright 2012, AIP Publishing LLC.

inertial fusion schemes. The hydrodynamic simulations could successfully reproduce the results of planar experiments at LLE, LULI and PALS, but the experiments on low energy installations are strongly limited by the multi-dimensional effects. For this reason, one needs to employ longer laser pulses in order to maintain the ablation for a sufficient time to form a high-intensity shock and to observe it with a high accuracy. In particular, the problem at PALS with a very short laser pulse duration of 250 ps is that numerical simulations can reproduce the target hydrodynamics but they also predict a quite low absorption of laser light, which is not seen in the experiment. The measured back reflected light, either due to parametric instabilities or reflection, is quite low. The scattering on large angles, outside of the laser focusing optics, needs to be measured.

Concerning the parametric instabilities and hot-electron generation, one could note that back reflected light is largely dominated by SBS (or reflection of the incident laser light) in the LULI and PALS experiments, while on OMEGA, the SRS is the dominant component, in agreement with the results of kinetic simulations presented in section 2.2. Such differences could be explained by the multi-dimensional effects and require 2D kinetic simulations. Also all planar experiments in the intensity range of a few PW cm^{-2} show a lower efficiency of hot-electron generation in apparent disagreement with the predictions of kinetic simulations presented in section 2.2. In the spherical experiments [46], the average energy of generated electrons is in the range 30–40 keV, in agreement with simulations. There are a number of physics issues in hot-electron generation and laser-plasma interaction that are not understood. Planar target experiments with multiple overlapping beams [87, 95] measure higher hot-electron temperatures that are increasing with laser intensity in contrast to spherical target experiments with isolated spike beams where a moderate hot electron temperature was measured that did not depend on the single-beam intensity. In addition, estimated hot-electron numbers from planar target experiments seem to be lower than what is predicted by simulations. Although kinetic simulations that were presented in section 2.2 seem to be in agreement with the spherical target results, the role of beam smoothing and the beam interference effects are not fully understood and larger scale 2D simulations with multiple beams are required to clarify the physics issues of laser–plasma interaction and hot-electron generation.

5. Conclusion

The shock-ignition scheme has a relatively short history of about five years of intense studies. Although serious issues related to laser–plasma interaction, energy transport and target hydrodynamics need further investigations, none of these present an insurmountable obstacle. The major feature of shock ignition combining the idea of separation of the implosion and ignition processes with a relatively low (sub-petawatt) ignition power makes it very attractive for direct testing on the major high energy laser installations NIF and LMJ. Although many problems remain to be solved, they are clearly identified.

The laser–plasma interaction is the major unresolved point in the shock-ignition scheme. The existing multi-kilojoule laser installations except NIF and LMJ cannot provide at the same time the needed laser intensity and the spot size. So, the possibility to realize the ablation pressure in the 300 Mbar range is not yet demonstrated. The experiments with laser intensities exceeding the level of 1 PW cm^{-2} are made with very small focal spots, with a size that is comparable to the distance between the absorption and ablation zones. Thus the absorbed energy flux was not transported to the shock formation region.

Several encouraging results have been already demonstrated. The OMEGA implosions in the spherical geometry show a clear improvement of the shell convergence ratio and the target areal density. The experimental results with warm shells are exceeding the theoretical expectations. Further experiments with the cryogenic targets will provide more information about the shock-wave propagation and its effect on the compressed core.

The parametric instabilities in plasma corona remain the important issue. The observed SBS and SRS reflectivities in many experiments are in the range of tens of per cent, which are comparable or below the theoretical estimates and numerical simulations. However, some experiments show higher reflectivity levels and production of energetic electrons. The simulations show the TPD instability near the quarter-critical density suppressed in the competition with the SRS, and this effect is corroborated in the OMEGA experiments. The methods of spatial and temporal laser beam smoothing are not yet studied for the shock-ignition conditions. They can

be applied in future experiments on the facilities with a larger laser energy. The hot electrons with energies in the range below 100 keV should not penetrate the shell, but they may contribute to creation of a stronger ablation pressure. This issue of the hot-electron transport needs further studies.

Awaiting first results of the integrated experiments on the NIF and LMJ in coming years, the studies of physical processes in the shock-ignition scheme are in progress. Tight connections between the experiments, numerical simulations and theoretical developments provide an excellent opportunity for better understanding and control of such crucial issues as the laser coupling efficiency, hot-electron transport, ablation pressure generation and the stability of shell implosion.

Acknowledgments

The authors acknowledge the fruitful collaboration and discussion with all colleagues who contribute to the studies presented in this review. This work was performed within the framework of the HiPER project EC FP7, project no 211737. It is partly supported by the EURATOM within the 'Keep-in-Touch' activities and the Aquitaine Regional Council. The work on OMEGA was supported by the US Department of Energy, Office of Fusion Energy Sciences under Contracts DE-FC02-04ER54789 and DE-FC52-08NA28302. The support to O.K. by the Czech Science Foundation, project P205/11/P660 is acknowledged. 1D PIC simulations were calculated on the HPC resources of CINES under the allocation 2013-056129 made by GENCI.

References

[1] Shcherbakov V.A. 1983 *Sov. J. Plasma Phys.* **9** 240
[2] Betti R. *et al* 2007 *Phys. Rev. Lett.* **98** 155001
[3] Lafon M., Ribeyre X. and Schurtz G. 2010 *Phys. Plasmas* **17** 052704
[4] Nora R. and Betti R. 2011 *Phys. Plasmas* **18** 082701
[5] Ribeyre X. *et al* 2009 *Plasma Phys. Control. Fusion* **51** 015013
[6] Perkins L.J. *et al* 2009 *Phys. Rev. Lett.* **103** 045004
[7] Canaud B. and Temporal M. 2010 *New J. Phys.* **12** 043037
[8] Schmitt A.J. *et al* 2010 *Phys. Plasmas* **17** 042701
[9] Atzeni S. 2013 Inertial fusion with advanced ignition schemes: fast ignition and shock ignition *Laser Plasma Interactions and Applications* (Scottish Graduate Series) ed P. McKenna *et al* (Switzerland: Springer)
[10] Fabbro R., Max C. and Fabre E. 1985 *Phys. Fluids* **28** 1463
[11] Lindl J. 1995 *Phys. Plasmas* **2** 3933
[12] Atzeni S. and Meyer-ter-Vehn J. 2004 *The Physics of Inertial Fusion* (Oxford: Clarendon)
[13] Moses E.I. and Wuest C.R. 2005 *Fusion Sci. Technol.* **47** 314
[14] Ebrardt J. and Chaput J.M. 2010 *J. Phys.: Conf. Ser.* **244** 032017
[15] Garban-Labaune C. *et al* 1982 *Phys. Rev. Lett.* **48** 1018
[16] Drake R.P. *et al* 1984 *Phys. Rev. Lett.* **53** 1739
[17] Michel P. *et al* 2011 *Phys. Rev.* E **83** 046409
[18] Solodov A.A. and Betti R. 2008 *Phys. Plasmas* **15** 042707
[19] Skupsky S. *et al* 2004 *Phys. Plasmas* **11** 2763
[20] Maire P.H., Abgrall R., Breil J., and Ovadia J. 2007 *SIAM J. Sci. Comput.* **29** 1781
[21] Kruer W. 1988 *The Physics of Laser Plasma Interactions* (New York: Addison-Wesley)
[22] Emery M.H. *et al* 1982 *Phys. Rev. Lett.* **48** 253
[23] Pesme D. *et al* 1993 Interaction collisionelle et collective *La Fusion Thermonucleaire par Laser* vol 1, ed R. Dautray and J.-P. Watteau (Paris: Eyrolles)
[24] Pesme D. *et al* 2002 *Plasma Phys. Control. Fusion* **44** B53
[25] Lushnikov P.M. and Rose H.A. 2006 *Plasma Phys. Control. Fusion* **48** 1501
[26] Grech M. *et al* 2009 *Phys. Rev. Lett.* **102** 155001
[27] Skupsky S. and Craxton R. S. 1999 *Phys. Plasmas* **6** 2157
[28] Vu H., DuBois D. and Bezzerides B. 2001 *Phys. Rev. Lett.* **86** 4306
[29] Rosenbluth M.N. 1972 *Phys. Rev. Lett.* **29** 565
[30] Liu C.S. and Rosenbluth M.N. 1976 *Phys. Fluids* **19** 967
[31] Simon A. *et al* 1983 *Phys. Fluids* **26** 3107
[32] Seka W. *et al* 2009 *Phys. Plasmas* **16** 052701
[33] Liu C.S., Rosenbluth M.N. and White R.B. 1974 *Phys. Fluids* **17** 1211
[34] Koch P. and Williams E.A. 1984 *Phys. Fluids* **27** 2346
[35] Menyuk C.R. *et al* 1985 *Phys. Fluids* **28** 3409
[36] Afeyan B. and Williams E. 1997 *Phys. Plasmas* **4** 3788
[37] Afeyan B. and Williams E. 1995 *Phys. Rev. Lett.* **75** 4218
[38] Afeyan B. and Williams E. 1997 *Phys. Plasmas* **4** 3845
[39] Weber S. *et al* 2012 *Phys. Rev.* E **85** 016403
[40] Vu H.X. *et al* 2010 *Phys. Plasmas* **17** 072701
[41] Yan R. *et al* 2012 *Phys. Rev. Lett.* **108** 175002
[42] Vu H.X. *et al* 2012 *Phys. Plasmas* **19** 102703
[43] Regan S.P. *et al* 2010 *Phys. Plasmas* **17** 020703
[44] Klimo O. *et al* 2010 *Plasma Phys. Control. Fusion* **52** 055013
[45] Klimo O. *et al* 2011 *Phys. Plasmas* **18** 082709
[46] Theobald W. *et al* 2012 *Phys. Plasmas* **19** 102706
[47] Weber S., Riconda C. and Tikhonchuk V.T. 2005 *Phys. Rev. Lett.* **94** 055005
[48] Klimo O. and Tikhonchuk V.T. 2013 *Plasma Phys. Control. Fusion* **55** 095002
[49] Riconda C. *et al* 2011 *Phys. Plasmas* **18** 092701
[50] Yin L. *et al* 2012 *Phys. Plasmas* **19** 056304
[51] Yin L. *et al* 2012 *Phys. Rev. Lett.* **108** 245004
[52] Malone R.C., McCrory R.L. and Morse R.L. 1975 *Phys. Rev. Lett.* **34** 721
[53] Spitzer L. and Härm R. 1962 *Phys. Rev.* **89** 977
[54] McCall G.H. *et al* 1983 *Plasma Phys.* **25** 237
[55] Tan T.H. *et al* 1983 *Phys. Fluids* **24** 754
[56] Burnett N.H. *et al* 1981 *Appl. Phys. Lett.* **38** 226
[57] Gus'kov S.Yu. *et al* 1983 *Sov. J. Quantum Electron.* **13** 498
[58] Evans R.G. 1983 *Laser Part. Beams* **1** 231
[59] Evans R.G. 1986 *Plasma Phys. Control. Fusion* **28** 157
[60] Betti R. *et al* 2007 *J. Phys.: Conf. Ser.* **112** 022024
[61] Bell A.R. and Tzoufras M. 2011 *Plasma Phys. Control. Fusion* **53** 045001
[62] Deutsch C., Furukawa H., Mima K. and Nishihara K. 2000 *Phys. Rev. Lett.* **85** 1140
[63] Li C.K. and Petrasso R.D. 2004 *Phys. Rev.* E **70** 067401
[64] Guskov S. *et al* . 2012 *Phys. Rev. Lett.* **109** 255004
[65] Ribeyre X. *et al* 2013 *Phys. Plasmas* **20** 062705
[66] Zhou C.D. and Betti R. 2007 *Phys. Plasmas* **14** 072703
[67] Ribeyre X. *et al* 2011 *Phys. Plasmas* **18** 102702
[68] Bodner S.E. 1981 *J. Fusion Energy* **1** 221
[69] Atzeni S., Schiavi A. and Marocchino A. 2011 *Plasma Phys. Control. Fusion* **53** 035010
[70] Hallo L. *et al* 2009 *Plasma Phys. Control. Fusion* **51** 014001
[71] Aglitskiy Y. *et al* 2009 *Phys. Rev. Lett.* **103** 085002
[72] Theobald W. *et al* 2008 *Phys. Plasmas* **15** 055503
[73] di Nicola J.-M. *et al* 2006 *J. Phys. IV (France)* **133** 595
[74] Depierreux S. *et al* 2009 *Phys. Rev. Lett.* **102** 195005
[75] Moody J.D. *et al* . 1996 *Phys. Rev. Lett.* **77** 1294
[76] Depierreux S. *et al* 2006 *J. Phys.* IV **133** 317
[77] Depierreux S. *et al* 2012 *Phys. Plasmas* **19** 012705
[78] Labaune C. *et al* 2006 *J. Phys.* IV **133** 29
[79] Baldis H.A. *et al* 1998 *Phys. Rev. Lett.* **80** 1900
[80] Drake R.P. *et al* 1996 *Phys. Rev. Lett.* **77** 79
[81] Fernandez J. *et al* 1998 *Phys. Rev. Lett.* **81** 2252
[82] Baldis H.A. *et al* 1996 *Phys. Rev. Lett.* **77** 2957
[83] Michel D.T. *et al* 2010 *Phys. Rev. Lett.* **104** 255001
[84] Baton S.D. *et al* 2012 *Phys. Rev. Lett.* **108** 195002
[85] Antonelli L. *et al* 2011 *Acta Tec.* **56** T57

[86] Batani D. *et al* 2011 *Plasma Phys. Control. Fusion* **53** 124041
[87] Hohenberger M. *et al* 2012 *Bull. Am. Phys. Soc.* **57** GO5.1
[88] Smid M., Antonelli L., Renner O. 2013 *Acta Polytech.* **53** 233
[89] Nejdl J. *et al* 2010 *Phys. Plasmas* **17** 122705
[90] Johnson J.D. 1994 *Los Alamos National Laboratory Report* No LA-UR-94-1451, see National Technical Information Service Document No DE94011699 'SESAME database' Copies may be ordered from the National Technical Information Service, Springfield, VA 22161
[91] Terry M.R., Perkins L.J., Sepke S.M. 2012 *Phys. Plasmas* **19** 112705
[92] Craxton R.S. *et al* 2010 *Bull. Am. Phys. Soc.* **55** 26
[93] Seguin F. *et al* 2003 *Rev. Sci. Instrum.* **74** 975
[94] Theobald W. *et al* 2009 *Plasma Phys. Control. Fusion* **51** 124052
[95] Yaakobi B. *et al* 2012 *Phys. Plasmas* **19** 012704
[96] Radha P.B. *et al* 2005 *Phys. Plasmas* **12** 056307
[97] Nora R. *et al* 2012 *Bull. Am. Phys. Soc.* **57** B04
[98] Nora R. *et al* 2011 *Bull. Am. Phys. Soc.* **56** 327

New Journal of Physics
The open-access journal for physics

Short pulse laser interaction with micro-structured targets: simulations of laser absorption and ion acceleration

O Klimo[1,4], J Psikal[1], J Limpouch[1], J Proska[1], F Novotny[1], T Ceccotti[2], V Floquet[2] and S Kawata[3]

[1] Czech Technical University, FNSPE, Brehova 7, 11519, Prague, Czech Republic
[2] CEA, IRAMIS, SPAM, F-91191 Gif sur Yvette, France
[3] Graduate School of Engineering, Utsunomiya University, Utsunomiya 321-8585, Japan
E-mail: ondrej.klimo@fjfi.cvut.cz

New Journal of Physics **13** (2011) 053028 (17pp)
Received 7 February 2011
Published 16 May 2011
Online at http://www.njp.org/
doi:10.1088/1367-2630/13/5/053028

Abstract. The interaction of an ultrashort intense laser pulse with thin foil targets is accompanied by the acceleration of ions from the target surface. To make this ion source suitable for application, it is of particular importance to increase the efficiency of laser energy transformation into accelerated ions and the maximum ion energy. This can be achieved by using a thin foil target with a microscopic structure on the front, laser-irradiated surface. The influence of the microscopic structure on the target surface on the laser target interaction and subsequent ion acceleration is studied here using numerical simulations. The influence of the shape and size of the microstructure, the density profile and the laser pulse incidence angle is also studied. Based on the simulation results, we propose to construct the target for ion acceleration experiments by depositing a monolayer of polystyrene microspheres of a size similar to the laser wavelength on the front surface of a thin foil.

[4] Author to whom any correspondence should be addressed.

Contents

1. Introduction

The interaction of an ultrashort intense laser pulse with a solid target is accompanied by the heating and acceleration of electrons. Their subsequent expansion from the target surface leads to space-charge separation, which is accompanied by the generation of a strong quasi-static electric field in the sheath on the target surface. This self-induced field decelerates expanding electrons and accelerates ions from the target surface into vacuum. The whole process is known as target normal sheath acceleration (TNSA) [1]–[3]. Laser-irradiated targets can thus serve as microscopic and intense sources of short pulses of ions, which are synchronized with the laser beam itself. The ions accelerated from the target surface in the TNSA process form a collimated beam with high laminarity [4, 5]. Such properties make them interesting for various applications, such as proton imaging, isochoric heating and warm dense matter, and for applications where energy deposition in a small volume inside an irradiated object is desired [6]. For most applications, however, it is necessary to increase the energy transformation efficiency into fast ions as well as their maximum and characteristic energy.

It has been demonstrated in recent experiments that the maximum proton energy as well as the energy transformation efficiency into accelerated protons can be increased by reducing the thickness [7] and lateral dimensions [8] of the target. This increase is caused by a higher surface-to-volume ratio, which makes hot electron refluxing more efficient and induces a situation such that hot electrons spend a great deal of their energy at the target surface to support the electrostatic field, which accelerates ions. However, targets with reduced dimensions, especially thickness, i.e. ultrathin foils, must be irradiated by high-contrast, prepulse-free laser pulses to avoid their premature disruption, which may otherwise reduce the efficiency of the TNSA process [9, 10].

The contrast of laser pulses has recently been increased by almost four orders of magnitude using, for instance, a double plasma mirror (DPM) [11]. A short high-contrast laser pulse with peak intensity $\lesssim 10^{20}\,\mathrm{W\,cm^{-2}}$ reflected from the DPM contains a relatively very small amount of energy in the ns and ps pedestal and thus the target is almost intact until the beginning of the interaction with the main laser pulse. At the same time, the plasma created on the target surface by the rising edge of a short main laser pulse does not have enough time to expand and the density profile on the surface is thus very steep during the interaction. The absence of a plasma

density profile may have a detrimental effect on laser absorption, especially at normal incidence and if the target surface is very flat. The laser energy absorption may be substantially increased when the pulse is incident obliquely. Nevertheless, most of the laser pulse energy is reflected even in this case. Moreover, the maximum intensity of an obliquely incident laser pulse in the focal spot on the target is decreased and the angular divergence of accelerated electrons may be increased. This may also have a negative effect on the acceleration of ions from the target surface.

The laser energy absorption may be boosted by the presence of microscopic structures on the laser-irradiated target surface, as demonstrated in recent experiments [12]–[19] and simulations [20]–[24]. Such targets have been widely used to increase the transformation efficiency of laser energy into x-ray emission [14, 16, 18, 19]. Recently, bulk Cu targets with nano-structures on the surface have also been used to study ion acceleration include by short intense laser pulses from the front, laser-irradiated target surface [25, 26]. In spite of the enhancement in the hard x-ray emission and in the flux of moderate energy ions owing to the presence of nano-particles on the surface, this experiment demonstrated that nano-particles reduce the maximum ion energy. However, the average size of nano-particles on the target surface was only 15 nm and the thickness of the layer containing these particles was about $0.2\,\mu$m. In such a case, the intensity contrast ratio of 10^{-6} may be insufficient for the main laser pulse intensity higher than $10^{16}\,\mathrm{W\,cm^{-2}}$, and it is not clear whether the nano-particles survive throughout the main laser pulse interaction [27]. Therefore, the results on the influence of surface structure on ion acceleration may not be conclusive. In contrast, according to PIC simulations [28], the presence of surface micro-structure (the size of particles is now comparable to the wavelength of the laser pulse) significantly increases the energy of the ions emitted from the rear side of the target if the target is thin enough and the laser contrast is sufficiently high.

As a consequence, a target with reduced dimensions and a micro-structure on the surface may benefit from both higher absorption and efficient hot electron refluxing; thus it is suitable for an efficient ion acceleration induced by ultra-short ultra-intense and high-contrast laser pulses. As will be shown in this paper, a suitable candidate for such a target may be a thin foil covered by a monolayer of polystyrene spheres with diameters of the order of the laser wavelength.

The interaction of short intense laser pulses with a target with or without a micro-structure on the laser-irradiated surface is studied in this paper using particle-in-cell (PIC) simulations. The simulation model is described in section 2. The dependence of laser energy absorption on the shape of the surface structure and on the size of the structure in the case of microspheres is studied in section 3. The influence of the enhanced absorption due to the presence of a micro-structure on the acceleration of ions from the target surface is also demonstrated and discussed. In section 3, it is also shown that the same result can be obtained even if the surface structure is irregular to some degree. The conversion efficiencies and maximum energies of fast protons are calculated for both normal (or near normal) and oblique incidence of the p-polarized laser pulse and are compared with the results calculated for the flat foil surface in section 4. The parameters of the laser pulse and of the foil better correspond to what is used in current ion acceleration experiments at Ti : sapphire laser systems with a power of several TW. The influence of a finite laser prepulse is also described. Ion acceleration from the front side of a bulk target in the backward direction (opposite to the laser incidence direction) is also discussed. In section 5, we summarize the most important results and present our concluding remarks.

2. Simulation model

Numerical simulations of the short intense laser pulse interactions with foil targets and of the subsequent ion acceleration are performed using our two-dimensional (2D) PIC code [29]. The code is relativistic and electromagnetic and takes into account all three components of particle velocities and electric and magnetic fields (2D3V). The relativistic equations of motion are solved by the two-step Boris algorithm and the fields in the positions of particles are determined by bilinear interpolation. The zigzag scheme [30] is employed for the calculation of current densities in order to guarantee an automatic compliance with the discrete continuity equation. The boundary conditions for particles are absorbing; particles reaching the boundaries of the simulation box are frozen there. For the solution of Maxwell's equations, damping layers are employed near the simulation box boundaries in order to eliminate spurious reflection of outgoing electromagnetic waves, as described in [31].

Two kinds of targets and laser pulse parameters are used in our PIC simulations. In the first part of this paper (section 3), the target consists of 0.2 μm thick foil, with or without a periodic structure attached to the front, laser-irradiated, surface (see figure 1). The shape of the structure is spherical, rectangular or triangular. The latter two shapes are more complicated for optimization as they offer an additional degree of freedom (sphere—diameter; rectangle—width and depth; triangle—height and opening angle). Moreover, it is observed that the shape of the surface structure does not have a significant effect on laser pulse absorption. Therefore, we have chosen to use a spherical shape in the reminder of this paper due to its simplicity. It is worth noting that targets with a surface layer of microspheres can be prepared relatively easily, as will be discussed in the first part of section 4. In this section, the foil thickness is increased to 0.5 μm, as such a thickness may better correspond to the optimum one for obtaining the maximum energy of the accelerated proton if the short laser pulse has a non-negligible prepulse. Moreover, a thicker foil can better support the surface structure without being damaged or bent.

All of the targets used in this paper consist of two species of ions (a homogeneous 1 : 2 mixture of C^{4+} and protons) and free electrons with the initial density of 40$\times$ critical density. The density profile on the target surface is step-like with the exception of section 4, where the influence of the density ramp is discussed. The targets are placed in a simulation box of size 17λ in the transverse direction. The incident laser pulse always propagates in the same direction (from the bottom) but the target may be rotated by the laser incidence angle. The simulation box size in the longitudinal direction thus depends on the incidence angle and ranges between approximately 21 and 35λ. The initial electron and ion temperatures are set to 50 eV, unless otherwise stated. This low temperature is used to ensure that the target does not significantly expand by itself on the simulation time scale. The characteristic velocity of target expansion, the ion acoustic velocity, multiplied by our typical simulation time (0.2 ps) gives the target expansion of about 10 nm, which is well below our typical target dimensions.

The targets are irradiated by p-polarized laser pulses with a wavelength of 800 nm and the temporal profile $\sin^2(\pi t/\tau)$, where τ is the laser pulse duration. A 20 fs long (full width at half maximum (FWHM)) laser pulse with a maximum intensity of 1.8×10^{19} W cm^{-2} is used in section 3, whereas in section 4 the pulse duration is increased to 40 fs and the maximum intensity is decreased to 9×10^{18} W cm^{-2}. The laser incidence is in the normal direction with respect to the target surface in section 3. Instead of normal incidence, we use a rather low incidence angle of 10° or the standard incidence angle of 45° in section 4. The transverse intensity profile of the laser pulse in our simulations is Gaussian with the FWHM of 4.7λ, and the laser pulse is always

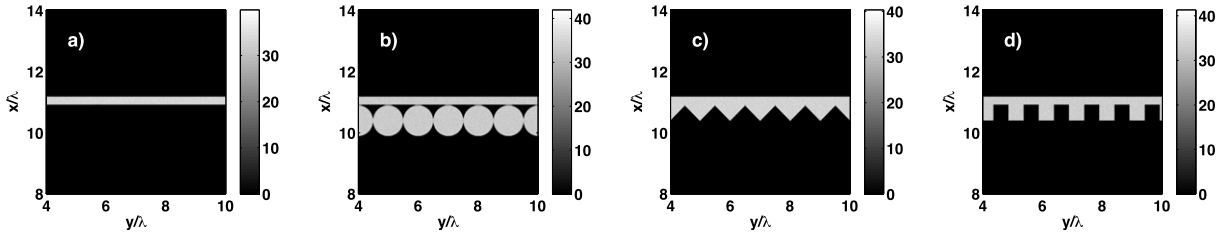

Figure 1. The targets used in our 2D PIC simulations to study the influence of the shape of the surface structure on laser pulse absorption. The initial free-electron density in the target is plotted in units of critical density. Only a small square section of the target is plotted. The laser pulse (with wavelength λ) is incident from the bottom.

Table 1. Comparison of the results of PIC simulations with the targets plotted in figure 1. The parameters of hot electrons are measured after the end of the laser target interaction. The electron divergence is the average angle of electrons with kinetic energy higher than the rest mass energy ($m_e(c)^2$) with respect to the target normal.

Target (figure 1)	Electron temperature (MeV)	Electron divergence (°)	Laser absorption (%)
(a)	0.10	14.8	3.8
(b)	0.40	39.7	55.2
(c)	0.42	41.8	80.5
(d)	0.37	40.9	43.9

launched at time 0 from the front side of the simulation box, which corresponds to the bottom side of figures containing ion density snapshots.

3. Laser absorption: dependence on the shape and the size of the surface structure

The results of PIC simulations concerning the absorption of laser pulses and the acceleration of hot electrons in the interaction with the targets plotted in figure 1 are summarized in table 1. These results indicate that surface structures with sizes of the order of the laser wavelength may boost laser energy absorption significantly. The energy is absorbed in particular by hot electrons. In the case of a flat foil surface, the temperature and the number of hot electrons are much lower; on the other hand, these electrons form a collimated beam. The structure on the target surface causes much higher absorption but the hot electron beam is very divergent. This behavior seems to be quite general, as it has been observed in all of our simulations with short (sub-100 fs) and intense ($I \gtrsim 10^{18}$ W cm^{-2}) laser pulses. This conclusion should apply neither to long laser pulses (> 1 ps), because the surface structure may expand during the interaction, nor to the ultra-relativistic regime ($I \gtrsim 10^{21}$ W cm^{-2}), where radiation pressure becomes extremely high and the energy absorption is dominated by different processes [32].

The enhancement of absorption of a short intense laser pulse due to the presence of a micro- or a nano-structure on the target surface has been ascribed to different processes in recent publications, e.g. surface plasmon resonance excitation [18, 33, 34] and multipass stochastic

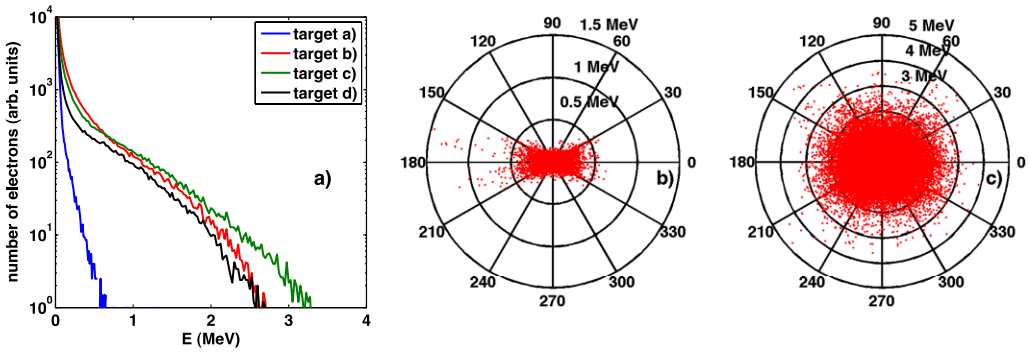

Figure 2. Energy distributions of electrons in the targets from figure 1 at the end of the laser target interaction (panel (a)). The angular distribution of electrons at the end of the laser target interaction for the case of a flat foil surface (panel (b)) and for the case of a structured foil surface (target c in figure 1, panel (c)). The angle is defined with respect to the laser incidence direction.

heating [35]. For a sphere with a diameter close to the laser wavelength, numerical solutions of Mie scattering theory demonstrate that the field at the surface of the sphere can be significantly higher than the field of the incident laser wave [36]. This enhancement of the field may be considered also as a source of increased absorption [17, 36]. However, such a field enhancement is not observed in our PIC simulations with bulk targets, which are discussed at the end of the next section. In simulations with thin foils, we observe that the maximum electric field is increased by about 50% for the same parameters. As there is no other difference than the target thickness, it is clear that the electric field enhancement in our simulations with thin foils is due to hot electron recirculation, because the main difference between thin and bulk targets lies in the efficiency of the recirculation process.

A number of different effects may contribute to higher absorption using structured targets. As structured targets have a significantly larger surface area, more particles can interact with the laser field. Moreover, as the angle of incidence of the laser pulse is not normal, vacuum heating [37] and resonance absorption [38] can take place. Last but not least, the structure is screening the incident laser wave but the accelerated electrons can propagate through it and consequently they can more easily get out of phase with the laser wave and thus gain its energy more efficiently. One can thus imagine a similar absorption process as the multipass stochastic heating in the case of clusters [35]. The enhanced dephasing of electrons due to the presence of surface structure may also be the source of the broader angular distribution of hot electrons, which is observed in our simulations.

The electron energy distributions and the angular distributions of electrons are plotted in figure 2. The plotted data essentially confirm the results presented in table 1. Namely, the number of hot electrons strongly increases if the target has a structured surface, but the angular distribution of hot electrons changes from a relatively narrow beam, which is typical of flat foil targets, into an almost isotropic one, which corresponds to laser interaction with clusters [39].

Electron energy distributions plotted in figure 2 represent all of the electrons in the simulation box, approximately at the time when the maximum laser intensity reaches the target. These distributions can be considered as distributions of the source of hot electrons in the case of short laser pulses, because according to our PIC simulations they are almost identical to the distributions of hot electrons propagating into bulk targets.

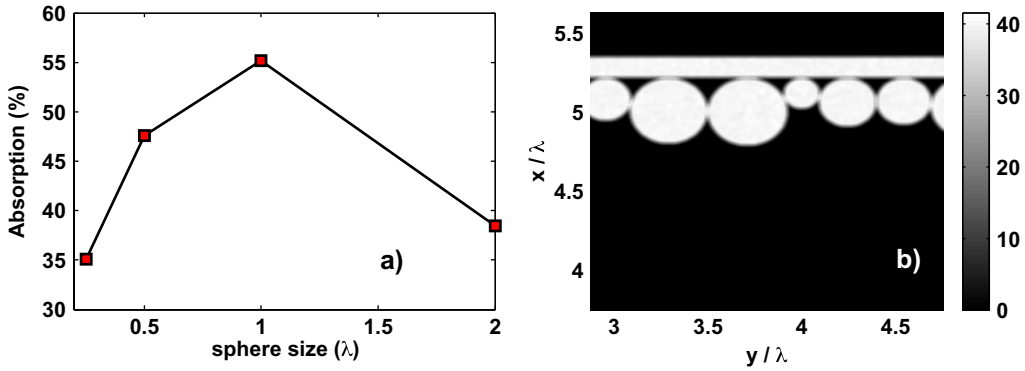

Figure 3. Laser energy absorption versus the diameter of microspheres on the target surface (panel (a)). Part of the target with a surface layer composed of microspheres with random diameter (panel (b)). The color bar gives the color scale for the electron density in units of critical density.

In figure 3(a), the dependence of laser energy absorption on the size of the surface structure is plotted for targets covered by spheres. The spheres in our simulations are always closely packed and thus there is just one parameter characterizing the structure—the sphere diameter. It results from figure 3(a) that the optimum size of spheres for obtaining absorption higher than 50% is close to the laser wavelength. The targets with rectangular and triangular surface structures have more degrees of freedom (at least width and height) and the dependence would be more complex, e.g. [23]. Recent PIC simulations [20] also indicate that it is possible to achieve almost complete absorption if the structure is tiny and sufficiently long in the laser propagation direction.

Until now, we have considered only targets with regular, grating-like structure on the surface. From the point of view of target fabrication, it is interesting to know whether this regularity is necessary or whether the structure can be irregular to some degree. To answer this question, we have performed a simulation placing an irregular surface structure on the target (figure 3(b)). The spheres on the surface have random diameter, which is in the range of 0.25–1λ, and they are closely packed. The other simulation parameters remain unchanged. The laser energy absorption of 57% we found in our simulation is even higher than the maximum absorption obtained in simulations with regular structure. One cannot draw a general conclusion from only one simulation with random parameters; nevertheless, this result indicates that absolute regularity of the structure is not necessary to obtain relatively high absorption.

3.1. Ion acceleration scaling with the size of the surface structure

In the previous section, we have shown that the structure on the target surface can significantly increase laser energy absorption and raise the temperature and the number of hot electrons. The aim of this section is to show whether and how efficiently the kinetic energy of hot electrons is transferred into fast ions in the sheath field at the target surface (TNSA). For the sake of simplicity, we concentrate again on targets with a spherical surface structure. Two important parameters describing accelerated ions and their dependance on the sphere size and the laser incidence angle are studied. In particular, we concentrate on the maximum ion energy and the total energy of accelerated ions normalized to the laser pulse energy (i.e. transformation efficiency of energy into fast ions).

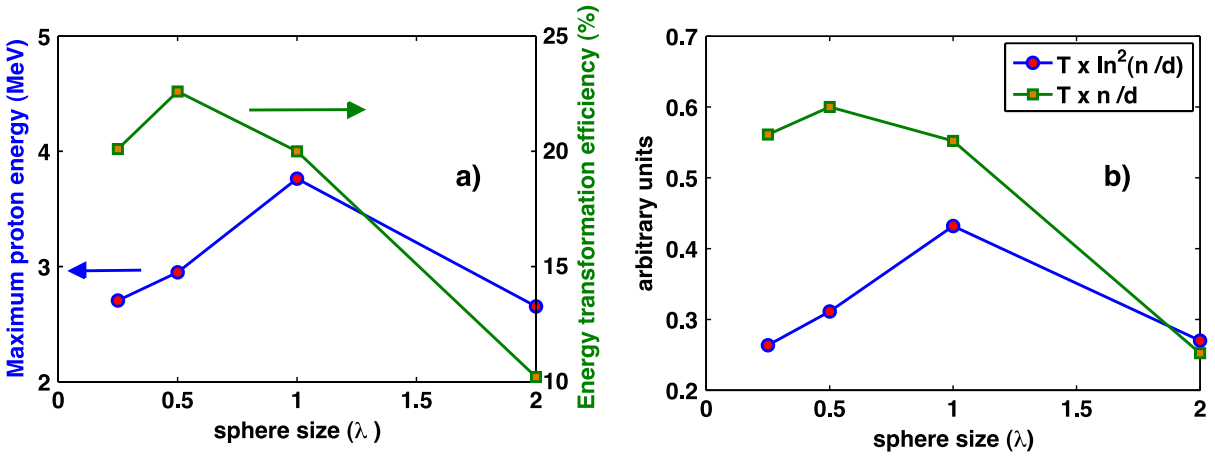

Figure 4. The maximum proton energy and the energy transformation efficiency from the laser pulse into all ions in simulations with microspheres on the target surface (panel (a)). The results correspond to the time of about 0.2 ps after the laser target interaction. In panel (b), there are two functions of hot electron temperature T, hot electron density n and the target thickness d, which includes the layer of spheres. These functions determine the maximum energy and the efficiency in panel (a). The electron temperatures and densities include all hot electrons in the simulation box after the laser–target interaction.

The maximum energy of accelerated protons and the energy transformation efficiency from the laser pulse into all ions are plotted in figure 4(a). The results are taken about 0.2 ps after the laser–target interaction. This time interval is long enough to enable the most important part of the ion acceleration process to be accomplished. Nevertheless, the transfer of energy from electrons to ions is still not over and thus one should read the results as qualitative features and not as exact numbers.

The dependence of maximum proton energy on the size of microspheres in figure 4(a) is quite similar to the dependence of laser energy absorption in figure 3(a). According to the analytical model [40] and the arguments of [41], the maximum energy of ions depends linearly on the hot electron temperature, whereas the dependence on the density of hot electrons is only logarithmic, i.e. $E_{\max} \sim T \times \ln^2(n)$. However, this theory does not take into account the effect of target thickness. If the target thickness d is smaller than the spatial length of the laser pulse (laser pulse duration times the velocity of light), hot electron recirculation may become important. This recirculation process manifests itself mainly with increasing the concentration of hot electrons, whose number scales approximately linearly with decreasing the target thickness. The recirculation of hot electrons is important also in our simulations and thus the dependence on hot electron density n should be replaced by the dependence on n/d. The function $T \times \ln^2(n/d)$ is plotted in figure 4(b) and its dependence on the sphere size is very similar to that of the maximum proton energy.

The energy transformation efficiency plotted in figure 4(a) attains its maximum at smaller sphere size than the maximum proton energy. The efficiency depends in particular on the product $T \times n$ [41], and as the density of hot electrons scales again with the target thickness, the dependence on target thickness is now much stronger. This reasoning is confirmed by

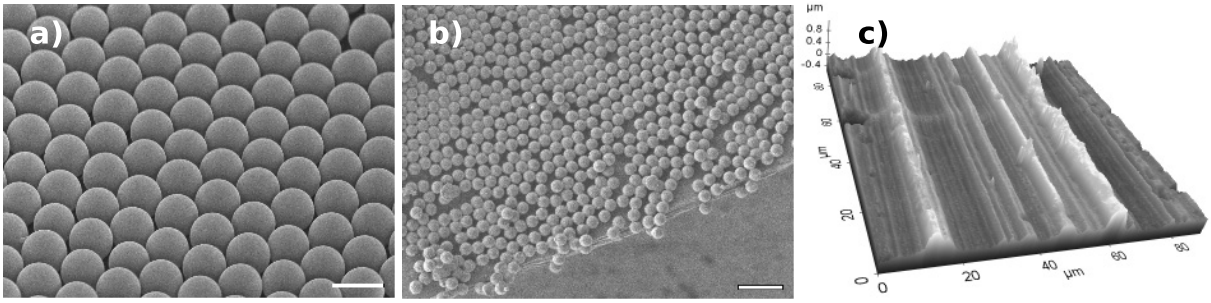

Figure 5. (a) Scanning electron microscope (SEM) image of the target surface covered by a monolayer of polystyrene spheres with a diameter of about 0.9 μm. (b) SEM image of a thin mylar foil (100 nm) covered by polystyrene spheres (0.26 μm). Image is taken at the border of the foil, where the spheres are not regularly arranged due to the cutting process. (c) Atomic force microscope image of the surface of a common commercially available (supplied by Goodfellow SARL) thin aluminum foil (2 μm thick).

comparing the efficiency in figure 4(a) with the function $T \times n/d$ in figure 4(b). Thus, it is possible to say that the advantage of small-size targets, where hot electrons efficiently recirculate, is more important for transformation efficiency than for the maximum ion energy, as recently experimentally confirmed [8]. It is also worth noting that increasing the depth of the surface structure may lead to higher absorption efficiency, but not always to a higher energy of accelerated ions.

4. Ion acceleration in targets covered by a monolayer of polystyrene microspheres

In the previous section, it has been demonstrated that a monolayer of microspheres deposited on the surface of the target may be suitable for increasing the laser energy absorption and electron and ion acceleration efficiency. The sphere size being similar to the laser wavelength has been identified as most suitable in this respect. A target covered by a layer of microspheres is not only relatively simple for theoretical and simulation studies but also suitable for initial experimental studies. Polystyrene microspheres with different diameters in the range of 100–1000 nm are commercially accessible and their deposition on the target surface is quite straightforward.

The method of deposition of the monolayer on the targets' surface is described below in a simplified way. A water dispersion of polystyrene microspheres is mixed with ethanol (usually 1 : 1) and carefully applied on the surface of water in a Petri dish using a glass pipette with a bent tip [42]. Self-assembly at the interface of water/air results in the creation of a compact monolayer of close-packed microspheres. The target is submerged under the monolayer and then lifted up slowly so that the monolayer remains on its upper side. The result is a piecewise homogeneous monolayer of closely packed microspheres attached to the target surface, which can be seen in figures 5(a) and (b).

At this point, we have to add a short note concerning the possible future experimental investigation of targets with a micro-structure on the surface. We have inspected the surface of commercially accessible 2 μm thick aluminum foil using atomic force microscopy. The result is plotted in figure 5(c). It can be seen that the foil surface looks like an irregular grating with

Table 2. Overview of the target and simulation parameters used in this section.

Target	A	B	C	D	E	F
Sphere diameter (λ)	0	0.5	1	0	0.5	1
Incidence angle	10°	10°	10°	45°	45°	45°

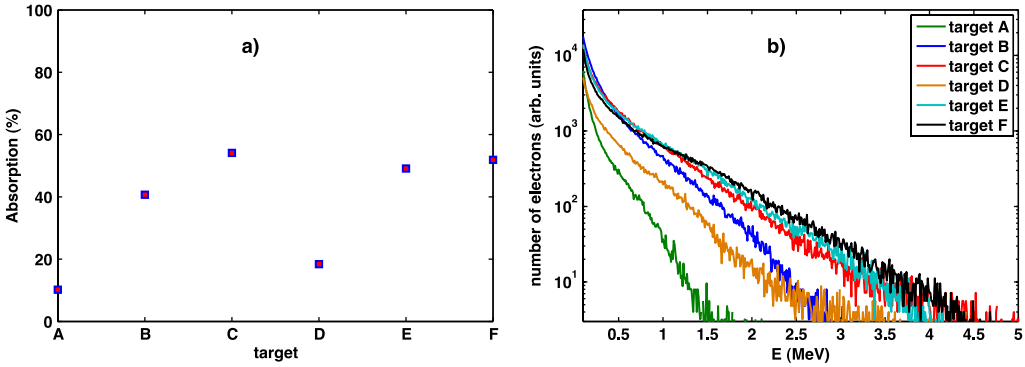

Figure 6. (a) Laser energy absorption in the targets specified in table 2. (b) Energy distributions of electrons accelerated in simulations with targets from table 2 recorded at the end of the interaction.

variable sized grooves probably due to the fabrication process. As the groove size is comparable to the wavelength of Ti:sapphire laser, which is most commonly used in ion acceleration experiments, it is clear that this grating can significantly influence the results of experiment. Therefore, one has to either polish the target surface using some chemical or mechanical method or contrast the target with optical quality surface requirements.

Let us return to the simulation results. In this section, we restrict ourselves only to the diameters of microspheres in the surface layer of 0.5 or 1λ, where λ is the laser wavelength, as, according to the discussion in the previous section, these sizes are most appropriate for efficient ion acceleration. The laser pulse incidence angle is either 45° or 10° with respect to the target surface normal direction. The angle of 10° is used instead of normal incidence because it is closer to the experimental practice aiming to avoid strong laser pulse back-reflection. An overview of targets and angles of incidence used in this section is presented in table 2.

The results of these simulations concerning laser energy absorption and electron acceleration are presented in figure 6. In panel (a), the laser energy absorption reaches almost 60% when the microspheres are present, and it does not strongly depend on the incidence angle or sphere size in the range considered here. The energy absorption of 60% is also in accordance with the absorption observed in the previous section in figure 3(a). Moreover, for smaller sphere size and almost normal incidence, the absorption drops to about 40%, which is also consistent with figure 3. For raw flat foils, the laser energy absorption is less than 20%, but significantly higher than the absorption for the normal incidence. This is due to the nonzero incidence angle. One can see that a weak change in the incidence angle may have a significant effect on laser energy absorption. The case of normal incidence onto an absolutely flat target is extremely inefficient and perhaps not fully realistic.

The energy distributions of electrons accelerated into the target are plotted in figure 6(b). These distributions are recorded in simulations with thin foil targets and they include all

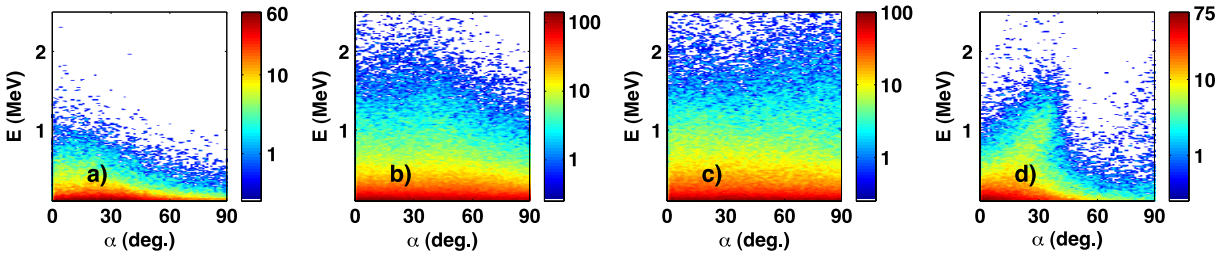

Figure 7. The energy–angular distributions of hot electrons accelerated in simulations with target configurations from table 2: configuration A, panel (a); B, panel (b); C, panel (c); and D, panel (d). The angle α is measured with respect to the target surface normal direction.

electrons in the entire simulation box at the end of the laser target interaction. Comparing these distributions with the ones calculated for bulk target (with the same parameters), where the electrons crossing an absorbing boundary in the target are recorded and substituted by thermal ones, it is found that the distributions are almost identical. This is not surprising for the very short laser pulse durations, as hot electrons do not have enough time to transfer a significant amount of energy to ions in a thin foil on the time scale of half the laser pulse duration (we assume that most of the hot electrons are generated at the time of peak laser intensity on the target). Therefore, one can consider the distribution of hot electrons calculated for a thin foil also as a source of hot electrons propagating into the bulk target.

In figure 6(b), it can be seen that the distributions for the target configurations C, E and F are quite similar, which is consistent with a similar laser energy absorption observed in figure 6(a). The hot electron temperature is about 500 keV in these three cases. The other two cases A and D, where the laser energy absorption is quite inefficient, correspond to the targets where the surface layer of microspheres is absent. These distributions have temperatures of about 190 and 310 keV. The increase in hot electron temperature in comparison with results for normal incidence presented in table 1 (target a) indicates that there are some additional absorption mechanisms in the case of oblique incidence, which are responsible for the production of more energetic electrons. As the density profile on the target surface is very steep, we can rule out resonance absorption and ascribe the hot electron production to vacuum heating.

As already discussed in the previous section, the angular distribution of hot electrons accelerated in the laser interaction with a structured target surface is almost isotropic. This can also be seen in figure 7, where the energy–angular distributions of electrons recorded in our simulations are presented. The cases in panels (a) and (d) correspond to flat target surfaces irradiated at 10° and 45°, respectively. The angle α is measured with respect to the target surface normal direction. It can be seen that for the flat target surface, hot electrons propagate in a collimated beam. The other two cases (panels (b) and (c)) both correspond to the incidence angle of 10° but for different sizes of microspheres at the surface. The angular distribution of hot electrons is rather wide and the source of hot electrons is nearly isotropic, like in the previous section. The dependence on the size of the microspheres is not observed in the range of sphere sizes used here. Similar distributions are also found for the 45° incidence angle and thus these distributions are omitted here.

The efficiency of conversion of laser energy into fast protons accelerated in the TNSA process from both surfaces of the thin foil (0.5 μm thickness excluding the microspheres) is

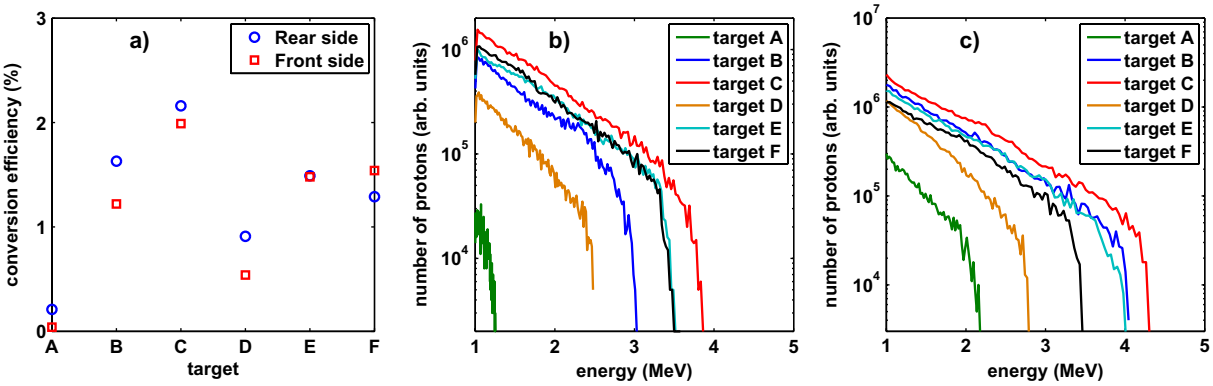

Figure 8. (a) The efficiency of conversion of laser energy into fast protons with energy higher than 1 MeV accelerated outside from the front and rear sides of the target. The energy distributions of fast protons accelerated by the TNSA process at the target front (b) and rear (c) sides. The target configurations A, B, etc correspond to the parameters specified in table 2.

plotted in figure 8(a). This efficiency includes only protons accelerated to energies higher than 1 MeV and it is measured 0.2 ps after the laser target interaction. As we do not include carbon ions and lower-energy protons, there is a large difference between this conversion efficiency and the one presented in figure 4(a). One may therefore arrive at the conclusion that only about one quarter of the total energy of ions is contained in fast protons. Otherwise, the conversion efficiency shows similar trends to the laser pulse absorption presented in figure 6(a).

In figures 8(b) and (c), the energy distributions of fast protons accelerated from the front and rear sides of the targets are presented. In general, one can say that all of the distributions are exponential with a high energy cut-off. The slopes of exponential distributions for the targets with microspheres are similar to each other; only the numbers of accelerated protons and the cut-off energy differ. The highest cut-off energy is obtained from both the target sides for the incidence angle of 10° and the sphere size of λ. This is consistent with the highest absorption (figure 6(a)) and conversion (figure 8(a)) efficiencies. However, the difference between the cut-off energies at the front and rear sides is not very significant for the targets with microspheres. At this point, we have to note that we have not observed any significant difference in angular distribution of protons accelerated from the targets with and without the structure on the surface. Therefore, we do not discuss the angular distribution here.

The distributions of protons accelerated from flat foils contain far fewer particles and they have much lower cut off energy. The extreme case is the distribution of protons accelerated from the target front side for the target configuration A (table 2). Here, one can see that the distribution of protons accelerated from the front side differs very significantly from the distribution of protons accelerated from the rear side, which is not the case in any other simulation. This difference can be better understood from the proton density snapshots presented in figure 9.

The initial density of protons in the target (in panel (a)) is homogeneous. In panel (b), the density snapshot taken 0.1 ps after the laser target interaction shows a bow-like shock propagating into the foil. These are the ions accelerated into the target by the radiation pressure of the laser pulse. The protons contained in this shock are of lower energy (less than 1 MeV) and

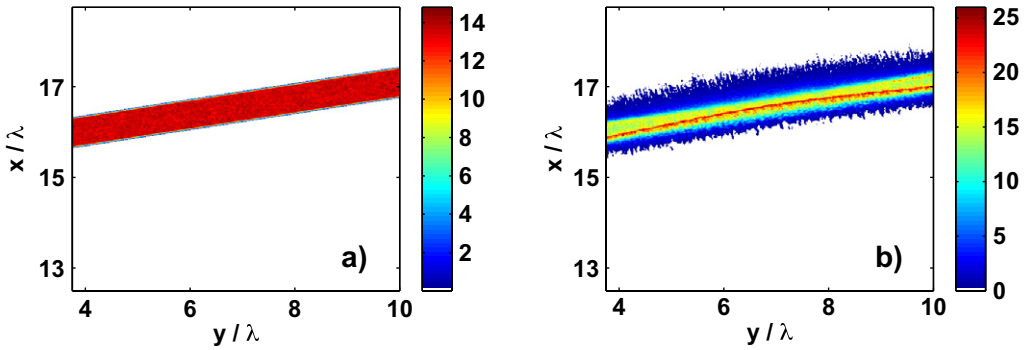

Figure 9. The density of protons in the target without the surface layer of microspheres irradiated at a 10° angle of incidence at the beginning (a) and 0.1 ps after the end of the laser target interaction (b). The laser pulse is incident from the bottom, and the density of protons in units of the critical density is represented by colors.

thus they are not interesting in the context of this paper. However, the shock accelerated into the target reduces the efficiency of proton acceleration in the TNSA process from the target front side. This shock is particularly strong in the case of near-normal incidence and a flat foil surface, when the TNSA process is suppressed due to low laser energy absorption into hot electrons.

4.1. Influence of the density gradient

Even very-low-intensity laser prepulses may induce some evaporation from the target surface and the vapor may be ionized by the rising edge of the main laser pulse [43]. Therefore, it is important to include a short steep plasma density profile on the target surface and to study its influence. The density profile can be included easily if the target surface is flat. However, the expansion of the structure is not planar (1D) and thus it is more complicated to describe the expanding plasma. To make the shape and the scale of the preplasma realistic also for the structured target surface, we have used the following procedure. The interaction with the main laser pulse is delayed by about 150 fs. The target is initialized as in the simulation without preplasma, but the temperatures of electrons and ions are both set to 1 keV. The plasma is allowed to expand from the front side of the target for about 100 fs (a reflecting boundary condition at the rear side precludes expansion during this period) and after that the particle energies are resampled from the Maxwellian distribution with the same temperature, as in previous simulations (i.e. 50 eV). This approach enables us to obtain a realistic density profile during a reasonably short computational time. Moreover, we start the interaction with the same temperatures of electrons and ions and thus we can observe the effect of the density profile in addition to other effects. The density profile on the target rear surface is not included.

The density profiles of targets with preplasma on the surface, which are studied in our simulations, are plotted in figure 10. The target in panel (a) is a simple flat foil with an exponential density profile on the front surface. The scale length L of the density profile is 0.04λ. An exponential density profile with a similar scale length is produced on the surface of the structured target using the approach described above. This target can be seen in panel (b). Apart from the density profiles on the front side, both of these targets correspond to configurations A and C described in table 2.

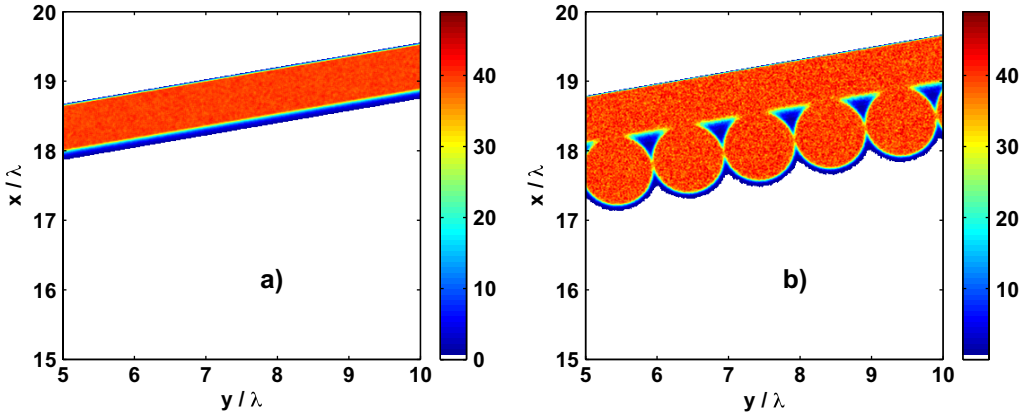

Figure 10. (a) The ion charge density (normalized on charge at critical density) profile at the beginning of the laser interaction with the flat target (target A), which has an exponential density ramp at the front, laser-irradiated side. (b) The same density profile for the target with microspheres on the surface (target C), which has significantly expanded prior to the interaction with the laser pulse. The laser pulse is incident from the bottom.

As one may expect, laser energy absorption in the case of a flat target surface increases with plasma density scale length (in the range of our interest, $L \ll \lambda$). For $L = 0.04\lambda$, the relative absorption increases from 11 to about 13% (18% relative increase). An opposite trend is observed for the target with the surface structure, where the density profile smoothes the sharp borders of the structure and thus weakens its effect. In this case, the absorption decreases from 59% to about 54% (7% relative decrease).

The energy distributions of protons accelerated from target rear sides are compared in figure 11(a). The effect of the density profile on ion acceleration is clearly significant only in the case of target A (from table 2). For this target, the maximum energies of accelerated protons and the conversion efficiency into fast protons with energy higher than 0.1 MeV have both increased by about 50%. This is not surprising as the temperature of fast electrons in the target with the density profile is significantly higher (250 keV) in comparison with the target without the profile (190 keV). In consequence, the large difference in the energy distribution of fast protons is caused by fast electrons, which are accelerated more efficiently at the surface of the flat target with the density profile. This result indicates the importance of the laser pulse contrast for experiments with targets having a micro-structure on the irradiated surfaces. If the contrast is not sufficient, the effect of surface structure may not be detected. In this respect, we would like to note that most previous experiments with micro-structure on the target surface have been performed with moderate laser intensity of the order of 10^{16} W cm^{-2} and thus the demands on the contrast were not so stringent.

4.2. Acceleration from the front side of a bulk target

Acceleration of ions from the front side of a bulk target into vacuum is not very interesting from the application point of view. The reason is that the efficiency of such an acceleration process is not so high as it takes place only during the laser–target interaction and cannot benefit from electron recirculation. When the laser field is over, there is no force to pull electrons from the

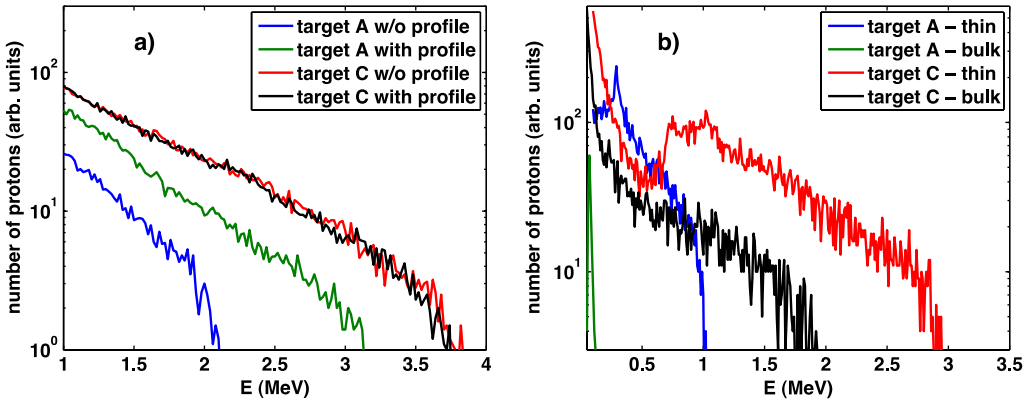

Figure 11. The energy distribution of protons accelerated from the rear side of targets A and C (from table 2) and the targets with density profiles plotted in figure 10. The distributions are compared 0.2 ps after the laser target interaction. (b) The energy distributions of protons accelerated out of the target from its front side. The distributions for thin and bulk targets are compared 130 fs after the laser target interaction.

target into vacuum, the electrons are dragged back into the target by a quasi-static electric field and their energy is absorbed in the target interior. After that, ion acceleration can be driven only by thermal expansion and such a process is not efficient in the case of short, femtosecond laser pulses.

Nevertheless, bulk targets may be relevant to proof of principle experiments studying the influence of surface micro-structure. As already mentioned, the targets with a structured surface should be compared with targets with a highly flat surface (e.g. of optical quality). It might be difficult to prepare a foil target, which is very flat and very thin at once. However, polishing surfaces of bulk targets is not so difficult and thus a very flat bulk target may serve as an intermediate step to experimentally demonstrate the effect of the target surface on ion acceleration driven by laser–target interaction.

In our simulations, bulk targets are realized by using an absorbing boundary condition at the rear side of the target. The particles reaching this boundary are absorbed and reemitted with the initial thermal distribution. The results calculated for bulk targets A and C (according to table 2) are compared in figure 11(b) with the results obtained for thin foils. The maximum energy and the efficiency of ion acceleration are significantly reduced in bulk targets, but the large difference between the results for targets with and without surface structure still exists.

5. Conclusions

Target normal sheath acceleration of ions from thin foil targets with a flat or structured front surface is studied in this paper using 2D PIC simulations. The structure on the front surface may significantly boost the energy absorption of intense laser pulses with ultra-high contrast and increase the hot electron temperature and density. This leads to higher ion acceleration efficiency and maximum ion energy in the case of thin foil targets, which may benefit from hot electron recirculation. The angular distribution of hot electrons accelerated in the interaction of the laser pulse with a structured surface is very wide. However, the angular distribution of accelerated ions is not significantly affected and the ions form a narrow beam.

The laser absorption process depends on the shape and size of the structure on the surface. The maximum laser pulse absorption is obtained when the characteristic size of the surface structure is comparable to the laser wavelength. The high energy cut-off of the ion energy distribution and the ion acceleration efficiency depend not only on laser energy absorption but also on efficient hot electron recirculation. Therefore, they reach their maximum value when the absorption is efficient but the layer on the target surface containing the structure is as thin as possible. These two conditions result in an optimum size of the structure. For a monolayer of closely packed microspheres on the target surface, this optimum is found in the range of 0.5–1λ, where λ is the laser wavelength. We propose to use a target with a monolayer of closely packed polystyrene microspheres in experiments and provide a short description of the target preparation process.

The influence of the angle of laser pulse incidence is studied in section 4. It is found that for targets with microspheres, there is a weak dependence of the results on the incidence angle, which is not the case for flat foil targets. For the target thickness used in our simulation, it is found that accelerations from both of the target surfaces are similar with the exception of the flat foil irradiated at a small incidence angle. In this case, absorption is inefficient and the laser radiation pressure launches a strong shock wave into the target, which suppresses ion acceleration efficiency from the front side.

The density profile on the target surface, which may be induced by a weak laser prepulse, is included at the target front side and its influence on ion acceleration is studied. The density profile weakens the effect of the surface structure, while it provides conditions for more efficient laser absorption by flat foils. If the scale length of the density profile becomes comparable to the size of the surface structure, the effect of the structure may disappear completely.

In the proof of principle experiments studying the influence of the surface structure on ion acceleration, it might be possible to study ion acceleration in the backward direction from the front side of a bulk target. The surface of a bulk target can be polished more easily and thus it could be possible to compare the influence of the structure with a really flat target surface. Moreover, the effect of the surface structure on ion acceleration in the bulk target should be sufficiently strong, as demonstrated in the last part of this paper.

Acknowledgments

This work was supported by the Czech Ministry of Education, Youth and Sports under project numbers LC528 and MSMT6840770022 and by the Czech Science Foundation under project number 205/11/1165. The authors are grateful to the Association of Innovative Entrepreneurship CR for support in the framework of the Franco-Czech academic cooperation Barrande, project number MEB021029. The French Ministry of Foreign and European Affairs is also acknowledged for financial support. SK thanks JSPS, MEXT and CORE (Center for Optical Research and Education, Utsunomiya University), Japan, for their support of the present work.

References

[1] Wilks S C *et al* 2001 *Phys. Plasmas* **8** 542–9
[2] Hatchett S P *et al* 2000 *Phys. Plasmas* **7** 2076
[3] Snavely R A *et al* 2000 *Phys. Rev. Lett.* **85** 2945–8
[4] Cowan T *et al* 2004 *Phys. Rev. Lett.* **92** 204801

[5] Borghesi M *et al* 2004 *Phys. Rev. Lett.* **92** 055003
[6] Borghesi M *et al* 2007 *J. Phys.: Conf. Ser.* **58** 74–80
[7] Ceccotti T *et al* 2007 *Phys. Rev. Lett.* **99** 185002
[8] Buffechoux S *et al* 2010 *Phys. Rev. Lett.* **105** 015005
[9] Batani D *et al* 2010 *New J. Phys.* **12** 045018
[10] Kaluza M *et al* 2004 *Phys. Rev. Lett.* **93** 045003
[11] Levy A *et al* 2007 *Opt. Lett.* **32** 310–2
[12] Hu G Y *et al* 2010 *Phys. Plasmas* **17** 083102
[13] Khattak F Y *et al* 2005 *Europhys. Lett.* **72** 242–8
[14] Kulcsar G *et al* 2000 *Phys. Rev. Lett.* **84** 5149–52
[15] Murnane M M *et al* 1993 *Appl. Phys. Lett.* **62** 1068–70
[16] Nishikawa T *et al* 2004 *J. Appl. Phys.* **96** 7537–43
[17] Palchan T *et al* 2007 *Appl. Phys. Lett.* **90** 041501
[18] Rajeev P *et al* 2003 *Phys. Rev. Lett.* **90** 115002
[19] Sumeruk H A *et al* 2007 *Phys. Rev. Lett.* **98** 045001
[20] Cao L *et al* 2010 *Phys. Plasmas* **17** 043103
[21] Mikhailova Y M *et al* 2005 *Quantum Electron.* **35** 38–42
[22] Raynaud M *et al* 2007 *Phys. Plasmas* **14** 092702
[23] Wang W M *et al* 2008 *Phys. Plasmas* **15** 030702
[24] Takahashi K *et al* 2010 *Phys. Plasmas* **17** 093102
[25] Bagchi S *et al* 2008 *Laser Part. Beams* **26** 259–64
[26] Bagchi S *et al* 2007 *Appl. Phys. Lett.* **90** 141502
[27] Gibbon P and Rosmej O N 2007 *Plasma Phys. Control. Fusion* **49** 1873–83
[28] Nodera Y *et al* 2008 *Phys. Rev.* E **78** 046401
[29] Psikal J *et al* 2006 *Czech. J. Phys.* **56** B515–B521
[30] Umeda T *et al* 2003 *Comput. Phys. Commun.* **156** 73–85
[31] Umeda T 2001 *Comput. Phys. Commun.* **137** 286–99
[32] Ping Y *et al* 2008 *Phys. Rev. Lett.* **100** 085004
[33] Boyd G T *et al* 1984 *Phys. Rev.* B **30** 519–26
[34] Hu G Y *et al* 2010 *Phys. Plasmas* **17** 083102
[35] Breizman B N *et al* 2005 *Phys. Plasmas* **12** 056706
[36] Sumeruk H A *et al* 2007 *Phys. Plasmas* **14** 062704
[37] Brunel F 1987 *Phys. Rev. Lett.* **59** 52–5
[38] Kruer W L 1988 *The Physics of Laser Plasma Interactions* (Reading, MA: Addison-Wesley)
[39] Shao Y L *et al* 1996 *Phys. Rev. Lett.* **77** 3343–6
[40] Mora P 2003 *Phys. Rev. Lett.* **90** 185002
[41] Psikal J *et al* 2010 *Phys. Plasmas* **17** 013102
[42] Kosiorek A *et al* 2004 *Nano Lett.* **4** 1359–63
[43] Wharton K *et al* 2001 *Phys. Rev.* E **64** 025401

Laser-Driven Proton Acceleration Enhancement by Nanostructured Foils

D. Margarone,[1] O. Klimo,[1,2] I. J. Kim,[3] J. Prokůpek,[1,2] J. Limpouch,[1,2] T. M. Jeong,[3] T. Mocek,[1] J. Pšikal,[1,2] H. T. Kim,[3] J. Proška,[2] K. H Nam,[3] L. Štolcová,[1,2] I. W. Choi,[3] S. K. Lee,[3] J. H. Sung,[3] T. J. Yu,[3] and G. Korn[1]

[1]*Institute of Physics of the ASCR, ELI-Beamlines/HiLASE project, Na Slovance 2, 18221 Prague, Czech Republic*
[2]*Czech Technical University in Prague, FNSPE, Brehova 7, 115 19 Prague, Czech Republic*
[3]*Advanced Photonics Research Institute, GIST, 1 Oryong-dong, Buk-gu, Gwangju 500-712, Republic of Korea*
(Received 3 June 2012; published 3 December 2012)

Nanostructured thin plastic foils have been used to enhance the mechanism of laser-driven proton beam acceleration. In particular, the presence of a monolayer of polystyrene nanospheres on the target front side has drastically enhanced the absorption of the incident 100 TW laser beam, leading to a consequent increase in the maximum proton energy and beam charge. The cutoff energy increased by about 60% for the optimal spheres' diameter of 535 nm in comparison to the planar foil. The total number of protons with energies higher than 1 MeV was increased approximately 5 times. To our knowledge this is the first experimental demonstration of such advanced target geometry. Experimental results are interpreted and discussed by means of $2\frac{1}{2}$-dimensional particle-in-cell simulations.

DOI: 10.1103/PhysRevLett.109.234801 PACS numbers: 41.75.Jv, 52.38.Ph, 52.50.Dg, 52.59.−f

Recently, the dramatic increase in attainable laser intensity by means of high power femtosecond lasers has generated a fast evolution of laser plasma sources. Production and acceleration of protons up to the 100 MeV level in very small distances (typically a few micrometers) are clearly visible through this evolution [1,2]. A great attention to potential medical application, especially in the hadron therapy [3], has been paid due to the spectacular high brightness, short pulse duration (∼ kA current), and extremely low emittance (100-fold better than typical rf accelerators) of laser-driven ions [4].

Currently the laser acceleration mechanism most investigated experimentally is the so-called target normal sheath acceleration (TNSA) when ions are accelerated at the rear-side of a thin target in a quasielectrostatic sheath created by fast electrons propagating from the target front side [5,6], as illustrated in Fig. 1. Theoretically, the possibility to generate monoenergetic ion bunches by accelerating ultrathin foils using very high contrast circularly polarized laser pulses at intensities higher than 10^{21} W/cm^2, in the so-called radiation pressure acceleration regime, has been identified [7–9] but not clearly demonstrated experimentally due to the lack of enough powerful lasers, although a first experimental evidence of the laser radiation pressure in a hybrid acceleration regime has been shown [10]. Recently, the acceleration of monoenergetic high energy proton beams by collisionless shocks in gas target has also been demonstrated [11].

Typical TNSA conversion efficiency (ratio between the laser energy and the total ion beam energy) by using 10–100 fs lasers can reach values up to a few percent [12]. However, the laser energy transformation into high energy protons has to be substantially raised for the majority of practical applications. Laser absorption may be boosted by the presence of sub-micrometer-scale structures on the laser-irradiated target surface, as demonstrated by experiments aimed to enhance the laser energy transformation into x-ray emission [13,14] and photoelectron generation at relatively low laser intensities [15]. Recent particle-in-cell (PIC) simulations have shown that the presence of microstructures with a characteristic size comparable to laser wavelength on the front side of a thin target may significantly increase the energy of hot electrons [16] and of ions emerging from its rear side, assuming a sufficiently high laser contrast [17].

The possibility of using a thin plastic foil covered by a monolayer of polystyrene microspheres with a diameter of the order of the laser wavelength has been studied by PIC simulations [18]. In this Letter we show the first

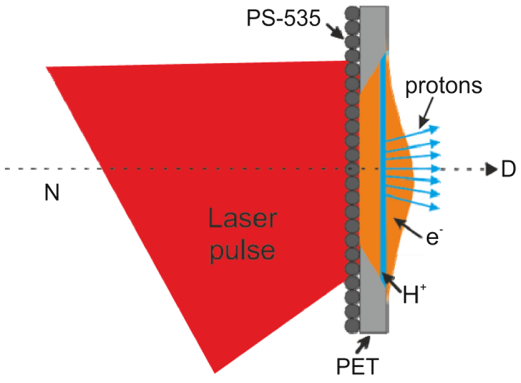

FIG. 1 (color online). TNSA mechanism with the target geometry used in the experiment (side view). The laser beam (p polarized) is absorbed at the nanospheres-vacuum interface with an incidence angle of 22.5 degrees (N denotes the target normal). The hot electrons (generated at the target front side) propagate forward and accelerate protons at the rear side. The proton or ion diagnostics (D) is placed along the N direction.

experimental demonstration of such advanced target geometry which allows us to strongly enhance both the maximum achievable proton energy and total number.

The nanostructured target geometry is depicted in Fig. 1. A monolayer of polystyrene (PS) nanospheres is located at the front-surface of a 1-μm thick mylar [polyethylene terephthalate (PET)] foil. Several targets having different sphere diameters, such as 266, 535, and 920 nm, have been used in our experimental campaign.

The experiment has been performed with the 10 Hz, 100 TW Ti:sapphire laser system at the Advanced Photonics Research Institute in Gwangju, South Korea, which is based on the chirped pulse amplification technique [19]. The laser pulse duration, wavelength, and energy after compression, monitored during the experiment, were about 30 fs (FWHM), 805 nm, and 2 J, respectively. The laser beam was focused onto the target surface by an $f/3.6$ off-axis parabolic mirror, which allowed us to reach a focal spot of about 5 μm in diameter (FWHM). The laser beam was p polarized on target (electric field parallel to the plane of incidence).

The intensity level of the laser nanosecond amplified spontaneous emission is a crucial parameter when using such advanced targets since the nanostructured surface must be preserved to ensure a genuine interaction (no preplasma formation) with femtosecond high-intensity pulses. In fact, we have experimentally estimated the ablation-threshold fluence in the ns regime for the irradiated targets [20], which is in the range of 1–10 J/cm^2 (corresponding to a laser intensity of about 10^9 W/cm^2 in our experimental conditions). Thus, the use of a double plasma mirror, which allowed us to achieve a laser intensity contrast of about 5×10^{11} up to 10 ps prior to the main pulse, was mandatory [21]. On the other hand, the laser pulse energy was reduced by a factor of 50% (about 1 J) on target at the expense of the laser intensity which finally was about 5×10^{19} W/cm^2.

The standard real-time ion diagnostics used consists of a Thomson parabola (TP) spectrometer and a time-of-flight (TOF) detector fully described in the literature [22]. The TP is a mass spectrograph where charged particles are deflected by static electric and magnetic fields parallel to each other and perpendicular to the particle stream motion; as a result of the laws of motion the particles draw different parabolas on an imaging plane. The TOF detector is based on the well known time-of-flight technique, which allows us to estimate the particle velocity (energy) by measuring the particle arrival time onto a detector placed at a given distance from the source (thin foil in our experiment).

The spectrometer was equipped with a microchannel plate (MCP) and a phosphor screen placed 20 cm away from the output of the magnetic (~ 0.2 T) and electric (3.5 kV/cm) field deflection region, and an ICCD camera. The calibration of the MCP-phosphor screen-ICCD system was performed by installing slotted CR-39 track detectors in front of the MCP following a similar experimental procedure reported in literature [23]. The TOF consisted of a plastic scintillator (placed at 283 cm from the plasma source), photomultiplier tube and fast oscilloscope. Both detectors were placed along the target normal and allowed us to perform simultaneous measurements (a small hole was located in the center of the scintillator to let ions go through and reach the TP spectrometer). The detection solid angles were 7.2×10^{-9} sr and 2.55×10^{-4} sr for the TP spectrometer and the TOF system, respectively.

Typical signals from TP and TOF measurements are shown in Fig. 2. Since the main target constituents are hydrogen and carbon, the strongest plasma ion products are protons and C^{n+} ($1 \leq n \leq 6$) as clearly shown in the TP spectrum. A comparison between TP and TOF signals has been performed in order to accurately determine the proton energy distribution, proton cutoff energy, and total ion charge. The proton beam divergence (i.e., the proton stream solid angle) was measured by a stack of CR39 track detectors placed near the target. This *ex-situ* diagnostic technique, performed for all configurations (i.e., for all targets with different nanosphere diameters and for all plane-foil targets of different thicknesses), has been used to estimate the total number of protons, taking into account that protons with different energy range have a different divergence.

The proton energy distributions were compared to numerical results coming out from $2\frac{1}{2}$-dimensional particle-in-cell simulations (with two spatial and three velocity components). The simulations assumed the same laser pulse intensity, wavelength, duration, polarization, and incidence angle used in the experiment. The target

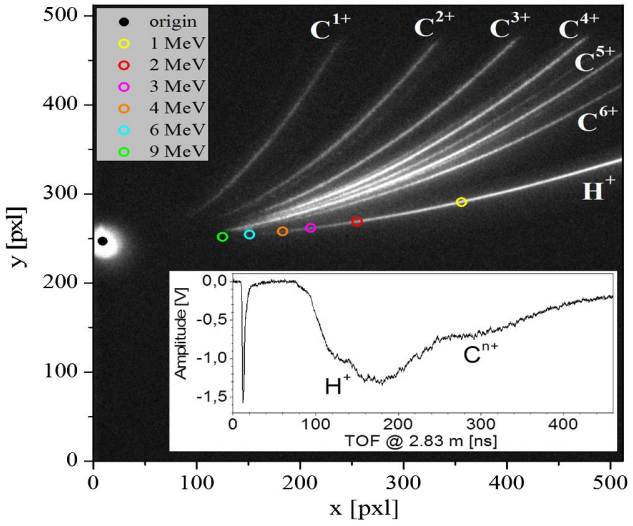

FIG. 2 (color online). TP and TOF typical spectra acquired simultaneously during irradiation of a PET-535 (1 μm thick polyethylene with 535 nm diameter polystyrene spheres) target. The circles from the right to the left hand side show increasing proton energies.

geometry was also the same and the target consisted of 1:1 mixture of C^{4+} ions and protons with electron density 40 times the critical density (1.72×10^{21} cm^{-3} for 800 nm wavelength of a Ti:sapphire laser). The transverse intensity distribution of the laser pulse was a Gaussian profile with a spot size of about 2 microns at FWHM [24]. The lateral losses are only one directional in 2D geometry used in simulations and thus they are reduced compared to the experiment. In order to compensate for this reduction, we have used a smaller focal spot in 2D simulations. This spot size in two dimensions has been estimated assuming that the density of hot electrons on the characteristic distance of ion acceleration ($d = \tau_l c_S$, where τ_l is the laser pulse duration and c_S the ion acoustic velocity) should be comparable to the one in three dimensions. The size of the hot electron cloud at a distance d is $2s = 2(d + l)\tan(\alpha) + 2r$, where α is the electron divergence, l is the target thickness, and r is the focal spot radius. Thus, in a first approximation, we can assume that $s_1/r_1 = {s_2}^2/{r_2}^2$ (the density in two dimensions is s_1/r_1 times smaller and in three dimensions is ${s_2}^2/{r_2}^2$ times smaller, when compared with an electron stream propagating without any divergence). Finally, assuming a hot electron temperature of 1 MeV and electron divergence of 45° estimated from PIC simulations for the above given parameters and supported by similar results reported in Ref. [18], a foil thickness $l = 1$ μm, and $r_2 = 2.5$ μm (given as experimental parameter, where the diameter $2r_2$ is assumed as focal spot size at FWHM), we have estimated $r_1 = 1.0$ μm. Nevertheless, we have also performed numerical simulation with the same focal spot diameter as in the experiment (5 μm) for all target geometries. The results predicted about 50% higher proton cutoff energies with respect to the case of lower spot size (2 μm) at constant laser intensity. The ratio of the maximum proton energies for different target geometries is practically constant in our PIC simulations when different spot sizes are used as inputs. Hence, the numerical results are qualitatively the same for various spot sizes, even if the absolute values differ.

The comparison for the irradiated targets without (PET) and with PS nanospheres (PET-266, PET-535, PET-920) on the front surface is reported in Fig. 3. The best acceleration performances during the experiment were achieved with the PET-535 target. The maximum proton energy measured by the TP spectrometer was about 8.6 MeV [Fig. 3(a)], showing a perfect agreement with the predicted PIC simulations [Fig. 3(b)]. The cutoff energy measured for the planar target (PET) was about 5.3 MeV, also showing a very good agreement with the simulation results. In general, the PIC calculations show a trend for different target geometries which is in agreement with the experimental results. However, the experimental cutoff energy in the case of the PET-920 and PET-266 targets was lower than the calculated ones, probably ascribable to the presence of surface inhomogeneities which has been identified

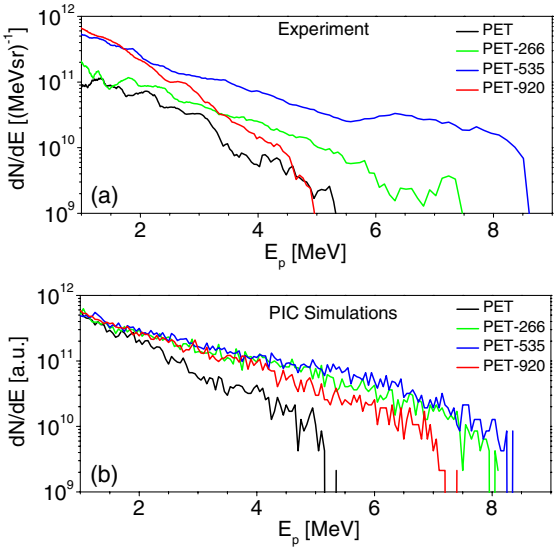

FIG. 3 (color online). Proton energy distributions from analysis of TP spectra (a) and PIC simulations (b) for different irradiated targets. The vertical axis in (b) was rescaled in order to match the experimental values. The experimental cutoff energy for PET, PET-266, PET-535, PET-920 is 5.3, 5, 7.5, and 8.6 MeV, respectively. The PIC simulation cutoff energy for PET, PET-266, PET-535, PET-920 is 5.2, 7.2, 8, and 8.4 MeV, respectively.

(only in the case of these two target geometries) scanning the target surface by scanning electron microscope after the fabrication process.

An accurate statistics has been performed in the experimental campaign and results are summarized in Fig. 4. Both experimental results and numerical simulations show that under optimal experimentally achievable acceleration conditions optimal proton maximum energy as well as total proton beam energy can be obtained when targets with 535 nm diameter spheres are used. Also the total ion energy (estimated from TOF spectra) shows a similar trend (blue dotted line in Fig. 4). The average proton cutoff energy (measured by the TP spectrometer) is about 7.5 and 4.7 MeV for PET-535 (nanostructured target) and PET (planar target), respectively. The average experimental cutoff energy in the case of a 1.5 μm thick PET planar target was (3 ± 0.6) MeV (green square in Fig. 4). Results obtained with 535 nm diameter spheres showed a total proton beam energy (ε_p) and ion beam energy (ε_i) which was increased by 6.3 and 3.9 times (average values), respectively, in comparison to the planar target geometry ($\varepsilon^o{}_p$ and $\varepsilon^o{}_i$). The relatively large experimental error bars reported in the plot are ascribable to the nonideal uniformity of the PS nanospheres on the sample surface and to the fluctuations in the measured proton beam divergence (energy dependent).

The proton cutoff energy and the total beam energy measured in the whole experimental campaign have been

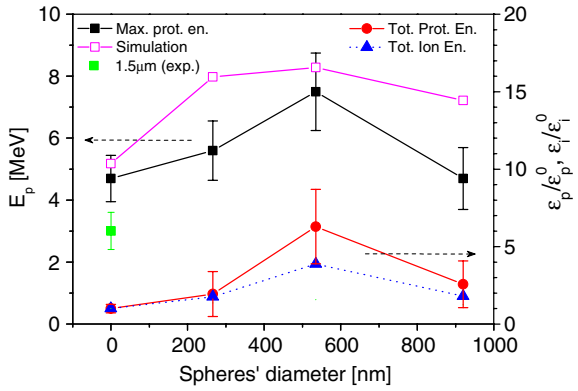

FIG. 4 (color online). Proton beam maximum energy (left-handed axis) and the total energy of the proton and ion beams, each normalized to the case of a planar foil (right-handed axis) for different target geometries.

correlated and plotted in Fig. 5 along with the simulation outputs (hollow symbols). The points for individual experimental shots clearly demonstrate the shot consistency and the growth of the total beam energy with the proton maximum energy, which implies a growth of the acceleration mechanism efficiency. The PIC simulation outputs reported in Fig. 5 also show an increase in the acceleration efficiency (proton cutoff energy and total energy) from a structured target (PET-535) with respect to a planar one (PET), when a similar geometry is used with Petawatt (PW)-class lasers (hollow stars).

The experimental results presented here clearly demonstrate that the use of nanostructured thin plastic foils on the target front side can strongly enhance the laser-driven proton beam acceleration mechanism. In fact, the maximum proton energy was increased by a factor of 1.6 ($\sim 60\%$ increment) for the optimal spheres' diameter of 535 nm in comparison to the planar foil. The effective target thickness did not play a crucial role in the cutoff

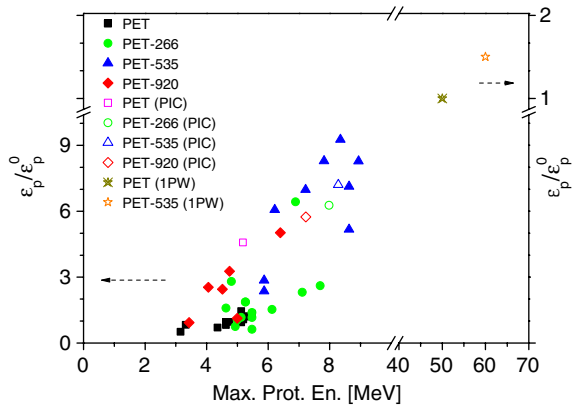

FIG. 5 (color online). Correlation between maximum proton energy and total proton energy in the spectrometer solid angle (full symbols are experimental points and hollow symbols are PIC simulation outputs).

proton energy, in fact in the best case a value of 3.8 MeV was achieved with a 1.5 μm thick PET planar target, which is much lower than the maximum proton energy measured in the case of the 0.9 μm thick PET planar target (about 5 MeV). The total number of protons (with energies exceeding 1 MeV) was increased about 5 times. This valuable experimental result implies a substantial increase in the laser-driven proton acceleration efficiency (about 6 times) that is mainly related to the enhancement of the laser absorption efficiency at the target front surface and to the subsequent increase of the hot electron population, which in turn is responsible for the proton acceleration mechanism [10–15].

The use of an ultrahigh laser contrast ($> 5 \times 10^{11}$) was crucial to ensure a genuine laser-nanosphere interaction allowing the experimental achievement of such enhanced TNSA regime. The slight disagreement between experimental and numerical results in the case of targets with 266 and 920 nm spheres' diameter can be ascribed to nonuniformities on the target surface detected after the target fabrication, which practically reduce the effective interaction of the laser beam with the structured surface (the number of nanospheres in the laser spot area is lower than the one used in our simulations).

A number of different effects may contribute to higher absorption for the used nanostructured targets. In fact, the nanosphere layer on the target front side implies an effective larger surface area; i.e., a higher number of particles can interact with the laser field. Moreover, the nanosphere screens the incident laser wave but the accelerated electrons can propagate through it, and, consequently, be easily out of the laser wave phase, thus gaining energy more efficiently along the longitudinal direction. This absorption process can be associated with the multipass stochastic heating in the case of laser interaction with clusters [25]. Unlike the case of laser coupling to a surface wave, where a resonant matching of the laser incidence angle and the structure period is required [16], the PIC simulations show that both the laser absorption and the proton acceleration efficiency are not particularly sensitive to the laser incidence angle [18]. However, along the experiment the laser incidence angle was not normal (with respect to the target surface); thus, vacuum heating [26] and resonance absorption [27] mechanisms might have played a role. Since the latter parameter has not been optimized during our experimental campaign (it was kept constant at 22.5° due to experimental constraints), the increase in TNSA acceleration efficiency might be further improved in future experiments.

The complex interplay of the above discussed physical mechanisms can lead to the experimental and numerical achievements reported here (similar results were presented in our previous theoretical paper [18]) showing an optimal target geometry (in terms of maximum proton energy and total number) in the case of spheres with a diameter of

535 nm. This results can be qualitatively explained in a very simplified picture: the 920 nm spheres are too large (too far each other) to maximize the collective interaction among the laser field and electrons belonging to neighboring spheres and a sort of ''photon scattering'' occurs; the 266 nm spheres are too small (too close each other) and a sort of ''smoothing'' in the collective interaction occurs leading to a condition similar to the case of a planar surface target. A similar result is reported in Ref. [14] where the highest x-ray yield (corresponding to an optimal laser absorption) is achieved for a sphere diameter slightly larger than half the laser wavelength (260 nm for a 400 nm wavelength in Ref. [14] and 535 nm for a 805 nm in our experiment).

Moreover, fine structures comparable to the laser spot size, e.g., microdots, might be additionally added on the target rear side in order to improve the energetic and/or angular characteristics of the accelerated ion bunches [28,29]. Such enhanced photo-proton sources may be considered as a compact alternative to low energy large conventional accelerators with a possible use for cancer therapy or other applications. In fact, our simulations show that a maximum proton energy of about 60 MeV (requested energy for eye melanoma treatment [30]) can be reached when using a PW-class laser beam with an intensity of about 2×10^{21} W/cm^2 (nominally 0.5 PW on target and 5 μm focal spot diameter) on the investigated nanostructured samples. The PIC simulations show that the maximum proton energy is also increased in this laser intensity regime (about 20%) as reported in Fig. 5.

This work benefitted from the support of the Czech Science Foundation (Project No. P205/11/1165), the Czech Republic's Ministry of Education, Youth and Sports to the HiLASE (CZ.1.05/2.1.00/01.0027), ELI-Beamlines (CZ.1.05/1.1.00/483/02.0061) and OPVK (CZ.1.07/2.3.00/20.0087) projects, the Academy of Sciences of the Czech Republic (M100101210 and KAN401220801), the CHARPAC Work Package of the Laserlab-Europe III (Project No. 284464), the Czech Technical University in Prague (RVO68407700) and the Ministry of Knowledge and Economy of Korea through the Ultrashort Quantum Beam Facility Project. Authors also thank Dr. J. Krasa, Dr. L. Laska, Dr. K. Jungwirth, and Professor S. V. Bulanov for the useful scientific discussions and Mr. S. W. Kang for the valuable technical support along the experiment.

[1] R. A. Snavely *et al.*, Phys. Rev. Lett. **85**, 2945 (2000).
[2] M. Borghesi, A. Schiavi, D. H. Campbell, M. G. Haines, O. Willi, A. J. MacKinnon, L. A. Gizzi, M. Galimberti, R. J. Clarke, and H. Ruhl, Plasma Phys. Control. Fusion **43**, A267 (2001).
[3] V. Malka, J. Faure, Y. A. Gauduel, E. Lefebvre, A. Rousse, and K. T. Phuoc, Nat. Phys. **4**, 447 (2008).
[4] T. E. Cowan *et al.*, Phys. Rev. Lett. **92**, 204801 (2004).
[5] S. P. Hatchett *et al.*, Phys. Plasmas **7**, 2076 (2000).
[6] S. C. Wilks, A. B. Langdon, T. E. Cowan, M. Roth, M. Singh, S. Hatchett, M. H. Key, D. Pennington, A. MacKinnon, and R. A. Snavely, Phys. Plasmas **8**, 542 (2001).
[7] T. Esirkepov, M. Borghesi, S. V. Bulanov, G. Mourou, and T. Tajima, Phys. Rev. Lett. **92**, 175003 (2004).
[8] A. Macchi, F. Cattani, T. V. Liseykina, and F. Cornolti, Phys. Rev. Lett. **94**, 165003 (2005).
[9] B. Qiao, S. Kar, M. Geissler, P. Gibbon, M. Zepf, and M. Borghesi, Phys. Rev. Lett. **108**, 115002 (2012).
[10] A. Henig *et al.*, Phys. Rev. Lett. **103**, 245003 (2009).
[11] D. Haberberger, S. Tochitsky, F. Fiuza, C. Gong, R. A. Fonseca, L. O. Silva, W. B. Mori, and C. Joshi, Nat. Phys. **8**, 95 (2012).
[12] Y. Sentoku, T. E. Cowan, A. Kemp, and H. Ruhl, Phys. Plasmas **10**, 2009 (2003).
[13] T. Nishikawa, H. Nakano, K. Oguri, N. Uesugi, K. Nishio, and H. Masuda, J. Appl. Phys. **96**, 7537 (2004).
[14] H. A. Sumeruk, S. Kneip, D. R. Symes, I. V. Churina, A. V. Belolipetski, T. D. Donnelly, and T. Ditmire, Phys. Rev. Lett. **98**, 045001 (2007).
[15] M. Raynaud and J. Kupersztych, Phys. Rev. B **76**, 241402 (2007).
[16] M. Raynaud, J. Kupersztych, C. Riconda, J. C. Adam, and A. Heron, Phys. Plasmas **14**, 092702 (2007).
[17] Y. Nodera, S. Kawata, N. Onuma, J. Limpouch, O. Klimo, and T. Kikuchi, Phys. Rev. E **78**, 046401 (2008).
[18] O. Klimo, J. Psikal, J. Limpouch, J. Proska, F. Novotny, T. Ceccotti, V. Floquet, and S. Kawata, New J. Phys. **13**, 053028 (2011).
[19] T. M. Jeong *et al.*, J. Korean Phys. Soc. **50**, 34 (2007).
[20] D. Margarone, A. Velyhan, L. Torrisi, M. Cutroneo, L. Giuffrida, A. Picciotto, J. Krasa, S. Cavallaro, J. Limpouch, O. Klimo, J. Psikal, J. Proska, and F. Novotny, Appl. Surf. Sci. (in press).
[21] I. J. Kim, I. W. Choi, S. K. Lee, K. A. Janulewicz, J. H. Sung, T. J. Yu, H. T. Kim, H. Yun, T. M. Jeong, and J. Lee, Appl. Phys. B **104**, 81 (2011).
[22] I. W. Choi *et al.*, Rev. Sci. Instrum. **80**, 053302 (2009).
[23] R. Prasad *et al.*, Nucl. Instrum. Methods Phys. Res., Sect. A **623**, 712 (2010).
[24] J. Psikal, J. Limpouch, S. Kawata, and A. A. Andreev, Czech. J. Phys. **56**, B515 (2006).
[25] B. N. Breizman, A. V. Arefiev, and M. V. Fomyts'kyi, Phys. Plasmas **12**, 056706 (2005).
[26] F. Brunel, Phys. Rev. Lett. **59**, 52 (1987).
[27] W. L. Kruer, *The Physics of Laser Plasma Interactions* (Addison-Wesley, Reading, MA, 1988).
[28] H. Schwoerer, S. Pfotenhauer, O. Jäckel, K.-U. Amthor, B. Liesfeld, W. Ziegler, R. Sauerbrey, K. W. D. Ledingham, and T. Esirkepov, Nature (London) **439**, 445 (2006).
[29] K. Takahashi, S. Kawata, D. Satoh, Y. Y. Ma, D. Barada, Q. Kong, and P. X. Wang, Phys. Plasmas **17**, 093102 (2010).
[30] G. Cuttone *et al.*, Eur. Phys. J. Plus **126**, 65 (2011).

JOURNAL OF APPLIED PHYSICS **114**, 083305 (2013)

Micro-sphere layered targets efficiency in laser driven proton acceleration

V. Floquet,[1] O. Klimo,[2] J. Psikal,[2] A. Velyhan,[3] J. Limpouch,[2] J. Proska,[2] F. Novotny,[2] L. Stolcova,[2] A. Macchi,[4,5] A. Sgattoni,[4,6] L. Vassura,[7,8] L. Labate,[4] F. Baffigi,[4] L. A. Gizzi,[4] Ph. Martin,[1] and T. Ceccotti[1,a)]

[1]*CEA, IRAMIS, SPAM, F-91191 Gif-sur-Yvette, France*
[2]*FNSPE, Czech Technical University in Prague, CR-11519 Prague, Czech Republic*
[3]*Institute of Physics v.v.i. ASCR, Na Slovance 1999, Prague, Czech Republic*
[4]*Istituto Nazionale di Ottica, Consiglio Nazionale delle Ricerche, research unit "Adriano Gozzini," Via G. Moruzzi 1, 56124 Pisa, Italy*
[5]*Dipartimento di Fisica "Enrico Fermi," Università di Pisa, largo Bruno Pontecorvo 3, 56127 Pisa, Italy*
[6]*Dipartimento di Energia, Politecnico di Milano, Milano, Italy*
[7]*LULI, UMR7605, CNRS-CEA-Ecole Polytechnique-Paris 6, 91128 Palaiseau, France*
[8]*Dipartimento SBAI, Università di Roma "La Sapienza," Via A. Scarpa 14, 00161 Roma, Italy*

(Received 12 July 2013; accepted 9 August 2013; published online 28 August 2013)

Proton acceleration from the interaction of high contrast, 25 fs laser pulses at $>10^{19}$ W/cm^2 intensity with plastic foils covered with a single layer of regularly packed micro-spheres has been investigated experimentally. The proton cut-off energy has been measured as a function of the micro-sphere size and laser incidence angle for different substrate thickness, and for both *P* and *S* polarization. The presence of micro-spheres with a size comparable to the laser wavelength allows to increase the proton cut-off energy for both polarizations at small angles of incidence (10°). For large angles of incidence, however, proton energy enhancement with respect to flat targets is absent. Analysis of electron trajectories in particle-in-cell simulations highlights the role of the surface geometry in the heating of electrons. © *2013 AIP Publishing LLC*. [http://dx.doi.org/10.1063/1.4819239]

I. INTRODUCTION

Acceleration of ions with high intensity laser pulses has been raising great interest for more than twelve years[1] and we nowadays have a detailed knowledge of the main acceleration mechanism, known as Target Normal Sheath Acceleration (TNSA). During the interaction of a high intensity laser pulse with a solid target (usually a micrometric thick foil), a fraction of the laser energy is transferred to a population of hot electrons. These latter migrate through the target and cross the rear target/vacuum interface, producing a sheath electric field of the order of some TV/m which accelerates ions (mainly protons due to their favorable mass/charge ratio). The characterization of proton emission provides a diagnostic for the processes of laser energy absorption and fast electron generation and transport in solid targets.[2] The energy, duration, flow, divergence, and laminarity characteristics of TNSA-accelerated ions allow to use them for several application such as isochoric heating,[3] ultrafast probing of electromagnetic fields in plasmas,[4] radiography of dense matter,[5] and radiobiological studies.[6] In addition, there is potential for laser-driven nuclear physics applications such as neutron production[7] and isotope production for positron emission tomography,[8] especially if ion acceleration can be optimized for femtosecond, small-scale laser systems.

With particular regard to the latter applications (and focusing on the acceleration of protons in the following), it is important to investigate strategies to enhance both the proton maximum energy and the laser energy conversion efficiency, and possibly to tailor their spectral distribution. One of the suggested ways is using structured targets in order to increase the coupling efficiency. Examples of such targets, having either nanometric[9] or micrometric[10] structures on the irradiated surface, have been already investigated. The observed X-ray yield enhancement[11] has been ascribed, for instance, to the action of multipass stochastic heating of the hot electrons in the oscillating laser field.[12]

This paper reports on an experimental study of "Micro-Spheres Targets" (MSTs) composed by a thin ($\sim\mu$m thick) plastic foil (substrate) with a mono-layer of hexagonally packed micrometer polystyrene spheres on its surface. The work here reported follows from previous indications by particle-in-cell simulations of MST targets,[13] showing enhancement of absorption and proton energy, and is complementary to similar measurements on a different laser system.[14,15] We studied the influence of laser polarization and incidence angle as well as of the structure size on the coupling efficiency of MSTs on the proton cut-off energies.

II. EXPERIMENTAL SET-UP AND TARGET STRUCTURE

The experiment was performed on the UHI-100 laser facility at CEA-Saclay. UHI-100 is a Ti:Sa laser delivering up to 2 J in a 25 fs pulse, with a contrast ratio better than 10^8 which is further improved to about 10^{12} using a double plasma mirror (DPM).[16] This latter feature is essential in order to preserve the MST surface structures. Laser wavefront correction is accomplished through a deformable mirror which enables to focus the laser pulse down to a 6 μm (FWHM) spot by using an f/3.75 off-axis parabola. The laser energy measured after the pulse compressor and the plasma

a)tiberio.ceccotti@cea.fr

mirror was 0.79 J, and after the focusing optics a 50% of such energy inside a $1/e^2$ spot was estimated. This corresponds to 0.2 J in the FWHM spot, leading to a peak intensity of $I = 2.8 \times 10^{19}$ W cm^{-2}. A rotating $\lambda/2$ wave plate was put on the laser path in order to study the influence of the pulse polarization (P or S). The incidence angle was varied from 10° up to 45° turning the target holder (around its vertical axis) without modifying the laser optical path. Proton emission was measured by a Thomson parabola, detecting proton energies ranging from 400 keV to 20 MeV (with a resolution $\Delta E/E \approx 5 \times 10^{-2}$ for the highest energies).

Targets were made of a thick Mylar substrate with different thicknesses (900 nm, 20 μm, and 40 μm) and a single layer of either 471 nm or 940 nm diameter polystyrene micro-spheres deposited at the surface in a hexagonal layout (see Fig. 1).

III. EXPERIMENTAL RESULTS

In Fig. 2, we show the measured cut-off proton energies as a function of the micro-sphere size for P polarized laser pulses at 10° incident angle. The 0 μm sphere size refers to simple foils without any structured layer. As expected on the basis of previous investigations with the same laser system, we did not detect any proton emission using 20 and 40 μm simple foils, due to their considerable thickness and to the small incidence angle. Nevertheless, repeating the measurements using 20 and 40 μm substrate MSTs, we observed that the presence of structures, and in particular of the 940 nm diameter micro-spheres, increases the proton energies above the detection threshold. Measurements in S polarization are reported too showing that the surface modulation induced by the spheres layer allows to transfer the laser energy to the target as effectively as in P polarization.

The observations are in qualitative agreement both with simulation results[13] and with independent experimental measurements.[14] With respect to the latter, quantitative differences in the energy values and in the "optimal" size of the spheres may be ascribed to different parameters, including target thickness, laser intensity and incidence angle. Taking the detection threshold as an upper limit for the proton

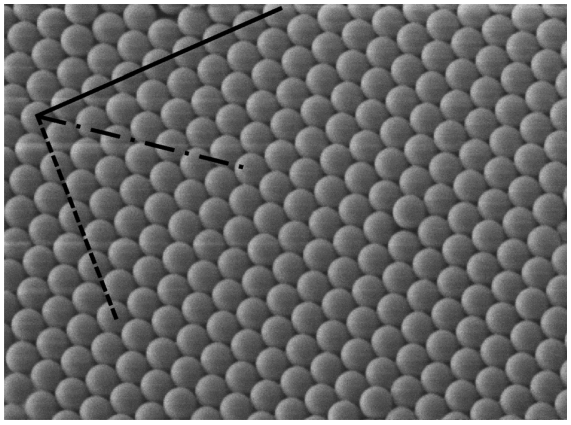

FIG. 1. Scanning Electron Microscopy picture of the 940 nm micro-sphere hexagonal layout of a MST. The lines indicate three different directions along which the structure would present a different spatial period.

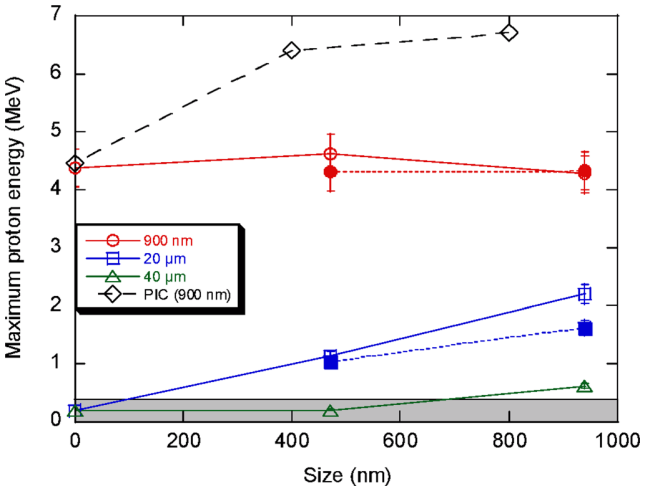

FIG. 2. Proton maximum energies as a function of micro-sphere size for different substrate thickness and PIC simulation data for a 900 nm substrate. P and S polarization measurements are reported as empty and filled marks respectively. Here and in Fig. 3, each point (error bar) represents the average value (statistical error) of five consecutive laser shots. Measurements falling under the diagnostic detection threshold (gray filled region in the plot) have been reported as an arbitrary 0.2 MeV constant value (for plot clarity sake, low energy S data have been omitted).

cut-off energy in flat targets, the relative enhancement in the case of 470 nm spheres is at least a factor of 2.5 and may further double for the 940 nm sphere, as shown in Fig. 2. Such enhancement factor is larger than observed in Ref. 14 at higher intensity. Furthermore, recent additional measurements[15] on the same laser system of Ref. 14 showed that both the relative increase with respect to flat targets and the dependence on the sphere's thickness become much smoother at higher intensity.

On the other hand, the 900 nm thick MSTs show energy values close to those observed for the simple foils, in contrast with 2D Particle-In-Cell (PIC) simulation results (see Ref. 13 for details), which foresee a cut-off energy enhancement of about 50% for both sphere sizes. Notice that the PIC simulations for flat thin targets reproduce well the observed energy cut-off, which is much higher than for thicker targets due to the contribution of electron recirculation process[17] (under our interaction conditions recirculation should enhance the proton energy for thicknesses approximately in the 500 nm–2μm range[18]). The strong discrepancy between experiment and simulation for the layered sphere case should then be ascribed to some technical or manufacturing issue with very thin foils, of thickness comparable to the diameter of the spheres, such as insufficient adhesion to the surface or wrapping and deformation of the foil. The exact nature of the failure to yield enhanced acceleration in the thinnest target case is not fully clear at present. In Ref. 14, the energy enhancement was observed for 1 μm thickness but with significant fluctuations, which supports the possibility of technical issues with thin targets.

Figure 3 reports the variation of proton energy as a function of the incidence angle, for P and S polarized laser pulses and the 20 μm thick, 940 nm spheres MST. While both P and S polarization give similar cut-off energies and a strong enhancement of proton energy with respect to flat targets at

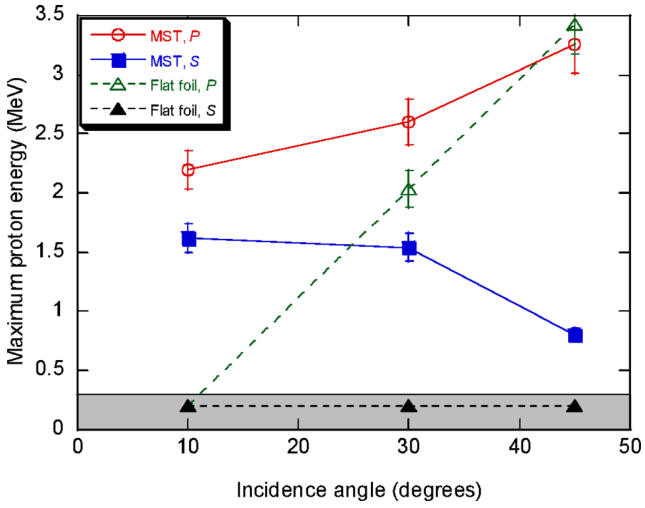

FIG. 3. Proton maximum energies as a function of the incidence angle for the 20 μm thick MST and a 20 μm flat Mylar foil, in P and S polarization.

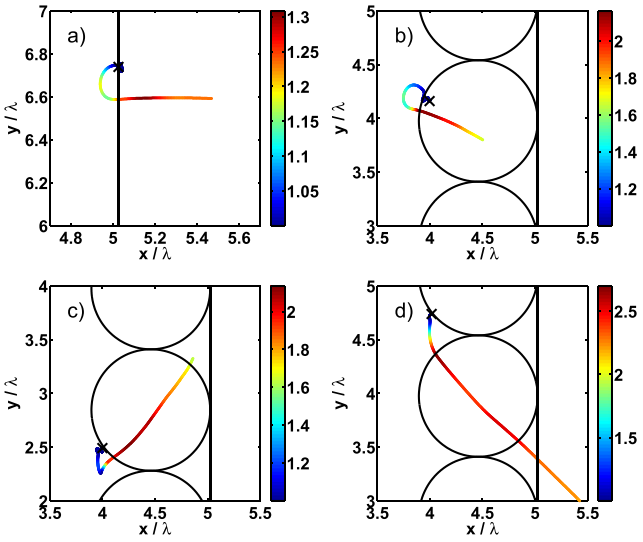

FIG. 4. 2D PIC simulations of electron trajectories for normal incidence ($a_0 = 1.5$) and stationary ions. Color represents the relativistic gamma factor of electrons. We considered a flat foil (a) and a MST with electrons leaving from the front part of the sphere and going back into the same sphere (b), or accelerated from the side part and re-entering the same sphere (c) or the neighboring one (d).

the smallest angle (10°), for the largest angle (45°) the behavior is very close to flat foils, with almost the same cut-off energy for P polarization and a much lower value for S polarization. This trend may be related to the increase of both the focal spot size and the geometrical shadow effect by the structured surface for increasing angles, so that the coupling with the spheres is reduced and the interaction conditions get eventually similar to those of a flat foil.

While a comparison with Ref. 14 is not possible since in that experiment a single angle of incidence (22.5°) was investigated, the decrease of proton energy enhancement as a function of the incidence angle using P polarized laser beam agrees qualitatively with absorption measurements using targets with surface roughness of similar size.[19] The femtosecond laser pulse absorption (which is connected with the efficiency of ion acceleration) reported in Ref. 19 was almost constant in the range between 20° and 60° for rough surfaced targets, whereas the absorption was increasing for flat targets. The latter may be simply attributed to "vacuum heating" (or Brunel effect),[20] which is driven by the electric field component of the laser field and is more efficient at large incidence angles. The absence of protons with energy above the cut-off threshold observed in the case of S polarization and flat targets suggests that the role of relativistic $J \times B$ heating[21] is negligible in the investigated regime of laser intensity and plasma density.

IV. SIMULATION RESULTS

To go deeper into the interpretation of the increased absorption due to the spheres layer, the trajectories of individual particles in PIC simulations (similar to those reported in Ref. 13) have been studied. Specifically, we analyzed the trajectories of 9000 electrons in 2D PIC simulations with a dimensionless peak amplitude $a_0 = 1.5$ and density $n_e = 40n_c$ (corresponding to an intensity of 4.9×10^{18} W cm^{-2} and $n_e = 6.9 \times 10^{22}$ cm^{-3} for $\lambda = 0.8$ μm). The simulation considered a plane laser wave and stationary ions. According to this analysis, we can distinguish three main components of the population of electrons which are accelerated in MSTs. The first one includes electrons that originate from the "top" of the spheres (see Fig. 4(b)) and release the energy they gain in the same sphere (releasing of energy is identified with re-entering the target at high velocity, as in the simple picture of the Brunel effect[20]). Another fraction of accelerated electrons comes from the side surface of spheres and re-enter into the same sphere too (Fig. 4(c)). These two processes are quite close to the corresponding mechanism observed in a flat foil at normal and oblique incidence respectively and gather about 40% of the overall electron population. However, the observed absorption increase is mainly due to the electrons accelerated from the side of the spheres which deposit their energy in the very neighboring sphere in half a laser period (Fig. 4(d)). Indeed, these last electrons may deposit their energy after getting the maximum acceleration and before being decelerated by the second half laser period. As a consequence, if the distance between two spheres is either too large or too small, this process shows a lower efficiency. This analysis of electron trajectory may help to explain the stochastic heating which takes place in the closely packed configuration of microspheres but it does not exclude other efficient laser absorption mechanisms with different electron trajectories if the separation distance between spheres is larger.

It may be noticed that MSTs are represented in 2D simulations as an array of adjacent, closely packed wires (3D spheres become wires in 2D due to the translational invariance in the direction normal to the simulation plane) with a fixed distance between the centers and tips of all the spheres (in other words the 2D system has a discrete translational symmetry, with a period equal to the sphere/wire diameter). Nonetheless, in a real target with an hexagonal MST layout, the electrons traveling on a line parallel to the surface would see a spatial periodicity equal to the size of the sphere only

along a limited set of directions (the three axes of symmetry passing through the midpoints of opposite sides and the center of the hexagonal lattice; see Fig. 1). According to their initial acceleration direction, electrons can cross a vacuum region between any couple of spheres or take a path showing an even more complicated periodicity of the system (dotted and dashed-dotted lines respectively in Fig. 1). Thus, multipass stochastic heating may behave differently in a real 3D geometry (not computationally accessible at present) and the acceleration dynamics may depend upon the angle between the laser polarization and the lattice symmetry axis, which is not controlled in the experiment.

V. CONCLUSIONS

In conclusion, an enhancement of the proton energy cutoff has been observed in thick plastic targets covered with a layer of microspheres, in broad agreement with previous simulation results and independent measurements. However, it has also been shown that the enhancement is not effective at large incidence angles for thick substrates. The analysis of electron trajectories in particle-in-cell simulations have highlighted their role in leading to absorption in a pattern of regularly packed sphere.

ACKNOWLEDGMENTS

The research leading to these results has received funding from LASERLAB-EUROPE (Grant Agreement No. 284464, EU's Seventh Framework Programme), proposal n.SLIC001693. We acknowledge the ANR Blanc (GOSPEL, project BLAN08-1 380251), the Triangle of Physics (APPEAL), the Labex PALM, EGIDE, the Ile-de- France region (SESAME), the SAPHIR consortium (OSEO) and the regional board of Essonne (ASTRE) for their financial support. Partial support by the Czech Science Foundation (Project P205/11/1165), by the MSMT ECOP project (CZ.1.07/2.3.00/20.0087), and by MIUR (Italy) via the FIR project "SULDIS" are also acknowledged.

[1]M. Borghesi, J. Fuchs, S. V. Bulanov, A. J. MacKinnon, P. K. Patel, and M. Roth, Fusion Sci. Technol. **49**, 412 (2006); available at http://www.ans.org/pubs/journals/fst/a_1159. H. Daido, M. Nishiuchi, and A. S. Pirozhkov, Rep. Prog. Phys. **75**, 056401 (2012); A. Macchi, M. Borghesi, and M. Passoni, Rev. Mod. Phys. **85**, 751 (2013).

[2]J. Fuchs, T. E. Cowan, P. Audebert, H. Ruhl, L. Gremillet, A. Kemp, M. Allen, A. Blazevic, J.-C. Gauthier, M. Geissel, M. Hegelich, S. Karsch, P. Parks, M. Roth, Y. Sentoku, R. Stephens, and E. M. Campbell, Phys. Rev. Lett. **91**, 255002 (2003); M. Kaluza, J. Schreiber, M. I. K. Santala, G. D. Tsakiris, K. Eidmann, J. Meyer-ter Vehn, and K. J. Witte, Phys. Rev. Lett. **93**, 045003 (2004); P. McKenna, D. C. Carroll, R. J. Clarke, R. G. Evans, K. W. D. Ledingham, F. Lindau, O. Lundh, T. McCanny, D. Neely, A. P. L. Robinson, L. Robson, P. T. Simpson, C.-G. Wahlström, and M. Zepf, Phys. Rev. Lett. **98**, 145001 (2007); P. McKenna, A. P. L. Robinson, D. Neely, M. P. Desjarlais, D. C. Carroll, M. N. Quinn, X. H. Yuan, C. M. Brenner, M. Burza, M. Coury, P. Gallegos, R. J. Gray, K. L. Lancaster, Y. T. Li, X. X. Lin, O. Tresca, and C.-G. Wahlström, Phys. Rev. Lett. **106**, 185004 (2011).

[3]P. K. Patel, A. J. Mackinnon, M. H. Key, T. E. Cowan, M. E. Foord, M. Allen, D. F. Price, H. Ruhl, P. T. Springer, and R. Stephens, Phys. Rev. Lett. **91**, 125004 (2003); A. Mancic, J. Robiche, P. Antici, P. Audebert, C. Blancard, P. Combis, F. Dorchies, G. Faussurier, S. Fourmaux, M. Harmand, R. Kodama, L. Lancia, S. Mazevet, M. Nakatsutsumi, O. Peyrusse, V. Recoules, P. Renaudin, R. Shepherd, and J. Fuchs, High Energy Density Phys. **6**, 21 (2010).

[4]M. Borghesi, L. Romagnani, A. Schiavi, D. H. Campbell, M. G. Haines, O. Willi, A. J. Mackinnon, M. Galimberti, L. Gizzi, R. J. Clarke, and S. Hawkes, Appl. Phys. Lett. **82**, 1529 (2003); A. J. Mackinnon, P. K. Patel, D. W. Price, D. Hicks, L. Romagnani, and M. Borghesi, Appl. Phys. Lett. **82**, 3188 (2003); N. L. Kugland, D. D. Ryutov, C. Plechaty, J. S. Ross, and H.-S. Park, Rev. Sci. Instrum. **83**, 101301 (2012).

[5]A. J. Mackinnon, P. K. Patel, M. Borghesi, R. C. Clarke, R. R. Freeman, H. Habara, S. P. Hatchett, D. Hey, D. G. Hicks, S. Kar, M. H. Key, J. A. King, K. Lancaster, D. Neely, A. Nikkro, P. A. Norreys, M. M. Notley, T. W. Phillips, L. Romagnani, R. A. Snavely, R. B. Stephens, and R. P. J. Town, Phys. Rev. Lett. **97**, 045001 (2006); A. B. Zylstra, C. K. Li, H. G. Rinderknecht, F. H. Séguin, R. D. Petrasso, C. Stoeckl, D. D. Meyerhofer, P. Nilson, T. C. Sangster, S. L. Pape, A. Mackinnon, and P. Patel, Rev. Sci. Instrum. **83**, 013511 (2012).

[6]A. Yogo, K. Sato, M. Nishikino, M. Mori, T. Teshima, H. Numasaki, M. Murakami, Y. Demizu, S. Akagi, S. Nagayama, K. Ogura, A. Sagisaka, S. Orimo, M. Nishiuchi, A. S. Pirozhkov, M. Ikegami, M. Tampo, H. Sakaki, M. Suzuki, I. Daito, Y. Oishi, H. Sugiyama, H. Kiriyama, H. Okada, S. Kanazawa, S. Kondo, T. Shimomura, Y. Nakai, M. Tanoue, H. Sasao, D. Wakai, P. R. Bolton, and H. Daido, Appl. Phys. Lett. **94**, 181502 (2009); A. Yogo, T. Maeda, T. Hori, H. Sakaki, K. Ogura, M. Nishiuchi, A. Sagisaka, H. Kiriyama, H. Okada, S. Kanazawa, T. Shimomura, Y. Nakai, M. Tanoue, F. Sasao, P. R. Bolton, M. Murakami, T. Nomura, S. Kawanishi, and K. Kondo, Appl. Phys. Lett. **98**, 053701 (2011); S. D. Kraft, C. Richter, K. Zeil, M. Baumann, E. Beyreuther, S. Bock, M. Bussmann, T. E. Cowan, Y. Dammene, W. Enghardt, U. Helbig, L. Karsch, T. Kluge, L. Laschinsky, E. Lessmann, J. Metzkes, D. Naumburger, R. Sauerbrey, M. Schürer, M. Sobiella, J. Woithe, U. Schramm, and J. Pawelke, New J. Phys. **12**, 085003 (2010); F. Fiorini, D. Kirby, M. Borghesi, D. Doria, J. C. G. Jeynes, K. F. Kakolee, S. Kar, S. Kaur, K. J. Kirby, M. J. Merchant, and S. Green, Phys. Med. Biol. **56**, 6969 (2011).

[7]J. M. Yang, P. McKenna, K. W. D. Ledingham, T. McCanny, L. Robson, S. Shimizu, R. P. Singhal, M. S. Wei, K. Krushelnick, R. J. Clarke, D. Neely, and P. A. Norreys, J. Appl. Phys. **96**, 6912 (2004); L. Willingale, G. M. Petrov, A. Maksimchuk, J. Davis, R. R. Freeman, A. S. Joglekar, T. Matsuoka, C. D. Murphy, V. M. Ovchinnikov, A. G. R. Thomas, L. V. Woerkom, and K. Krushelnick, Phys. Plasmas **18**, 083106 (2011).

[8]S. Fritzler, V. Malka, G. Grillon, J. P. Rousseau, F. Burgy, E. Lefebvre, E. d'Humiéres, P. McKenna, and K. W. D. Ledingham, Appl. Phys. Lett. **83**, 3039 (2003); K. W. D. Ledingham, P. McKenna, T. McCanny, S. Shimizu, J. M. Yang, L. Robson, J. Zweit, J. M. Gillies, J. Bailey, G. N. Chimon, R. J. Clarke, D. Neely, P. A. Norreys, J. L. Collier, R. P. Singhal, M. S. Wei, S. P. D. Mangles, P. Nilson, K. Krushelnick, and M. Zepf, J. Phys. D: Appl. Phys. **37**, 2341 (2004); M. Fujimoto, K. Matsukado, H. Takahashi, Y. Kawada, S. Ohsuka, and S. Aoshima, Rev. Sci. Instrum. **80**, 113301 (2009); K. Ogura, T. Shizuma, T. Hayakawa, A. Yogo, M. Nishiuchi, S. Orimo, A. Sagisaka, A. Pirozhkov, M. Mori, H. Kiriyama, S. Kanazawa, S. Kondo, Y. Nakai, T. Shimoura, M. Tanoue, A. Akutsu, T. Motomura, H. Okada, T. Kimura, Y. Oishi, T. Nayuki, T. Fujii, K. Nemoto, and H. Daido, Appl. Phys. Express **2**, 066001 (2009).

[9]S. Bagchi, P. Prem Kiran, M. K. Bhuyan, S. Bose, P. Ayyub, M. Krishnamurthy, and G. Ravindra Kumar, Laser Part. Beams **26**, 259 (2008).

[10]G. Yue Hu, A. Le Lei, J. Wei Wang, L. Gen Huang, W. Tao Wang, X. Wang, Y. Xu, B. Fei Shen, J. Sheng Liu, W. Yu, R. Xin Li, and Z. Zhan Xu, Phys. Plasmas **17**, 083102 (2010).

[11]H. A. Sumeruk, S. Kneip, D. R. Symes, I. V. Churina, A. V. Belolipetski, T. D. Donnelly, and T. Ditmire, Phys. Rev. Lett. **98**, 045001 (2007).

[12]B. N. Breizman, A. V. Arefiev, and M. V. Fomyts'kyi, Phys. Plasmas **12**, 056706 (2005).

[13]O. Klimo, J. Psikal, J. Limpouch, J. Proska, F. Novotny, T. Ceccotti, V. Floquet, and S. Kawata, New J. Phys. **13**, 053028 (2011).

[14]D. Margarone, O. Klimo, I. J. Kim, J. Prokůpek, J. Limpouch, T. M. Jeong, T. Mocek, J. Pšikal, H. T. Kim, J. Proška, K. H. Nam, L. Štolcová, I. W. Choi, S. K. Lee, J. H. Sung, T. J. Yu, and G. Korn, Phys. Rev. Lett. **109**, 234801 (2012).

[15]D. Margarone, O. Klimo, I. J. Kim, J. Prokupek, J. Limpouch, T. M. Jeong, T. Mocek, J. Psikal, H. T. Kim, J. Proska, K. H. Nam, I. W. Choi, T. Levato, L. Stolcova, S. K. Lee, M. Krus, F. Novotny, J. H. Sung, J. Kaufman, T. J. Yu, and G. Korn, Proc. SPIE **8780**, 878023 (2013).

[16]A. Lévy, T. Ceccotti, P. D'Oliveira, F. Réau, M. Perdrix, F. Quéré, P. Monot, M. Bougeard, H. Lagadec, P. Martin, J.-P. Geindre, and P. Audebert, Opt. Lett. **32**, 310 (2007).
[17]Y. Sentoku, T. E. Cowan, A. Kemp, and H. Ruhl, Phys. Plasmas **10**, 2009 (2003); T. Ceccotti, A. Lévy, H. Popescu, F. Réau, P. D'Oliveira, P. Monot, J. P. Geindre, E. Lefebvre, and P. Martin, Phys. Rev. Lett. **99**, 185002 (2007).
[18]V. Floquet, T. Ceccotti, S. D. Dufrenoy, G. Bonnaud, L. Gremillet, P. Monot, and P. Martin, Phys. Plasmas **19**, 094501 (2012).
[19]M. Cerchez, M. Swantusch, M. Bemke, M. Toncian, T. Toncian, C. Röde, G. Paulus, A. Andreev, and O. Willi, "Absorption of variable contrast femtosecond laser pulses by overdense plasmas in the relativistic regime," in *ECA (Euroconference Abstracts)*, ECA Europhysics Conference Abstracts,(European Physical Society (EPS), 2010), Vol. 34A, p. 5.205.
[20]F. Brunel, Phys. Rev. Lett. **59**, 52 (1987).
[21]W. L. Kruer and K. Estabrook, Phys. Fluids **28**, 430 (1985).

Evidence of Resonant Surface-Wave Excitation in the Relativistic Regime through Measurements of Proton Acceleration from Grating Targets

T. Ceccotti,[1,*] V. Floquet,[1] A. Sgattoni,[2,3] A. Bigongiari,[4] O. Klimo,[5,6] M. Raynaud,[7] C. Riconda,[4] A. Heron,[8] F. Baffigi,[2] L. Labate,[2] L. A. Gizzi,[2] L. Vassura,[9,10] J. Fuchs,[9] M. Passoni,[3] M. Květon,[5] F. Novotny,[5] M. Possolt,[5] J. Prokůpek,[5,6] J. Proška,[5] J. Pšikal,[5,6] L. Štolcová,[5,6] A. Velyhan,[6] M. Bougeard,[1] P. D'Oliveira,[1] O. Tcherbakoff,[1] F. Réau,[1] P. Martin,[1] and A. Macchi[2,11,†]

[1]*CEA/IRAMIS/SPAM, F-91191 Gif-sur-Yvette, France*
[2]*Istituto Nazionale di Ottica, Consiglio Nazionale delle Ricerche, research unit "Adriano Gozzini," 56124 Pisa, Italy*
[3]*Dipartimento di Energia, Politecnico di Milano, 20133 Milano, Italy*
[4]*LULI, Université Pierre et Marie Curie, Ecole Polytechnique, CNRS, CEA, 75252 Paris, France*
[5]*FNSPE, Czech Technical University in Prague, CR-11519 Prague, Czech Republic*
[6]*Institute of Physics of the ASCR, ELI-Beamlines project, Na Slovance 2, 18221 Prague, Czech Republic*
[7]*CEA/DSM/LSI, CNRS, Ecole Polytechnique, 91128 Palaiseau Cedex, France*
[8]*CPHT, CNRS, Ecole Polytechnique, 91128 Palaiseau Cedex, France*
[9]*LULI, UMR7605, CNRS-CEA-Ecole Polytechnique-Paris 6, 91128 Palaiseau, France*
[10]*Dipartimento SBAI, Università di Roma "La Sapienza," Via A. Scarpa 14, 00161 Roma, Italy*
[11]*Dipartimento di Fisica "Enrico Fermi," Università di Pisa, Largo Bruno Pontecorvo 3, I-56127 Pisa, Italy*

(Received 24 May 2013; published 28 October 2013)

The interaction of laser pulses with thin grating targets, having a periodic groove at the irradiated surface, is experimentally investigated. Ultrahigh contrast ($\sim 10^{12}$) pulses allow us to demonstrate an enhanced laser-target coupling for the first time in the relativistic regime of ultrahigh intensity $>10^{19}$ W/cm^2. A maximum increase by a factor of 2.5 of the cutoff energy of protons produced by target normal sheath acceleration is observed with respect to plane targets, around the incidence angle expected for the resonant excitation of surface waves. A significant enhancement is also observed for small angles of incidence, out of resonance.

DOI: 10.1103/PhysRevLett.111.185001 PACS numbers: 52.38.−r, 41.75.Jv, 52.27.Ny

An efficient coupling between high-intensity laser pulses and solid targets with sharp density profiles is the key to several applications, such as ion acceleration via the target normal sheath acceleration (TNSA) mechanism [1], production of coherent and incoherent x-rays [2], isochoric heating and creation of warm dense matter [3], and studies of electron transport [4]. The laser-plasma interaction at the target surface is strongly sensitive to both the longitudinal profile and transverse modulations of the density on the scale of the laser wavelength (or even a smaller scale). Femtosecond laser pulses may be short enough that the surface structuring is preserved during the interaction and not washed away by hydrodynamical expansion, allowing a more efficient coupling and enhancing particle and radiation emission [5]. In particular, targets with a periodic surface modulation (gratings) allow the resonant coupling of the laser pulse with surface waves (SWs) [6] as it is widely used in plasmonics applications at low laser intensity [7]. So far, however, most of the studies on structured targets and on SW-induced absorption [8] have been limited to intensities $I \lesssim 10^{16}$ W/cm^2 because of the effect of "prepulses," typical of chirped pulse amplification laser systems, which lead to early plasma formation and destruction of surface structures before the main pulse. Techniques such as the plasma mirror [9] to achieve ultrahigh pulse-to-prepulse contrast ratios now offer the opportunity to extend such studies at very high intensity. Recently, the effects of a periodic grating structure on high harmonic generation have been experimentally demonstrated at $I > 10^{20}$ W/cm^2 [10].

There is no detailed nonlinear theory of SWs in the regime where relativistic effects may become dominant. However, SW coupling at high intensity has been observed in particle-in-cell (PIC) simulations of laser interaction with a grating target (designed for resonant SW excitation according to linear, nonrelativistic theory), which showed a strong enhancement of both absorption and energetic electron production [11–13] and, in turn, higher energies for the protons accelerated by TNSA. Thus, besides the interest of using grating targets for more efficient TNSA, the latter also provides a diagnostic for the study of SW-enhanced absorption.

This Letter reports on an experimental study of ultrashort laser interaction with grating targets in conditions of relativistically strong intensity ($>10^{19}$ W/cm^2) and very high contrast ($\sim 10^{12}$). The coupling enhancement was detected through simultaneous single-shot measurements of TNSA proton emission and of target laser pulse reflection, as a function of the incidence angle and for different laser polarization and target thickness. The data show a peak of proton cutoff energies and a drop in the target reflectivity for P-polarized pulses when the incidence

angle is close to the resonant value for SW excitation. A significant enhancement of proton energy with respect to flat targets is also observed for small incidence angles, far from resonance. The analysis is supported by two-dimensional (2D) PIC simulations.

The experiment was performed at the Saclay Laser Interaction Center facility, using the UHI100 laser delivering 80 TW ultrashort pulses (25 fs) at a central wavelength of 790 nm. The contrast of the beam was raised to about 10^{12} (high contrast, HC) thanks to a double plasma mirror [14,15] whereas the focal spot was optimized through the correction of the laser pulse wave front using a deformable mirror. The beam was focused using an off-axis $f = 300$ mm parabola, with 40% of total laser energy enclosed on a spot size of 10 μm (diameter at $1/e^2$), corresponding to an intensity of about 2.5×10^{19} W cm^{-2}.

Grating targets (GTs) were produced by heat embossing into mylar foils. Three different values of the foil thickness (23, 40, and 0.9 μm) and two values of the peak-to-valley depth (0.5 and 0.3 μm) were tested. The grating period was $d = 2\lambda$ corresponding to a resonant angle of incidence $\alpha_{\mathrm{res}} \simeq 30°$ according to the relation $\sin\alpha_{\mathrm{res}} + \lambda/d = \sqrt{(1 - n_e/n_c)/(2 - n_e/n_c)}$ valid for a cold plasma and assuming $n_e \gg n_c$ with $n_c = 1.1 \times 10^{21}$ cm$^{-3}(\lambda/\mu\mathrm{m})^{-2}$ the cutoff density. The angle of incidence α was changed by pivoting the target holder around its vertical axis.

Proton spectra were recorded with a Thomson parabola instrument inside the vacuum chamber, equipped with a 100 μm diameter entrance pinhole at a distance of 150 mm from the target chamber center (TCC). Detection was provided by a microchannel plate plus a phosphor screen imaged onto a 12 bit charged coupled device camera. For each value of α the Thomson parabola was moved around the TCC and realigned with the normal to the rear surface of the target. (see Fig. 1). The reflected laser light was imaged on a frosted glass placed about 200 mm from TCC and recorded by a 12 bit coupled device camera, in order to estimate variations in the target reflectivity. An optical fiber spectrometer was used to simultaneously record second harmonic (2ω) and three-halves harmonic ($3\omega/2$) signals. Finally, a radiochromic film (RCF) stack was arranged in order to form a 50 mm diameter retractable ring around the target (Fig. 1) and collect the particle and radiation emission over an angle of almost 2π radians (a 30° window was left open for laser entrance). The stack was composed by three HD-810 Gafcromic film layers, screened from visible and low-energy x-ray emission by a 2 μm aluminized Mylar film, and mostly sensitive to protons with energies of 2.5, 3.75, and 5 MeV, respectively.

A confirmation that the grating pattern is preserved until the interaction was provided by the RCF stack. Figures 2(a) and 2(b) show the first two layers of the RCF stack after a shot on a GT with HC pulses at 30° incidence angle that corresponds to 0° on the axis in the figure. Besides the expected proton spots in the forward (30°) and backward (−150°) target normal directions (which is a typical

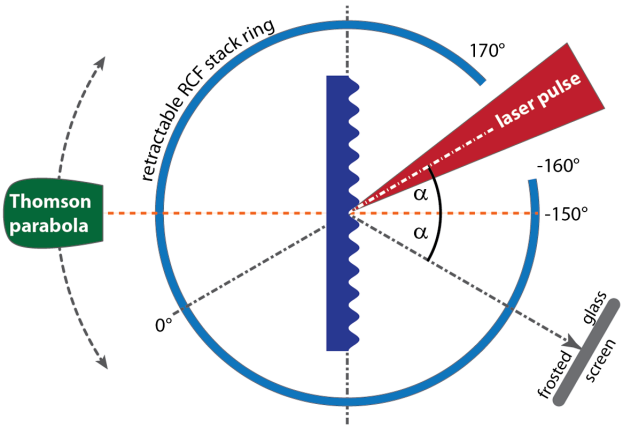

FIG. 1 (color online). Schematic top view of the experimental setup. The Thomson parabola and the frosted glass screen were located along the target normal direction and the laser specular directions, respectively.

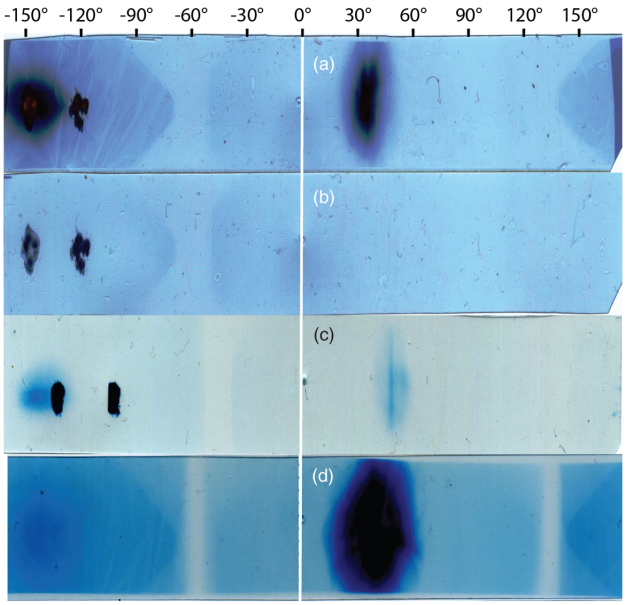

FIG. 2 (color online). Frames (a) and (b): first two layers of the exposed RCF at high laser contrast conditions, showing the typical proton forward (30°) and backward (−150°) proton spots as well as two smaller spots ($\simeq -125°$ and $\simeq -155°$) attributed to laser reflection at 0 and +1 grating diffraction orders. The position 0° corresponds to the incident laser axis. The parabolic "shadows" are due to the boundary of the target holder, which screens diffuse radiation (such as electrons and hard x-rays) from the plasma. Frame (c): same as (a), but for an angle of incidence different by 15°, leading to a shift of the diffraction spots. Frame (d): first RCF layer in low laser contrast conditions, for which both the backward proton and the diffraction spots disappear. All sets of RCFs have been exposed to three laser shots.

feature of HC conditions [16]) on the first stack film, two burn spots were obtained on the Al cover foil, corresponding to the two small structures at $\simeq -125°$ and $\simeq -155°$ in Figs. 2(a) and 2(b). According to their angular positions and because of the reflected laser intensity on the RCF ($\sim 10^{14}$ W/cm^2), the spots can be attributed to reflection at the 0 and +1 grating diffraction orders. The spots are still present (with the expected angular shift) at an incidence angle to 45° [Fig. 2(c)] but disappear under low contrast (10^8) conditions [Fig. 2(d)]. The presence of an underdense preplasma was also ruled out by the absence of optical emission at the $3\omega/2$ frequency since the latter is tightly correlated to the plasma scale length at the $n_e = n_c/4$ layer, where the underlying process of two-plasmon decay occurs [17].

The maximum proton energy was measured for both GT and plane targets (PTs) as a function of α. The results for 20 μm thick plane targets and 23 μm thick GT are shown in Fig. 3. Most of the data have been obtained for a grating depth of 0.5 μm, with a few points from 0.3 μm deep GT yielding very similar energy values. The PTs show a variation of proton energy with α, which is well fitted by a $\sin^2\alpha/\cos\alpha$ function. Such scaling may be simply understood as due to the variation of the normal component of the electric field **E** ($\propto \sin\alpha$) and of the focal spot size ($\propto 1/\cos\alpha$) [16]. In contrast, for GT the proton energy has a broad maximum (corresponding to ≈ 2.5 times the plane target energy for the same angle) near the resonant angle of 30°. Figure 3 suggests that the resonant peak overlaps to the "geometrical" $\sin^2\alpha/\cos\alpha$ scaling; thus, the energy might be increased using gratings with larger resonant angles. The reflected light signal from the frosted glass (also reported in Fig. 3) shows a dip around 30° for the grating targets, which is not observed for PT and is a signature of increased absorption.

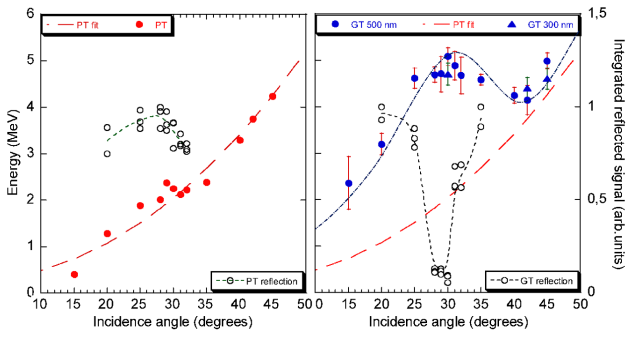

FIG. 3 (color online). Maximum proton energy (filled data points) and reflected light signal (empty data points) as a function of incidence angle α. Left and right frames correspond to 20 μm thick plane targets and to 23 μm thick grating targets, respectively. Filled circles and triangles correspond to 0.5 and 0.3 μm deep gratings, respectively. The (red) dashed line is proportional to $\sin^2\alpha/\cos\alpha$. The other lines are guides for the eye.

A significant enhancement of the proton energy is also observed for small incidence angles (down to 15°), far from the resonant value. This effect is explained by a mechanism similar to that observed in targets covered with regular pattern of microspheres [18]. At a structured surface, electrons can be dragged out in vacuum from the tip of a modulation by the component of **E** parallel to the target plane even at normal incidence and may reenter into the plasma near the tip of a neighboring modulation there delivering their energy, similar to the simple model of "vacuum heating" absorption [19] that thus becomes efficient also at small angles. For large angles of incidence and P polarization, the electron motion near the laser-plasma interface is dominated by the component of **E** perpendicular to the surface; thus, the structured targets behave more similarly to the plane ones. With the use of S polarization, for which both vacuum heating of electrons by **E** and SW excitation in GT are ruled out, no protons of energy above the detection threshold of $\simeq 400$ keV were observed for both PT and GT. This suggests that "$\mathbf{J} \times \mathbf{B}$" heating effects are negligible due to the high plasma density despite the relativistically strong intensity.

Two simulation campaigns using different PIC codes, EMI2D [12] and ALADYN [20], were performed to support the interpretation of the experimental results. The EMI2D simulations considered a 20 μm thick, proton plasma slab with density $n_e = 100n_c = 1.56 \times 10^{23}$ cm^{-3} and initial temperatures $T_e = 1$ keV, $T_i = 0.1$ keV and a laser pulse of 30 fs duration (FWHM of Gaussian envelope), 1.6×10^{19} W/cm^2 peak intensity, and homogeneous in the transverse direction (plane wave). The ALADYN simulations considered a $n_e = 120n_c = 1.87 \times 10^{23}$ cm^{-3}, $T_e = T_i = 0$, two-species slab composed of a 0.8 μm thick $Z/A = 1/2$ layer, a 0.05 μm thick rear layer of protons, and a laser pulse with 25 fs duration (FWHM of $\sin^2$ envelope), 2×10^{19} W/cm^2 peak intensity, and a Gaussian transverse profile with 4 μm focal waist diameter. The grating periodicity was $2\lambda = 1.6$ μm in both cases and as in the experiment, and different values of the peak-to-valley grating depth δ were investigated ($\delta = 0.53$ μm for EMI2D and $\delta = 0.2$–0.4 μm for ALADYN, respectively).

Figure 4 shows simulation results for the maximum energy of protons and the fractional absorption, as a function of the incidence angle. A quantitative comparison with experimental data is not implied because of the unavoidable computational limitations in the PIC modeling of TNSA and the reduction to a 2D geometry (see e.g., Ref. [21]). Nevertheless, the qualitative behavior observed in the experiment is reproduced by both sets of simulations, the maximum energy being in correspondence with the resonant angle. The agreement is improved for the smallest value of the grating depth ($\delta = 0.2$ μm), about half the nominal value; in this case, the cutoff energy for GTs is close to the plane targets value at 45°, and the enhancement factor at 15° also gets closer to the experimental

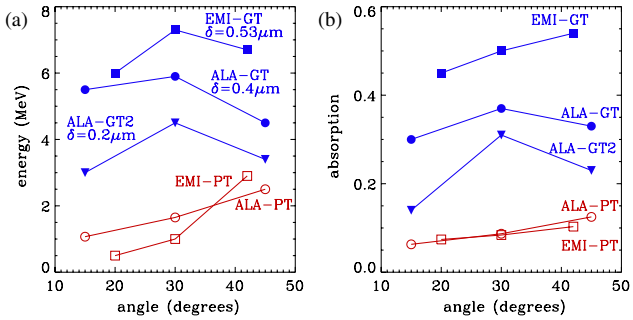

FIG. 4 (color online). 2D PIC simulation results: (a) cutoff energy of protons; (b) fractional absorption. Empty and filled symbols refer to PTs and GTs, respectively. Squares are data from EMI2D (EMI) simulations with grating depth $\delta = 0.53$ μm for GT, and circles and triangles are data from ALADYN (ALA) simulations for $\delta = 0.4$ and 0.2 μm, respectively. The data correspond to a time $t = 350$ fs for EMI2D and $t = 200$ fs for ALADYN, respectively, relative to the time $t = 0$ at which the pulse peak reaches the target.

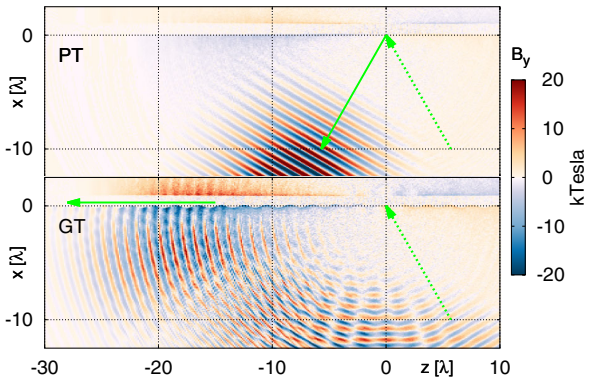

FIG. 5 (color online). 2D PIC simulation results: snapshots at $t = 75$ fs of the magnetic field B_y (normal to the simulation plane) in the interaction at 30° with both plane (PT) and grating (GT) targets of 0.8 μm thickness. The laser axis of incidence is marked by the dashed arrows. For the GT, a wave propagating near the target surface (on the left upper side) and reflection at several diffraction orders are apparent, whereas the PT plot is dominated by the specularly reflected pulse. The thick arrows give the propagation direction of the surface (for GT) and reflected (for PT) waves. See the text for parameters.

result. This observation suggests that some smoothing of the surface modulation occurs during the interaction or prior to it, as for instance, a residual picosecond pedestal to the femtosecond pulse may lead to some preheating and expansion of the target. A smaller depth of the grating reduces the "geometrical enhancement" out of resonance but does not prevent the latter from occurring since the periodicity is preserved. Additional EMI2D simulations confirmed that the energy enhancement in GT disappears neither in the presence of a sub-λ density gradient at the front side nor for longer 60 fs pulses (which favor expansion and smoothing during the interaction), allowing us to obtain energies up to 18 MeV [22].

For both codes, additional simulations showed that the resonance smears out by either decreasing the plasma density or increasing the laser intensity. This observation further supports the evidence that the interaction occurs at solid density and that at high intensity there is a significant SW resonance broadening due either to "detuning" of the plasma frequency, which depends on the field amplitude in the relativistic regime, or to strong absorption. The latter is strongly increased in grating targets simulations, although not strictly proportional to the proton energy as shown in Fig. 4(b).

Figure 5 (from ALADYN thin foil simulations) shows the magnetic field component B_y normal to the simulation plane in the case of incidence 30°, for both a PT and a resonant GT. In the latter case, the strong component localized near the surface and propagating in the direction of incidence is a signature of the SW excitation. The phase velocity v_f and wavelength are very close to c and λ, respectively, in agreement with the SW dispersion relation that gives $v_f/c \simeq 1 - n_c/(2n_e) = 0.996$ for $n_e/n_c = 120$. The comparison also shows the lower amplitude of the field reflected from the GT as well as the reflection at several diffraction orders.

In conclusion, we have provided experimental evidence of absorption enhancement that is consistent with the resonant excitation of a surface wave in a grating target, at laser intensities higher than 10^{19} W cm^{-2}. The increase in coupling efficiency has been observed most clearly through the measurement of maximum proton energies emitted from the target. To further increase the proton energy, either different values of the grating periodicity and the target thickness may be used or the grating modulation might be embedded in complex target designs (see e.g., Ref. [23]). Our results show that the availability of laser system with ultrahigh contrast may allow us to use structured targets for enhanced absorption also at the highest intensities available today and to extend investigations of plasmonics in the relativistic regime.

The authors acknowledge fruitful discussions with Dr. P. Audebert (LULI, France). The research leading to these results has received funding from LASERLAB-EUROPE (Grant No. 284464, EC's 7th Framework Programme), proposal n.SLIC001693. This work was also supported by the Conseil Général de l'Essonne (ASTRE program) by Region Ile de France (SESAME Project), by Saphir Consortium (OSEO), the RTRA Triangle de la Physique, the French Agence Nationale de la Recherche (ANR) under Ref. BLAN08-1_380251, by the Czech Science Foundation (Project No. P205/11/1165), by ECOP project No. CZ.1.07/2.3.00/20.0087, by ELI-Italy funded by CNR, and by MIUR (Italy) via the FIR project SULDIS. EMI2D simulations were performed using HPC resources from GENCI-CCRT (Grant No. 2012-t2012056851). For ALADYN simulations, we acknowledge PRACE for access to resource FERMI based in Italy at CINECA, via the project LSAIL.

*tiberio.ceccotti@cea.fr
†andrea.macchi@ino.it

[1] M. Borghesi *et al.*, Fusion Sci. Technol. **49**, 412 (2006); H. Daido, M. Nishiuchi, and A. S. Pirozhkov, Rep. Prog. Phys. **75**, 056401 (2012); A. Macchi, M. Borghesi, and M. Passoni, Rev. Mod. Phys. **85**, 751 (2013).

[2] R. Toth, S. Fourmaux, T. Ozaki, M. Servol, J. C. Kieffer, R. E. Kincaid, and A. Krol, Phys. Plasmas **14**, 053506 (2007); L. M. Chen *et al.*, Phys. Rev. Lett. **100**, 045004 (2008); A. Lévy *et al.*, Appl. Phys. Lett. **96**, 151114 (2010); Z. Zhang *et al.*, Opt. Express **19**, 4560 (2011).

[3] S. Dobosz, G. Doumy, H. Stabile, P. D'Oliveira, P. Monot, F. Réau, S. Hüller, and Ph. Martin, Phys. Rev. Lett. **95**, 025001 (2005); J. Osterholz, F. Brandl, T. Fischer, D. Hemmers, M. Cerchez, G. Pretzler, O. Willi, and S. Rose, Phys. Rev. Lett. **96**, 085002 (2006); F. Perez *et al.*, Phys. Rev. Lett. **104**, 085001 (2010).

[4] J. J. Santos *et al.*, Phys. Rev. Lett. **89**, 025001 (2002); P. Köster *et al.*, Plasma Phys. Controlled Fusion **51**, 014007 (2009); P. McKenna *et al.*, Phys. Rev. Lett. **106**, 185004 (2011).

[5] G. Kulcsár, D. AlMawlawi, F. Budnik, P. Herman, M. Moskovits, L. Zhao, and R. Marjoribanks, Phys. Rev. Lett. **84**, 5149 (2000); S. Bagchi, P. P. Kiran, M. K. Bhuyan, S. Bose, P. Ayyub, M. Krishnamurthy, and G. R. Kumar, Appl. Phys. B **88**, 167 (2007); H. Sumeruk, S. Kneip, D. Symes, I. Churina, A. Belolipetski, T. Donnelly, and T. Ditmire, Phys. Rev. Lett. **98**, 045001 (2007); S. Kneip *et al.*, High Energy Density Phys. **4**, 41 (2008); U. Chakravarty, P. A. Naik, B. S. Rao, V. Arora, H. Singhal, G. M. Bhalerao, A. K. Sinha, P. Tiwari, and P. D. Gupta, Appl. Phys. B **103**, 571 (2011); S. Mondal *et al.*, Phys. Rev. B **83**, 035408 (2011); A. Zigler *et al.*, Phys. Rev. Lett. **106**, 134801 (2011).

[6] H. Raether, *Surface Plasmons on Smooth and Rough Surfaces and on Gratings*, Springer Tracts in Modern Physics No. 111 (Springer, New York, 1988).

[7] S. A. Maier and H. A. Atwater, J. Appl. Phys. **98**, 011101 (2005).

[8] J.-C. Gauthier *et al.*, Proc. SPIE Int. Soc. Opt. Eng. **2523**, 242 (1995); S. Kahaly, S. Yadav, W. Wang, S. Sengupta, Z. Sheng, A. Das, P. Kaw, and G. Kumar, Phys. Rev. Lett. **101**, 145001 (2008); G. Hu *et al.*, Phys. Plasmas **17**, 033109 (2010); S. Bagchi, P. P. Kiran, W.-M. Wang, Z. M. Sheng, M. K. Bhuyan, M. Krishnamurthy, and G. R. Kumar, Phys. Plasmas **19**, 030703 (2012).

[9] B. Dromey, S. Kar, M. Zepf, and P. Foster, Rev. Sci. Instrum. **75**, 645 (2004); C. Thaury *et al.*, Nat. Phys. **3**, 424 (2007).

[10] M. Cerchez, A. L. Giesecke, C. Peth, M. Toncian, B. Albertazzi, J. Fuchs, O. Willi, and T. Toncian, Phys. Rev. Lett. **110**, 065003 (2013).

[11] M. Raynaud, J. Kupersztych, C. Riconda, J. C. Adam, and A. Heron, Phys. Plasmas **14**, 092702 (2007).

[12] A. Bigongiari, M. Raynaud, C. Riconda, A. Héron, and A. Macchi, Phys. Plasmas **18**, 102701 (2011).

[13] A. Bigongiari, M. Raynaud, C. Riconda, and A. Héron, Phys. Plasmas **20**, 052701 (2013).

[14] A. Lévy *et al.*, Opt. Lett. **32**, 310 (2007).

[15] H. C. Kapteyn, M. M. Murnane, A. Szoke, and R. W. Falcone, Opt. Lett. **16**, 490 (1991).

[16] T. Ceccotti, A. Lévy, H. Popescu, F. Réau, P. D'Oliveira, P. Monot, J. Geindre, E. Lefebvre, and Ph. Martin, Phys. Rev. Lett. **99**, 185002 (2007).

[17] L. Veisz, W. Theobald, T. Feurer, H. Schillinger, P. Gibbon, R. Sauerbrey, and M. S. Jovanović, Phys. Plasmas **9**, 3197 (2002); A. Tarasevitch, C. Dietrich, C. Blome, K. Sokolowski-Tinten, and D. von der Linde, Phys. Rev. E **68**, 026410 (2003); L. A. Gizzi *et al.*, Proc. SPIE Int. Soc. Opt. Eng. **6634**, 66341H (2007).

[18] D. Margarone *et al.*, Phys. Rev. Lett. **109**, 234801 (2012); V. Floquet *et al.*, J. Appl. Phys. **114**, 083305 (2013).

[19] F. Brunel, Phys. Rev. Lett. **59**, 52 (1987).

[20] C. Benedetti, A. Sgattoni, G. Turchetti, and P. Londrillo, IEEE Trans. Plasma Sci. **36**, 1790 (2008).

[21] A. Sgattoni, P. Londrillo, A. Macchi, and M. Passoni, Phys. Rev. E **85**, 036405 (2012).

[22] A. Bigongiari, Ph.D. thesis, Ecole Polytechnique, 2012.

[23] S. A. Gaillard *et al.*, Phys. Plasmas **18**, 056710 (2011).

Monoenergetic ion beams from ultrathin foils irradiated by ultrahigh-contrast circularly polarized laser pulses

O. Klimo,* J. Psikal, and J. Limpouch

Faculty of Nuclear Sciences and Physical Engineering, Czech Technical University in Prague, Brehova 7, 115 19 Praha 1, Czech Republic

V. T. Tikhonchuk

Centre Lasers Intenses et Applications, Université Bordeaux 1-CNRS-CEA, 33405 Talence Cedex, France

(Received 3 September 2007; published 17 March 2008)

Acceleration of ions from ultrathin foils irradiated by intense circularly polarized laser pulses is investigated using one- and two-dimensional particle simulations. A circularly polarized laser wave heats the electrons much less efficiently than the wave of linear polarization and the ion acceleration process takes place on the front side of the foil. The ballistic evolution of the foil becomes important after all ions contained in the foil have been accelerated. In the ongoing acceleration process, the whole foil is accelerated as a dense compact bunch of quasineutral plasma implying that the energy spectrum of ions is quasimonoenergetic. Because of the ballistic evolution, the velocity spread of an accelerated ion beam is conserved while the average velocity of ions may be further increased. This offers the possibility to control the parameters of the accelerated ion beam. The ion acceleration process is described by the momentum transfer from the laser beam to the foil and it might be fairly efficient in terms of the energy transferred to the heavy ions even if the foil contains a comparable number of light ions or some surface contaminants. Two-dimensional simulations confirm the formation of the quasimonoenergetic spectrum of ions and relatively good collimation of the ion bunch, however the spatial distribution of the laser intensity poses constraints on the maximum velocity of the ion beam. The present ion acceleration mechanism might be suitable for obtaining a dense high energy beam of quasimonoenergetic heavy ions which can be subsequently applied in nuclear physics experiments. Our simulations are complemented by a simple theoretical model which provides the insights on how to control the energy, number, and energy spread of accelerated ions.

DOI: 10.1103/PhysRevSTAB.11.031301 PACS numbers: 52.38.Kd, 52.50.Jm, 52.65.Rr, 52.40.Kh

I. INTRODUCTION

Collimated beams of energetic ions produced in interactions of short intense laser pulses with solid density thin foil targets have been demonstrated in experiments [1–4] and particle simulations [5]. These ion beams are attracting much attention due to a wide range of their potential applications covering high resolution radiography imaging, probing for strong electrostatic fields induced in plasmas, radioisotope production, isochoric heating, cancer therapy etc. [6]. Many of these applications require a narrow (quasimonoenergetic) energy spectrum of accelerated ions with a relatively low energy spread. The depth-dose distributions of energy deposited by such ion beams exhibit a strong Bragg peak at the end of the penetration range and thus they can heat a relatively small and well-defined volume inside the target to high temperatures.

The energy distribution of energetic ions obtained in the current experiments is usually exponential with almost 100% energy spread up to a cutoff energy [7]. A tailoring of the energy distribution of ions has been demonstrated via the target material composition [8,9]. In this case, a quasimonoenergetic spectrum of light ions may be produced from their interaction with the fastest heavy ions. However, a significant fraction of the absorbed laser energy is contained in the heavy ion bunch and thus acceleration of light ions is not really efficient. Moreover, only the light ions demonstrate a remarkable peak in the energy spectrum and this process is not suitable for acceleration of monoenergetic bunches of heavy ions.

In this paper, an alternative and a fairly efficient mechanism capable of producing monoenergetic bunches of ions of varies species is presented and studied using the particle-in-cell (PIC) simulations. This ion acceleration mechanism takes place in the radiation pressure dominant regime. The laser beam pushes electrons from the front surface into the target via the ponderomotive force. A strong positive quasistatic electric field is induced due to the resulting charge separation and through this field the momentum acquired by electrons from the laser beam is efficiently transferred to ions. We find that the momentum transfer is maximized when an ultrahigh-contrast circularly polarized laser wave is normally incident on the surface of an overdense foil. In this case most electron heating mechanisms (resonance absorption, vacuum heating, heating by the oscillating ponderomotive force) are inefficient and the laser beam is largely reflected. The acceleration process is accompanied by the ballistic evo-

*klimo@watt.fjfi.cvut.cz

lution of the target itself. Because of this evolution, the momentum delivered by the laser pulse is distributed among the target ions so that most of them attain approximately the same velocity in the laser propagation direction. Therefore, it is possible to accelerate the whole foil as a compact dense block of quasineutral plasma. An ultrathin foil accelerated this way can be regarded as a plasma mirror copropagating with the laser pulse like in [10]. Moreover, the presented mechanism enables one to control both the energy and the number of ions contained in the monoenergetic bunch.

Acceleration of ions from ultrathin foils has been theoretically studied in several recent papers [11–13] for similar laser-target interaction conditions. The main difference in our approach is in utilization of a circular laser polarization that inhibits a strong electron heating. Energetic electrons are really undesirable in our approach as they may cause a premature explosion of the foil, whereas it is necessary to confine the ions in a relatively small volume for their efficient acceleration. The interaction of a circularly polarized laser beam with a dense target has been studied by Macchi *et al.* [14] and we will develop the ideas presented in their paper. We consider a thinner foil and a longer or more energetic laser pulse. This enables us to go a step further and to describe an acceleration process after the whole target is set in motion.

This paper presents the results of our PIC simulations and their interpretations based on a simple analytical model. Comparison with the experimental results is not provided. To our knowledge, the only experiment of ion acceleration with the circularly polarized laser pulse has been published in [15]. However, the parameters of the laser pulse and of the foil used in [15] do not fall into the range of applicability of our ion acceleration model as the foil is too thick and dense and the laser pulse is not enough energetic to set the whole foil into motion. Nevertheless, the results of this experiment confirm the crucial point of our ion acceleration model, namely, that the efficiency of electron heating is largely suppressed when a high-contrast circularly polarized laser pulse is used in comparison with the linearly polarized pulse.

The paper is organized as follows. Our numerical models based on the 1D3V and 2D3V PIC simulation codes are presented in Sec. II. Section III A describes the theory of the ion acceleration process and introduces the basic principles of our ion acceleration mechanism. Ions are accelerated, in particular, in the forward laser incidence direction in the case of this mechanism. Therefore, the backward acceleration of ions will not be discussed here. The role of electron heating and the influence of the laser wave polarization are of prime importance and they are described in Sec. III B. The results of our 1D3V PIC simulations are presented and discussed in detail in Sec. III C. It is explained how the monoenergetic distribution of the accelerated ions emerges naturally in this case. Our results are accompanied by a simple analytical model which provides the basic insight into the ion acceleration mechanism and which can be used for reasonably accurate estimates. The simulations of a multiple species target are presented and discussed in Sec. III D. The effects related to the second, lateral dimension are studied in Sec. III E by using the 2D3V PIC simulation code. The main results and ideas presented in this paper are summarized in Sec. IV together with our concluding remarks.

II. PARTICLE-IN-CELL SIMULATION MODELS

Numerical simulations of the laser beam interaction with a foil target and of the process of ion acceleration are performed using one- and two-dimensional particle-in-cell (PIC) codes. Both codes are relativistic and electromagnetic and they take into account all three components of particle velocities and electric and magnetic fields (1D3V and 2D3V). The one-dimensional PIC code [16] evolved from the code LPIC + + [17]. It includes elastic collisions and variable plasma ionization, but for computational reasons neither of these features is employed in the simulations presented in this paper. To resolve the processes taking place during the interaction with enough accuracy and to avoid significant numerical noise, the size of the computational cell in one-dimensional simulation is smaller than 0.3 nm and each cell is occupied by more than 600 particles. The simulation box is always sufficiently large so that no particles can reach the boundaries during the simulation time.

The two-dimensional simulations have been performed with our newly developed collisionless PIC code [18] which is parallelized via OpenMP scheme. In this code, the relativistic equations of motion are solved by the two-step Boris rotation and the fields in the positions of particles are determined by bilinear interpolation. The zigzag scheme [19] is employed for calculation of current densities in order to guarantee an automatic compliance with the continuity equation. The boundary conditions for particles are absorbing, particles reaching the boundaries of the simulation box are frozen. For the solution of Maxwell's equations, damping layers are added near the simulation box boundaries in order to eliminate spurious reflection of outgoing electromagnetic waves. The corresponding algorithm described for the one-dimensional geometry in Ref. [20] was successfully adopted for two-dimensional case in our code.

III. THEORETICAL MODEL AND THE SIMULATION RESULTS

A. Ion acceleration process—basic principles

In the interaction of a short intense laser pulse with an overdense foil target, the ions are accelerated by the quasistatic charge-separation fields induced on both target surfaces, at the front and the rear sides. The electrostatic field

on the front side of the target is generated by fast electrons accelerated into the target. This field gives rise to the return current and also to acceleration of ions toward the target interior. Moreover, the fast electrons penetrating through the target create an electrostatic field at the rear surface of the foil which is responsible for acceleration of ions into the vacuum. The latter process is known as the target normal sheath acceleration (TNSA) [5].

It has been demonstrated [21] that acceleration of ions at the rear surface is more efficient and it is responsible for the highest energy and best collimated ion beams in the conditions of many recent experiments. This is, in particular, due to a steep plasma density profile on the rear surface of the target which remains undisturbed until the energetic electrons arrive there. In consequence, the self-induced rear side quasistatic electric field can be very strong and concentrated in a very narrow region. On the other hand, the density profile on the front surface of the target, which is formed due to absorption of the laser prepulse, is usually relatively long, the electrostatic field extends over a wider spatial region, and it is weaker. Moreover, the front surface is bent by the ponderomotive force of the laser pulse during the interaction and thus the accelerated ions may have a relatively large angular spread. The formation of preplasma on the laser side of the target has been suppressed in recent experiments [22,23] where the contrast of laser pulse was improved by using the plasma mirrors. In this case, acceleration of ions from the front surface of the target may also be efficient. The fast electron circulation across the foil makes a little difference in front and rear side acceleration in ultrathin targets in this case.

The ion acceleration process described in this paper makes use of ultrathin foils and ultrahigh-contrast laser pulses as well. However, the essential requirements of the presented ion acceleration mechanism are the suppression of the electron heating and enhancement of the front side acceleration (FSA) process via the laser ponderomotive force. Compliance to these conditions enables one to accelerate the target as a compact block of a quasineutral plasma. This is achieved by a combination of the FSA process and the ballistic evolution of the target itself. Because of the localization of the ponderomotive force on the front side, all ions of the target are successively crossing the acceleration zone and gaining approximately the same velocity. Moreover, the slower and heavier ions are stronger accelerated since they are affected for a longer time by the force. This naturally results in acceleration of the whole target to a well-defined macroscopic propagation velocity. The relatively cold electrons are enabling a good screening of the electrostatic field and thus preventing the accelerated ions from the Coulomb explosion.

B. Fast electrons—influence of the laser polarization

The role of fast electrons is very important in most of the recently proposed ion acceleration mechanisms [5,13,21]. Here, the term ''fast electrons'' stands especially for those relativistic electrons, which are energetic enough to easily cross the potential barrier formed by the quasistatic charge-separation field at the front side of the target and to penetrate the foil subsequently. These electrons contribute to the electrostatic field at the front surface, which is responsible for the FSA process. However, in a steep plasma density profile the fast electron density is much less than the plasma density, and the electrostatic charge-separation field may be largely screened by the return current cold electrons in this region. Thus, the contribution of fast electrons to the FSA process is not essential. Consequently, the generation of fast electrons should be suppressed in order to inhibit the rear side acceleration.

It was demonstrated in Refs. [14,24] and confirmed also in our simulations, that the strong electron heating is suppressed in a circularly polarized laser wave if it is incident normally onto a very steep overdense plasma. This is a direct consequence of the absence of the component of the laser electric field perpendicular to the target surface, the absence of the oscillating part of the ponderomotive force, and the absence of the underdense plasma. This allows one to avoid the well-known electron acceleration processes such as the ponderomotive acceleration by the oscillating $\mathbf{j} \times \mathbf{B}$ force, the resonance absorption, the vacuum heating, and the parametric instabilities. The laser pulse energy is largely reflected, at least in the initial stage of the interaction, and the laser pulse acts on the target surface as a piston by the force of radiation pressure.

There is also another reason for avoiding the electron heating. As the foil considered in this ion acceleration concept should be very thin, the fast electrons circulate freely across the target and create the electrostatic field almost symmetrically on the front and rear surfaces. This produces the target expansion and an initially ultrathin foil may explode before the end of the acceleration process and become transparent for the laser light. This is a self-enhancing effect, as the scale length of the density profile on the front side of the target increases, the laser pulse penetrates deeper and generation of fast electrons becomes more and more efficient during the foil expansion.

The difference between the circular polarization (CP) and the linear polarization (LP) of the laser wave interacting with an ultrathin foil is clearly seen in Figs. 1 and 2. These figures result from one-dimensional (1D) PIC simulations where a 100 fs long ($\sin^2$ temporal envelope) laser pulse with the wavelength $\lambda = 800$ nm and the maximum intensity of 1.5×10^{20} W/cm^2 is normally incident (from the left) on the foil. The density of ions in the foil is 3.5×10^{22} cm^{-3} and the initial thickness of the foil is 32 nm. The foil has a steplike density profile on both surfaces and it is composed of cold fully ionized carbon ions and electrons with initial temperature $T_0 = 1$ keV.

In the case of CP pulse shown in Fig. 1(a), the energy distribution of electrons follows approximately a two-

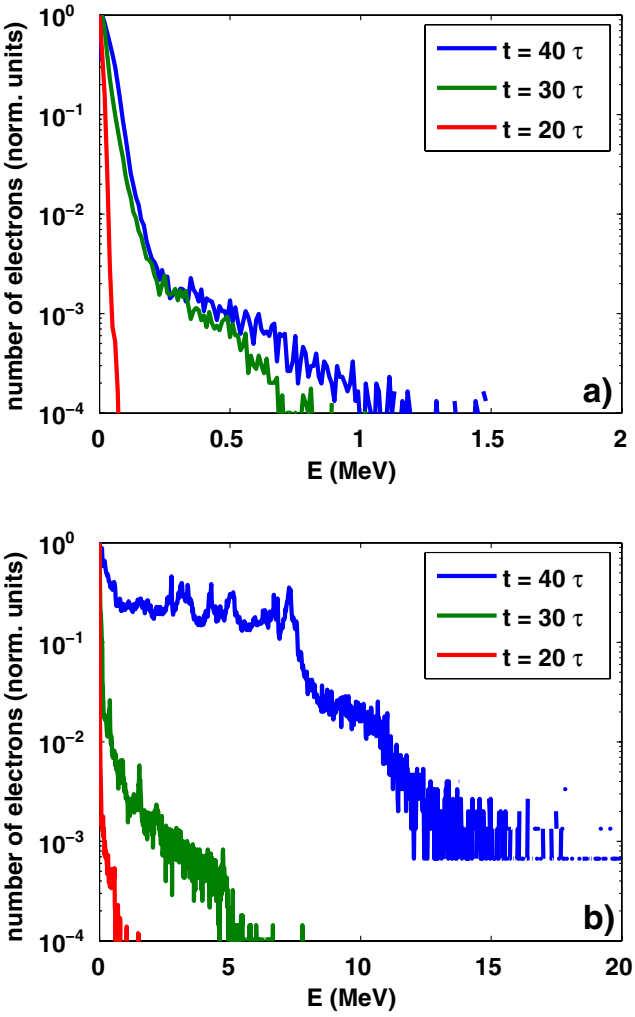

FIG. 1. (Color) Temporal evolution of the electron energy distributions in the 1D3V PIC simulation during the interaction of circularly (a) and linearly (b) polarized relativistic ($I_L = 1.5 \times 10^{20}$ W/cm^2) laser pulse with ultrathin (32 nm) overdense ($n_e = 2.1 \times 10^{23}$ cm^{-3}) foil. The distributions contain all simulation electrons and they are normalized to have the same maximum values. The laser pulse is 100 fs long (sin^2 temporal envelope) and the time is measured in laser periods τ. At the time 40τ (maximum intensity on the target), the foil irradiated by the linearly polarized laser pulse becomes transparent to the laser pulse. Note the different scales on abscissas.

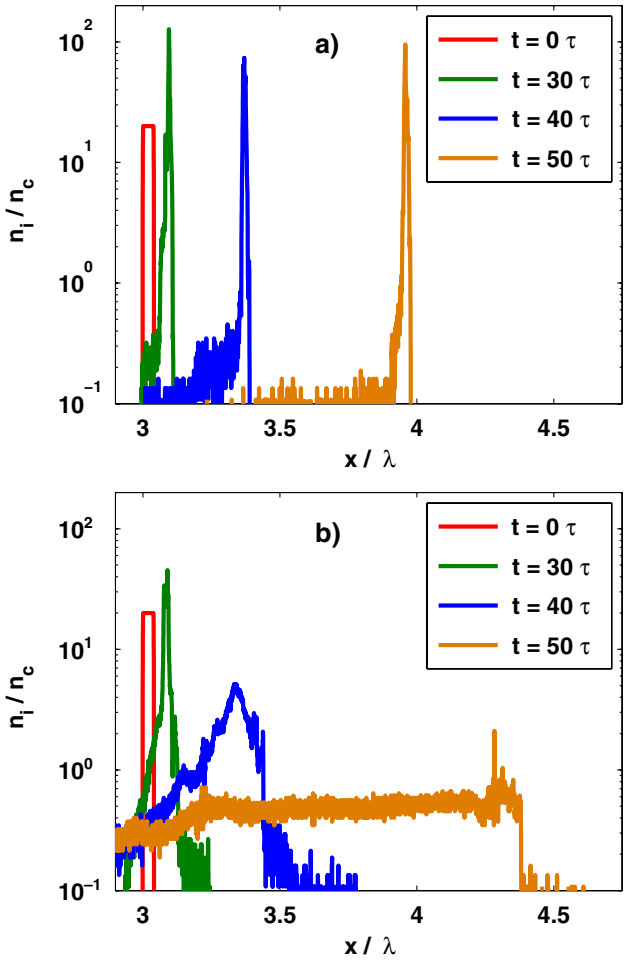

FIG. 2. (Color) Temporal evolution of the ion density profiles obtained in the same simulation as in Fig. 1. The foil irradiated by the CP laser pulse propagates in the laser incidence direction and it conserves its initial volume [panel (a)]. The foil irradiated by the LP laser pulse explodes [panel (b)].

temperature Maxwellian function. The higher temperature corresponds to the electrons located in the laser-target interaction region, whereas the lower temperature corresponds to the bulk electrons which are deeper inside the target. The temperatures of both components change only weakly around the laser pulse maximum. In the case of the LP pulse shown in Fig. 1(b), the temperature of electrons is much higher and, moreover, it rises many times during the interaction. Almost all electrons are relativistic around the laser pulse maximum ($t = 40\tau$, where $\tau = \lambda/c$ is the laser wave period) in this case and the foil is already underdense to the relativistic laser pulse at this time (as can be seen in Fig. 2). Thus, the electrons have also the velocity component associated with oscillations in the field of the laser wave.

Considering the difference between electron heating with CP and LP laser pulse, it is also possible to argue by the motion of a single electron in the field of the laser wave and the plasma field. In the case of the CP laser pulse, electrons are confined in the laser-target interaction region by the quasistatic electric field induced in plasma, as will be demonstrated in the next subsection. On the front surface of the region where electrons are compressed, the smoothly changing ponderomotive force of the laser pulse is balanced by the electrostatic force and the motion of electrons in the target normal direction is negligible. Thus, the electron trajectory is smoothly circular in the plane parallel with the target surface and the kinetic energy of electrons depends, in particular, on the laser pulse ampli-

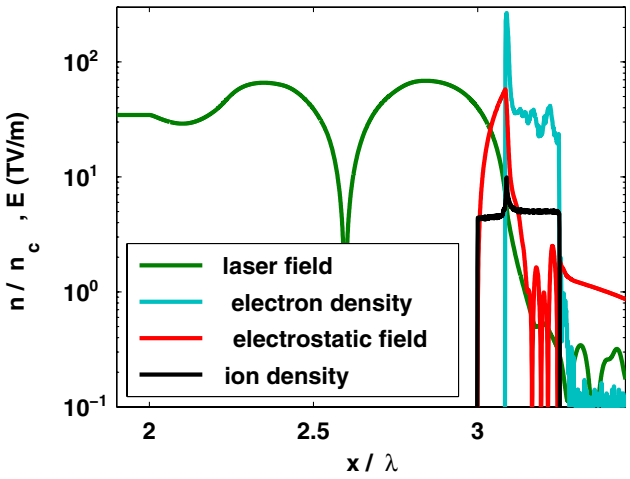

FIG. 3. (Color) Snapshot of the electric field, $|\vec{E}|$, and the densities of electrons and ions taken from the 1D3V PIC simulation. The 80 fs long (a rectangular temporal envelope) CP laser pulse with the wavelength of 800 nm and the intensity of 3.5×10^{20} W/cm^2 is normally incident (from the left) on the ultrathin (200 nm) overdense ($n_e = 5.25 \times 10^{22}$ cm^{-3}) fully ionized carbon foil. The time is one laser period after the beginning of the interaction. The densities are normalized to the critical density.

tude. On the contrary, the motion of electrons in the case of the LP laser pulse may be very rough as the ponderomotive force drives their oscillations across the target surface and their energy may change between the maximum and zero at twice the laser period.

Figure 2 shows that the whole foil is accelerated in the laser propagation direction in both cases at the early stage of the interaction, $t < 30\tau$. Nevertheless, near the laser pulse maximum, the foil irradiated by the LP wave explodes in both directions due to a very high electron temperature, whereas the foil irradiated by the CP wave still conserves its initial volume. The same behavior as the one observed in our PIC simulations with CP laser pulse, Fig. 2(a), has also been presented in [25] (in Fig. 3). That paper is however concerned with electron compression by the CP laser pulse inside an ultrathin foil and it does not discuss this behavior in the context of ion acceleration.

Further simulations presented in the next section provide more details of the ion acceleration process driven by the CP laser pulse.

C. Circular polarization—formation of a monoenergetic ion spectrum

The 1D3V PIC simulation results included in this subsection rely on the following parameters. A circularly polarized laser wave with the wavelength $\lambda = 800$ nm and the intensity $I_L = 3 \times 10^{20}$ W/cm^2 is normally incident (from the left) onto the front surface of the foil. The laser pulse is 80 fs long (30τ) and it has a rectangular temporal envelope. This temporal profile is chosen to simplify the analytical estimates that accompany our simulation results. This has no major effect on the ion acceleration process. It behaves the same way as it is shown in Fig. 2. The foil used in our simulation is 200 nm thick (0.25λ) and it is composed of cold fully ionized carbon ions of the density 8.75×10^{21} cm^{-3}. The initial electron temperature is $T_0 = 1$ keV. The foil has steplike density profiles on both surfaces and it is initially located 3λ from the left boundary of the simulation box.

The laser-target interaction can be divided into several subsequent steps, each of them taking place on a different time scale. The first step is characterized by a very rapid response of electrons to the electromagnetic field of the laser wave. Namely, the ponderomotive force pushes all electrons from the target surface deeper into the target. This stage is very short and it lasts only until a quasisteady state is established where the radiation pressure is balanced by the electrostatic pressure. This pressure balance is also included in the ion acceleration model of Macchi *et al.* [14]. Amplitude of the electrostatic field on the front surface of the cloud of compressed electrons is consequently given by the relation

$$\frac{1}{2}\varepsilon_0 E_{\mathrm{es}}^2 = \frac{1+R}{c} I_L, \tag{1}$$

where I_L is the laser pulse intensity, c is the velocity of light, and R is the target reflectivity. (We assume $R \simeq 1$ in the following estimates.) According to Eq. (1), the electrostatic field has the same amplitude as the laser field. This is confirmed by the snapshot shown in Fig. 3 which was taken from the PIC simulation just one laser period after the beginning of interaction. The amplitudes of both the electrostatic and the laser electric field are presented there. The incident laser electric field amplitude should be constant in the case of a circular polarization and a rectangular temporal profile. The oscillating structure observed in Fig. 3 in the front of the target is due to the interference of the incident and the reflected laser waves. This interference results from the very fast (adiabatic) compression of electrons by the radiation pressure and it is not so significant if the laser pulse has a smooth temporal envelope.

The amplitude of the incident laser field, 34 TV/m, can be deduced from the plateau before the spatial position 2λ in Fig. 3. This is comparable to the electrostatic field amplitude 57.5 TV/m. The structure of the electrostatic field conforms with our essential requirement of the dominance of the FSA process.

As the equilibrium state is established, the compressed electrons do not further propagate deeper into the target because they are confined by the strong electrostatic field in a thin layer. (This layer is denoted as compressed electron cloud in the following.) As the electrons are expelled from the laser field, their heating is suppressed. Therefore, the whole population of electrons in the compressed electron cloud has a single temperature and they

form the higher temperature Maxwellian part in the energy distribution shown in Fig. 1(a).

The electrostatic field in the electron depletion layer is defined by the space charge separation. Its amplitude can be calculated from the Poisson equation as

$$E_{\mathrm{es}}(l) = en_{e0}l/\varepsilon_0, \tag{2}$$

where n_{e0} is the initial free electron density in the target and l is the thickness of the electron depletion layer. Combining the Poisson equation with the pressure balance given in Eq. (1), one can estimate l as follows:

$$l = \sqrt{\frac{4I_L\varepsilon_0}{cn_{e0}^2e^2}}. \tag{3}$$

This equation gives the thickness of electron depletion layer of 70.8 nm for the parameters of Fig. 3. This is in agreement with the calculated value of 66.8 nm.

As the ion acceleration scheme presented in this paper relies on the front side acceleration process, it is desired to confine the strongest electrostatic field at the target front surface or in its close vicinity. Consequently, the target thickness d should be larger than l. Otherwise, the electrostatic pressure would not be able to balance the radiation pressure and the electron cloud will be fully expelled from the target volume. This will result in an acceleration of all ions with the strongest electrostatic field at the target rear side as it was described in Ref. [12]. However, we are not interested in this regime, as the acceleration process there cannot benefit from the ballistic evolution.

Ions start to respond to the strong electrostatic field in the second step of interaction as it was described in the model [14]. The charge-separation field in the electron depletion layer is not uniform. It is increasing with the distance from the initial target surface up to the position of the compressed electron cloud, where it attains its maximum given by Eq. (1). The velocity of ions in the electron depletion layer thus depends on their initial position. The velocity of ions in the compressed electron cloud can be found by equating the electrostatic pressure and the dynamic pressure

$$\rho v_i^2 = \varepsilon_0 E_{\mathrm{es}}^2, \tag{4}$$

where $\rho = m_i n_i$ is the ion mass density and the dynamic pressure due to electrons has been neglected. It results from the equation of motion with the Lorentz force and Eq. (4) that the electrostatic field with amplitude E_{es} accelerates ions to the velocity v_i during the time interval of $\tau_2 = 1/\omega_{pi}$ (≈ 1.5 laser period for the parameters used in the PIC simulation); that is, the characteristic time scale of the second step is the inverse ion plasma frequency.

As a first approximation, let us assume that all ions in the compressed electron cloud gain the same velocity v_i. Then they will cross the electron cloud and form a shock structure propagating into the target with this velocity. For the sake of simplicity, let us further neglect any ion acceleration process taking place behind the compressed electron cloud. Then the population of ions deeper inside the target consists of three distinct groups: the stationary unperturbed ions, the ions accelerated inside the compressed electron cloud to the velocity v_i, and the ions originating from the electron depletion layer with the velocities ranging between v_i and $2v_i$.

The phase space of ions in the second stage is shown in Fig. 4(a) at the time of 4τ after the beginning of interaction. The gray color transition in the background depicts the strength of the electrostatic field versus the spatial position. The electrostatic field is strongest at $x = 3.15\lambda$, at the instantaneous position of the front of the compressed electron cloud. According to Eqs. (1) and (4), the velocity v_i gained by ions in the compressed electron cloud should be approximately $0.05c$. However, as the electrostatic field in the PIC simulation is slightly weaker than the one predicted

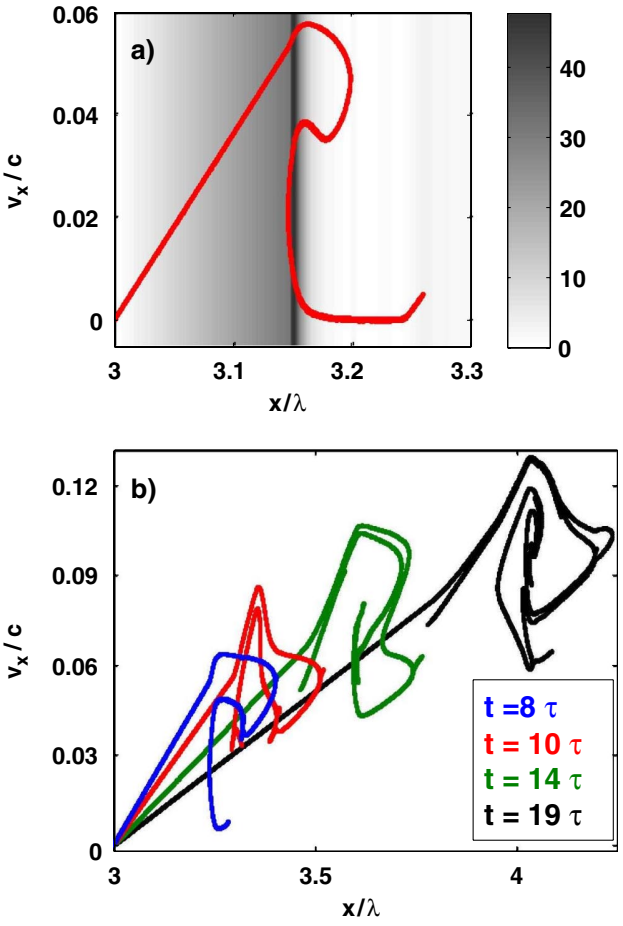

FIG. 4. (Color) (a) Ion phase space at the interaction time 4τ. The gray color transition in the background denotes the actual strength of the electrostatic field in the units of TV/m (see the colorbar for the scale). (b) Snapshots of the ion phase space at time 8, 10, 14, and 18τ. The loop originates from the combination of the front side acceleration and the ballistic evolution. The simulation parameters are the same as in Fig. 3.

by Eq. (1), the velocity of ions accelerated in the electron cloud is lower, $0.038c$. The ions with velocities higher than v_i are originating from the electron depletion layer as discussed above. One can also distinguish acceleration of ions from the target rear side which was initially located at the spatial position of 3.25λ. This is in agreement with the structure of the electrostatic field observed in Fig. 3. However, this process is much weaker and it is neglected in what follows.

Up to this point, the theory and simulation results presented here are in accordance with the ion acceleration model of Macchi *et al.* [14]. However, we follow the acceleration of ions further. Once all ions in the compressed electron cloud are accelerated and enter the nonperturbed target, the electron cloud is pushed deeper into the target as well. It can move only a distance of the order of skin depth because there it encounters the next layer of stationary ions. These ions start to experience the strong electrostatic field and they are accelerated just like the ones before. The acceleration of ions thus proceeds layer by layer and because of the constant radiation pressure assumed here, more and more ions are gradually accelerated to the same velocity v_i. In reality, the acceleration process is not steplike but continuous. The inertia of electrons is much lower than that of ions. Therefore, the compressed electron cloud adjusts its position and density self-consistently to the moving ions. The electrostatic potential at the front side of the target does not change, and the acceleration proceeds as a stationary wave.

This third step of ion acceleration lasts until the moment when the compressed electron cloud reaches the position of the former rear target surface. At that moment all ions are accelerated to nearly the same velocity v_i, Eq. (4). That gives us an opportunity to estimate the duration of this interaction stage, τ_3, from the condition that the momentum of the whole target (per unit area) equals the radiation pressure exerted on the target surface during that time,

$$\rho v_i d = 2I_L \tau_3 / c. \tag{5}$$

According to this expression, the third stage terminates at 10τ after the beginning of the interaction in our PIC simulation. This is confirmed by the temporal evolution of the ion phase space in Fig. 4(b), where all the ions from inside of the foil have already been accelerated to velocities higher than v_i at the time 10τ. The ions from the electron depletion layer are an exception. Some of these ions remain relatively slow and because of the electrostatic field shape they will not be able to catch the moving foil any more.

The fourth stage begins after the whole target has been accelerated. This stage is actually the most important one in the present context. The ballistic evolution of the accelerated ions plays an important role there. The slower particles are overtaken by the faster ones and, consequently, they appear on the actual target front side where they are strongly accelerated. In fact, the fourth stage can be characterized by a series of loops of the accelerated ion bunch in the phase space. The first of these loops is demonstrated in the temporal evolution of the ion phase space in Fig. 4(b). The ballistic evolution combined with the continuing front side acceleration naturally results in acceleration of all ions to a well-defined macroscopic propagation velocity. Moreover, the velocity spread of accelerated ions does not increase with time as can be also seen in Fig. 4(b). In consequence, the target volume is conserved and therefore it is possible to maintain the acceleration process in the same form for a long time. One may accelerate the ion bunch to a very high velocity comparable with the velocity of light. This is a big advantage in comparison with the TNSA mechanism, where the accelerating electrostatic field decreases with time.

The velocity of the ion bunch after the interaction, v_f, can be found from Eq. (5) by setting the time on the right-hand side to the laser pulse duration t_L. Using this macroscopic approach, we neglect the laser absorption and the dispersion of ion velocities, which is justified by the fact that the target occupies a relatively small volume of the phase space during the interaction. The final velocity v_f of the accelerated ion bunch calculated in this manner is about $0.152c$. The average velocity of ions in the accelerated foil in the PIC simulation after the interaction is $0.149c$, if the slower ions from the electron depletion layer are not included (the velocity averaged over all ions is $0.145c$). The mean velocity dispersion in this example is about $0.014c$, that is, less than 10%.

From the final velocity of the ion bunch, v_f, one can calculate its kinetic energy, $\rho d v_f^2/2$, and estimate the fraction of the laser beam energy, $\eta I_L t_L$, absorbed by ions as

$$\eta = \frac{2I_L t_L}{c^2 \rho d} = \frac{v_f}{c}. \tag{6}$$

It is obvious that this expression and all the estimates given above are valid only in the limit $v_f \ll c$. The theory can be generalized to include the relativistic mass of ions and the laser pulse absorption due to the Doppler shift of the reflected light. However, as will be demonstrated below, it does not seem to be realistic to accelerate the whole foil to a relativistic velocity where these corrections are necessary. The laser pulse energy absorption into ions is 14.3% in the present PIC simulation.

Equation (6) states that the efficiency of the acceleration process increases linearly with the laser pulse duration for a given laser intensity. Such a behavior is not common in short pulse laser-target interactions, and it results from the fact that the fourth stage of interaction is characterized by a direct momentum transfer from the laser pulse to the whole target. On the contrary, during the third stage of interaction the number of accelerated ions scales linearly with the time, while their maximum velocity remains constant.

Then the efficiency of laser energy transformation, $\eta = v_i/c$, is independent on time.

If the desired energy of monoenergetic ions is given, their momentum is also defined, assuming that these ions propagate only in the laser incidence direction. The maximum momentum that can be transferred to the target is $2I_L t_L/c$. As this ion acceleration scheme relies purely on the momentum transfer from the laser pulse to the monoenergetic ion beam, it should be the most efficient ion acceleration mechanism in terms of the total energy contained in the monoenergetic bunch of ions. In all other ion acceleration schemes, a significant amount of momentum (energy) may be contained in the population of hot electrons or in the population of ions with different energies.

It can be seen in Fig. 5, that the velocity spread of the ion beam does not increase during the fourth stage of interaction. This spread is less than $2v_i$ at the end of the third stage, and the majority of accelerated ions have their velocities in the range $v_f \pm v_i$ after the interaction. For the case of simulation presented here, the ratio between v_f and v_i is only 3.8. By increasing the laser pulse duration, one can increase the final velocity v_f while keeping the same velocity v_i. This opens a possibility to control the energy spread of ions through the foil thickness and the laser pulse duration.

For example, to keep the number density and the energy of the accelerated ions constant, one should prescribe the foil areal density and the laser pulse energy. Then the interaction of a longer laser pulse with a thinner foil should provide the ion beam with a lower energy spread. This is demonstrated in the PIC simulation with the 2 times longer laser pulse and 2 times denser foil in Fig. 5. According to Eq. (4), the initial velocity spread of ions is decreased 2 times in this case and thus the width of the energy distribution is reduced to one-half of the energy distribution in the former case.

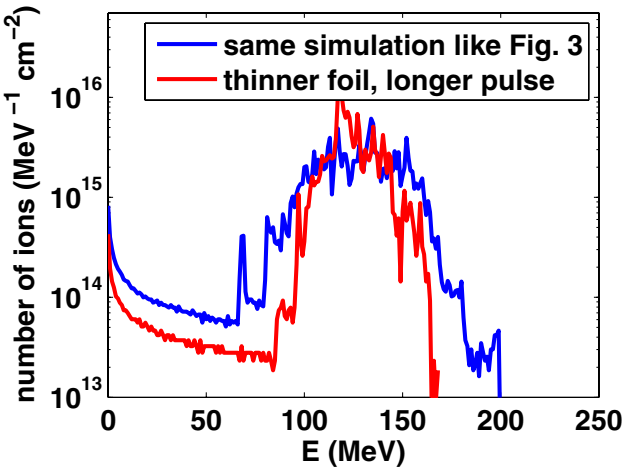

FIG. 5. (Color) Energy distributions of ions at the end of the laser foil interaction. The wider distribution (blue) corresponds to the simulation parameters given in Fig. 3, the narrower distribution (red) corresponds to the simulation where the foil is 2 times thinner and 2 times denser and the laser pulse is 2 times longer and 2 times less intense.

The fifth stage is the last one. It covers the target evolution after the end of the laser pulse. The temperature of electrons increases immediately after the radiation pressure is removed. Then the electrostatic field accelerates electrons across the front boundary of the target and they are gaining the energy $\epsilon_e \sim 2I_L/cn_{e0} \approx 3$ MeV. As the ion bunch still occupies a relatively small volume, the accelerated electrons start to circulate across the bunch creating electrostatic fields which accelerate ions from both surfaces of the target. Nevertheless, if the fourth stage of interaction is sufficiently long, the kinetic energy of ions, $\sim \frac{1}{2} m_i v_f^2$, is significantly higher than the kinetic energy of accelerated electrons, ϵ_e, and, therefore, the electrons should not broaden much the energy spectrum of ions. The electrons are gradually cooling, whereas the dense bunch of ions evolves also ballistically. Thus, in the later time, the electron Debye length becomes smaller than the dimension of the bunch and the Coulomb repulsion becomes insignificant.

The crucial point of the ion acceleration approach discussed here is that the overall quasineutrality of the target is maintained until the end of the laser-target interaction. Accordingly, the Coulomb repulsion takes place only at the late stage of the process and plays a much less important role than in the TNSA. It is possible to maintain a narrow ion spectrum until they hit a detector or a secondary target.

A good one-dimensional stability of the ion acceleration process and reliability of our analytical estimates have been tested in PIC simulations covering a wide range of interaction parameters. The laser pulse intensity has been varied in the range between 3×10^{19} and 3×10^{20} W/cm^2, the laser pulse duration between 40 and 400 fs, the foil thickness between 30 and 300 nm, and the foil mass density between 0.08 and 0.8 g/cm^3. The acceleration process remains stable even if the density profile on the foil surface is not steplike but steep, with a relatively short scale length $L < 0.1\lambda$. The process described above should theoretically be stable whenever the radiation pressure is much higher than the thermal pressure and the electron heating is inhibited so that the ion acceleration process takes place, in particular, on the target front side.

D. Targets composed of multiple species of ions

Because of their highest charge to mass ratio, protons are accelerated with a higher efficiency than other heavier ions in most ion acceleration experiments. Even if the target material does not contain protons, they are usually present in thin layers of contaminants on the target surface. These contaminants have to be removed in order to accelerate higher Z ions efficiently with the TNSA process. However,

in the case of the ponderomotive ion acceleration, the light ions do not radically inhibit the acceleration efficiency of heavier ions and thus the contamination of the target surface does not pose a serious problem.

At the first sight, it might be surprising, but there is no charge state dependence in the theory given above. In fact, the only two parameters depend on the charge state of ions. These are the thickness of the electron depletion layer (through the dependence on $n_{e0} = Zn_{i0}$) and the ion plasma frequency. For example, with a lower charge state, the ion plasma frequency is shorter and the ion acceleration takes a longer time. On the other hand, the thickness of the electron depletion layer is larger in this case and thus more ions are accelerated at the same moment. These two effects cancel each other and, consequently, the charge state dependence is removed from the theory. Therefore, in addition to a narrow energy spread in the bunch of accelerated ions, the presented ion acceleration process is also advantageous in the sense that all ions are accelerated to the same velocity irrespectively to their charge to mass ratio. Moreover, due to the ballistic evolution of the target during the acceleration process, all ions acquire the same velocity even in the targets composed of multiple species. This means that higher Z ions may attain much higher energy than protons without the need of removing any proton rich contaminants from the target surface.

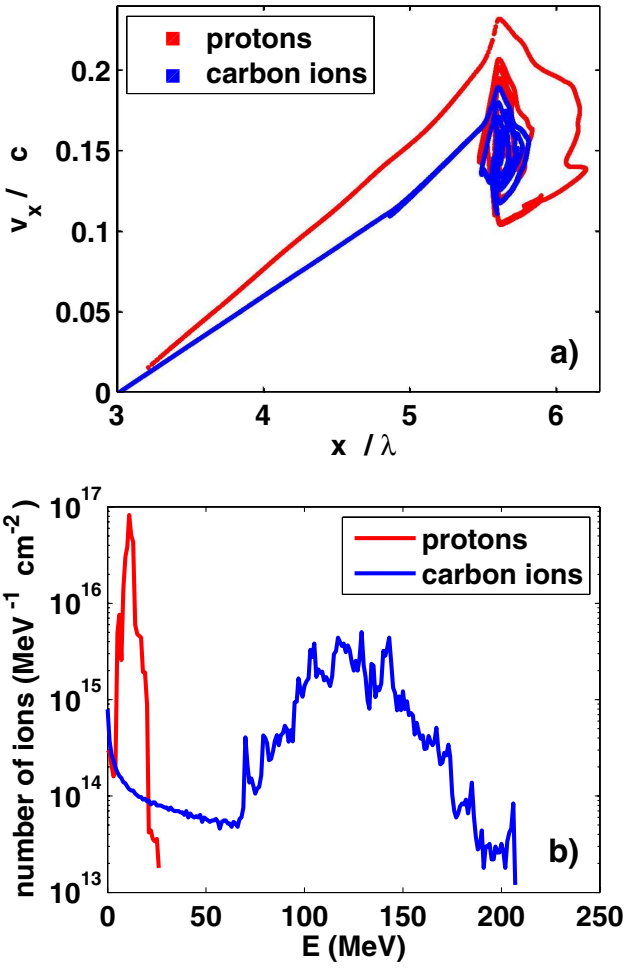

FIG. 6. (Color) Ion phase space (a) and ion energy distributions (b) at the end of the interaction of the laser pulse with a foil composed of fully ionized carbon ions and protons. The density of carbon ions is 7.5×10^{21} cm^{-3} and the density of protons is 2 times higher. The other simulation parameters are the same as in Fig. 3 (the mass density of the foil is the same as well).

For demonstration, the results of ion acceleration in 1D3V PIC simulation with a multispecies target are presented in Fig. 6. The parameters of the laser pulse and the foil are the same as in the previous subsection with the exception of the material composition. The foil now contains the carbon ions with the density of 7.5×10^{21} cm^{-3} and protons with the density of 1.5×10^{22} cm^{-3} (a low density plastic foil CH_2). The mass density of the foil is not changed. The ion phase space at the end of the interaction plotted in Fig. 6(a) demonstrates that both ion species are accelerated to a nearly same velocity. To be exact, the average velocity of carbon ions is $0.143c$ and the average velocity of protons is $0.155c$. A higher charge to mass ratio of protons results in their stronger acceleration (higher v_i) in the electrostatic field which is confined on the target front side by the heavier carbon ions. Therefore, some protons propagate ahead of the beam of carbon ions and the beam of accelerated protons has also slightly higher velocity spread. However, in spite of a higher number density of protons, the efficiency of acceleration of carbon ions is not decreased significantly and their narrow energy distribution is not affected, as can be seen in Fig. 6(b).

Multispecies targets may even be advantageous in this ion acceleration process as in the fifth stage after the end of laser pulse, the protons help to confine the narrow spectrum of carbon ions. The response of protons to the electrostatic field is faster and thus they, at least partially, screen the field produced by fast electrons on the foil surface.

E. Two-dimensional simulations

The presented ion acceleration process may be sustained in nearly the same form for a long time in one spatial dimension and it seems possible to accelerate ion beams to relativistic velocities. However, multiple spatial dimensions bring some additional constraints, which might be difficult to overcome. Let us consider the same laser intensity (3×10^{20} W/cm^2), the same foil thickness (200 nm), and the same foil mass density (0.176 g/cm^3) like in the previous subsection. According to Eq. (5), the protons will be accelerated to 1 GeV with the laser pulse duration of 460 fs. In fact, the pulse would have to be even longer if one accounts for the relativistic mass correction and the finite reflectivity. As the acceleration force is constant in time, one easily calculates the distance, $\sim$60 μm, which the foil moves during the acceleration process. This distance is typically longer than the

Rayleigh length of the focused laser pulse. Therefore, one has to account for the laser pulse divergence or a laser pulse guiding has to be considered. The radial dependence of the laser intensity may also increase the energy spread in the ion bunch, according to Eq. (5).

Another constraint comes from the finite size of the laser focal spot on the target. Because of the radial dependence of the laser intensity, the foil feels spatially dependent acceleration force and its surface becomes curved during the interaction. Once the curvature of the foil surface becomes significant, the local angle of incidence of the laser beam may provoke an enhanced absorption and a strong electron heating in certain spatial regions. The foil shape $s(r)$ at the time $t < t_L$ can be calculated in the same manner as above, supposing that the laser intensity radial distribution is known:

$$s = \frac{I_L(r)}{2c\rho d} t^2. \tag{7}$$

The incidence angle of the laser pulse is ~45° at the points where $ds/dr \sim 1$. At the moment when this condition is verified, the electron heating becomes efficient and the surface of the hole created in the foil starts to feel a strong acceleration force in the radial direction. This is the result of the ponderomotive force of the laser pulse, which is reflected from the lateral surface of the hole inward the hole. Let us suppose that the laser beam has a Gaussian intensity profile, $I_L(r)$, with the full width at half maximum σ. Then from Eq. (7) we estimate the time interval, where the presented ion acceleration model is applicable, as

$$t_{\max} \simeq \sqrt{\sigma c \rho d / I_0}. \tag{8}$$

For the parameters considered above and for $\sigma = 10$ μm, the maximum acceleration time is about 200 fs and the maximum velocity and energy of the monoenergetic beam of protons are about $0.36c$ and 70 MeV, respectively. The ratio between the duration τ_3 of the first three stages of the acceleration process and $t_{\max}$ depends on the ratio between the focal spot size and the target thickness. One has to use relatively large focal spots with a flattop intensity profile for acceleration to high ion energies, which makes this acceleration process more complicated with respect to the experimental feasibility. It is also possible to increase $t_{\max}$ by shaping the foil or by using the foil with spatially dependent thickness or mass density. However, it would be difficult to realize such an optimization in experiment because of the pointing accuracy of the laser beam. One may also think of utilizing an ultrasmall foil with spatial dimensions smaller than the laser focal spot. However, fast electrons would be efficiently produced on the borders of such a foil and the ion acceleration process will be significantly affected [26].

Nevertheless, as the above constraints come from the motion of the foil, the limiting factor is the velocity of ions, not their energy. Therefore, the ion acceleration process described in this paper is better suited for acceleration of heavier ions, which may attain kinetic energies in the hundred MeV range.

The effects of the radial intensity distribution on the ion acceleration were studied with our 2D3V PIC code. The laser pulse has a flattop intensity profile on the target surface as shown in Fig. 7. It has a Gaussian spatial intensity profile with $\sigma = 2.9$ μm at the edges and a 5 μm intensity plateau in the central part. The carbon foil is 14 μm wide in the transverse dimension and other parameters are the same as in the 1D simulation presented in Sec. III C. The spatial density profile of ions in the simulation box is shown in Fig. 8 at two time instants. The ion density is in units of the critical density (1.75×10^{21} cm^{-3}). In panel (a), the ion density is plotted in the time 8τ which is slightly before the end of the third ion acceleration stage. The imprint of the laser intensity profile on the density of ions is clearly seen. The interaction time is 28τ in panel (b) and the hole in the center of the foil is observed. The time 28τ is still smaller than $t_{\max}$, which is 37τ for our simulation parameters. The laser incidence angle onto the lateral borders of the hole is about 35°.

The electric field E_x, pointing in the laser propagation direction, is plotted in Fig. 9. At the time 8τ [panel (a)], one sees the front side electrostatic field which is accelerating the ions. The longitudinal electric field of the laser wave which is due to the finite focal spot can be seen in front of the target. This field may be responsible for enhanced electron heating if the laser beam is tightly focused [27]. Nevertheless, this electron heating does not play an important role in the simulations of the ion acceleration process presented here. The structure of the electric field E_x is more complex in panel (b) at 28τ. It contains the front

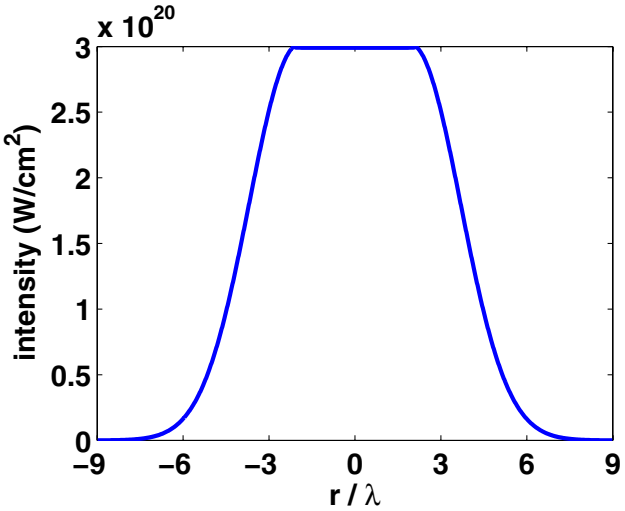

FIG. 7. (Color) Spatial laser intensity profile used in 2D3V PIC simulations. This profile has 5 μm plateau in the central part and it is Gaussian on both sides of the plateau (with the characteristic scale of 2.9 μm).

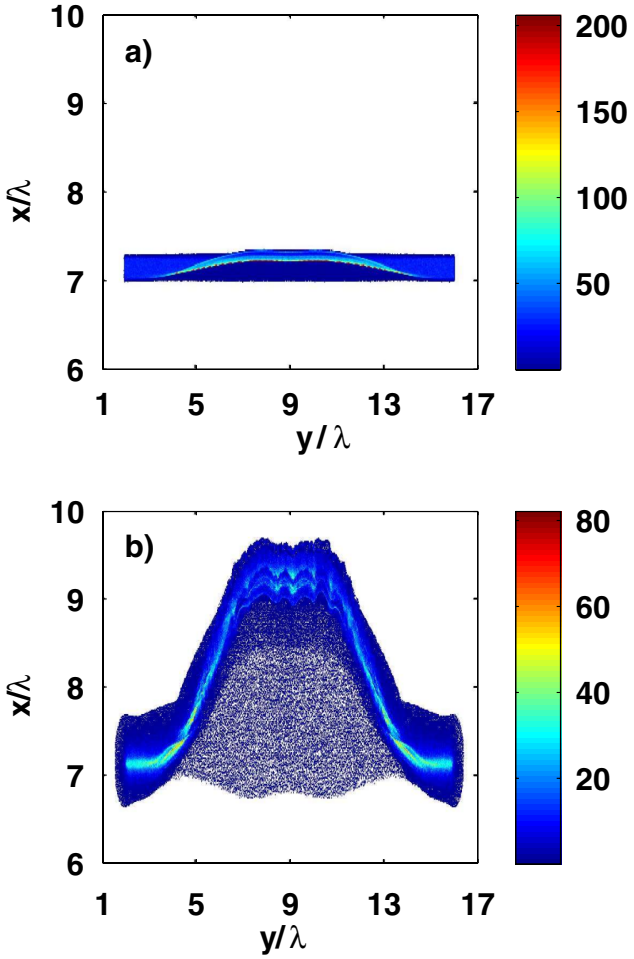

FIG. 8. (Color) Spatial ion density profile in the 2D3V PIC simulation in the interaction time 8τ (a) and 28τ (b). In the interaction time 28τ a hole bored in the central part of the foil can be observed. The simulation parameters are the same as in Fig. 3 with the radial intensity profile of the laser pulse shown in Fig. 7. The ion density is normalized to the critical density and the spatial coordinates are normalized to the laser wavelength. The midpoint of the simulation box is at 9λ and the laser pulse is incident from the bottom.

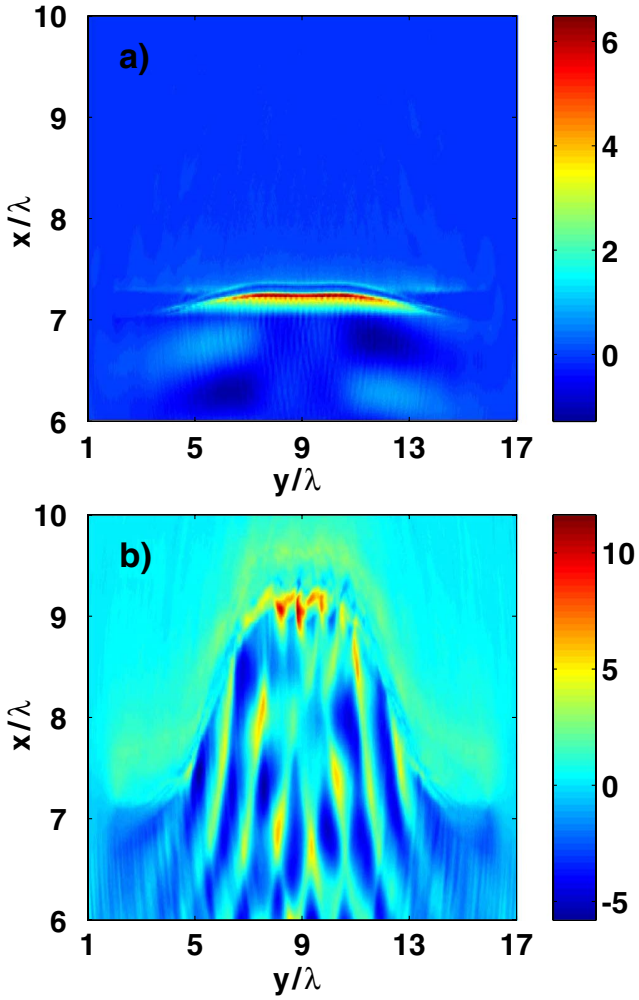

FIG. 9. (Color) Electric field in the laser incidence direction, E_x, in the normalized units $(m_e c\omega/e)$. The simulation parameters and time instants are the same as in Fig. 8. At the interaction time 28τ the field in the central part contains also the specularly reflected part of the laser wave.

side electrostatic field and also the field on the rear side of the foil, which is due to already accelerated fast electrons. Moreover, the laser field reflected from the lateral borders of the hole is clearly visible in the central part. As this field is almost as strong as the field of the incident laser pulse, the radiation pressure strongly pushes the borders of the hole in the transverse direction as well.

The electrostatic field on the front surface of the foil in Fig. 9(b) exhibits a regular structure in the central part. This structure corresponds to the ion density fluctuations observed in the same spatial position in Fig. 8(b). The density fluctuations are probably resulting from the radiation dominated Rayleigh-Taylor instability, which was analyzed in Refs. [10,28]. The growth rate of this instability is

$$\gamma = \sqrt{k_y v_i^2 / 3 l_s}, \tag{9}$$

where k_y is the wave number of the unstable mode, v_i is the ion velocity given by Eq. (4) (in [28] denoted as the Alfvén velocity), and l_s is the collisionless skin depth. The wave number of density fluctuations observed in Fig. 8(b) is about $4\pi/\lambda$ and for the conditions of our simulations, the growth time of this mode (9) should be $\sim 2\tau$. This is approximately the same as the characteristic response time of ions to the electrostatic field $(1/\omega_i)$ and the ion density corrugations become visible in the interaction time of about 25τ.

The phase space of ions plotted in Fig. 10(a) provides a clear evidence that the ion acceleration process in the central part of the foil works in the same way as in the 1D simulation. Only the ions located in the 2λ wide central

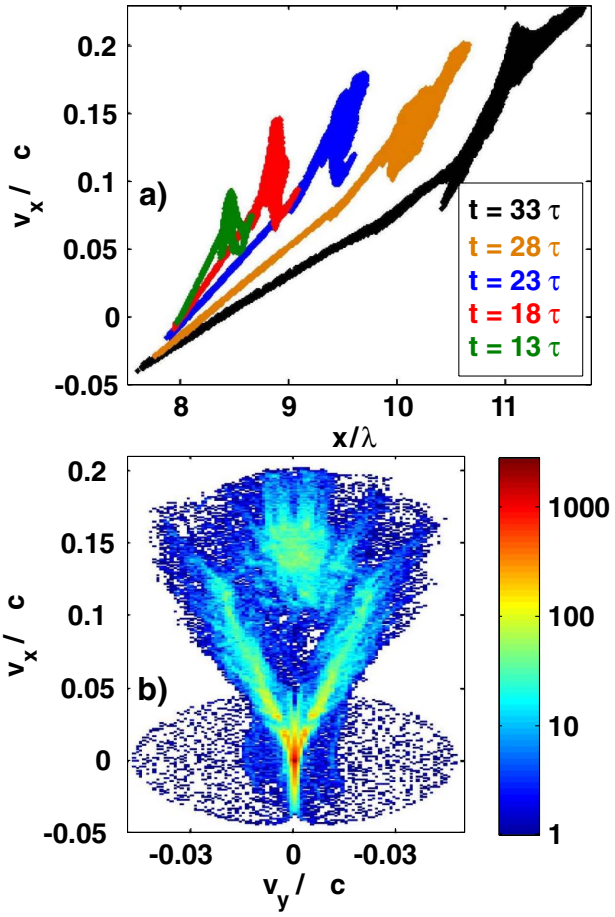

FIG. 10. (Color) Temporal evolution of the ion phase space [panel (a)] and the ion velocity distribution in the interaction time 28τ [panel (b)] in the 2D3V PIC simulation. The parameters are the same as in Fig. 8. The ion phase space contains only ions located in the 2λ wide central part of the simulation box. All ions are included in the velocity distribution in panel (b), where the color scale is logarithmic and the number of ions is in arbitrary units.

region ($8\lambda \leq y \leq 10\lambda$) are included in this figure. It can be seen that, up to the interaction time of 28τ, most of the ions are contained in a single dense bunch, which has a well-defined macroscopic velocity and a relatively low velocity spread. However, the bunch of ions is significantly dispersed at the time 33τ. Therefore, the interaction should be terminated before the time of about 30τ to preserve a narrow spectrum of accelerated ions. Thus, the limiting time given by Eq. (8), which is about 37τ in this case, is slightly overestimated.

The distribution function plotted in Fig. 10(b) at the time of 28τ contains all ions. The monoenergetic bunch accelerated in the central part of the foil can be recognized here. As the bunch propagates with the velocity of about $0.15c$ in the x direction and its velocity spread in the y direction is lower than $0.02c$, this bunch of ions is relatively well collimated. The transversely expanding borders of the hole created in the foil are also clearly observed. They form a conical jet with the opening angle of about 12°, which is related with the radial distribution of the laser beam intensity. In fact, this is a good sign as it indicates that the slower ions with a broad energy spectrum form a divergent ring structure around the central collimated monoenergetic bunch and thus the slower ions may be easily filtered out. One can also see a significant population of ions which are located outside the focal region and therefore they remain relatively cold.

The energy distributions of ions and electrons in the central part of the foil ($8\lambda \leq y \leq 10\lambda$) are plotted in Fig. 11. The energy distribution of ions in panel (a) exhibits a peak structure, which significantly broadens in time (compare the curves corresponding to the simulation times 28τ and 33τ). However, the peak is clearly visible all the interaction time (33τ). The broadening is due to interaction of ions with the field produced by fast electrons, which are efficiently accelerated in the later stage of the interaction process. To verify that the ion energy distribution remains quasimonoenergetic after the end of the laser-target interaction, we have performed an additional simulation run with a shorter laser pulse (duration of 20τ). The energy distribution of ions resulting at the end (38τ) of this simulation is included in Fig. 11(a). This energy distribution did not change significantly during the last 5τ in the simulation which confirms that the strongest ion acceleration process is over at this time instant.

For comparison, the energy distribution of ions resulting at the end of 1D simulation is also included. The peak from the 1D simulation is narrower, but the difference is in the edges. It is also remarkable that the ions in the 2D simulation attain the same energy earlier than in the 1D simulation, and the final energy of the ion bunch is significantly higher. This feature is again connected to the fast electrons, which contribute not only to the energy spread of accelerated ions but they also increase the average energy of the ion bunch.

The conversion efficiency of the laser pulse energy into the quasimonoenergetic ion bunch accelerated from the central part of the foil ($8\lambda \leq y \leq 10\lambda$) in the 2D simulation with the 20τ long laser pulse is 5.5%. To confirm that acceleration of ions to very high energies is enhanced by using the circularly polarized laser wave, we have also performed 2D simulation with the same parameters but with a linearly polarized laser pulse. The conversion efficiency of laser energy into all ions in the simulation box with energy higher than 50 MeV is 12.2% in the case of circular polarization and only 2.5% in the case of linear polarization.

The temporal evolution of the electron energy spectra in the 2D simulation with the longer (30τ) laser pulse is plotted in Fig. 11(b). In the first part of the interaction ($t \lesssim 23\tau$), the temperature of electrons is relatively low, below

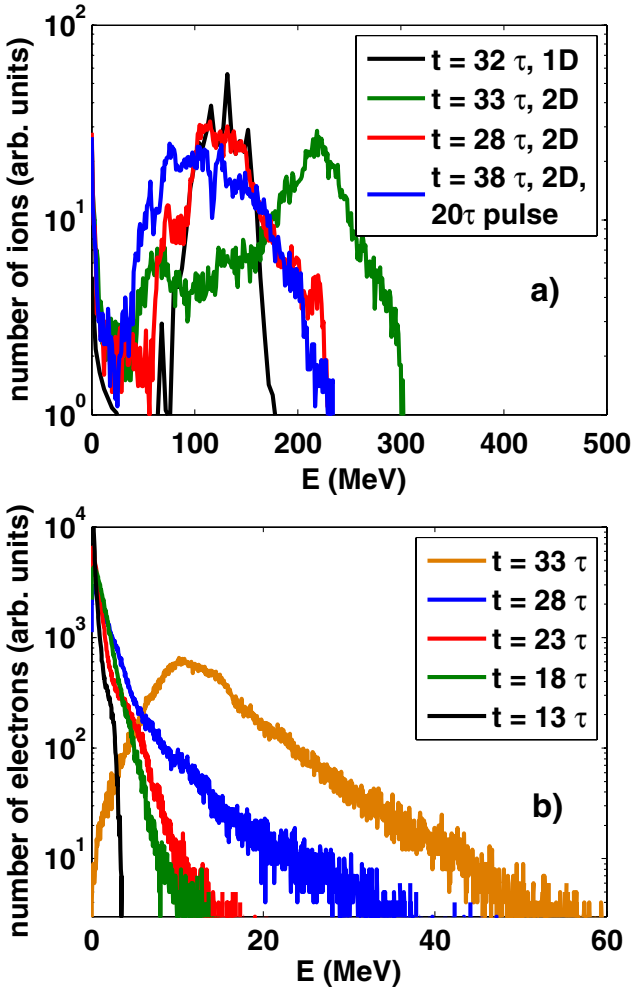

FIG. 11. (Color) The energy distributions of ions [panel (a)] and electrons [panel (b)] in the 2λ wide central part of the simulation box in the 2D3V PIC simulation with the parameters of Fig. 8. The distribution from 1D3V PIC simulation with the same parameters is included for comparison in panel (a). The energy distribution of ions resulting from the 2D3V PIC simulation with a shorter (20τ long) laser pulse is plotted in the time 18τ after the end of the laser-target interaction to demonstrate that the quasimonoenergetic distribution is preserved. The energy distribution of electrons in panel (b) is peaked at very high energy in the time 33τ. This is the consequence of the explosion of the central part of the foil which became underdense to the laser pulse before this time.

1.9 MeV. However, as soon as the surface of the foil gets curved significantly, the temperature of electrons strongly rises and it is already about 3 times higher at the time of 28τ. As noted above, the interaction should be terminated before this time to maintain a narrow energy spread in the bunch of accelerated ions as in the case of the shorter (20τ long) laser pulse. As a consequence of electron heating, the target starts to explode and it becomes transparent to the relativistic laser pulse at the end of the run (33τ). The energy of electrons raises to about 10 MeV.

The limitations imposed on acceleration by laser beam edges could be relaxed significantly, if the target ions are much heavier than the carbon ions considered here.

IV. SUMMARY AND CONCLUSIONS

In this paper, we propose a new mechanism of a monoenergetic ion beam generation that is especially suitable for acceleration of heavy ions where the existing ion acceleration mechanisms are inefficient. This mechanism is based on the interaction of a short intense circularly polarized laser pulse with an ultrathin overdense foil. It is demonstrated that this interaction may result in acceleration of a single dense collimated bunch of ions, which is appropriate for many applications. The formation of a monoenergetic ion spectrum results from a combination of acceleration of ions in the electrostatic field on the front side of the target with the ballistic evolution of the target itself. The unwanted electron heating is suppressed by using the circular laser polarization, a high intensity contrast, and the normal incidence.

The process of formation of a monoenergetic ion bunch proceeds in four subsequent stages: (i) an adiabatic compression of electrons in a thin layer on the front surface of the target, (ii) an acceleration of ions on the front surface of the target in the electron depletion layer and the compressed electron cloud, (iii) a gradual acceleration of all ions contained in the foil, and (iv) a further acceleration of the propagating ion bunch which itself evolves ballistically.

The ion acceleration process is described by a simple analytical theory, which is successfully compared with the results of our one-dimensional PIC simulation model. It is found that the ponderomotive force of a circularly polarized laser wave accelerates the whole ultrathin foil as a compact dense block of quasineutral plasma, which propagates with a well-defined macroscopic velocity. The acceleration process is thus well described by the momentum transfer from the laser pulse to the foil and the efficiency of this process scales with the foil velocity. It may be relatively high and the energy contained in the beam of monoenergetic ions is probably the highest possible of all ion acceleration processes because the ion energy spectrum is formed directly by the laser ponderomotive force.

In the final stage of acceleration, the ballistic evolution of the foil allows for the slower ions to be more strongly accelerated and the macroscopic velocity of the foil increases, while the velocity spread of ions contained in the foil remains constant. The velocity spread of ions in the beginning of this stage is related to the foil density and the laser pulse intensity, and it can be controlled through these parameters. It is also found that during this stage all species of ions attain nearly the same velocity irrespective of their charge to mass ratio. This means that a contamination of the target by lighter ions (protons) is not a hinderance in the acceleration process as both species of ions attain the same velocity and the heavier ions absorb more energy.

The ion acceleration process becomes more complex and less efficient in multiple spatial dimensions. The main obstacle is curving of the front surface of the foil under the radial profile of the laser pulse intensity. To obtain a quasimonoenergetic and well collimated beam of ions, the laser pulse must have a flattop intensity distribution in the focal spot and the interaction must be terminated before the hole bored in the foil becomes too deep and the electron heating starts to be efficient. It is possible to obtain bunches of quasimonoenergetic ions with energies of tens MeV per nucleon. As the constraints on the interaction time in multiple dimensions come from the displacement of the central part of the foil, the limiting factors are connected with the velocity of the ion bunch. By using foils composed of heavier ions, one may attain energies in the hundred MeV range per nucleon. Such ion beams may be especially interesting in nuclear physics experiments.

In two-dimensional PIC simulations, the ion density corrugations caused by the radiation dominated Rayleigh-Taylor (RT) instability are seen at the later stage of the interaction. Such density corrugations may increase the efficiency of electron heating, which may cause an explosion of the quasimonoenergetic ion bunch in both the longitudinal and the transverse dimensions. However, our 2D simulation results indicate that the radial intensity profile of the laser pulse influences the ion acceleration process in the later stage more strongly than the RT instability, and the laser beam intensity distribution poses stronger constraints on the stability of the ion acceleration process.

ACKNOWLEDGMENTS

This work was supported by the Czech Ministry of Education, Youth and Sports under Project No. LC528 and by the Czech Science Foundation under Project No. 202/06/0801. The authors are grateful to John von Neumann Institute for computing in Juelich, Germany, for providing the computational resources, Project No. ECZ040.

Note added.—At this point, we also have to refer to two very recent papers of Zhang *et al.* [29] and of Robinson *et al.* [30], which came to our attention after this paper had been accepted and where acceleration of ions from ultrathin foils by circularly polarized laser pulse had been studied for similar conditions like in this paper. Our theory and results are therefore partially similar and partially complementary to those of [29,30].

[1] S. P. Hatchett *et al.*, Phys. Plasmas **7**, 2076 (2000).
[2] A. Maksimchuk, S. Gu, K. Flippo, D. Umstadter, and V. Y. Bychenkov, Phys. Rev. Lett. **84**, 4108 (2000).
[3] R. A. Snavely *et al.*, Phys. Rev. Lett. **85**, 2945 (2000).
[4] B. M. Hegelich, B. J. Albright, J. Cobble, K. Flippo, S. Letzring, M. Paffett, H. Ruhl, J. Schreiber, R. K. Schulze, and J. C. Fernandez, Nature (London) **439**, 441 (2006).
[5] S. C. Wilks, A. B. Langdon, T. E. Cowan, M. Roth, M. Singh, S. Hatchett, M. H. Key, D. Pennington, A. MacKinnon, and R. A. Snavely, Phys. Plasmas **8**, 542 (2001).
[6] J. F. M. Borghesi and O. Willi, J. Phys.: Conf. Ser. **58**, 74 (2007).
[7] M. Zepf *et al.*, Phys. Rev. Lett. **90**, 064801 (2003).
[8] S. Ter-Avetisyan, M. Schnurer, P. V. Nickles, M. Kalashnikov, E. Risse, T. Sokollik, W. Sandner, A. Andreev, and V. Tikhonchuk, Phys. Rev. Lett. **96**, 145006 (2006).
[9] A. V. Brantov, V. T. Tikhonchuk, O. Klimo, D. V. Romanov, S. Ter-Avetisyan, M. Schnurer, T. Sokollik, and P. V. Nickles, Phys. Plasmas **13**, 122705 (2006).
[10] F. Pegoraro and S. V. Bulanov, Phys. Rev. Lett. **99**, 065002 (2007).
[11] J. Denavit, Phys. Rev. Lett. **69**, 3052 (1992).
[12] T. Esirkepov, M. Borghesi, S. V. Bulanov, G. Mourou, and T. Tajima, Phys. Rev. Lett. **92**, 175003 (2004).
[13] L. Yin, B. J. Albright, B. M. Hegelich, K. J. Bowers, K. A. Flippo, T. J. T. Kwan, and J. C. Fernandez, Phys. Plasmas **14**, 056706 (2007).
[14] A. Macchi, F. Cattani, T. V. Liseykina, and F. Cornolti, Phys. Rev. Lett. **94**, 165003 (2005).
[15] M. Kado *et al.*, Laser Part. Beams **24**, 117 (2006).
[16] O. Klimo, J. Limpouch, and N. Zhavoronkov, J. Phys. IV **133**, 1181 (2006).
[17] R. Lichters, R. E. W. Pfund, and J. Meyer-ter Vehn, Technical Report No. 225, Max-Planck Institute für Quantenoptik, Garching, 1997.
[18] J. Psikal, J. Limpouch, S. Kawata, and A. A. Andreev, Czech. J. Phys. **56**, B515 (2006).
[19] I. Umeda, Y. Omura, T. Tominaga, and H. Matsumoto, Comput. Phys. Commun. **156**, 73 (2003).
[20] T. Umeda, Y. Omura, and H. Matsumoto, Comput. Phys. Commun. **137**, 286 (2001).
[21] Y. Sentoku, T. E. Cowan, A. Kemp, and H. Ruhl, Phys. Plasmas **10**, 2009 (2003).
[22] D. Neely, P. Foster, A. Robinson, F. Lindau, O. Lundh, A. Persson, C. G. Wahlstrom, and P. McKenna, Appl. Phys. Lett. **89**, 021502 (2006).
[23] T. Ceccotti, A. Lévy, H. Popescu, F. Réau, P. D'Oliveira, P. Monot, J. P. Geindre, E. Lefebvre and P. Martin, Phys. Rev. Lett. **99**, 185002 (2007).
[24] T. V. Liseikina and A. Macchi, Appl. Phys. Lett. **91**, 171502 (2007).
[25] B. F. Shen and J. Meyer-ter Vehn, Phys. Plasmas **8**, 1003 (2001).
[26] F. He, H. Xu, Y. W. Tian, W. Yu, P. X. Lu, and R. X. Li, Phys. Plasmas **13**, 073102 (2006).
[27] V. I. Berezhiani and N. L. Shatashvili, Europhys. Lett. **76**, 70 (2006).
[28] E. G. Gamaly, Phys. Rev. E **48**, 2924 (1993).
[29] X. Zhang, B. Shen, X. Li, Z. Jin, F. Wang, and M. Wen, Phys. Plasmas **14**, 123108 (2007).
[30] A. P. L. Robinson, M. Zepf, S. Kar, R. G. Evans, and C. Bellei, New J. Phys. **10**, 013021 (2008).